NASA Technical Memorandum 4309

The NASA Langley Laminar-Flow-Control Experiment on a Swept, Supercritical Airfoil

Evaluation of Final Perforated Configuration

Charles D. Harris, Edward V. Brooks, Jr.,
Patricia G. Clukey, and John P. Stack

APRIL 1992

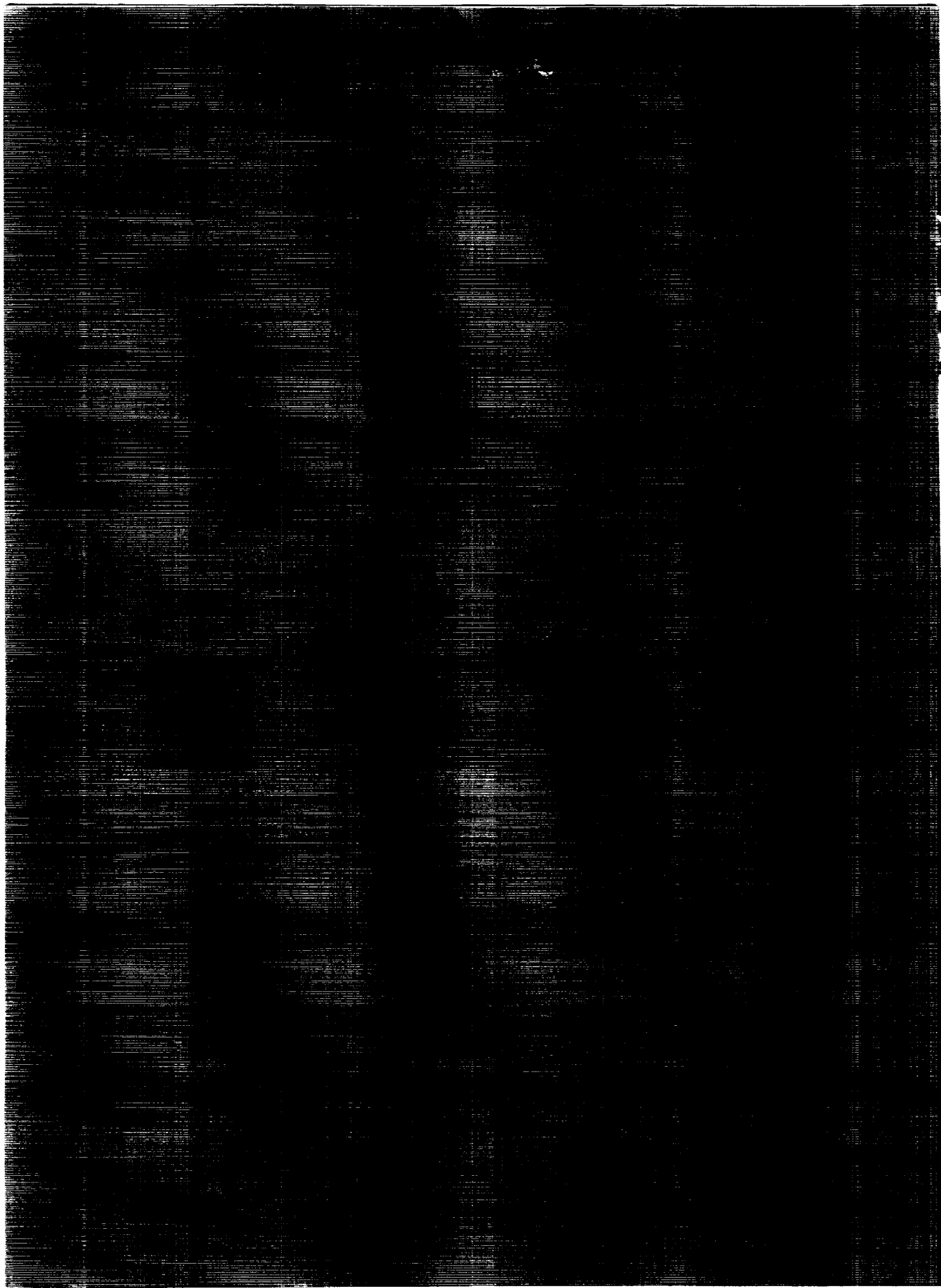

NASA Technical Memorandum 4309

The NASA Langley Laminar-Flow-Control Experiment on a Swept, Supercritical Airfoil

Evaluation of Initial Perforated Configuration

Charles D. Harris, Cuyler W. Brooks, Jr.,
Patricia G. Clukey, and John P. Stack
Langley Research Center
Hampton, Virginia

National Aeronautics and
Space Administration

Office of Management

Scientific and Technical
Information Program

1992

Contents

Summary

The initial perforated-model and tunnel configurations for the laminar-flow-control (LFC) experiment in the Langley 8-Foot Transonic Pressure Tunnel were evaluated and the results are presented. Several general conclusions were reached: (1) the pressure distribution on the model was very sensitive to small variations in angle of attack because of the proximity of the test section wall; (2) within the range of stagnation temperatures investigated (80°F to 100°F), the transition pattern deteriorated with increased temperature; (3) the effects of variations in flap deflection on the model pressure distribution were generally minimal; and (4) the metering holes underneath the perforated surface limited the suction capability of the model. Because of the limited suction capability, this phase of the LFC was interrupted so that the model could be disassembled and the metering holes on the forward and central upper-surface perforated panels enlarged.

Introduction

Large decreases in friction drag can be realized on airfoils if a laminar boundary layer can be maintained either by passive natural laminar flow (NLF), which is controlled through geometric shaping, or by active laminar-flow control (LFC), which usually combines both shaping and local mass transfer through the surface. Experiments have been defined with the overall objective of investigating the physical phenomena associated with active laminar-flow control on advanced supercritical airfoils in the Langley 8-Foot Transonic Pressure Tunnel (8-ft TPT). These experiments were intended to evaluate two concepts for active LFC suction surfaces in combination with supercritical airfoil technology at conditions typical of high-performance transports with swept wings. One suction surface concept involved removing the slow-moving air near the surface through discretely spaced spanwise slots and the other accomplished this by suction through perforated spanwise strips. Requirements for these experiments included modifications to the wind tunnel to achieve the necessary flow quality and contouring of the test section walls to simulate free airflow about a swept-wing model with infinite span at transonic speeds.

An overview of the LFC experiment is reported in reference 1; design concepts of the supercritical LFC airfoil are discussed in reference 2; design of the contoured wind-tunnel liner is discussed in reference 3; modifications to the tunnel are described in reference 4; analytical development of the suction drag equations is given in reference 5; and derivation of the suction coefficient definition is given in reference 6. Evaluation of the swept airfoil with discrete suction slots is presented in reference 7. Design and fabrication of the perforated upper-surface suction panels are discussed in reference 8.

This report is a sequel to references 1 through 7. It documents, in a chronological manner, the evaluation of the initial configuration of an LFC model with perforated upper surface and describes deficiencies in the suction capability of the perforated panels as designed. Since the results presented herein pertain only to the initial configuration, they are presented with limited discussion.

Symbols

b	model reference span, distance along swept span between floor and ceiling of liner substructure, 91.146 in.
C_p	pressure coefficient, $\frac{p-p_\infty}{q_\infty}$
$C_{p,\text{sonic}}$	pressure coefficient corresponding to local Mach number of 1.0
C_Q	coefficient of suction through wing surface, $\frac{(\rho w)_{ws}}{(\rho U)_\infty}$
c	model chord parallel to free-stream direction, 7.07 ft
c_l	section lift coefficient
M	Mach number
p	pressure, psf or atm
q	dynamic pressure, psf
R	Reynolds number
R_c	Reynolds number based on free-stream conditions and streamwise chord
R_d	Reynolds number based on orifice diameter
t/c	model thickness-to-chord ratio
U_∞	free-stream velocity
u, v, w	velocity component in x-, y-, and z-direction, respectively
x	distance along model chord from leading edge (positive toward trailing edge)
y	distance along model span from centerline of test section (positive toward top of test section)

z	distance perpendicular to model chord plane (positive toward model upper surface)
α	angle of attack, deg
δ	flap deflection, deg
Λ	leading-edge sweep angle, deg
ρ	density, slug/ft^3

Subscripts:

b	bottom flap
c	central flap
ℓ	lower surface
N	normal to leading edge
t	top flap
u	upper surface
ws	wing surface
∞	free-stream property

Abbreviations:

LFC	laminar-flow control
T-G	Taylor-Görtler
8-ft TPT	Langley 8-Foot Transonic Pressure Tunnel

Test Apparatus

Schematics of the overall LFC experimental setup in the 8-ft TPT are shown in figure 1 along with facility modifications. Major components consisted of a large-chord, swept, supercritical, LFC airfoil model that spanned the full test section height; a contoured test section liner; facility disturbance-suppression devices; and a model suction system. Photographs of the installed liner and model are shown in figure 2.

Brief descriptions of the major components of the experiment are given in the following sections. More detailed descriptions are presented in reference 1.

Wind-Tunnel Model

The LFC model with a chord of 7.07 ft was mounted vertically from floor to ceiling with 23° of sweep and extended through the test section liner which covered the existing slots in the 8-ft TPT test section. It was located about 10 ft forward of the calibrated region of the slotted test section and was displaced from the tunnel centerline toward the lower surface by approximately 15 percent chord to allow development of the supersonic zone in the flow field above the upper surface. The angle of attack could be varied ±2° about the quarter-chord line in a plane normal to the leading edge. Since the ends of the model were buried in the liner, changes in angle of attack required removal of portions of the liner and collar suction ducts; also, elaborate methods were needed to measure very small changes in angle of attack.

The leading-edge sweep angle was chosen to simulate flight cross-flow Reynolds numbers on transport planes with the moderately swept, high-aspect-ratio wings envisioned for LFC application. The streamwise chord length of 7.07 ft, initially dictated by size limitations set by slot-duct construction constraints and the required limitations on Reynolds number based on roughness height for laminar flow, remained the same for the perforated model. The ratio of tunnel height to model chord and the wing-panel aspect ratio were somewhat less than 1.

The model was assembled with an aluminum wing box (fig. 3), to which six individual panels (three upper surface and three lower surface) were attached. The wing box used for the perforated model was not the same one used during the slotted experiment. It was shorter in span, and the floor and ceiling mounting apparatus extended farther from the walls. The wing box was shortened to allow provision for testing different sweep angles with a modified mounting apparatus. Another reason for using a different wing box was to permit mating of the perforated panels to the wing box while the slotted experiment was still in progress.

The perforated upper-surface suction panels were fastened to the wing box from the underside to minimize roughness due to bolt and pinhole fill on the upper surface. Following installation of the upper-surface panels, the nonsuction panel on the forward lower surface and the two aft slotted panels on the lower surface were fastened directly to the wing box with bolts through the lower surface.

As shown in figure 3, the forward upper- and lower-surface panels were cantilevered off the leading edge of the wing box and were bolted together from the underside, where they contacted along a spanwise mating surface at the leading edge. The aft upper- and lower-surface panels were cantilevered off the trailing edge of the wing box and were bolted together from the underside, where they contacted along spanwise mating surfaces near the 77-percent-chord station and at the trailing edge of the panels.

The trailing edge of the model consisted of a 10.9-percent-chord, three-segment flap configuration that replaced the five-segment flap configuration used

on the slotted model. Segmentation of the flap compensated for decambering of the airfoil due to viscous effects along the span associated with the turbulent wedges originating from junctures of the leading edge of the model and the liner (fig. 4). Since it was necessary to build new flaps to attach and mate to the new perforated aft upper-surface panel, and since results from the slotted experiment indicated only minimal effect on the upper-surface pressure distribution due to variations in flap deflections, a less complicated three-flap configuration was used on the perforated model. In addition, the central flap was designed to be remotely operated by means of a spanwise shaft through the top outer flap with an offset cam on the end, which rotated in a short slot with circular ends near the top, or ceiling end, of the central flap. The two outer flaps were manually positioned in a manner similar to that for the five flaps on the slotted model. The outermost spanwise portions of the two outer flaps were buried in the liner; this required removal of part of the liner around the ends of the model when outer-flap deflections were changed.

Airfoil

Slotted-airfoil design. The slotted LFC airfoil was designed (airfoil design parameters shown in fig. 5) for shock-free flow at high free-stream Mach numbers, with lift performance comparable to that of current turbulent supercritical airfoils. The intent was to design an LFC airfoil that, through choices of geometry and pressure distribution, retained the advantages of a supercritical airfoil while it minimized boundary-layer instability problems and suction requirements.

The "near final" shock-free design pressure distribution and sonic lines normal to the leading edge for the resultant airfoil (as calculated by the transonic airfoil analysis code of ref. 9) are shown in figure 6. Three types of boundary-layer instabilities considered during the design process are identified in the regions in which they dominate. Earlier design efforts are reported in references 2 and 10 with comparisons of numerical results presented in references 11 and 12.

The airfoil analysis code of reference 9 did not include provisions for a laminar boundary layer; and, in view of the extremely thin laminar boundary layer expected with suction, the flow was treated inviscidly by assuming zero displacement thickness up to the point of specified transition. Transition was specified during design to occur near the end of the suction regions—96 percent chord on the upper surface and 84 percent chord on the lower surface. Suction did not extend completely to the trailing edge of the upper surface because of the high suction requirements and marginal benefits and because the trailing edge was extremely thin (0.020 in.). Suction was not required over the aft region of the lower surface for several reasons: (1) the adverse pressure gradients in the concave region tended to generate cross flows opposite in circulation to those generated in the favorable pressure gradient regions, thus minimizing suction requirements; (2) Taylor-Görtler instability was controlled by geometric shaping rather than by suction; and (3) there was no room for lower-surface suction ducts beyond 84 percent chord.

Airfoil thickness was reduced in the front and in the rear by undercutting the lower surface to optimize lift (for a given thickness and Mach number) or Mach number (for a given thickness and lift) and to reduce pitching moments. The center of the airfoil provided bending strength and torsional stiffness without any significant lift contribution. This concept provided less pitching moment than conventional aft-loaded supercritical airfoils. Undercutting the forward lower surface also produced a low-velocity region of near-constant pressure coefficient that was conducive to laminar flow without suction. This low-velocity region also reduced sensitivity to surface roughness, which might permit laminar flow over local surface discontinuities associated with leading-edge devices such as Krueger flaps.

The upper-surface pressure distribution was characterized by a steep acceleration around the leading edge (because of the relatively sharp and specially designed leading edge) followed by a gradual and progressively slower deceleration to about 40 percent chord. Over the midchord region, the pressure gradient was near zero. Downstream of 70 percent chord, the flow decelerated progressively more rapidly through a steep subsonic pressure rise toward the trailing edge, in a manner similar to a Stratford-type pressure recovery (ref. 13). The rear transition from supersonic to subsonic flow was located in a region of relatively strong surface curvature. This location better ensured a gentle slope of the sonic line toward the upper surface at around 80 percent chord and delayed the onset of shocks in this particularly critical region. The supersonic zone on the upper surface extended over about 80 percent of the chord of the airfoil, and the maximum local Mach number was about 1.11.

As discussed in reference 14, cross-flow disturbance growth was believed to depend more on the time spent in a pressure gradient than on the steepness of the gradient. Growth may be minimized by

confining steep gradients to short distances along the chord. Consequently, steep gradients are indicated in the four regions labeled "cross flow" in figure 6.

On the lower surface, the flow accelerated rapidly around the small leading edge toward the concave region at high static pressure, with a local deceleration at about 10 percent chord. The flow then accelerated rapidly in a second acceleration to sonic velocity in the midchord region. The small pocket of supersonic flow in the midchord region was followed by a Stratford-type rear pressure recovery to a high static pressure in the rear concave-curvature region. The flow finally accelerated to the trailing-edge static pressure.

As noted in reference 2, feasibility of the LFC airfoil depended on the ability to maintain laminar flow in the concave-curvature regions on the lower surface, where centrifugal Taylor-Görtler (T-G) type boundary-layer instabilities dominate. In a manner similar to that of cross-flow disturbances, T-G disturbance growth depends more on the time spent in a concave-curvature region than on the magnitude of the curvature. One technique for minimizing the growth of T-G instabilities was to turn the flow through a given angle over the shortest possible chordwise distance in the concave-curvature regions at one or more "corner" locations instead of using a gradual turn over a longer chordwise distance. As a result, the two concave regions on the lower surface had local regions of high curvature, and two dips labeled "Taylor-Görtler" appear in the pressure distribution of figure 6.

To provide suitable computational resolution to analyze spikes in the pressure distributions at such corners, the incompressible Eppler code (ref. 15) was used with extra grid points in the low-speed flow of the forward and aft concave regions of the lower surface. These corners and the resulting pressure spikes were then superimposed on the "near final" calculations of figure 6, and the "final" composite design pressure distribution is shown in figure 7. The resulting airfoil profile is shown in figure 8, and the coordinates are presented in table I. As described in reference 12, there were two concave corners in the forward region and two in the aft region, where boundary-layer suction was provided to prevent laminar separation. There were four additional concave corners in the region downstream of where the suction ended. Reference 12 also compares the final configuration with earlier configurations and describes the detailed geometry of the lower-surface corners.

Perforated-airfoil design. The shape of the upper surface of the perforated airfoil was identical to that of the slotted airfoil. Suction on the perforated upper-surface panels ended at about 89 percent chord (immediately ahead of the flap hinge line), whereas, on the slotted upper surface, suction extended beyond the hinge line onto the central flap.

The shape of the aft lower surface was not changed, which permitted use of the same central and aft lower-surface slotted panels used on the slotted model. This allowed retention of boundary-layer suction over the aft lower-surface cusp region, where the flow had been observed to separate at chord Reynolds numbers greater than about 14×10^6 during the slotted-model experiment. Suction was eliminated on the forward lower-surface panel since it was anticipated that applications of LFC would probably be limited to the upper surface for the foreseeable future.

Elimination of suction in the lower forward region allowed the forward lower-surface panel to be redesigned as a solid, nonsuction panel. The leading-edge radius was retained but the concavity of the cusp was reduced and the corners rounded off to eliminate the sharp corners in the forward-cusp region. As discussed in reference 1, the flow decelerates as it approaches such sharp corners, and high values of local suction were required on the slotted model to prevent laminar separation. Eliminating suction made it necessary, therefore, that the corners be smoothed.

Coordinates of the perforated model with the modified lower surface are presented in table II, and sketches of the airfoil are shown in figure 9.

The supercritical, shock-free design pressure distribution (normal to the leading edge) for the perforated airfoil, as calculated by the analysis code of reference 9, is shown in figure 10 and is compared with the "near final" design pressure distribution of the slotted airfoil. The same extent of laminar flow was assumed during the design of the perforated airfoil as was assumed for the slotted airfoil.

Perforated Panels

The perforated panels (fig. 11) were of sandwich construction with electron-beam-perforated titanium skin bonded to a fiberglass corrugated core (forming flutes for subsurface airflow transfer) and a fiberglass and graphite inner face sheet. Imperviously bonded areas divided the panel surface such that suction occurred through spanwise perforated strips. Metering holes located in the bottom of the suction flutes transferred flow to aluminum ducts located in the substrate and from which flow exited the model.

The panels were built by the McDonnell-Douglas Aircraft Corp. using practical aerospace

manufacturing techniques to ensure that fabrication methods would be compatible with industry work practices and assembly line techniques. In general, the perforated panels were fabricated to production standards, whereas the slotted panels were fabricated to more stringent wind-tunnel standards. Reference 8 discusses fabrication of the panels in detail, but a few features are briefly summarized herein for convenience.

An electron-beam process was used to drill surface holes approximately 0.0026 in. in diameter in a 0.025-in-thick titanium skin (see ref. 8). Hole spacing was 0.025 in., yielding an open area porosity ratio of 0.8 percent. This drilling process resulted in a slag-free tapered hole (fig. 11(b)) with inner-surface diameter approximately twice that of the outer diameter. This protected the holes from becoming clogged by small debris being pulled through the skin. As discussed in reference 8, photographic techniques showed that generally about 10 to 15 percent of the holes were blocked because of defects in the electron-beam drilling process, and about 5 percent more were blocked because of adhesive flow from skin bonding.

Figure 11(c) shows how the flute and skin were bonded together. Because of the bonded skin construction, flutes alternated between being active (suction) and inactive (nonsuction), the result being spanwise strips of perforated suction surface. There were 74 active flutes between 3 percent chord and the flaps with nominal chordwise suction length of 0.6 in. The nominal chordwise length of the bonded inactive flutes was 0.3 in. There were 76 active flutes included in the design of the panels, but the first two, forward of 3 percent chord (fig. 11(d)), were constructed without metering holes and were inactive.

Each active flute was separated into spanwise compartments with chordwise baffles to control spanwise flow of air and reduce the potential for inflow and outflow through the skin due to spanwise gradients of pressure. The baffles were trapezoidally shaped bulkheads conforming to the inside contour of the flute and were mounted in skewer fashion on a long rod that extended the spanwise length of the flute. These bulkheads were spaced 2.3 in. apart in the first 57 active flutes and 13.8 in. apart in active flutes 58 through 61. No bulkheads were installed in active flutes 62 through 74 because of the large amount of suction applied on the aft panel.

Metering holes to provide passage of air from the active flutes to internal ducts were drilled through thin aluminum squares bonded to the backsides of the active flutes. The metal squares allowed cleanly drilled circular holes as opposed to irregular holes that would result from drilling directly through the graphite and fiberglass. Hole size and spacing were chosen to meter the flow through each flute. Flute locations as well as metering hole size and number per flute are given in table III.

The skin-flute assemblies were attached to the aluminum substrates in which ducts were machined (fig. 11(c)) by cap screws installed from the bottom side through the duct walls to threaded aluminum inserts located in inactive flutes.

Wind Tunnel

The investigation was conducted in the Langley 8-Foot Transonic Pressure Tunnel. This tunnel is a continuous-flow, variable-pressure wind tunnel with controls that permit independent variations of Mach number, stagnation pressure and temperature, and humidity. The standard test section is square with filleted corners and a cross-section area approximately equal to that of an 8-ft-diameter circle. The floor and ceiling of the test section are slotted to permit continuous variation of the test section Mach number from 0.2 to 1.3.

Tunnel stagnation pressure can be varied from a minimum of about 0.2 atm at all test Mach numbers to about 1.5 atm at transonic speeds and about 2.0 atm at Mach numbers of 0.4 or less. Tunnel air is dried until the dew point is reduced enough to avoid condensation. Temperature is controlled with water from an outside cooling tower circulating through cooling coils across the corner of the tunnel circuit upstream of the test section.

Wind-Tunnel Liner

The conventional slotted test section was reshaped with a contoured, solid wall liner to account for wall interference associated with the large-chord model. Reference 3 discusses the analytical design of the liner. The liner was 54 ft long (fig. 1(b)) and extended from the tunnel contraction region (the 24-ft tunnel station) through the test section and into the diffuser (the 78-ft tunnel station). The 50-ft tunnel station in the liner coordinate system corresponded to the slot origin of the 8-ft TPT slotted test section.

All four walls were contoured to produce a transonic wind-tunnel flow that conformed to the computed streamline flow field around the slotted model at design conditions ($M_\infty = 0.82$, $c_l = 0.47$, and $R_c = 20 \times 10^6$) and that simulated unbounded, free airflow around a swept-wing model of infinite span. Its contours were corrected for the growth of the tunnel wall boundary layer throughout the test section and diffuser. The liner was not modified to account

for the small differences in the flow field over the forward lower surface of the perforated model with the nonsuction forward lower-surface panel. Measurements with surveying equipment indicated that installed liner contours were generally within about 0.040 in. of design values.

Facility Disturbance-Suppression Devices

The success of the LFC experiment depended to a large extent on the environmental disturbance levels, since the ability to maintain laminar boundary layers in wind tunnels depends on the characteristic disturbance levels in the flow..

To prevent facility-generated pressure disturbances in the diffuser from feeding forward into the test section, an adjustable sonic throat consisting of two-dimensional, bell-crank-operated plates (fig. 12) positioned on the liner along opposing tunnel sidewalls was included as part of the liner design. These sonic choke devices were located about 1 chord downstream of the model trailing edge between the test section and the diffuser (figs. 1 and 2). The test section was vented to the plenum chamber surrounding it through porous strips on the surface of the choke plates, downstream of the maximum deflection point, to equalize pressures across the liner during transients due to changes in operating conditions.

Downstream propagating disturbances such as pressure and vorticity fluctuations were reduced by installing a honeycomb and five screens in the settling chamber (fig. 1) upstream of the test section. It was concluded in reference 16 that, as a result of these disturbance-suppression devices, discrete disturbances measured in the free-stream flow did not correspond to predicted Tollmien-Schlichting disturbances at frequencies that were expected to cause transition. Therefore, the flow quality did not appear to adversely affect an onset of instabilities that could have significantly influenced the transition process on the LFC model.

Suction System

LFC by boundary-layer removal on the initial perforated configuration was achieved with suction through strips of closely spaced perforations on the upper surface and through closely spaced slots extending spanwise on the two aft lower-surface panels. The two aft lower-surface panels were the same panels used in the slotted experiment (ref. 1). The widths of the spanwise running slots (fig. 13(a)) varied from about 0.0031 to 0.0053 in. and extended in the chordwise direction from about 25.7 (behind the first joint) to 84.1 percent chord. Slot width and spacing are presented in table IV.

After passing through the perforations or slots, the air passed through appropriately spaced metering holes (figs. 13(b) and 13(c)) and was collected by spanwise ducts with suction nozzles located at the ends (fig. 13(d)). Air from the nozzles passed through model evacuation lines (fig. 13(e)), through airflow control boxes that controlled the amount of suction to the individual duct suction nozzles, through variable sonic nozzles, through hoses to a collector manifold (fig. 13(f)), and, finally, to a 10 000 ft^3/min compressor, which supplied the suction, with a 4.5:1 compression ratio.

Design suction distribution. Figure 14 shows the theoretical chordwise suction distributions over the perforated upper surface in terms of the suction coefficient C_Q for chord Reynolds numbers from 8×10^6 to 40×10^6. Suction extended in the chordwise direction from 3 to 89 percent chord.

Because of the turbulent wedges sweeping across the ends of the model, spanwise variations in suction were required with more suction toward the ends of the model, and separate suction controls were designed for the laminar and turbulent test zones. This was accomplished with bulkheads (fig. 15) in the spanwise suction ducts located to approximate the turbulent wedge boundaries and separate the laminar regions on both surfaces from the turbulent regions. Figure 16 shows the spanwise design suction distributions for the perforated upper surface at several chordwise stations. Design values of suction in the turbulent zones are shown as multiples of the suction values in corresponding laminar zones. In general, the suction levels in the laminar zones extended the full span to about 60 percent chord before increased suction in the turbulent zones was required.

Because the upper surface was of primary interest during this phase of the experiment, suction requirements for the hybrid lower surface with the solid, nonsuction forward panel were not calculated. Design suction characteristics of the fully slotted lower-surface configuration are discussed in reference 1.

Ducts, nozzles, and evacuation lines. Figure 15 shows a sketch and a photograph of the airflow suction system for the perforated upper surface. In some laminar ducts, where the predicted C_Q levels were high, a nozzle was placed at each end to ensure that low velocities were maintained in the duct. Although not shown, the duct and nozzle arrangement on the slotted lower-surface panels was very similar to that shown for the upper surface and is presented in reference 1.

Airflow control boxes. Suction levels in individual model ducts were controlled by airflow control boxes (fig. 17) that were connected by hoses to the suction nozzles inside the model. Each control box contained 27 remotely operated, motor-driven needle valves for individual control of the mass flow from each model suction duct.

Variable sonic nozzles. Figure 18 is a photograph of the sonic nozzles that were located downstream of the individual airflow control boxes. The sonic nozzles provided control of the flow from the suction compressor and blocked feedback noise through the system. In general, the design of the sonic nozzles was based on the sonic plug principle and included a motor-driven needle assembly very similar to those in the airflow control boxes. Sonic flow at the contraction was achieved by longitudinal adjustment of the needle with varying flow rates.

The initial design of the suction control system called for a variable sonic nozzle for each of the five suction airflow control boxes. However, it was found during the slotted-airfoil experiment that, in order to attain the required suction levels, it was necessary to eliminate all but the two largest sonic nozzles on the boxes controlling the laminar region suction. These two remaining sonic nozzles were adjusted to have a shock pressure drop of 0.5 to 1.0 psi.

Liner suction collar. Suction was applied through slots in collar ducts in the liner around the ends of the model (fig. 19) to prevent the turbulent boundary layer on the liner from separating in the vicinity of the model-liner juncture. The plenums, metering holes, ducting, suction nozzles, and evacuation hoses were similar to those of the model suction system and are discussed in reference 1. The collar suction slots, approximately 0.025 in. wide, were wider than those on the model.

Measurements and Instrumentation

Conventional measurement techniques and instrumentation were used to measure tunnel reference temperature and pressures, model and liner surface pressures, variations of stagnation and static pressures across the wake rake, and pressures and temperatures in the various elements of the suction systems. These measurement techniques and instrumentation are described in detail in reference 1.

Surface Static-Pressure Measurements

There were 90 static-pressure orifices distributed along 7 upper-surface rows and 94 static-pressure orifices distributed along 12 lower-surface rows oriented along theoretically determined surface streamlines, as shown in figure 20. The orifices were staggered about theoretical streamlines to prevent wedges of orifice-generated disturbances from cascading and inducing premature transition. The orifices were located on the nonsuction spanwise strips on the perforated upper surface and centered between the suction slots on the lower surface.

Boundary-Layer Thin-Film Gauges

Fifty-one flush-mounted thin-film gauges were distributed over the upper and lower surfaces (fig. 21) to measure fluctuating local surface heat transfer characteristics as qualitative indicators of whether the boundary layer was laminar, transitional, or turbulent.

Liner and Choke

Approximately 700 static-pressure orifices were located along computed streamlines distributed over the four walls of the liner (fig. 22) from the 24-ft tunnel station at the upstream end of the contraction region to the 53-ft station immediately upstream of the movable choke plates. Approximately 240 more static-pressure orifices were located on 14 streamwise rows distributed around the test section between the 53-ft and 59-ft stations in the vicinity of the choke plates. Starting at the 60-ft station and extending to the 78-ft station downstream of the choke, approximately 70 static-pressure orifices were located on 4 streamwise rows near the vertical and horizontal centerline planes of the tunnel.

Modifications to Test Setup During Experiment

Three modifications were made to the test section during the slotted-model phase of the experiment that were retained during the early phase of the perforated experiment. The first modification was the installation of two 8-ft-long area strips (one on the ceiling and another on the floor of the test section) that extended streamwise from the 51.13-ft tunnel station to the 59.13-ft tunnel station (fig. 2). The maximum cross-sectional area of each strip was 40 in^2 at the 55.13-ft station, which corresponded to the tunnel station at which maximum movement of the flexible chokes occurred. These strips, made from the same foam material as the liner and attached to the liner surface with screws and adhesive, were installed to act as fixed chokes and to minimize movement of the flexible choke plates into the flow. The intent was to reduce the possibility of choke vibration affecting the stability of the model boundary layer, although no conclusive evidence of such vibration was established.

The second modification was the installation of a single streamwise area strip, identified as floor area strip no. 6, along the floor near the juncture of the airfoil upper surface and the liner. This strip was made from the same foam material as the liner and was attached to the liner surface with screws and adhesive. It extended from the airfoil leading edge to the trailing edge (fig. 2) and had a maximum cross-sectional area of 5.3 in^2 near the model 60-percent-chord station. The floor area strip was effective in forcing the upper-surface shock wave, which tended to be more forward near the floor than near the ceiling, to a more rearward position, thereby improving the two-dimensional character of the upper-surface pressure distribution.

The third modification involved the installation of vortex generators (fig. 2) on the tunnel walls at two locations downstream of the choke to energize the wall boundary layer in the corners, thus delaying and reducing separation in the diffuser. One array, consisting of eight vortex generators (two in each corner), was located at the 59.50-ft tunnel station, immediately downstream of the sonic wall choke. The second array, also consisting of eight vortex generators (two in each corner), was located at the 71.25-ft tunnel station, immediately downstream of the test section access door.

Discussion

The experimental data presented and discussed herein are based on free-stream conditions rather than on flow characteristics normal to the leading edge. The theoretical pressure distribution normal to the leading edge shown in figure 10 has, therefore, been adjusted for sweep effects by the cosine squared of the sweep angle so that it may be compared directly with the experimental data.

Establishing Minimum Reynolds Number

For lower test Reynolds numbers, the tunnel circuit had to be evacuated to very low stagnation pressures. For example, for $R_c = 10 \times 10^6$ and $M_\infty = 0.82$, stagnation pressure was about $\frac{1}{3}$ atm. The pressure on the model upper surface was even lower since the local static pressure at design conditions ($M_{\text{local}} > 1.0$ in supersonic zone) was approximately one-half the stagnation pressure (i.e., $p_{\text{local}}/p_{\text{stagnation}} = 0.528$ for $M_{\text{local}} = 1.0$). Because the 10 000 ft^3/min compressor had a compression ratio of only 4.5:1, it was exhausted to the stagnation pressure of the tunnel circuit (fig. 1) rather than to outside ambient conditions.

In normal operation of the tunnel, the compressor exhaust would be vented to the atmosphere through an automatic modulating valve to maintain a constant stagnation pressure (constant Reynolds number) against piping and access hatch leaks. It was impossible in this experiment, however, to do this and simultaneously satisfy the suction requirements for the reason outlined above. Therefore, an auxiliary compressor (2000 ft^3/min capacity) was installed during the slotted-model experiment to balance the tunnel stagnation pressure against leaks.

While bringing the tunnel on line, the 10 000 ft^3/min compressor was used to evacuate the tunnel circuit to a minimum of about $\frac{1}{4}$ atm. Fan speed, which controls Mach number, was kept below about 200 rpm to reduce loads across the model outer skin, since the 10 000 ft^3/min compressor was not available to apply suction to the model while it was being used to evacuate the tunnel. Once the minimum stagnation pressure was reached, the 10 000 ft^3/min compressor was switched over to apply suction to the model and was exhausted to tunnel stagnation pressure through hollow turning vanes at the end of the diffuser. As the fan speed was then increased to that required for design Mach number, it followed that stagnation pressure, and consequently Reynolds number, was forced to increase since the 10 000 ft^3/min compressor was no longer available to maintain constant stagnation pressure. The auxiliary 2000 ft^3/min compressor, which was used primarily to maintain stagnation pressure against leaks, was not capable of maintaining constant stagnation pressure against rapid Mach number increases. By the time the design Mach number of 0.82 was reached, the chord Reynolds number had drifted up to near 9×10^6 (depending on how fast fan speed was increased), and this was the minimum chord Reynolds number that could be stabilized.

Operational Design Mach Number

Because of the tendency for the supersonic bubble on the upper surface to apparently collapse and the shock wave to move very rapidly toward the leading edge with small changes in Mach number (ref. 7), it was not possible to set experimental conditions at the predetermined "theoretical design Mach number" of $M_\infty = 0.82$ and get the desired proper pressure distribution. The resulting "operational design Mach number" was a Mach number high enough to force the supersonic zone to the rear of the airfoil, but low enough to cause the shock wave at the end of the supersonic zone to be as weak and as close to the shock-free theoretical curve as possible before it collapsed to near the leading edge. Consequently, the operational design Mach number varied slightly from run to run depending on small variations in model

and test conditions. It also depended to some extent on the subjective judgment of the test engineer as to how low the Mach number could be decreased while the flow over the model remained stable during a data recording cycle. A data cycle lasted for just a few seconds if only the electroscanning pressure system was used to acquire model data. When liner pressure data were acquired with a mechanical stepping valve system, however, a data cycle required that the flow remain steady for almost a minute.

Initial Configuration

The initial model and tunnel configurations for the perforated-model LFC experiment were kept very close to the final configuration of the slotted-model LFC experiment in order to provide a logical basis for comparison. The two fixed choke strips (ceiling and floor) and floor area strip no. 6 were retained from the slotted-model experiment. Although there was some rearranging of suction hoses, the needle valve settings in the airflow control boxes were also left unchanged. Because a new wing box with different mounting blocks was used, the perforated model was located about 0.060 in. farther from the tunnel centerline than was the slotted model. The initial deflections of the fixed outer-flap were 2.1° on the top (ceiling) flap and 2.6° on the bottom (floor) flap. The deflection of the central flap was remotely adjustable. These outer-flap deflections on the three-flap configuration were chosen to approximate the flap deflections of the five-flap configuration at the end of the slotted LFC experiment (ref. 7), which were 2.3°, 0.5°, 0.1°, 0.6°, and 2.8° from the ceiling to the floor.

The flap settings were not particularly critical. It was observed during the slotted-model LFC experiment, and confirmed during the present perforated-model experiment, that the flaps were not effective in changing the upper-surface pressure distribution because the supersonic bubble on the upper surface extended to the wall at the design Mach number and blocked the upstream influence of the flaps. The primary effect of the flaps was observed to be small influences on the degree of separation in the aft lower-surface cusp, and on the Mach number at which the operational design conditions occurred (discussed subsequently in more detail).

The model angle of attack was initially set to the design value of 0.51° by measuring the position of the wing box relative to the tunnel centerline before the panels were installed. After the panels were installed, the relative location of the leading edge of the forward panel and of the trailing edge of the aft panel (measured from the tunnel centerline with a transit and two vertical wire crosshairs stretched between the floor and the ceiling at the 50-ft and 63-ft tunnel stations) indicated that the model angle of attack was nearer 0.42° for the first run.

With this initial model and test section configuration, a free-stream Mach number no higher than 0.814 could be achieved for $R_c = 10 \times 10^6$, with the movable chokes completely out of the flow (fig. 23(a)). For a Reynolds number of 15×10^6 (fig. 23(b)), a slightly higher Mach number of 0.817 was achieved. The pressure distributions for these two maximum Mach numbers are compared in figure 24. The upper-surface pressure distribution was saddleback in character with an acceleration peak around 70 percent chord. The aft lower-surface cusp region was completely separated, with a strong shock near 60 percent chord. As shown in figure 24, these characteristics became more pronounced with increasing Mach number.

In order to permit a higher free-stream Mach number, the fixed choke on the floor was removed, the result being an increase in Mach number to 0.822 at $R_c = 10 \times 10^6$ (fig. 25). As shown in figure 26, the result of this higher Mach number was an upper-surface pressure distribution that remained saddleback in shape, but with a much stronger acceleration and shock wave developing around 80 percent chord. On the lower surface, increasing the Mach number had only a small effect up to the location of the shock wave, but significantly increased the separation in the aft cusp region. The effect on the pressure distribution forward of the shock wave on the lower surface was small because the supersonic bubble on the lower surface extended all the way to the test section wall opposite the lower surface (maximum Mach number measured on the liner wall opposite the lower surface was 1.04) and choked the flow in the channel between the model lower surface and test section wall. The maximum Mach number measured on the liner wall opposite the upper surface at these conditions was 0.94.

Effects of Remotely Controlled Central Flap

It was observed early in the experiment that movement of the remotely controlled central flap had no effect in altering the pressure distribution. Static-test loading of the central flap to design load revealed that no matter what position the shaft and cam arrangement was rotated to, the flap deformed to near zero deflection. Since the remotely controlled central flap was ineffectual because of excessive deformation under aerodynamic loading, the central flap was set at a relatively large deflection of 1.0° to determine its effectiveness in eliminating the lower-surface shock

and in reducing separation in the aft lower-cusp region. This was accomplished by filling the gap between the aft panel and the flap with a hard filler material. After filling the gap, the flap was again statically test loaded, and deformations of only a few thousandths of an inch at the trailing edge were observed.

The resulting pressure distribution is shown in figure 27 and is compared with that of the configuration with the movable central flap in figure 28. There were only minimal differences in the pressure distributions with the movable and fixed flaps. The small differences that are shown (favorable effect on lower-surface cusp separation and weaker upper-surface shock) may be attributed, in part, to the slightly lower Mach number. The resultant lower Mach number with increased flap deflection is consistent with effects of flap deflections discussed later.

Effect of Increasing Angle of Attack From 0.42° to 0.60°

At this point, the angle of attack was increased from 0.42° to 0.60° in an attempt to increase velocities in the midchord region of the upper surface and to flatten out the saddleback pressure distribution. As previously noted, changing the angle of attack required removal of the liner and collar blocks from around the ends of the model and, since the floor area strip was attached to the liner in this vicinity, removal of the area strip as well. During prior experiments, the area strip had only minimal effect in the midspan region of the model; thus, it was omitted for the evaluation of the angle-of-attack increase. Figure 29 presents the variation of pressure distribution with an increasing Mach number for the new angle of attack of 0.60°. Figure 30 compares the pressure distributions at two Mach numbers for $\alpha = 0.60°$, and figure 31 compares the pressure distributions for angles of attack of 0.42° and 0.60° at the same Mach number of 0.821.

The highest Mach number attained (with the ceiling fixed choke still present) with an angle of attack of 0.60° was 0.824 (fig. 29(e)). The velocities over the forward region of the upper surface were increased, pulling the forward shock back to approximately 30 percent chord, but the Mach number was not high enough to pull the supersonic zone back to the rear of the airfoil. Since the angle of attack was adjusted by rotating the model about $x/c = 0.25$, increasing the angle of attack moved the trailing edge of the model away from the liner wall opposite the upper surface and thus reduced the flow-channeling effect between the model and the liner. Increasing the angle of attack, therefore, tended to reduce the acceleration and associated shock wave near 80 percent chord on the upper surface (fig. 31). The effect on the lower surface of increasing the angle of attack was to reduce the shock strength and the severity of separation in the aft cusp region.

Floor area strip no. 6 was reinstalled and, with the more two-dimensional flow over the model near the floor, an increase in free-stream Mach number to 0.826 was achieved (fig. 32). With this small increase in Mach number, the velocities over the mid upper surface approached the design values, although the chordwise distribution had the same uneven character as that observed for the slotted LFC model. The strength of the upper-surface shock at 80 percent chord increased, as did the severity of the separation in the aft lower-surface cusp region. At these conditions, the supersonic bubble on both the upper and lower surfaces extended all the way to the test section walls. The local Mach number on the wall opposite the upper surface approached 1.02; on the wall opposite the lower surface it was about 1.04, an indication of choked flow conditions at the model.

The next step taken was to remove the ceiling fixed choke to determine its effect on free-stream Mach number. Removal of the ceiling fixed choke had no effect on the maximum Mach number obtained (0.826), however, since the supersonic bubbles on the upper and lower surfaces already extended to the walls and the flow was choked at the model (fig. 33).

At the same time that the ceiling fixed choke was removed, the top outer-flap deflection was increased from 2.1° to 3.2° because data from the slotted model had indicated that increases in top-flap deflection had small favorable effects on lower-surface separation with only minimal effects on the upper surface. Figures 32 and 33 show a small improvement in the severity of separation on the lower surface for the larger top-flap deflection. Since the data for the larger flap deflection were taken at a slightly lower tunnel fan rpm, this improvement was not clear cut. Although the wall data indicated that the flow was choked both at the model and on the movable chokes, changes in fan rpm did seem to have an effect on the severity of separation on the aft lower surface. The pressure distribution was so removed from the theoretical design conditions that the effect of fan rpm was never fully explored.

Channel Flow Between Model and Wall

The effects of increasing the angle of attack from 0.42° to 0.60° and the results from the slotted experiment (ref. 7) indicated that since the supersonic bubble extended to the liner wall, the behavior of the flow

on the upper surface was dominated by interactions between the model and the liner and the resultant supersonic channeling effects in the flow above the upper surface. Increasing the angle of attack moved the trailing edge of the model away from the liner wall, thus increasing the area of the channel between the model and the wall and weakening the shock wave on the upper surface. This channeling effect was amplified by the deformation of the model (discussed in more detail in ref. 7) since, under load, the rear panel of the model, which was cantilevered off the trailing edge of the wing box, moved closer to the wall.

Effect of Increasing Angle of Attack From 0.60° to 0.81°

It was apparent from the strength of the upper- and lower-surface shock waves that the angle of attack was still too low, so it was further increased to 0.81° while the same flap deflections were retained. The result, shown in figures 34 and 35, was an upper-surface pressure distribution much nearer design at a lower Mach number of 0.815 and without the strong acceleration around 80 percent chord. In addition, the more positive angle of attack, combined with the lower Mach number, eliminated the shock wave on the lower surface and substantially reduced the severity of separation. The overall level of velocities on the upper surface was higher than design, and the supersonic bubble still extended to the wall above the model. The maximum local Mach number on the wall opposite the upper surface approached 1.01. On the wall opposite the lower surface, the maximum local Mach number had decreased to about 0.96.

Transition Patterns

Figure 36 shows sketches of the pattern of laminar flow on the upper and lower surfaces for the test conditions of figure 34. The shaded transition zones are the regions between thin films that indicated the boundary layer to be 20 percent or less turbulent and thin films that indicated the boundary layer to be 80 percent or more turbulent. On the upper surface, transition swept forward from the ceiling to the floor. On the lower surface, transition occurred near the joint between the first and second panel.

Temperature Effects

The pattern of laminar flow on the upper surface tended to be longer chordwise at the top end of the model and shorter toward the bottom, but flow patterns were not consistent from run to run. Repeatability was difficult, and much time and effort were expended on cleaning and polishing the model surface to prevent premature transition. Often, the extent of laminar flow seemed to deteriorate with time, suggesting erosion of the model surface condition or clogging of orifices during a run. Finally, it was recognized that much of the differences in laminar-flow patterns were associated with subtle temperature differences and the length of time it took for the model to reach equilibrium. These temperature effects were confirmed by repeating temperature variations on consecutive runs without cleaning the model surface in order to eliminate model surface contamination as a contributing factor.

At the time of the year these temperature effects were studied, early summer, outside temperatures were in the high 80's to low 90's, and the tunnel could only be cooled to around 80°F, with full cooling at $M_\infty = 0.82$. With a stagnation temperature of 80°F, the temperatures in the duct cooled to around 70°F. As the model slowly reached equilibrium, the extent of laminar flow toward the top of the model improved from the pattern shown in figure 37(a) until it reached the pattern shown in figure 37(b). When the stagnation temperature was then slowly allowed to increase to 100°F, the transition pattern deteriorated to that shown in figure 37(c). As the model heated up and reached equilibrium, the laminar-flow pattern deteriorated further to that shown in figure 37(e). As the equilibrium conditions of the model changed, the movable sidewall chokes had to be continually adjusted to keep the upper-surface shock from strengthening or sweeping forward with changes in aerodynamic camber due to changing transition location.

The extent of laminar flow shown in figure 37(b) was the best laminar-flow pattern achieved at $R_c = 10 \times 10^6$ during this initial phase of the perforated-model evaluation. Slightly longer areas of laminar flow were achieved toward the top of the model for lower Reynolds numbers of $R_c = 8 \times 10^6$ and 9×10^6 (fig. 38).

Effects of Collar Suction

Each collar suction duct around the ends of the model was evacuated by individual 1-in. hoses through manifolds one manifold for the top or ceiling end of the model and a second for the bottom or floor end of the model (fig. 39). From the two manifolds, the air from the collar ducts passed through 6-in lines, equipped with remotely operated valves, to the 10 000 ft^3/min compressor collector manifold. In addition, there was a manually operated, lever-type valve in each 1-in. hose between the individual ducts and the collar-duct manifold. With such an arrangement, when the valve in the 6-in. line was closed

to shut off suction from the compressor to the collar ducts in either end of the model, there remained the potential for a small amount of passive suction (through the collar manifold, from the higher velocity and lower pressure flow on the upper surface) on the lower surface unless the manually controlled, individual 1-in. hose valves were also closed.

Variations in suction through the upper-surface collar ducts had no observable effects on either the pressure distributions on the model or the laminar-flow patterns. A small amount of suction through the lower-surface collar ducts seemed to have a small favorable effect in reducing the velocity over the lower-surface midchord high-velocity plateau. This small favorable effect, which disappeared with too much collar suction, could be achieved by slightly opening both 6-in. lines and completely opening the 1-in. hoses; closing the 6-in. line and leaving all manual valves in the 1-in. hoses open, which effectively applied passive suction to the lower surface; or by simply closing the valves in the 1-in. hoses to the upper surface. Since upper-surface collar suction had no observable effect on the model, the third option of shutting off all collar suction on the upper surface, which provided better control over the lower surface, was used.

Effects of Juncture Blowing

At one point during the experiment, while the liner blocks around the ends of the model were removed to allow access to suction hoses, 1/4-in. air tubes were installed in the lower-surface model-liner junctures. The tubes blew jets of high-pressure air chordwise from near the 24-percent-chord station in an attempt to reduce the severity of separation in the lower-surface aft cusp region. Experience had shown that blowing in the model-sidewall junctures during two-dimensional airfoil tests had beneficial effects on separation in the juncture region. It was believed that similar favorable interaction might be achieved by blowing into the separated region on the lower surface, but no effects could be observed during subsequent testing for blowing pressure up to 70 psi.

Evaluation of Model Suction Capability

Figure 40 shows the measured and theoretical suction distributions on the upper surface for $R_c = 10 \times 10^6$ and $R_c = 20 \times 10^6$. The measured suction was generally equal to, or slightly higher than, the theoretically required suction. In general, both measured suction distributions corresponded to the maximum suction capability of each suction duct combined with the maximum suction capacity of the compressor system used to provide suction to the model.

A comparison of maximum measured suction distributions on the upper surfaces of perforated and slotted models (ref. 7) at $R_c = 10 \times 10^6$ is presented in figure 41. The data show that the suction capability of the perforated surface was substantially less than that of the slotted surface.

During the early phases of the initial evaluation of the perforated surface, when it was recognized that suction levels were too low, one modification that was thought to hold potential for increasing suction was to reduce the length (and associated pressure drop or line loss) of the small-diameter jumper hoses that connected the upper-surface laminar duct nozzle extensions to the larger 1-in-diameter hoses leading to the airflow control boxes. These small-diameter jumper hoses were about 18 in. long and were shortened to about 6 in. However, no measurable effect was observed.

Figure 42 shows theoretical limits at which sonically choked flow would be expected in various elements of the model suction system. The theoretical limits for the duct nozzle and nozzle extension were computed by standard pipe flow equations which assumed that where a duct had two nozzles—one at either end of the duct—the total flow in the duct was divided equally between the two nozzles. The theoretical limits for the metering holes were computed by standard orifice flow equations which assumed that all metering holes for a given duct were the same size, there were no internal leaks between ducts, and the flow was divided proportionally among the metering holes. The theoretical choking limits of the perforated skin (fig. 42(b)) were computed with unpublished equations obtained from the McDonnell-Douglas Aircraft Corp., who manufactured the perforated panels. These equations were semiempirical and based on data for flows with extremely small Reynolds numbers based on orifice diameter ($R_d < 100$). These calculations clearly showed that the maximum suction of the perforated panels was limited by the size of the metering holes.

Effects of Flap Deflections

The results discussed in the previous section indicated that the metering holes in the perforated panels would have to be enlarged to provide increased suction. To enlarge the metering holes, it was necessary to remove the model from the tunnel and disassemble the panels. Before interrupting the experiment to remove the model from the tunnel, a complete package of data was obtained for several flap deflections.

These experimental pressure distributions were as close to design as possible to provide comparisons with data taken after suction system modifications were made. Varying flap deflection had only minor effects on the pressure distribution in the midspan region of the model.

The tunnel configuration for this flap investigation included floor area strip no. 1 instead of floor area strip no. 6 as indicated for previous figures. Both extended from the leading edge of the model to the trailing edge, but floor area strip no. 1 had a larger maximum cross-section area of 8 in^2 at 75 percent chord. Several variations of area distribution had been tried on the floor area strip during the slotted experiment, but the effects of different strips on the initial perforated model were never fully explored because of the many other problems that dominated the flow. These dominant factors included inadequate suction through the porous upper surface, temperature effects on transition, upper-surface model-wall interactions, and lower-surface pressure distributions that were so far off design conditions that the validity of the upper-surface results might be jeopardized because of global flow effects. Consequently, it was decided to use the area strip that happened to be in place at the time floor area strip no. 1.

When tested at the same Mach number, the upper-surface shock was slightly farther rearward for the more positive (3.3°) top-flap deflection (fig. 43(a)). When the Mach number for the 3.3° top-flap configuration was decreased slightly (fig. 43(b)), the pressure distributions for the two top-flap deflections were identical. Similar results for bottom-flap deflections are shown in figure 44.

The central flap appeared to have a similar, but slightly stronger, effect on the pressure distribution in the midspan region of the model, as shown in figure 45. When compared at the same Mach number (fig. 45(a)), the upper-surface shock was farther rearward for the more positive central-flap deflection. When upper-surface pressure distributions were matched (fig. 45(b)), the only differences between the pressure distributions for the two central-flap deflections were slightly lower velocities in the midchord region of the lower surface and slightly less severe separation in the aft cusp for the configuration with the more positive central-flap deflection of 1.0° (compared with 0.3°). The trend of lower velocities over the lower-surface plateau region was also shown for a much larger central-flap deflection (fig. 46) earlier in the experiment, but with slightly different outer-flap deflections. Although not illustrated, negative central-flap deflections (trailing edge toward the upper surface) had a somewhat stronger effect on the lower surface; velocities in the midchord plateau region appeared to increase substantially.

In general, the primary effect on the upper surface of changing flap deflections seemed to be a slightly different Mach number at which the operational design Mach number occurred. On the lower surface, flap deflection had only a minimal effect on the plateau velocities over the midchord region. The central flap was, therefore, returned to near 1.0° ($\delta_c = 0.9°$); and the outer-flap deflections of 2.6° and 3.5° were retained as the final configuration for this phase of the experiment. Figure 47 shows the resulting pressure distribution and compares it with the $\delta_c = 0.3°$ pressure distribution of figure 45(b).

Mach Number Accuracy

The Mach numbers shown in figures 43 through 47 were presented to four decimal places. The absolute precision of the tunnel reference pressure instrumentation (sonar manometers) was ±0.2 psf, checked daily by comparing the stagnation-pressure sonar manometer to the static-pressure sonar manometer and readjusting the manometers if they differed by more than 0.2 psf. This level of precision in the reference pressures would lead to a level of precision in the computed Mach number of ±0.0007, at the design Mach number of 0.82 and $R_c = 20 \times 10^6$ for a worst case condition of maximum errors of opposite sign occurring in the two manometers simultaneously. However, even though it is not possible to maintain the manometers to precisions better than ±0.2 psf, they can be read to ±0.03 psf (0.03 being the electronic noise-level jump in the display). Pressure errors of ±0.03 psf yield, in the worst-case conditions defined above, a Mach number error of ±0.0001; for this reason, real-time data displayed Mach numbers to four decimal places. It was believed that for small changes in pressure associated with choke plate adjustment, any change greater than the 0.03 psf was meaningful in a relative sense. When experience showed that Mach number changes in the fourth decimal place could be consistently associated with changes in the wing pressure distribution, the decision was made to retain the fourth decimal place in the published Mach number, even though absolute precision levels would only justify three decimal places. The effects of very small variations in Mach number on the wing pressure distributions discussed in the following section, for example, would be meaningless without the fourth decimal place.

The preceding analysis of free-stream Mach number precision, based on the capability of the primary pressure standards of the 8-ft TPT, is not a statistical analysis. Flow-off discrepancy of as much

as ±0.2 psf between the primary pressure standards (which gives the Mach number error of ±0.0007) is a systematic error that varies from day to day but not during a given run and therefore is not susceptible to statistical analysis. Thus, a Mach number error of ±0.0007 is the worst case based on the floating systematic error of the primary pressure standards. The Mach number error of ±0.0001 derived from the ±0.03 psf electronic noise error of the primary pressure standard is the smallest Mach number error that could be computed from these pressure standards, because no pressure data variation can be obtained within the jump level; that is, there is no way to choose between, for example, a pressure of 1456.03 psf and a pressure of 1456.06 psf when the instrumentation cannot measure intermediate pressure.

Effects of Varying Mach Number at $R_c = 10 \times 10^6$

Figure 48 shows the change in pressure distribution near the midspan as the Mach number was reduced in very small increments (by moving the adjustable chokes into the flow) near the design Mach number at $R_c = 10 \times 10^6$. Figure 49 presents the corresponding spanwise pressure distributions. The chordwise orifice row, with its last orifice located at $2y/b = -0.06$ and identified as station 8, corresponds to the midspan distributions of figure 48. Figures 50 and 51 show similar pressure distributions for $R_c = 10 \times 10^6$, but over a wider Mach number range. Since flap deflections were shown to have only minimal effects on the pressure distributions, the somewhat arbitrary but reasonable flap deflections of 2.6°, 0.9°, and 3.5° (from ceiling to floor) were chosen for these Mach number variations.

The collapse of the supersonic bubble above the upper surface and the rapid movement of the shock wave toward the leading edge with very small changes in Mach number (fig. 48) did not follow a smooth progression but were consistent with what would be expected in supersonic channel flow. Similar results were observed for the slotted LFC configuration and are discussed in more detail in reference 7.

Effects of Varying Reynolds Number Near Design Mach Number

Figure 52 shows the effects of increasing Reynolds number on the chordwise pressure distribution near the midspan at the operational design Mach numbers. Figure 53 shows the corresponding spanwise pressure distributions. Figure 54 shows a comparison of the measured and theoretical chordwise pressure distributions at the operational design Mach numbers for $R_c = 10 \times 10^6$ and $R_c = 20 \times 10^6$, and figure 55 shows the corresponding laminar-flow patterns. As previously noted, transition on the upper and lower surfaces was well forward even at $R_c = 10 \times 10^6$, and separation was present in the lower-surface aft cusp region. Consequently, the pressure distribution did not change much with increases in Reynolds number.

Concluding Remarks

The initial perforated-model and tunnel configuration for the laminar-flow-control (LFC) experiment in the Langley 8-Foot Transonic Pressure Tunnel were evaluated. Several general conclusions were reached: (1) the pressure distribution on the model was very sensitive to small variations in angle of attack because of the proximity of the liner wall; (2) within the range of stagnation temperatures investigated (80°F to 100°F), the transition pattern deteriorated with increasing temperature; (3) the effects of variations in flap deflection on the the model pressure distribution were generally minimal; and (4) the metering holes underneath the perforated surface limited the suction capability of the model. Because of the limited suction capability, this phase of the LFC experiment was interrupted so that the model could be disassembled and the metering holes on the forward and central upper-surface perforated panels enlarged. Before the model was removed from the tunnel, a complete package of data was taken to provide comparisons with data taken after suction system modifications were made.

NASA Langley Research Center
Hampton, VA 23665-5225
February 27, 1992

References

1. Harris, Charles D.; Harvey, William D.; and Brooks, Cuyler W., Jr.: *The NASA Langley Laminar-Flow-Control Experiment on a Swept, Supercritical Airfoil Design Overview.* NASA TP-2809, 1988.

2. Pfenninger, W.; Reed, Helen L.; and Dagenhart, J. R.: Design Considerations of Advanced Supercritical Low Drag Suction Airfoils. *Viscous Flow Drag Reduction,* Gary R. Hough, ed., American Inst. of Aeronautics and Astronautics, c.1980, pp. 249–271.

3. Newman, Perry A.; Anderson, E. Clay; and Peterson, John B., Jr.: *Aerodynamic Design of the Contoured Wind-Tunnel Liner for the NASA Supercritical, Laminar-Flow-Control, Swept-Wing Experiment.* NASA TP-2335, 1984.

4. Harris, Charles D.; and Brooks, Cuyler W., Jr.: *Modifications to the Langley 8-Foot Transonic Pressure Tunnel for the Laminar-Flow-Control Experiment.* NASA TM-4032, 1988.

5. Brooks, Cuyler W., Jr.; Harris, Charles D.; and Harvey, William D.: *The NASA Langley Laminar-Flow-Control Experiment on a Swept, Supercritical Airfoil Drag Equations.* NASA TM-4096, 1989.

6. Brooks, Cuyler W., Jr.; Harris, Charles D.; and Harvey, William D.: *The NASA Langley Laminar-Flow-Control Experiment on a Swept, Supercritical Airfoil – Suction Coefficient Analysis.* NASA TM-4267, 1991.

7. Harris, Charles D.; Brooks, Cuyler W., Jr.; Clukey, Patricia G.; and Stack, John P.: *The NASA Langley Laminar-Flow-Control Experiment on a Swept Supercritical Airfoil – Basic Results for Slotted Configuration.* NASA TM-4100, 1989.

8. Maddalon, Dal V.; and Poppen, William A., Jr.: *Design and Fabrication of Large Suction Panels With Perforated Surfaces for Laminar Flow Control Testing in a Transonic Wind Tunnel.* NASA TM-89011, 1986.

9. Bauer, Frances; Garabedian, Paul; Korn, David; and Jameson, Antony: *Supercritical Wing Sections II.* Volume 108 of *Lecture Notes in Economics and Mathematical Systems*, M. Beckmann and H. P. Kuenzi, eds., Springer-Verlag, 1975.

10. Allison, Dennis O.; and Dagenhart, John R.: Design of a Laminar-Flow-Control Supercritical Airfoil for a Swept Wing. *CTOL Transport Technology 1978*, NASA CP-2036, Part I, 1978, pp. 395–408.

11. Allison, Dennis O.: *Inviscid Analysis of Two Supercritical Laminar-Flow-Control Airfoils at Design and Off-Design Conditions.* NASA TM-84657, 1983.

12. Allison, Dennis O.; and Dagenhart, J. Ray: *Two Experimental Supercritical Laminar-Flow-Control Swept-Wing Airfoils.* NASA TM-89073, 1987.

13. Stratford, B. S.: The Prediction of Separation of the Turbulent Boundary Layer. *J. Fluid Mech.*, vol. 5, pt. 1, Jan. 1959, pp. 1–16.

14. Pfenninger, Werner: Laminar Flow Control Laminarization. *Special Course on Concepts for Drag Reduction.* AGARD-R-654, June 1977, pp. 3-1–3-75.

15. Eppler, Richard; and Somers, Dan M.: *A Computer Program for the Design and Analysis of Low-Speed Airfoils.* NASA TM-80210, 1980.

16. Jones, Gregory S.; Stainback, P. Calvin; Harris, Charles D.; Brooks, Cuyler W., Jr.; and Clukey, Steven J.: Flow Quality Measurements for the Langley 8-Foot Transonic Pressure Tunnel LFC Experiment. AIAA-89-0150, Jan. 1989.

Table I. Theoretical Coordinates of Slotted LFC
Supercritical Airfoil Normal to Leading Edge

$(x/c)_N$	$(z/c_N)_u$
0.000000	0.000000
.000126	.001024
.000389	.002089
.000795	.003181
.001349	.004289
.002052	.005406
.002910	.006526
.003922	.007646
.005088	.008757
.006406	.009849
.007888	.010911
.009549	.011946
.011397	.012964
.013434	.013967
.015651	.014950
.018055	.015916
.020650	.016867
.023433	.017810
.026399	.018749
.029546	.019678
.032873	.020598
.036384	.021511
.040071	.022420
.043934	.023324
.047966	.024221
.052169	.025110
.056541	.025989
.061081	.026859
.065787	.027723
.070656	.028577
.075686	.029423
.080875	.030257
.086223	.031082
.091725	.031897
.097378	.032701
.103182	.033494
.109136	.034277
.115235	.035050
.121473	.035810
.127851	.036557

$(x/c)_N$	$(z/c_N)_u$
0.134371	0.037292
.141029	.038014
.147817	.038723
.154734	.039418
.161778	.040100
.168950	.040768
.176244	.041423
.183656	.042061
.191183	.042684
.198823	.043292
.206572	.043884
.214430	.044459
.222392	.045019
.230455	.045561
.238617	.046088
.246871	.046599
.255218	.047093
.263652	.047570
.272172	.048030
.280774	.048470
.289453	.048892
.298206	.049295
.307031	.049679
.315924	.050045
.324881	.050391
.333900	.050719
.342975	.051028
.352105	.051318
.361284	.051588
.370509	.051839
.379778	.052069
.389086	.052279
.398431	.052469
.407807	.052639
.417210	.052788
.426639	.052917
.436089	.053025
.445557	.053111
.455040	.053175
.464532	.053218

$(x/c)_N$	$(z/c_N)_u$
0.474029	0.053239
.483529	.053238
.493030	.053215
.502527	.053170
.512015	.053104
.521490	.053015
.530948	.052903
.540387	.052769
.549803	.052613
.559194	.052435
.568553	.052235
.577880	.052012
.587168	.051766
.596415	.051498
.605618	.051207
.614772	.050892
.623874	.050553
.632921	.050191
.641910	.049806
.650837	.049395
.659698	.048960
.668491	.048501
.677212	.048018
.685858	.047511
.694427	.046979
.702914	.046424
.711315	.045842
.719626	.045233
.727844	.044595
.735968	.043930
.743999	.043238
.751931	.042519
.759761	.041771
.767487	.040996
.775103	.040192
.782607	.039358
.789998	.038493
.797275	.037591
.804442	.036651
.811497	.035676

Table I. Continued

$(x/c)_N$	$(z/c_N)_u$
0.818442	0.034665
.825269	.033620
.831976	.032537
.838567	.031409
.845049	.030237
.851485	.029011
.856436	.028031
.861386	.027025
.866337	.026004
.871287	.024974
.876238	.023941
.881188	.022906
.886139	.021871
.891089	.020837
.896040	.019802
.900990	.018767
.905941	.017733
.910891	.016698
.915842	.015663
.920792	.014630
.925743	.013597
.930693	.012565
.935644	.011535
.940594	.010505
.945545	.009476
.950495	.008449
.955446	.007422
.960396	.006397
.965347	.005374
.970297	.004353
.975248	.003335
.980198	.002318
.985149	.001303
.990099	.000290
.995050	.000721
1.000000	.001730

$(x/c)_N$	$(z/c_N)_\ell$
0.000000	0.000000
.000019	.000956
.000201	−.001824
.000574	.002590
.001170	−.003259
.002015	−.003848
.003121	.004375
.004484	.004868
.006098	−.005328
.007967	.005755
.010103	.006161
.012503	.006569
.015157	−.006988
.018058	−.007417
.021208	.007857
.024596	.008306
.028212	.008760
.032059	.009223
.035891	.009673
.036881	.009789
.038861	.010021
.042822	.010484
.046782	.010948
.050743	.011411
.054703	.011874
.058663	.012338
.062624	.012801
.066584	.013264
.070545	.013728
.074505	.014191
.078465	.014654
.082426	.015118
.086386	−.015581
.090347	.016045
.094307	−.016508
.098267	−.016971
.100990	−.017290
.103465	−.017588
.105446	−.017869
.106931	.018170
.108416	−.018584
.110396	.019250
.113366	.020315
.117327	.021743
.121782	−.023350

$(x/c)_N$	$(z/c_N)_\ell$
0.127835	0.025535
.135118	.028162
.140594	.030138
.144554	.031566
.147525	.032639
.150000	.033538
.151980	.034290
.153465	.034930
.154950	.035668
.156436	.036474
.158416	.037584
.160891	.038982
.164067	.040777
.167228	.042563
.170464	.044392
.176424	.047725
.182162	.050623
.187889	.053088
.193737	.055206
.199755	.057071
.205949	.058755
.212309	.060304
.218818	.061743
.225460	.063084
.232232	.064334
.239130	.065502
.246151	.066598
.253282	.067625
.260515	.068583
.267853	.069479
.275295	.070318
.282831	.071101
.290451	.071830
.298158	.072503
.305950	.073124
.313817	.073693
.321752	.074210
.329758	.074677
.337834	.075096
.345971	.075465
.354164	.075786
.362413	.076060
.370714	.076286
.379061	.076464
.387448	.076593

Table I. Concluded

$(x/c)_N$	$(z/c_N)_\ell$
0.395874	-0.076674
.404340	-.076707
.412837	-.076692
.421361	-.076628
.429910	-.076518
.438482	-.076359
.447071	-.076151
.455672	-.075894
.464283	-.075589
.472903	-.075234
.481526	-.074830
.490147	-.074375
.498762	-.073868
.507372	-.073310
.515971	-.072699
.524552	-.072036
.533115	-.071319
.541656	-.070548
.550174	-.069721
.558658	-.068839
.567107	-.067899
.575514	-.066899
.583873	-.065836
.592180	-.064704
.600430	-.063497
.608620	-.062206
.616747	-.060820
.624811	-.059324
.632822	-.057702
.640795	-.055943
.648750	-.054040
.656709	-.051988
.664701	-.049797
.672750	-.047489
.680868	-.045093
.689604	-.042483
.698515	-.039806
.704455	-.038018
.714356	-.035038
.724257	-.032057
.734158	-.029077
.744059	-.026097
.753960	-.023117
.763861	-.020137
.773762	-.017156

$(x/c)_N$	$(z/c_N)_\ell$
0.783663	-0.014176
.793564	-.011196
.801980	-.008663
.807921	-.006876
.811961	-.005661
.815130	-.004709
.817110	-.004114
.818694	-.003641
.819882	-.003298
.821070	-.002997
.822258	-.002750
.823447	-.002540
.825031	-.002280
.826724	-.002006
.828699	-.001686
.830392	-.001412
.832085	-.001137
.833778	-.000860
.835471	-.000582
.837447	-.000257
.839140	.000021
.840724	.000277
.841912	.000456
.843100	.000602
.844288	.000701
.845476	.000766
.847060	.000839
.848753	.000911
.850729	.000993
.852422	.001063
.854115	.001135
.855808	.001207
.857501	.001280
.859476	.001367
.861386	.001452
.863366	.001542
.866337	.001675
.871287	.001898
.876238	.002121
.881188	.002344
.886139	.002565
.889109	.002691
.891089	.002763
.893069	.002818
.896040	.002881

$(x/c)_N$	$(z/c_N)_\ell$
0.899010	0.002938
.902970	.003011
.907921	.003101
.914851	.003216
.921782	.003291
.926733	.003289
.930693	.003235
.934653	.003128
.939604	.002929
.946535	.002571
.953465	.002174
.958416	.001882
.962376	.001647
.965347	.001462
.968317	.001263
.970297	.001118
.972277	.000958
.975248	.000699
.980198	.000240
.985149	-.000229
.988119	-.000521
.990099	-.000732
.992079	-.000965
.995050	-.001342
1.000000	-.001986

Table II. Theoretical Coordinates of Initial Perforated LFC Supercritical Airfoil With Nonsuction Forward Lower-Surface Panel Normal to Leading Edge

x/c	$(z/c_N)_u$
0.000000	0.000000
.000126	.001024
.000389	.002089
.000795	.003181
.001349	.004289
.002052	.005406
.002910	.006526
.003922	.007646
.005088	.008757
.006406	.009849
.007888	.010911
.009549	.011946
.011397	.012964
.013434	.013967
.015651	.014950
.018055	.015916
.020650	.016867
.023433	.017810
.026399	.018749
.029546	.019678
.032873	.020598
.036384	.021511
.040071	.022420
.043934	.023324
.047966	.024221
.052169	.025110
.056541	.025989
.061081	.026859
.065787	.027723
.070656	.028577
.075686	.029423
.080875	.030257
.086223	.031082
.091725	.031897
.097378	.032701
.103182	.033494
.109136	.034277
.115235	.035050
.121473	.035810
.127851	.036557

x/c	$(z/c_N)_u$
0.134371	0.037292
.141029	.038014
.147817	.038723
.154734	.039418
.161778	.040100
.168950	.040768
.176244	.041423
.183656	.042061
.191183	.042684
.198823	.043292
.206572	.043884
.214430	.044459
.222392	.045019
.230455	.045561
.238617	.046088
.246871	.046599
.255218	.047093
.263652	.047570
.272172	.048030
.280774	.048470
.289453	.048892
.298206	.049295
.307031	.049679
.315924	.050045
.324881	.050391
.333900	.050719
.342975	.051028
.352105	.051318
.361284	.051588
.370509	.051839
.379778	.052069
.389086	.052279
.398431	.052469
.407807	.052639
.417210	.052788
.426639	.052917
.436089	.053025
.445557	.053111
.455040	.053175
.464532	.053218

x/c	$(z/c_N)_u$
0.474029	0.053239
.483529	.053238
.493030	.053215
.502527	.053170
.512015	.053104
.521490	.053015
.530948	.052903
.540387	.052769
.549803	.052613
.559194	.052435
.568553	.052235
.577880	.052012
.587168	.051766
.596415	.051498
.605618	.051207
.614772	.050892
.623874	.050553
.632921	.050191
.641910	.049806
.650837	.049395
.659698	.048960
.668491	.048501
.677212	.048018
.685858	.047511
.694427	.046979
.702914	.046424
.711315	.045842
.719626	.045233
.727844	.044595
.735968	.043930
.743999	.043238
.751931	.042519
.759761	.041771
.767487	.040996
.775103	.040192
.782607	.039358
.789998	.038493
.797275	.037591
.804442	.036651
.811497	.035676

Table II. Continued

x/c	$(z/c_N)_u$
0.818442	0.034665
.825269	.033620
.831976	.032537
.838567	.031409
.845049	.030237
.851485	.029011
.856436	.028031
.861386	.027025
.866337	.026004
.871287	.024974
.876238	.023941
.881188	.022906
.886139	.021871
.891089	.020837
.896040	.019802
.900990	.018767
.905941	.017733
.910891	.016698
.915842	.015663
.920792	.014630
.925743	.013597
.930693	.012565
.935644	.011535
.940594	.010505
.945545	.009476
.950495	.008449
.955446	.007422
.960396	.006397
.965347	.005374
.970297	.004353
.975248	.003335
.980198	.002318
.985149	.001303
.990099	.000290
.995050	.000721
1.000000	.001730

x/c	$(z/c_N)_\ell$
0.000000	0.000000
.000019	.000956
.000201	−.001824
.000574	−.002590
.001170	.003259
.002015	.003848
.003121	−.004375
.004484	−.004868
.006098	−.005328
.008000	−.005780
.011000	.006376
.015000	−.007115
.020000	−.008030
.025000	−.008945
.030000	−.009860
.035000	−.010775
.040000	−.011690
.045000	.012605
.050000	−.013520
.055000	−.014435
.060000	.015350
.065000	−.016265
.070000	.017180
.075000	−.018099
.080000	−.019030
.085000	−.019984
.090000	−.020980
.095000	.022050
.100000	.023200
.105000	.024440
.110000	.025770
.115000	−.027190
.120000	−.028690
.125000	.030270
.130000	−.031923
.135000	−.033640
.140000	−.035410
.145000	−.037225
.150000	.039072
.155000	−.040930
.160000	−.042790
.165000	.044650
.170000	−.046510
.175000	−.048373
.179500	−.050044

x/c	$(z/c_N)_\ell$
0.184000	−0.051714
.188500	−.053366
.193737	−.055206
.199755	−.057071
.205949	.058755
.212309	−.060304
.218818	−.061743
.225460	−.063084
.232232	−.064334
.239130	.065502
.246151	−.066598
.253282	.067625
.260515	−.068583
.267853	−.069479
.275295	−.070318
.282831	−.071101
.290451	.071830
.298158	−.072503
.305950	−.073124
.313817	.073693
.321752	−.074210
.329758	.074677
.337834	−.075096
.345971	−.075465
.354164	−.075786
.362413	−.076060
.370714	.076286
.379061	−.076464
.387448	−.076593
.395874	.076674
.404340	.076707
.412837	.076692
.421361	−.076628
.429910	.076518
.438482	−.076359
.447071	.076151
.455672	.075894
.464283	−.075589
.472903	−.075234
.481526	.074830
.490147	−.074375
.498762	−.073868
.507372	−.073310
.515971	−.072699
.524552	.072036

Table II. Concluded

x/c	$(z/c_N)_\ell$
0.533115	0.071319
.541656	.070548
.550174	.069721
.558658	.068839
.567107	.067899
.575514	.066899
.583873	.065836
.592180	.064704
.600430	.063497
.608620	.062206
.616747	.060820
.624811	.059324
.632822	.057702
.640795	.055943
.648750	.054040
.656709	.051988
.664701	.049797
.672750	.047489
.680868	.045093
.689604	.042483
.698515	−.039806
.704455	−.038018
.714356	.035038
.724257	.032057
.734158	.029077
.744059	.026097
.753960	.023117
.763861	.020137
.773762	.017156
.783663	−.014176
.793564	.011196
.801980	.008663
.807921	.006876
.811961	−.005661
.815130	−.004709
.817110	.004114
.818694	.003641
.819882	.003298
.821070	−.002997
.822258	.002750
.823447	−.002540
.825031	.002280
.826724	−.002006
.828699	−.001686
.830392	−.001412

x/c	$(z/c_N)_\ell$
0.832085	−0.001137
.833778	−.000860
.835471	−.000582
.837447	−.000257
.839140	.000021
.840724	.000277
.841912	.000456
.843100	.000602
.844288	.000701
.845476	.000766
.847060	.000839
.848753	.000911
.850729	.000993
.852422	.001063
.854115	.001135
.855808	.001207
.857501	.001280
.859476	.001367
.861386	.001452
.863366	.001542
.866337	.001675
.871287	.001898
.876238	.002121
.881188	.002344
.886139	.002565
.889109	.002691
.891089	.002763
.893069	.002818
.896040	.002881
.899010	.002938
.902970	.003011
.907921	.003101
.914851	.003216
.921782	.003291
.926733	.003289
.930693	.003235
.934653	.003128
.939604	.002929
.946535	.002571
.953465	.002174
.958416	.001882
.962376	.001647
.965347	.001462
.968317	.001263
.970297	.001118

x/c	$(z/c_N)_\ell$
0.972277	0.000958
.975248	.000699
.980198	.000240
.985149	−.000229
.988119	.000521
.990099	.000732
.992079	.000965
.995050	.001342
1.000000	.001986

Table III. Perforated Upper-Surface Duct and Flute Locations

Panel	Duct (laminar)	Duct (turbulent)	Flute	x/c flute center	Metering hole diameter, in.	Holes per flute, partitioned region
1	1	1	1	0.034	0.024	1
↓	1	↓	2	.050	.024	↓
	2		3	.059	.026	
	2		4	.062	↓	
	2	↓	5	.081		
	3	2	6	.089		
	3	↓	7	.101		
	3		8	.112		
	4		9	.124		
	4		10	.135		
	4	↓	11	.147		
	5	3	12	.158		
	5	↓	13	.169		
	6		14	.181		
	6		15	.192		
	6	↓	16	.204		
	7	4	17	.217		
	↓	↓	18	.228		
			19	.238		
↓			20	.249		
2	8	5	21	.265		
↓	↓	↓	22	.276		
			23	.287		
			24	.297		
			25	.308		
			26	.318		
	9	6	27	.333		
	↓	↓	28	.344		
			29	.356		
			30	.367		
			31	.379		
			32	.390		
	10	7	33	.402		
	↓	↓	34	.414		
			35	.425		
			36	.437		
			37	.448		
			38	.460		
	11	8	39	.471		
	↓	↓	40	.483		
			41	.494		
			42	.506		
↓	↓	↓	43	.517	↓	↓

Table III. Concluded

Panel	Duct (laminar)	Duct (turbulent)	Flute	x/c flute center	Metering hole diameter, in.	Holes per flute, partitioned region
2	12	9	44	0.532	0.026	1
↓	↓	↓	45	.544	↓	↓
↓	↓	↓	46	.555	↓	↓
↓	↓	↓	47	.567	↓	↓
↓	↓	↓	48	.578	↓	↓
3	13	10	49	.594	↓	↓
↓	↓	↓	50	.605	↓	↓
↓	↓	↓	51	.616	↓	↓
↓	↓	↓	52	.626	↓	↓
↓	14	11	53	.635	↓	↓
↓	↓	↓	54	.646	↓	↓
↓	↓	↓	55	.658	↓	↓
↓	↓	↓	56	.669	↓	↓
↓	↓	↓	57	.681	↓	↓
↓	15	12	58	.692	.113	4
↓	15	12	59	.703	↓	↓
↓	15	12	60	.715	↓	↓
↓	16	13	61	.726	↓	↓
↓	↓	↓	62	.744	.161	60
↓	↓	↓	63	.755	↓	60
↓	↓	↓	64	.767	↓	60
↓	17	14	65	.778	↓	58
↓	17	14	66	.790	↓	58
↓	17	14	67	.801	↓	58
↓	18	15	68	.813	↓	56
↓	18	↓	69	.824	↓	56
↓	19	↓	70	.836	↓	54
↓	19	↓	71	.847	.104	21
↓	20	16	72	.857	.154	56
↓	20	16	73	.869	.100	22
↓	21	16	74	.881	.161	49

Table IV. Lower-Surface Slot Locations for Initial Perforated LFC Airfoil Configuration

Duct	Slot	$(x/c)_N$	Slot width, in.
		Joint	
8	28	0.25683	0.0035
	29	.28050	.0031
	30	.30098	.0032
	31	.32019	.0037
	32	.33862	.0032
9	33	.35783	.0039
	34	.37448	.0034
	35	.38984	.0039
	36	.40419	.0034
	37	.41852	.0042
10	38	.43287	.0037
	39	.44619	.0039
	40	.45950	.0044
	41	.47282	.0036
	42	.48511	.0044
11	43	.49741	.0043
	44	.50893	.0038
	45	.52046	.0047
	46	.53134	.0045
	47	.54158	.0038
	48	.54894	.0049
		Joint	
12	49	.56446	.0043
	50	.56937	.0042
	51	.57718	.0046
	52	.58499	.0046
	53	.58970	.0044
13	54	.60061	.0046
	55	.60843	.0053
	56	.61624	.0051
	57	.62136	.0050
	58	.62571	.0052
	59	.63006	.0048
	60	.63442	.0048
	61	.63800	.0048
14	62	.64158	.0047
	63	.64517	.0045
	64	.64838	.0043
	65	.65157	.0042
	66	.65477	.0040
	67	.65798	.0039
	73	.67719	.0036

Table IV. Continued

Duct	Slot	$(x/c)_N$	Slot width, in.
15	68	.66118	.0038
↓	68	.66118	.0038
	69	.66438	.0037
	70	.66758	.0037
	71	.67078	.0036
	72	.67398	.0036
16	74	.68039	.0036
↓	75	.68358	.0035
	76	.68679	.0034
	77	.68999	.0034
	78	.69319	.0033
	79	.69640	.0033
	80	.69959	.0032
↓	81	.70279	↓
17	82	.70600	
↓	83	.70920	
	84	.71240	
	85	.71560	↓
	86	.71880	.0031
	87	.72200	.0031
	88	.72521	.0031
	89	.72841	.0030
	90	.73160	↓
	91	.73480	
↓	92	.73801	↓
18	93	.74121	.0031
↓	94	.74441	.0033
	95	.74800	.0033
	96	.75158	.0032
	97	.75517	↓
	98	.75875	
	99	.76234	
	100	.76592	↓
↓	101	.76951	.0033
19	102	.77751	.0034
↓	103	.78027	.0034
	104	.78385	.0033
	105	.78727	.0034
	106	.79050	.0031
↓	107	.79357	.0030
20	108	.79651	.0030
↓	109	.79933	.0029
	110	.80202	.0028
	111	.80458	.0026
	112	.80689	.0026
	113	.80919	.0025
↓	114	.81124	.0024

Table IV. Concluded

Duct	Slot	$(x/c)_N$	Slot width, in.
21	115	.81316	.0022
↓	116	.81475	.0021
	117	.81613	.0020
	118	.81741	↓
	119	.81869	
	120	.81997	
	121	.83258	.0026
	122	.83488	.0026
	123	.83719	.0026
	124	.83911	.0025
↓	125	.84072	.0025

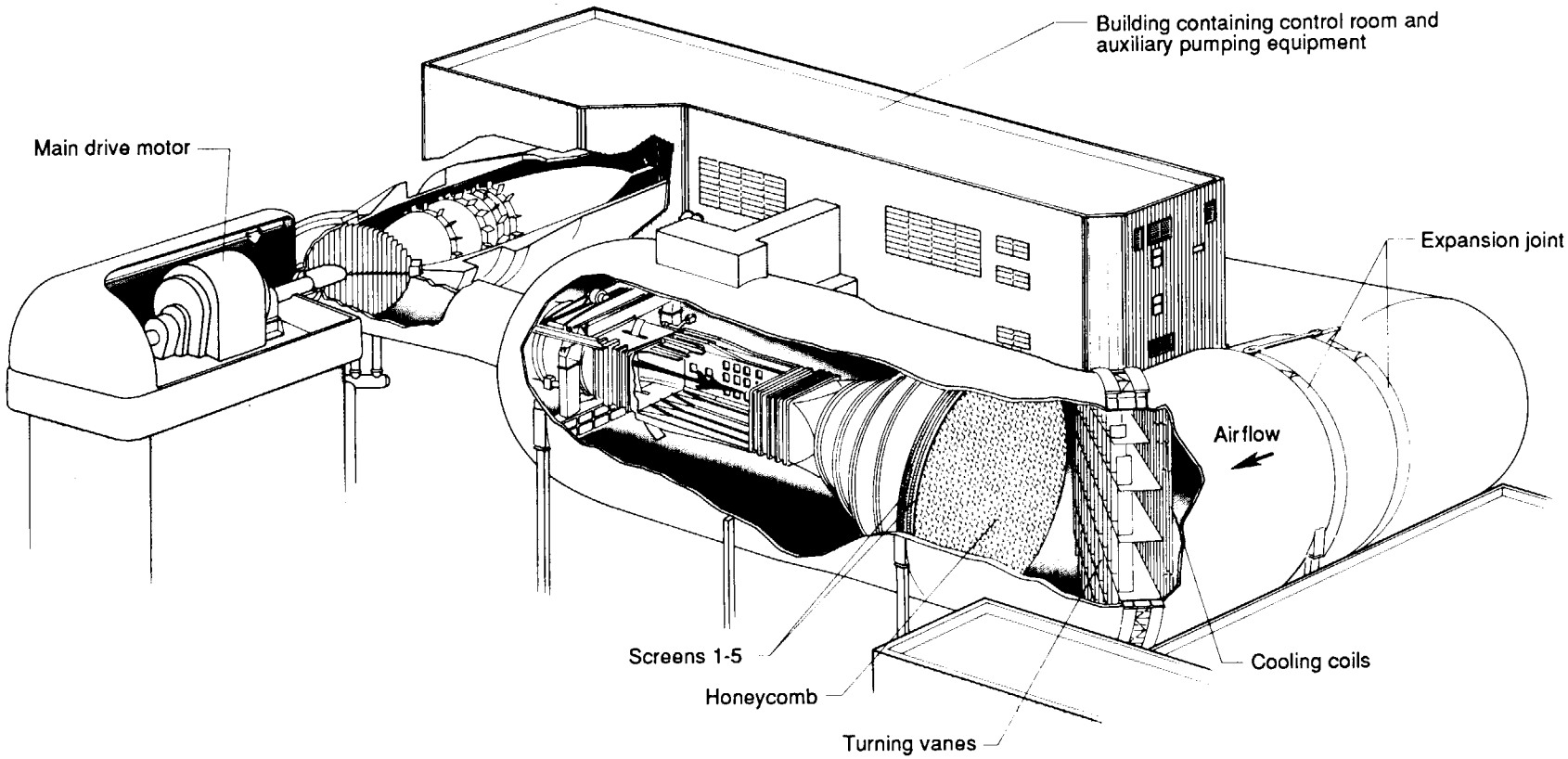

(a) Artist's conception of tunnel.

Figure 1. General test setup in 8-Foot Transonic Pressure Tunnel.

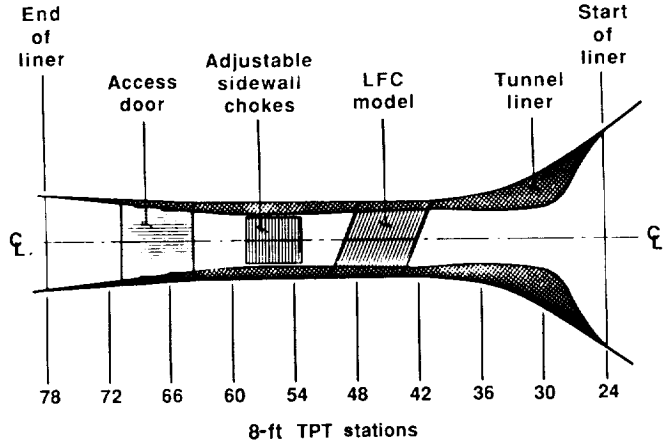

(b) Liner layout.

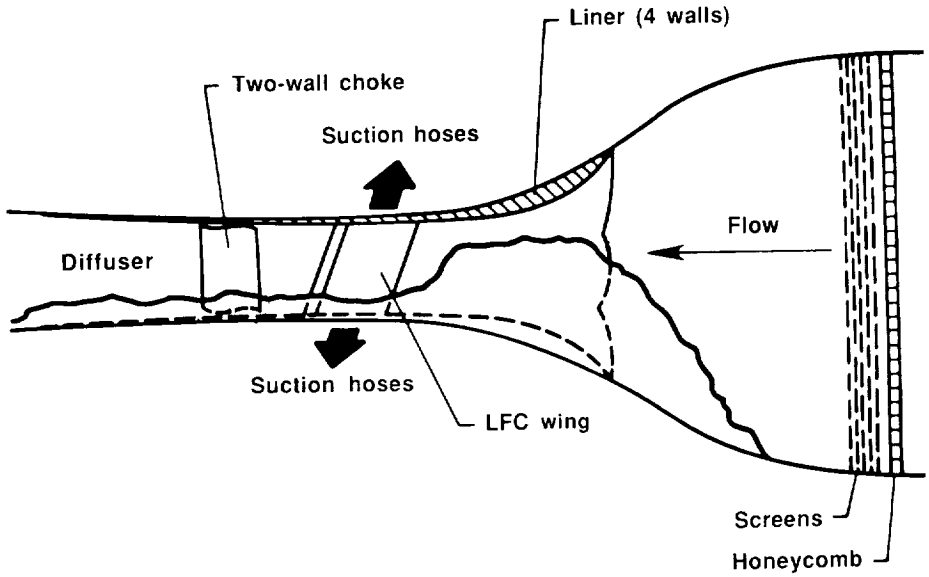

(c) General layout of liner and its location relative to honeycomb and screens.

Figure 1. Continued.

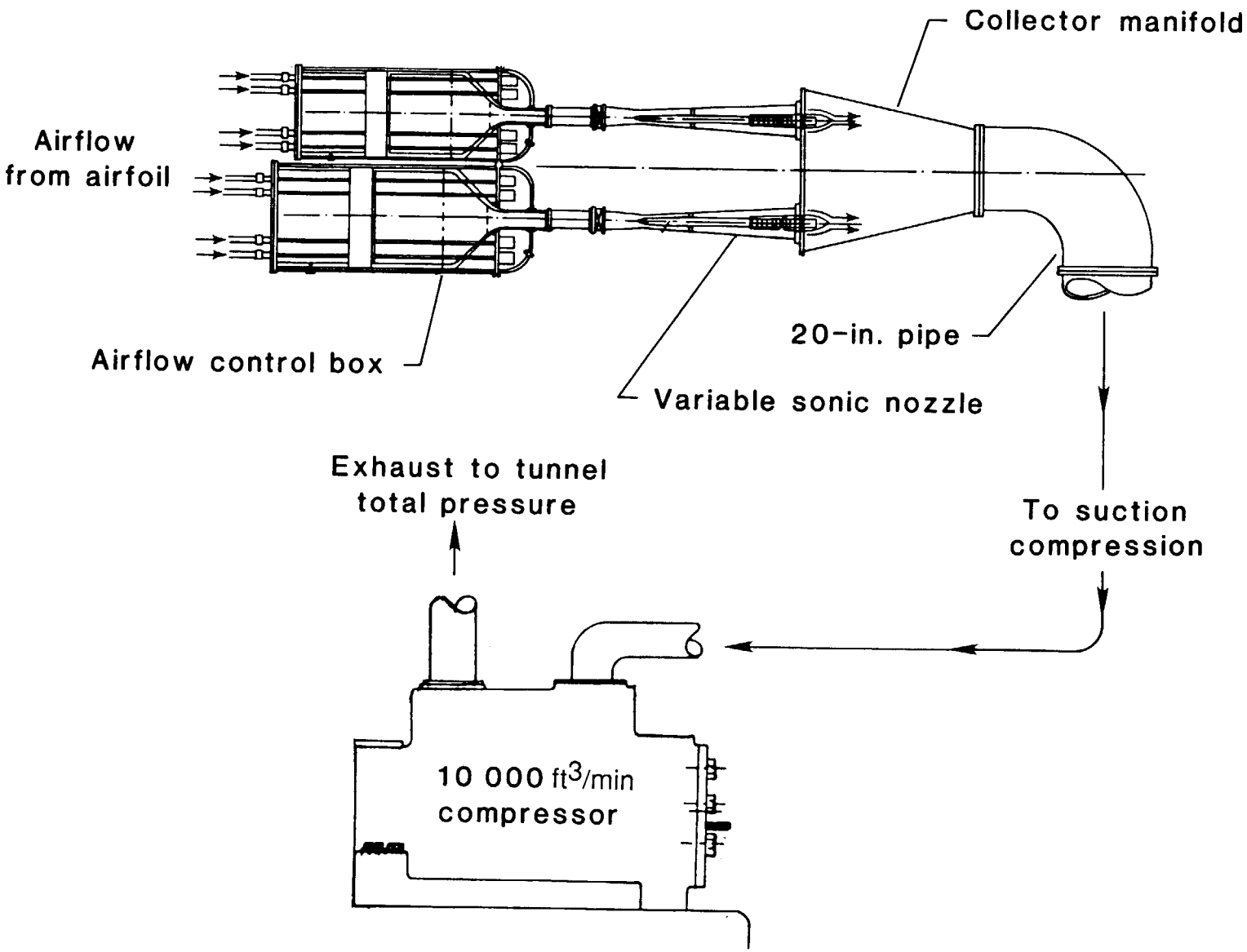

(d) Suction airflow system.

Figure 1. Concluded.

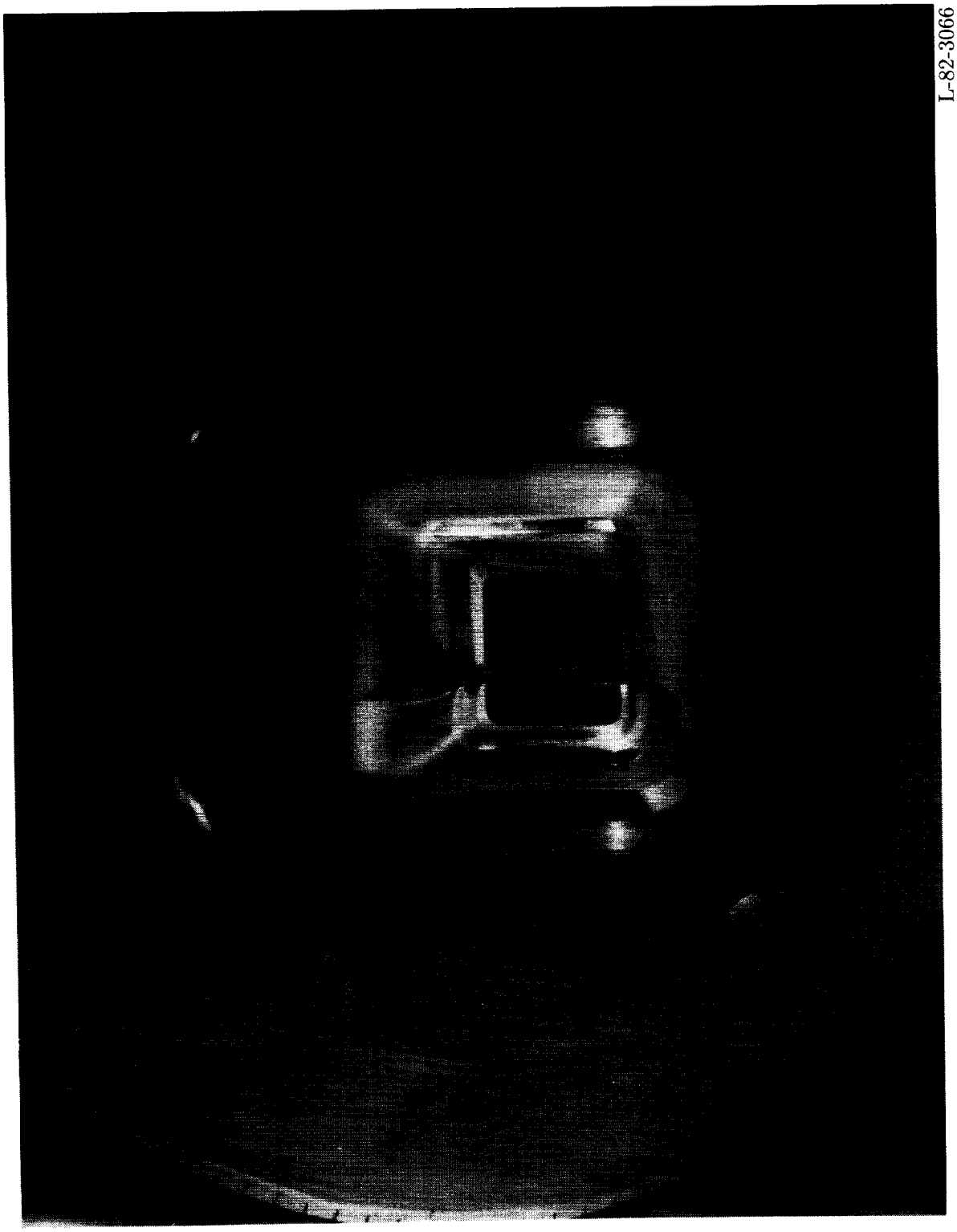

L-82-3066

(a) Upstream view of installed model and liner from diffuser.

Figure 2. Photographs of installed liner and model.

ORIGINAL PAGE
BLACK AND WHITE PHOTOGRAPH

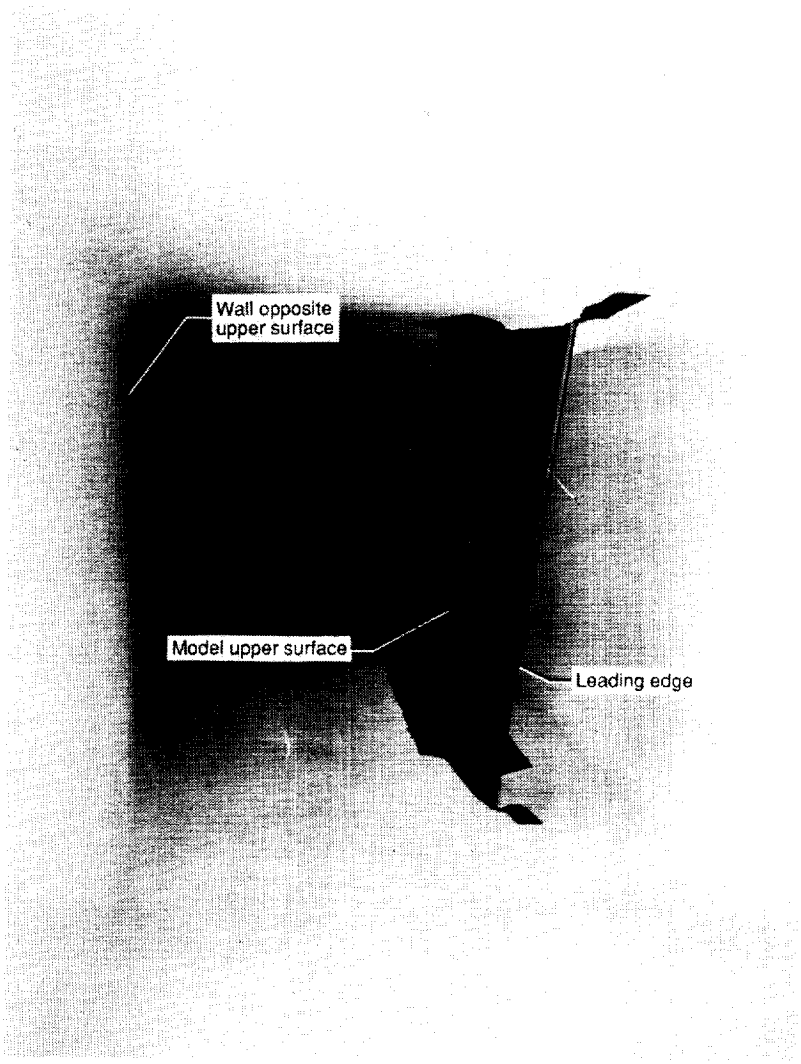

L-82-3619

(b) Downstream view of model.

Figure 2. Continued.

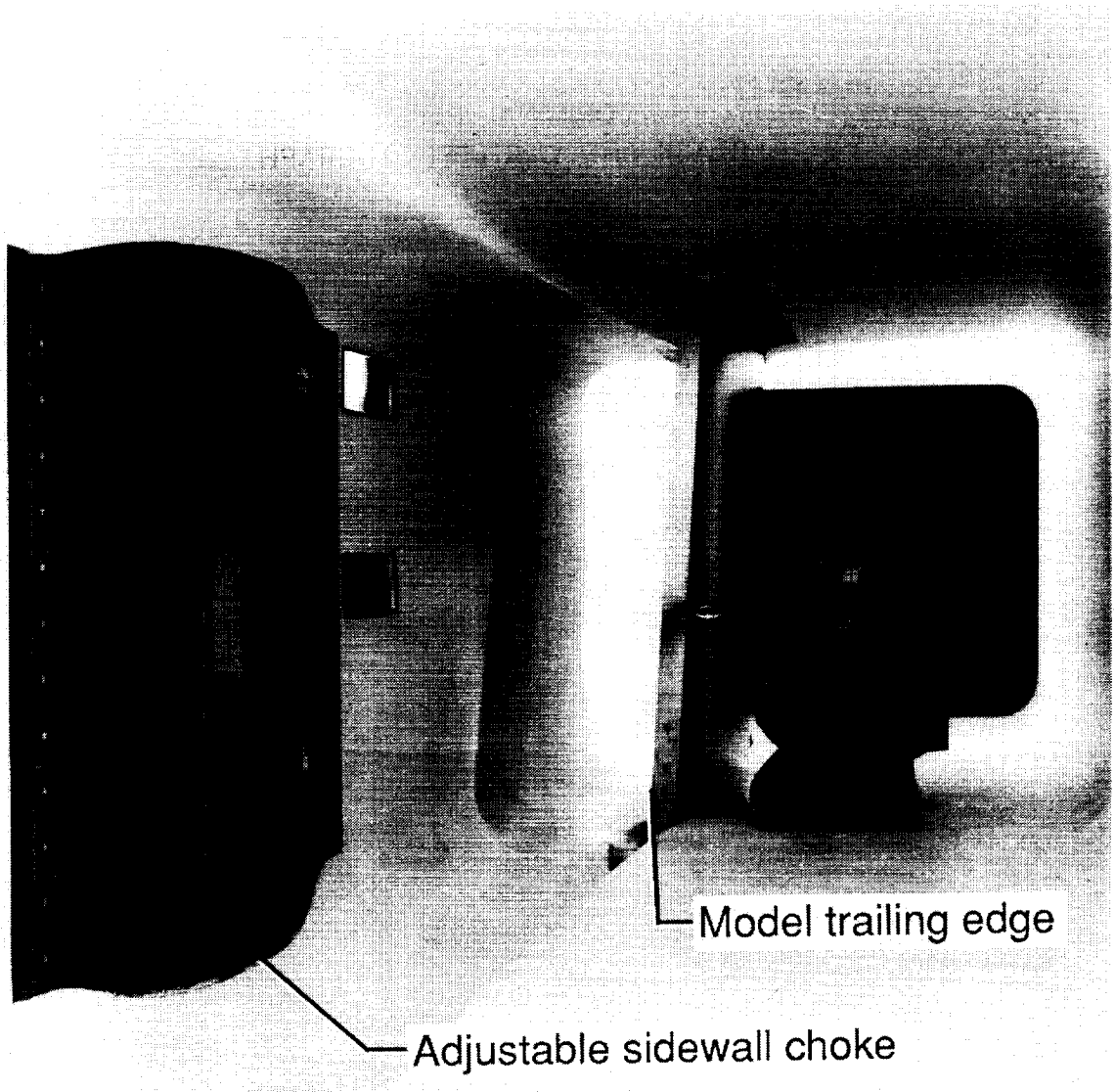

L-82-3071

(c) Upstream view of adjustable choke (on wall opposite lower surface) and trailing edge of model.

Figure 2. Continued.

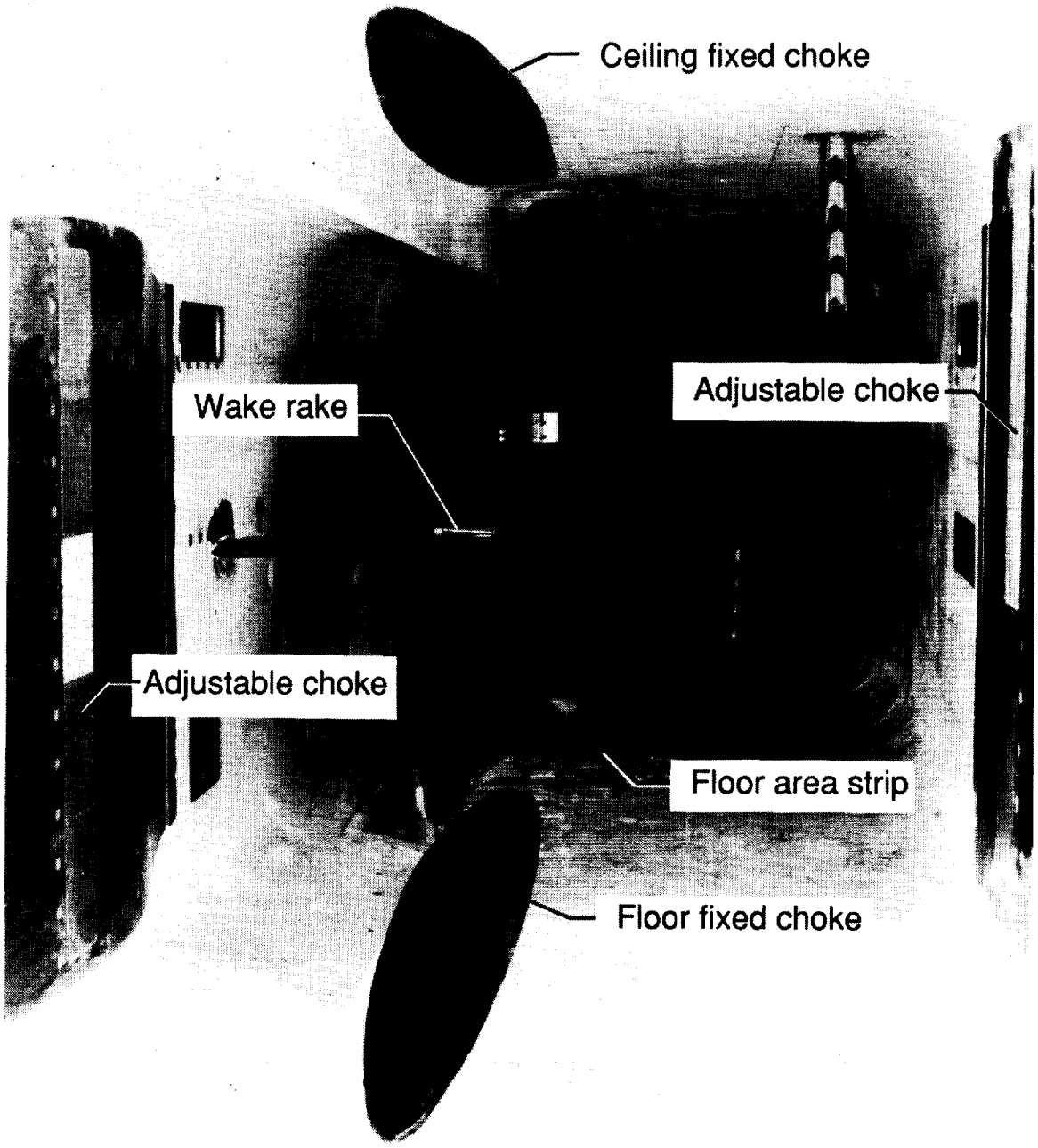

L-84-12,369

(d) Upstream view of fixed choke on floor and floor area strip above model upper surface.

Figure 2. Continued.

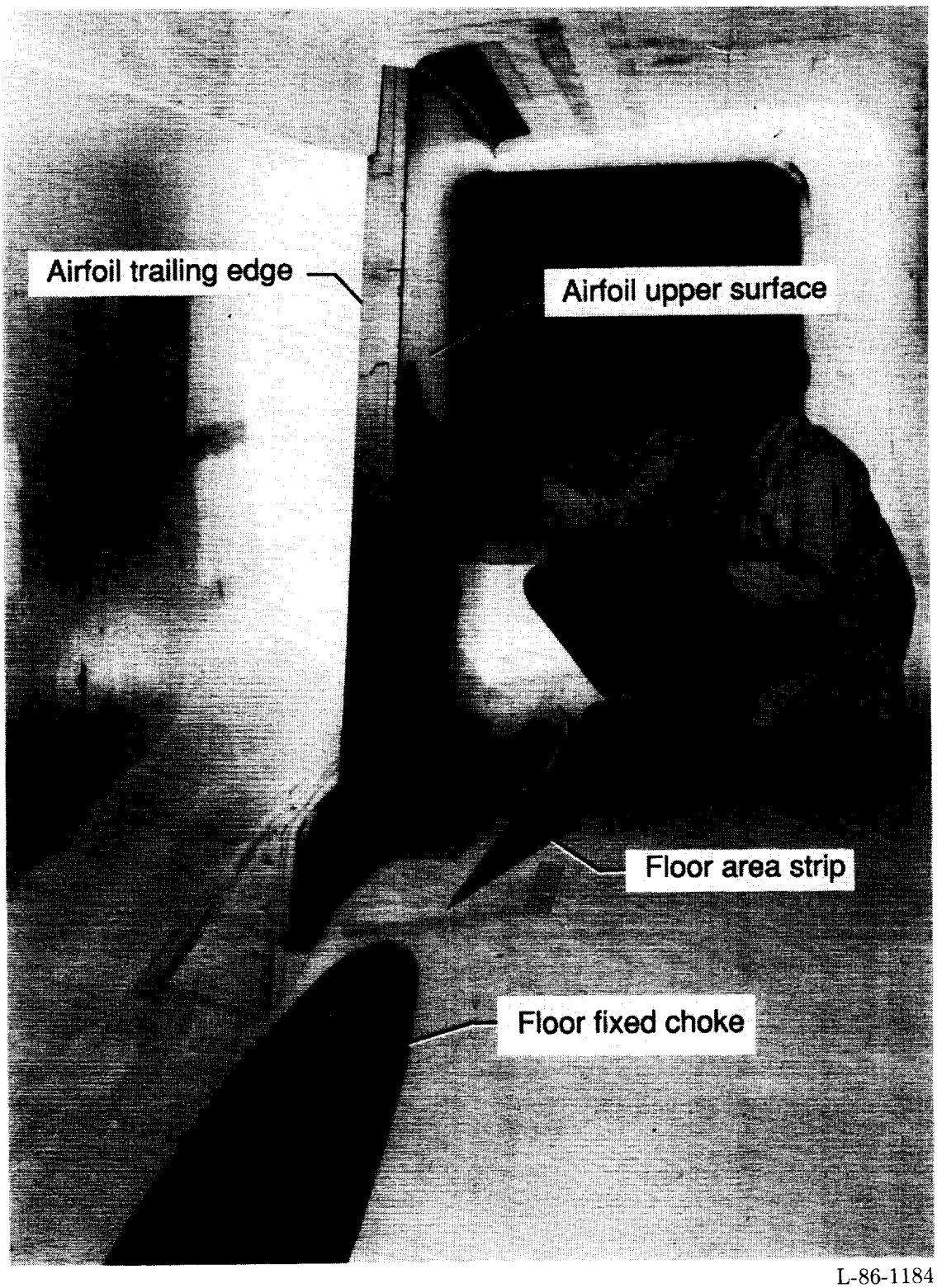

L-86-1184

(e) Upstream view of forward portion of fixed choke on floor and floor area strip.

Figure 2. Continued.

ORIGINAL PAGE
BLACK AND WHITE PHOTOGRAPH

L-86-1185

(f) Upstream view of model with vortex generators in corners.

Figure 2. Concluded.

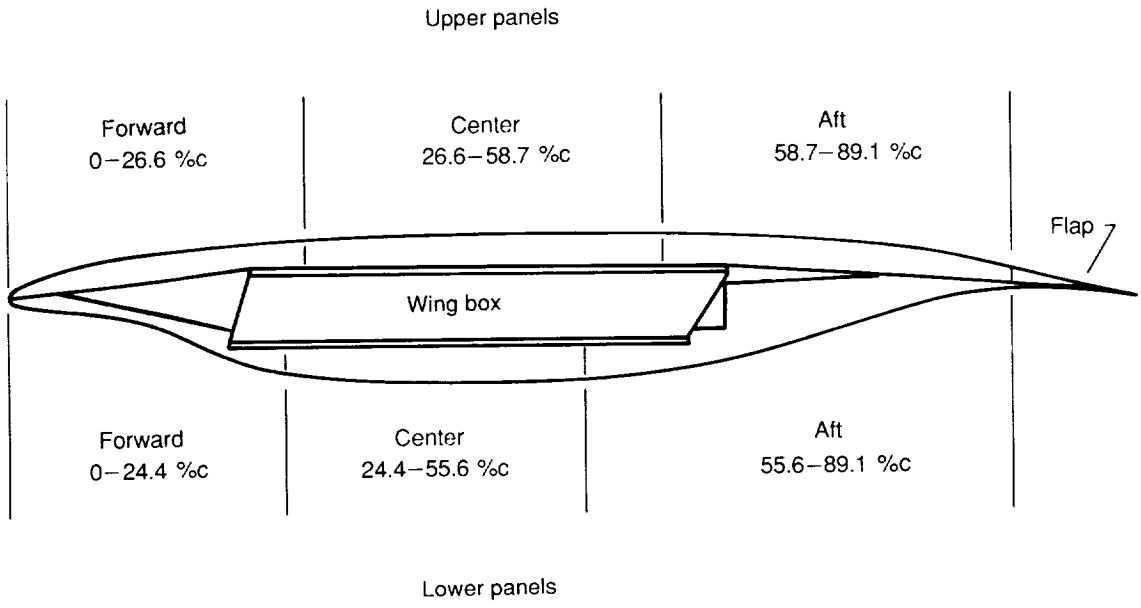

(a) Slotted model.

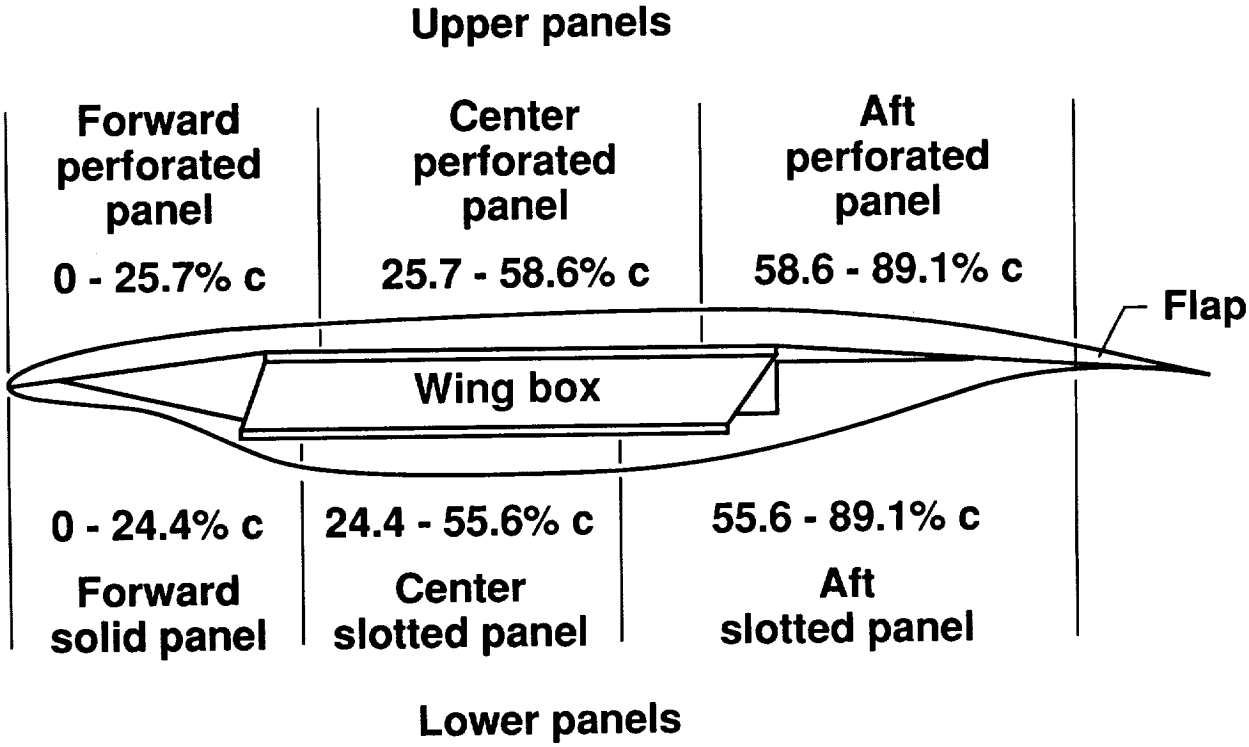

(b) Perforated model.

Figure 3. Cross section of panel arrangement normal to leading edge.

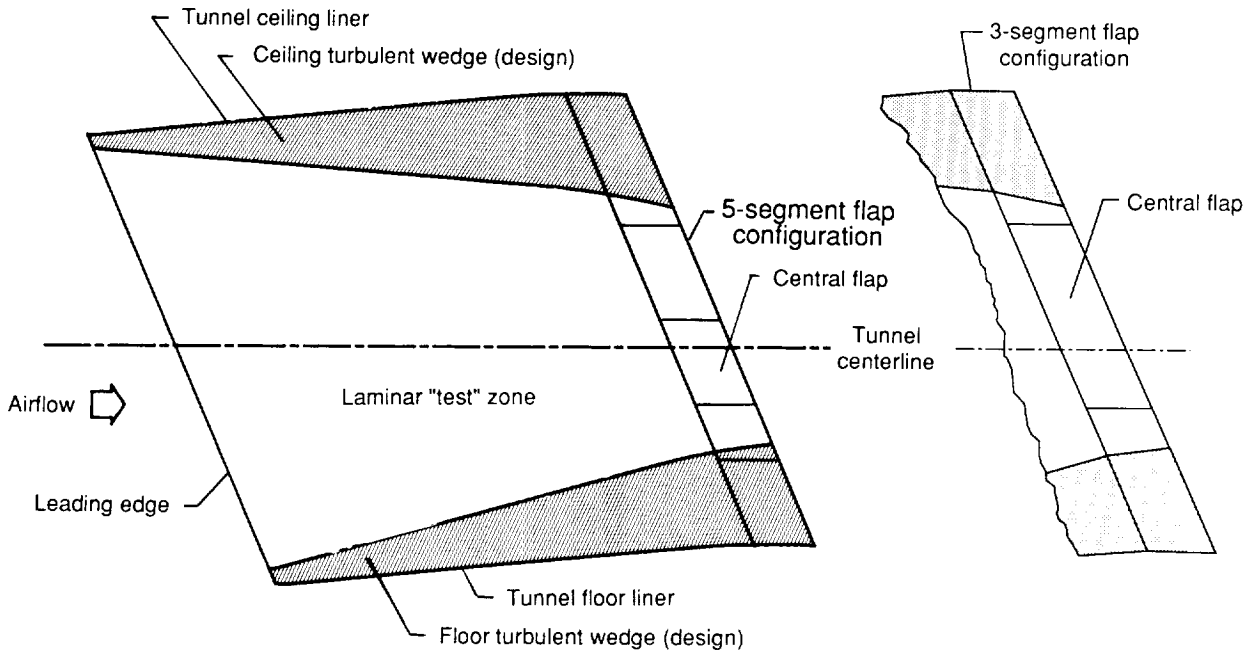

(a) Upper-surface planform as viewed through model from beneath lower surface.

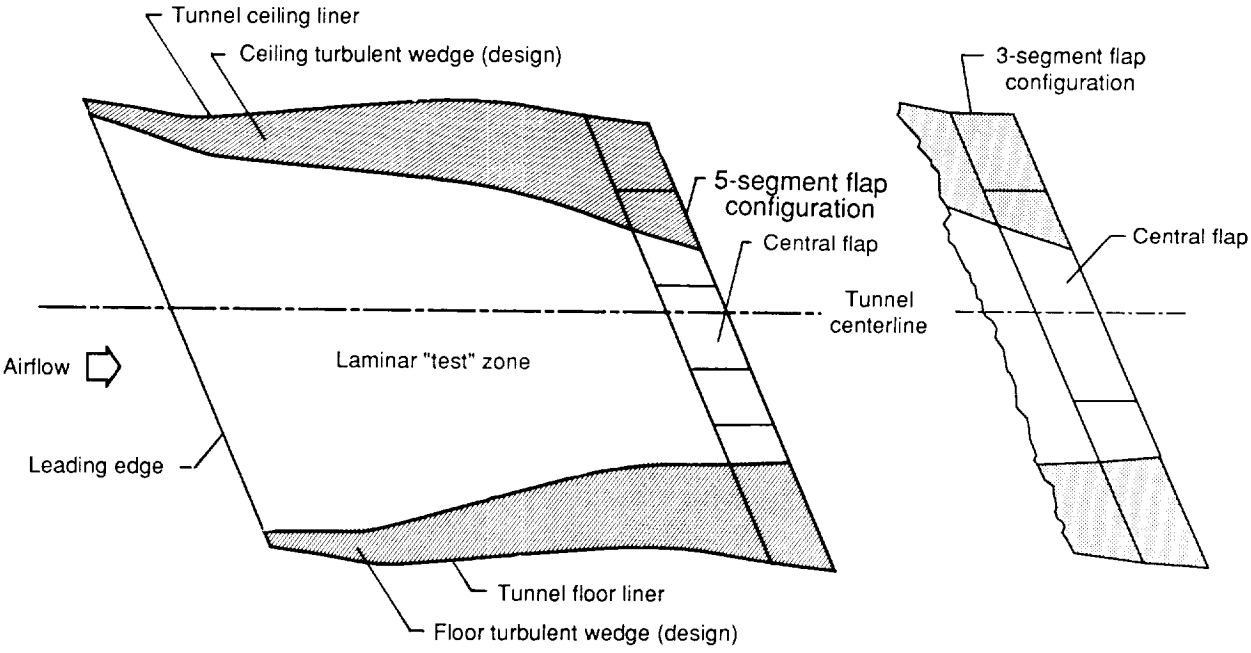

(b) Lower-surface planform as viewed from beneath lower surface.

Figure 4. Laminar "test" zones and turbulent wedges for slotted model.

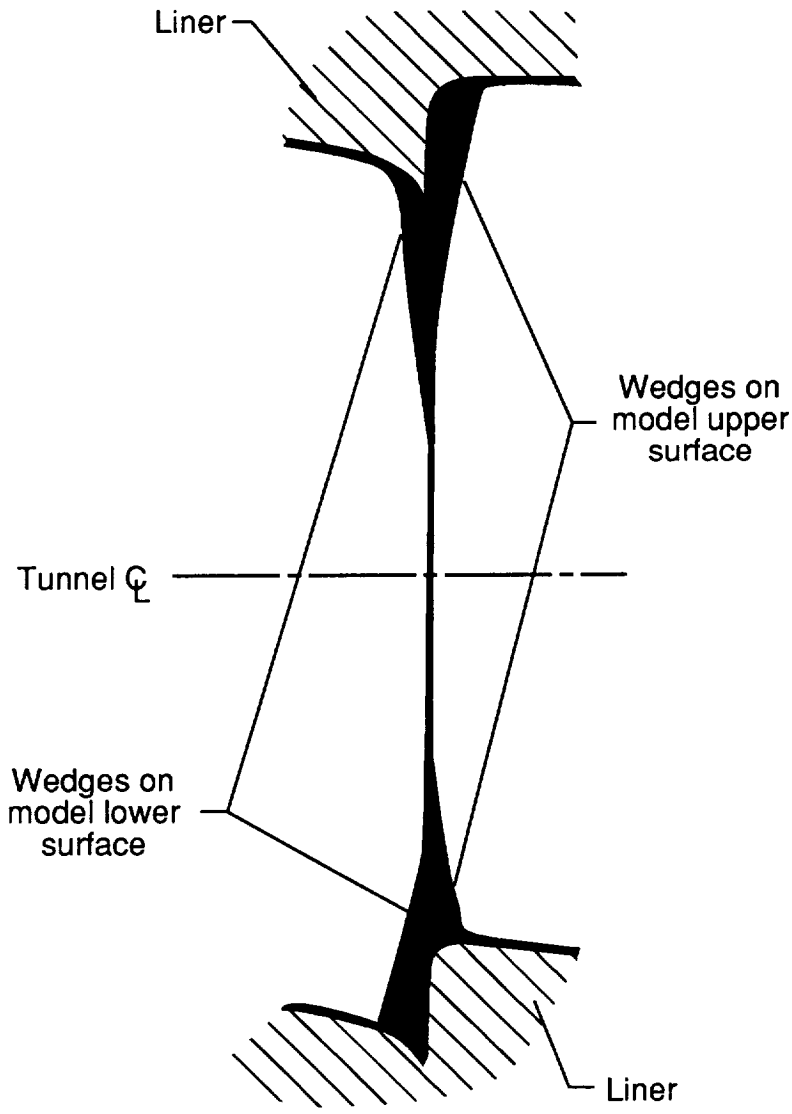

(c) Trailing-edge view of turbulent wedges in junctures of model and liner.

Figure 4. Concluded.

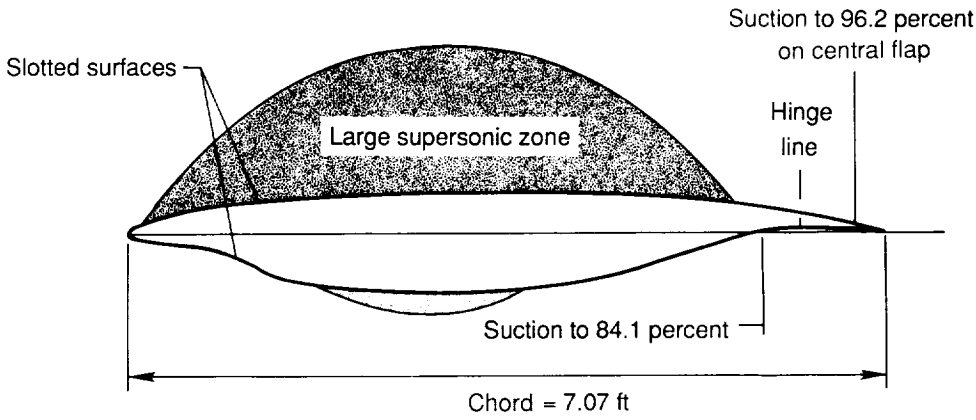

Free-stream design conditions	Design conditions normal to leading edge
$M_\infty = 0.82$	$M_N = 0.755$
$\Lambda = 23°$	$c_N = 6.508$ ft
$c = 7.07$ ft	$R_{c,N} = 16.9 \times 10^6$
$R_c = 20 \times 10^6$	$(t/c)_N = 13.0$ percent
$c_l = 0.47$	$c_{l,N} = 0.55$

(a) Slotted model.

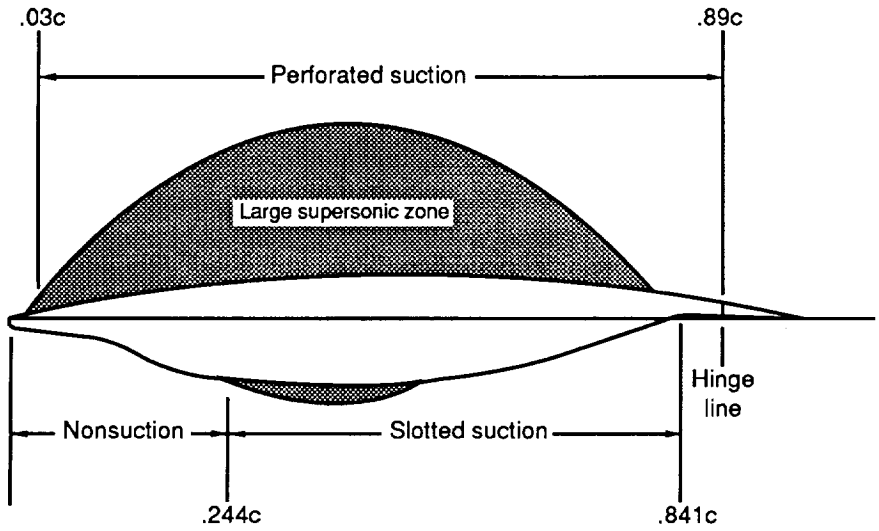

Free-stream design conditions	Design conditions normal to leading edge
$M_\infty = 0.82$	$M_N = 0.755$
$\Lambda = 23°$	$c_N = 6.508$ ft
$c = 7.07$ ft	$R_{c,N} = 16.9 \times 10^6$
$R_c = 20 \times 10^6$	$(t/c)_N = 13.0$ percent
$c_l = 0.47$	$c_{l,N} = 0.55$

(b) Perforated model.

Figure 5. Airfoil design parameters.

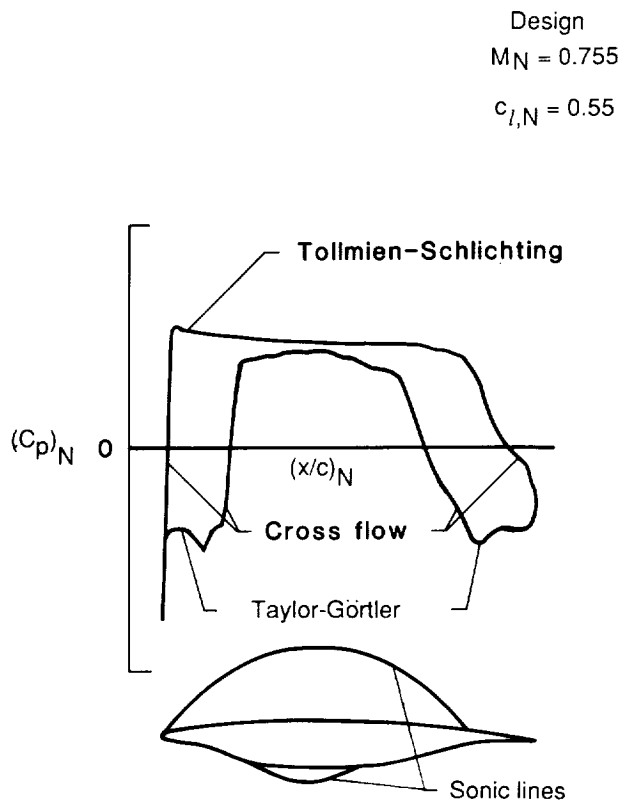

Figure 6. Theoretical pressure distribution and sonic line for "near final" shock-free design normal to leading edge.

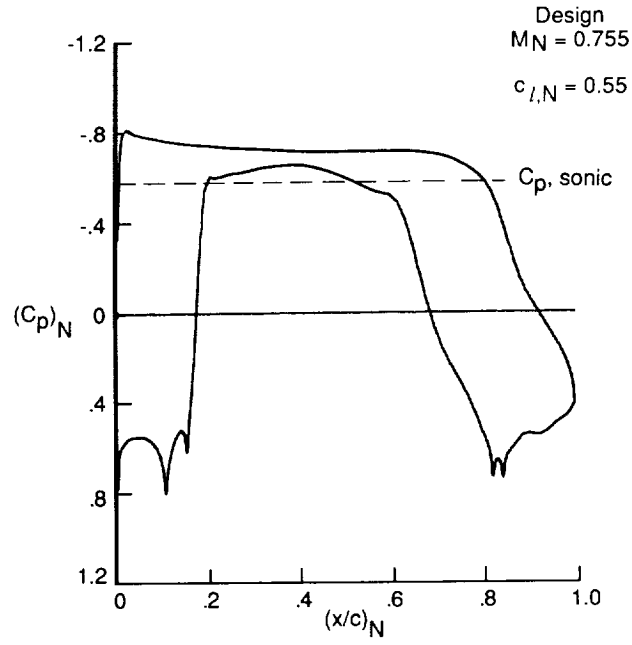

Figure 7. "Final" theoretical pressure distribution normal to leading edge combining Korn-Garabedian (ref. 9) and Eppler calculations (ref. 15).

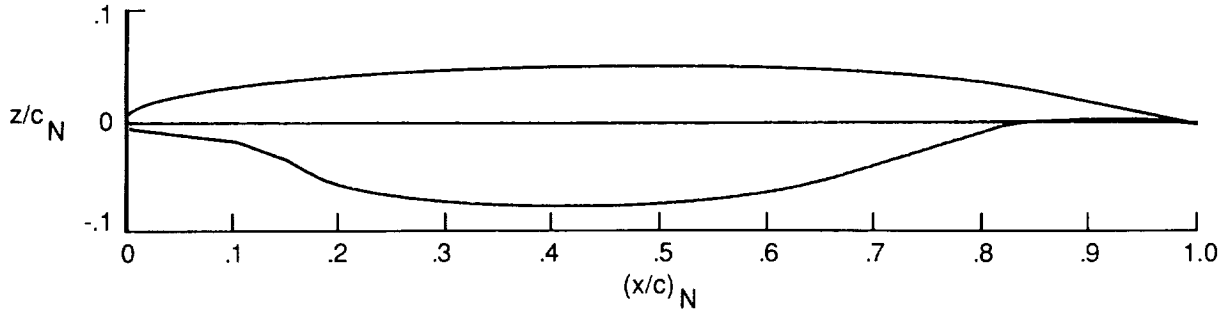

(a) Upper- and lower-surface contours.

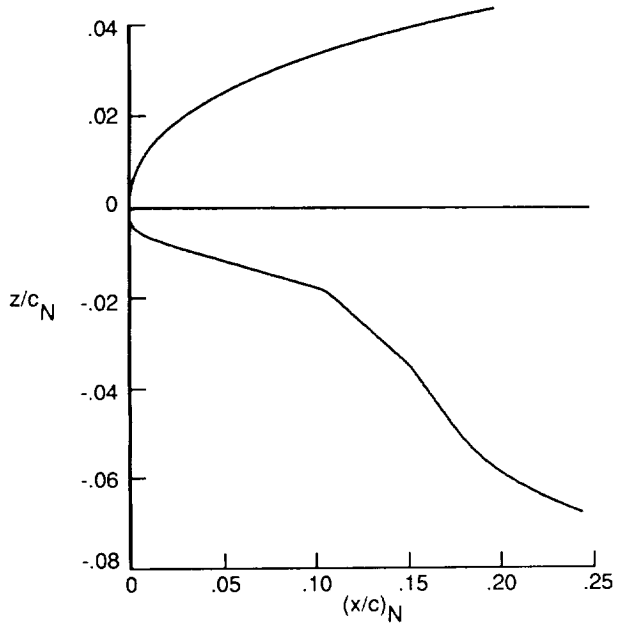

(b) Forward lower surface.

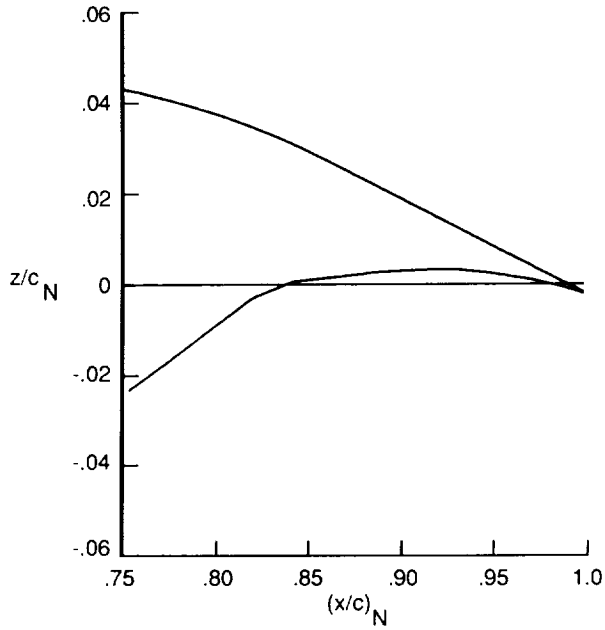

(c) Aft lower surface.

Figure 8. Sketches of slotted LFC airfoil normal to leading edge.

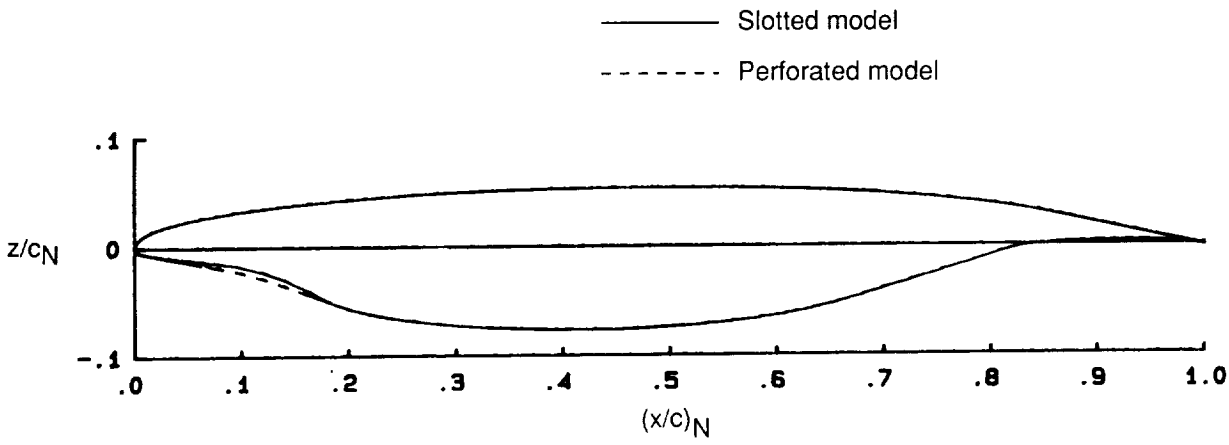

(a) Upper- and lower-surface contours.

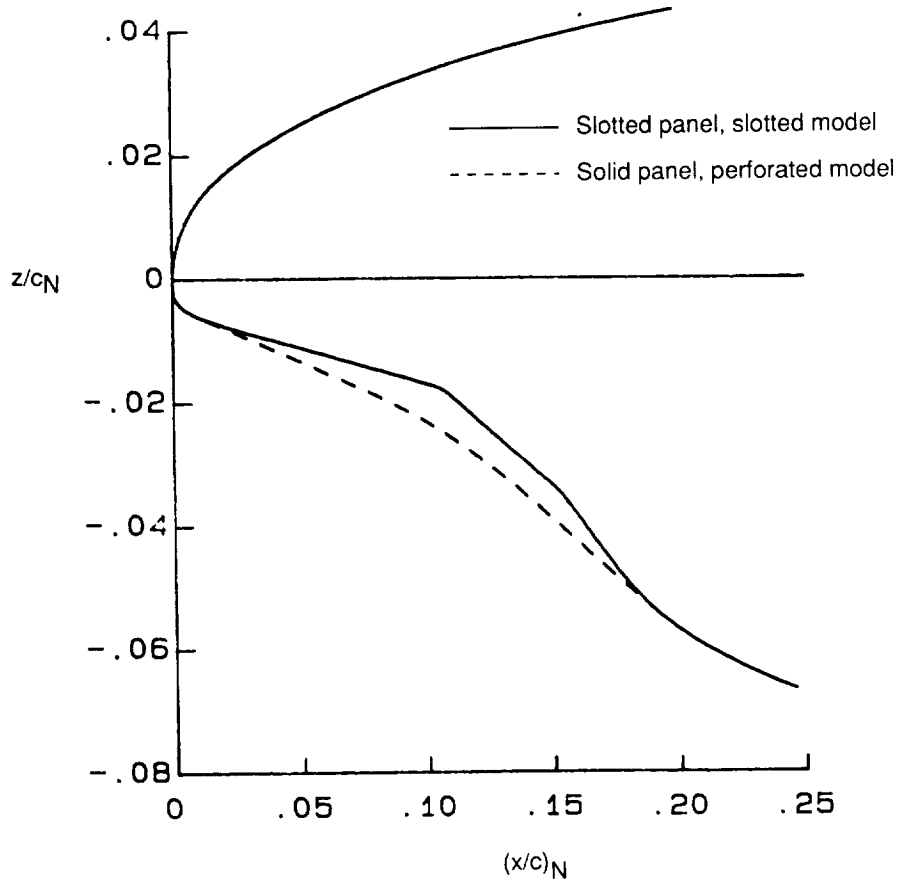

(b) Forward lower surface.

Figure 9. Sketches of perforated LFC airfoil normal to leading edge.

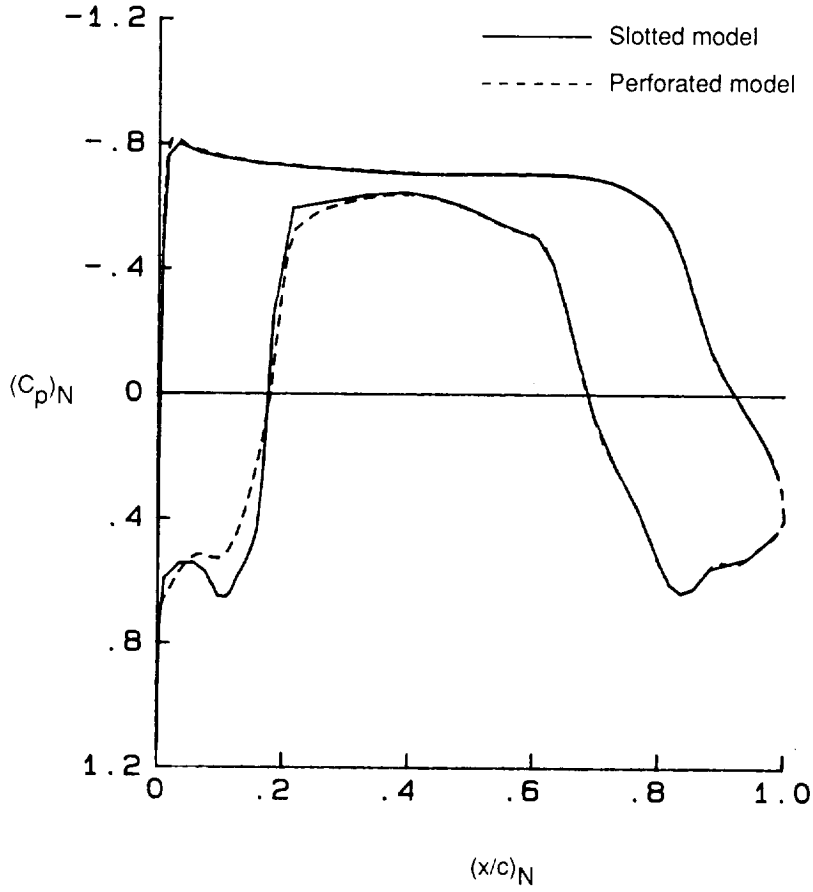

Figure 10. Comparison of design pressure distributions.

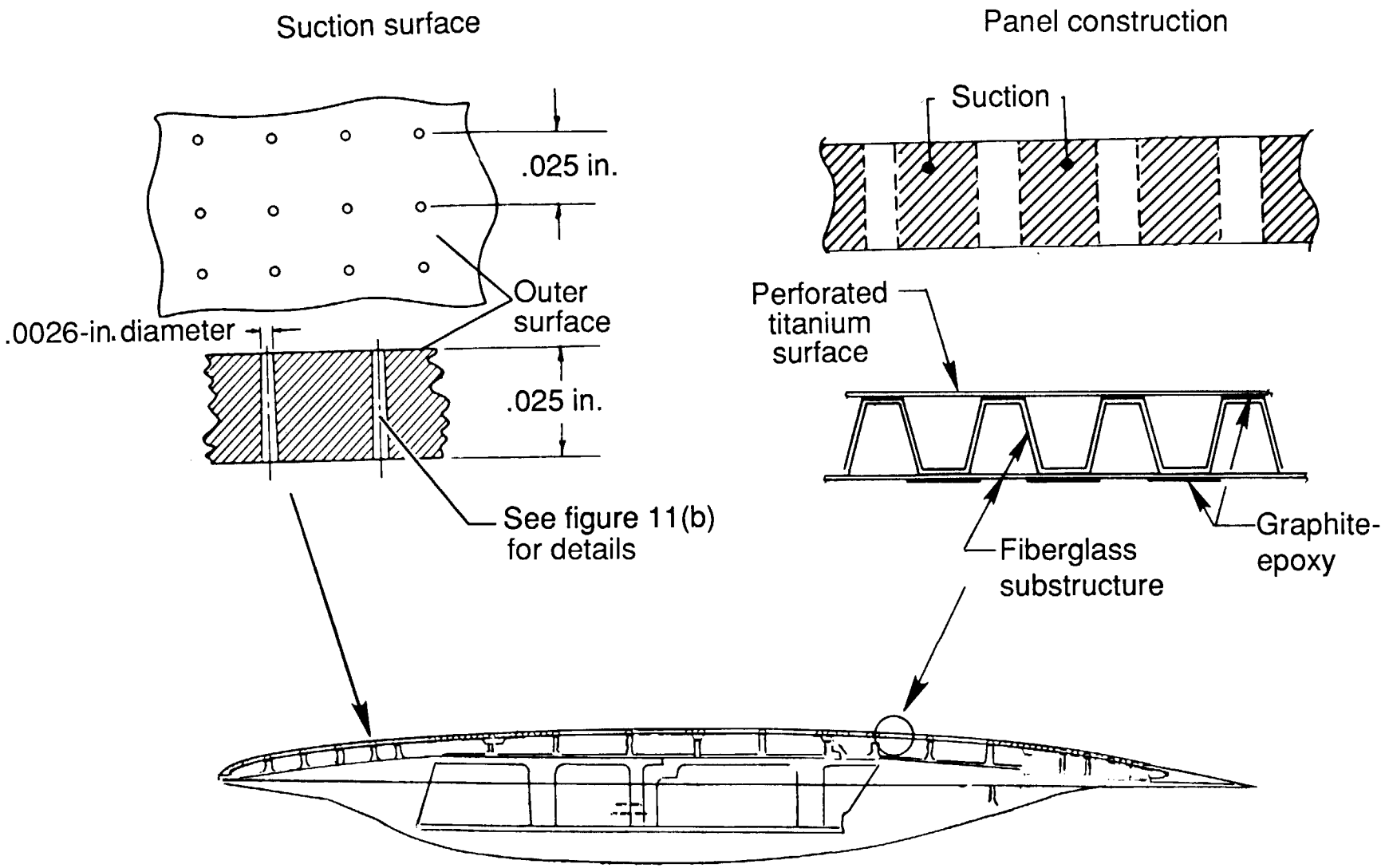

(a) Perforated panels.

Figure 11. Sketches of select elements of perforated LFC model.

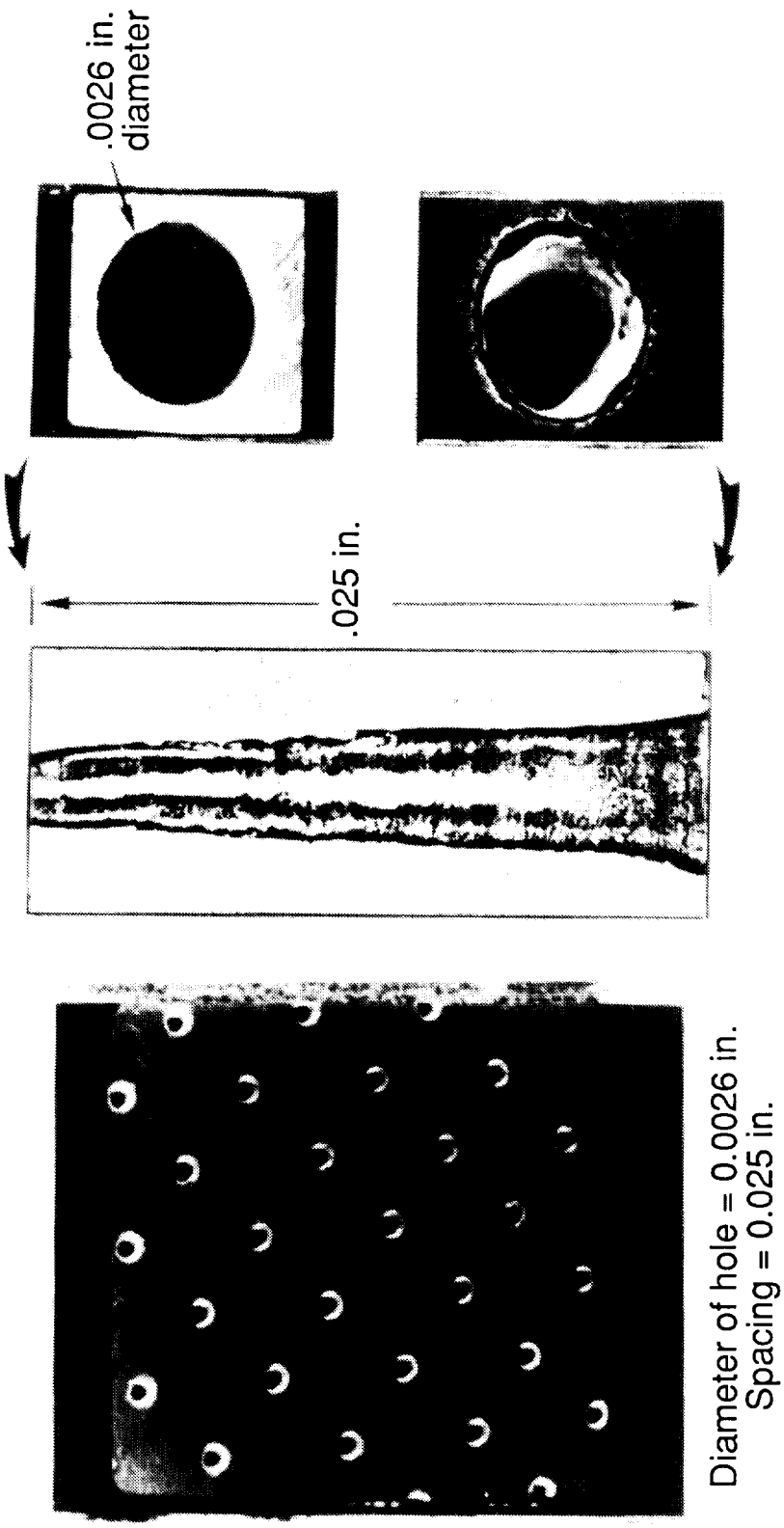

(b) Electron-beam-perforated titanium skin.

Figure 11. Continued.

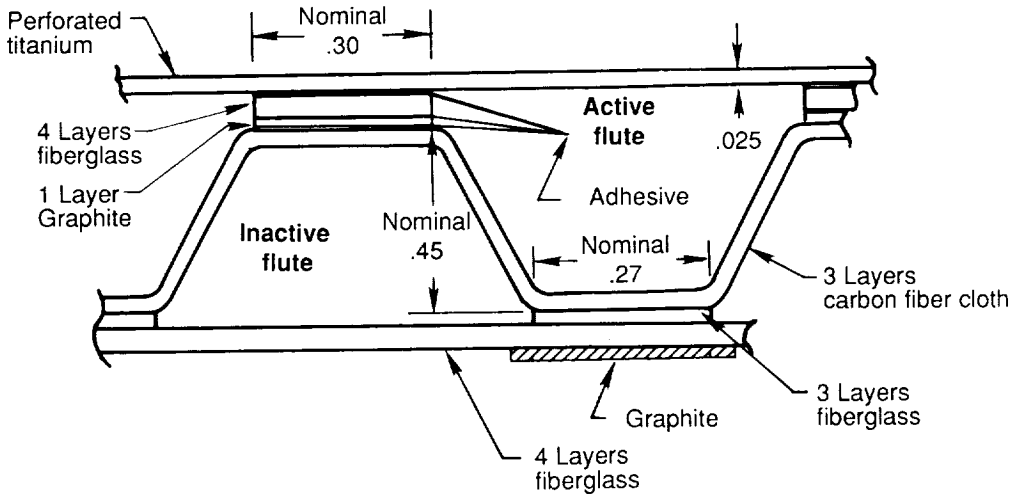

(c) Skin-flute construction.

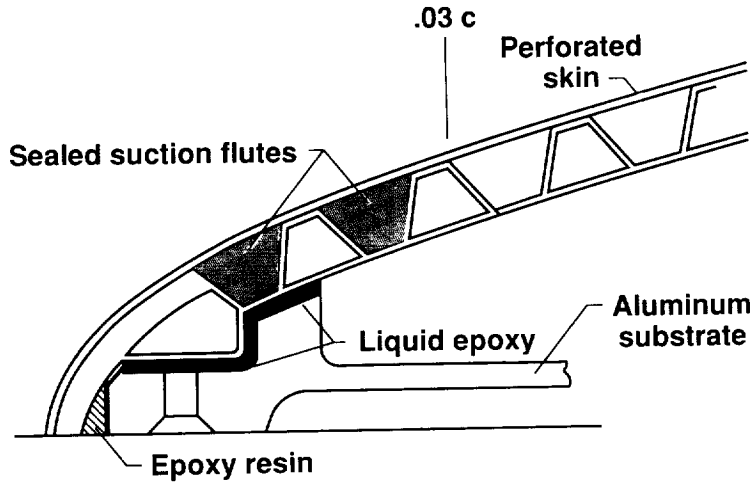

(d) Leading-edge construction.

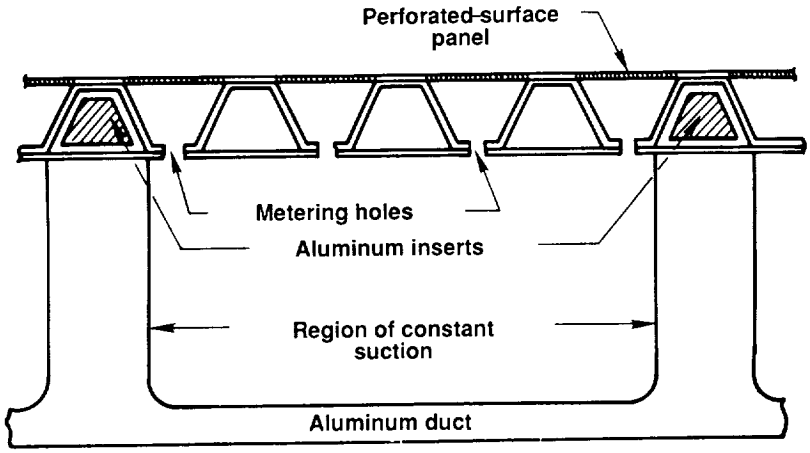

(e) Skin-flute–duct construction.

Figure 11. Concluded.

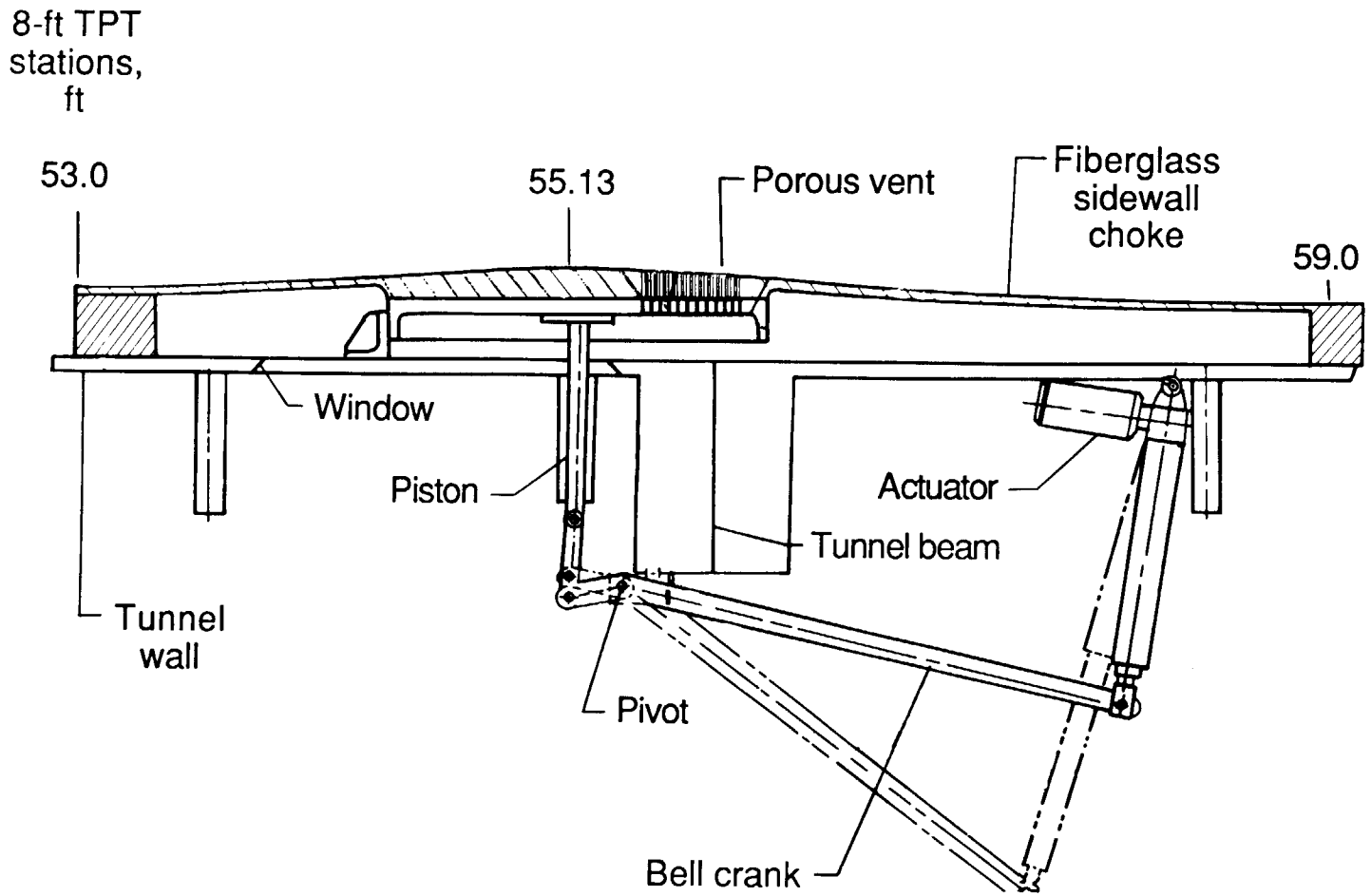

Figure 12. Cross-sectional schematic of choke plates.

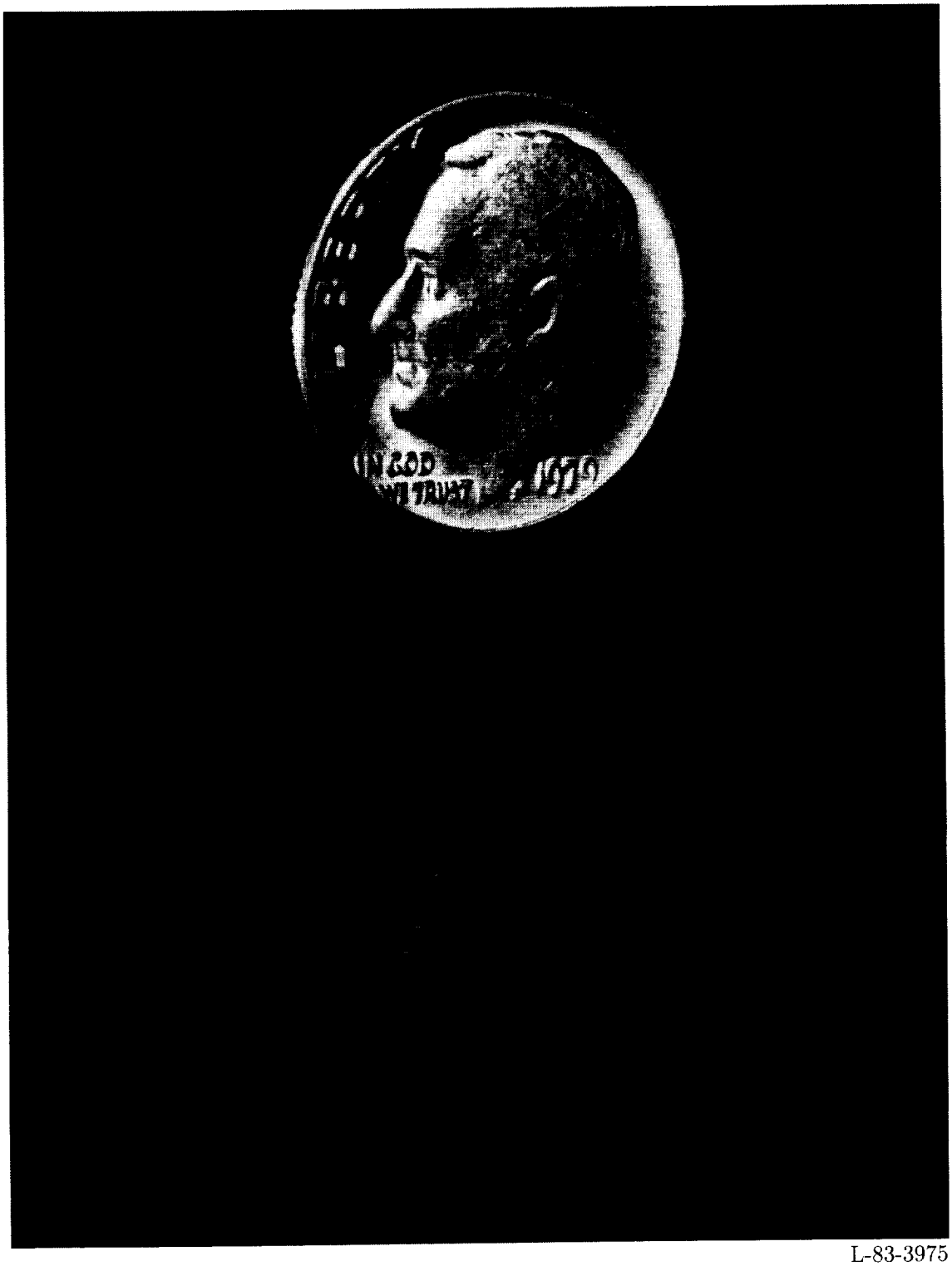

L-83-3975

(a) Photograph of slotted suction surface.

Figure 13. Components of the suction system on the slotted model.

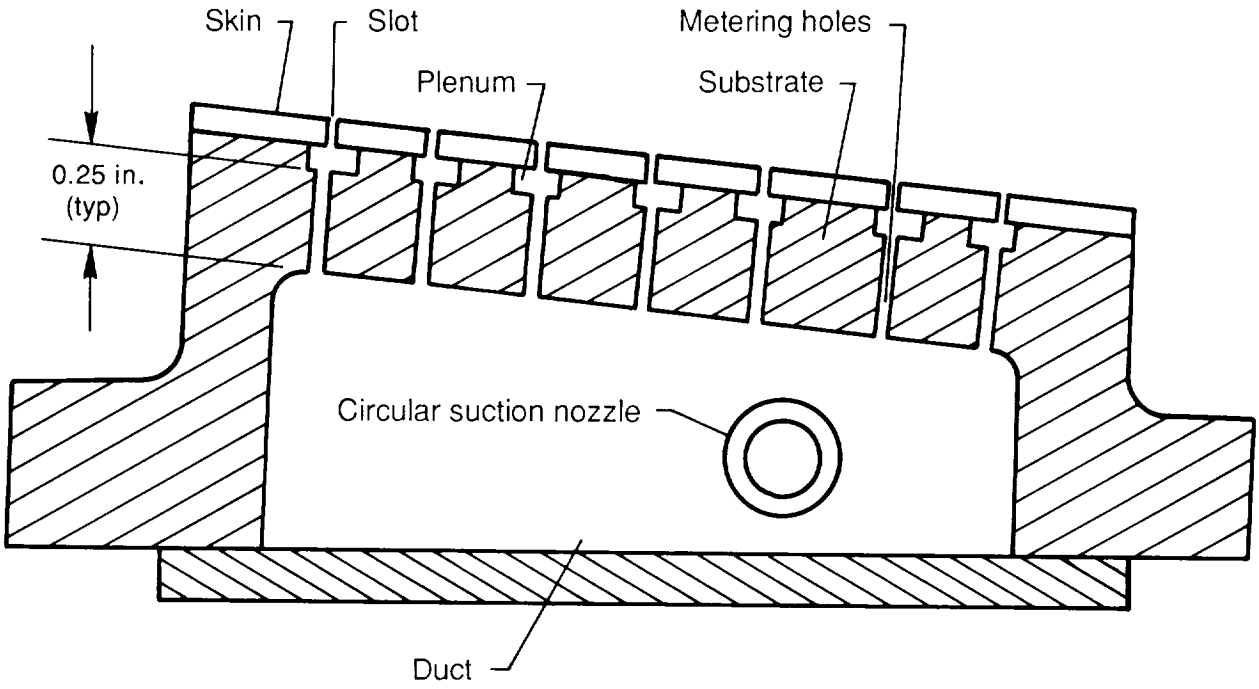

(b) Cross section of suction duct.

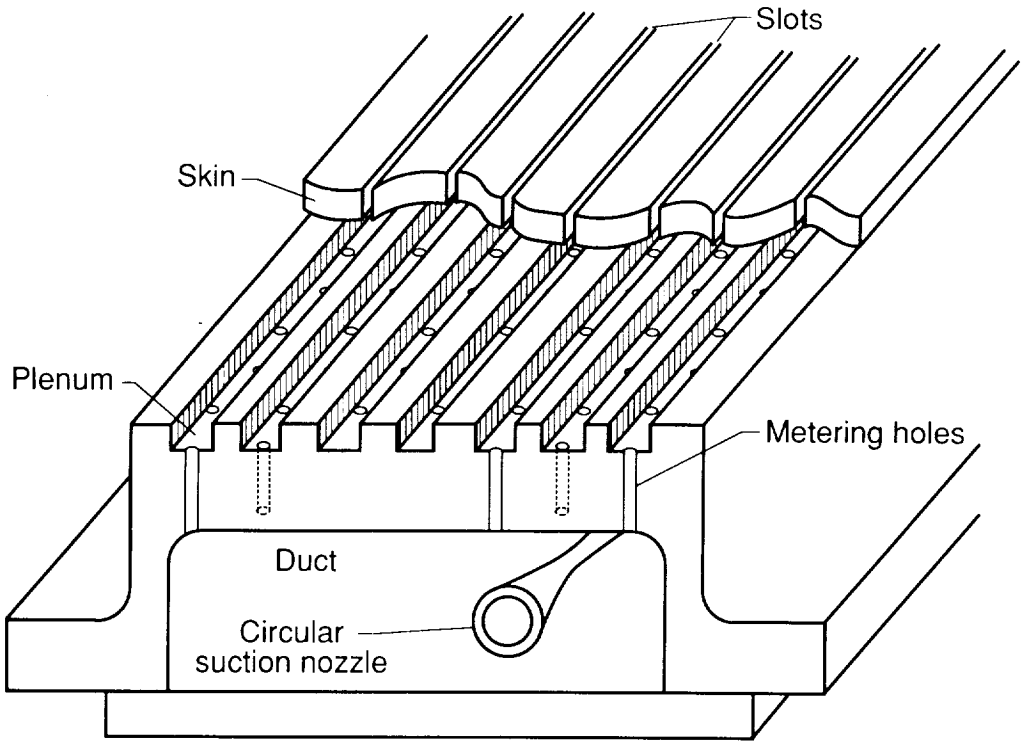

(c) Isometric sketch of suction duct.

Figure 13. Continued.

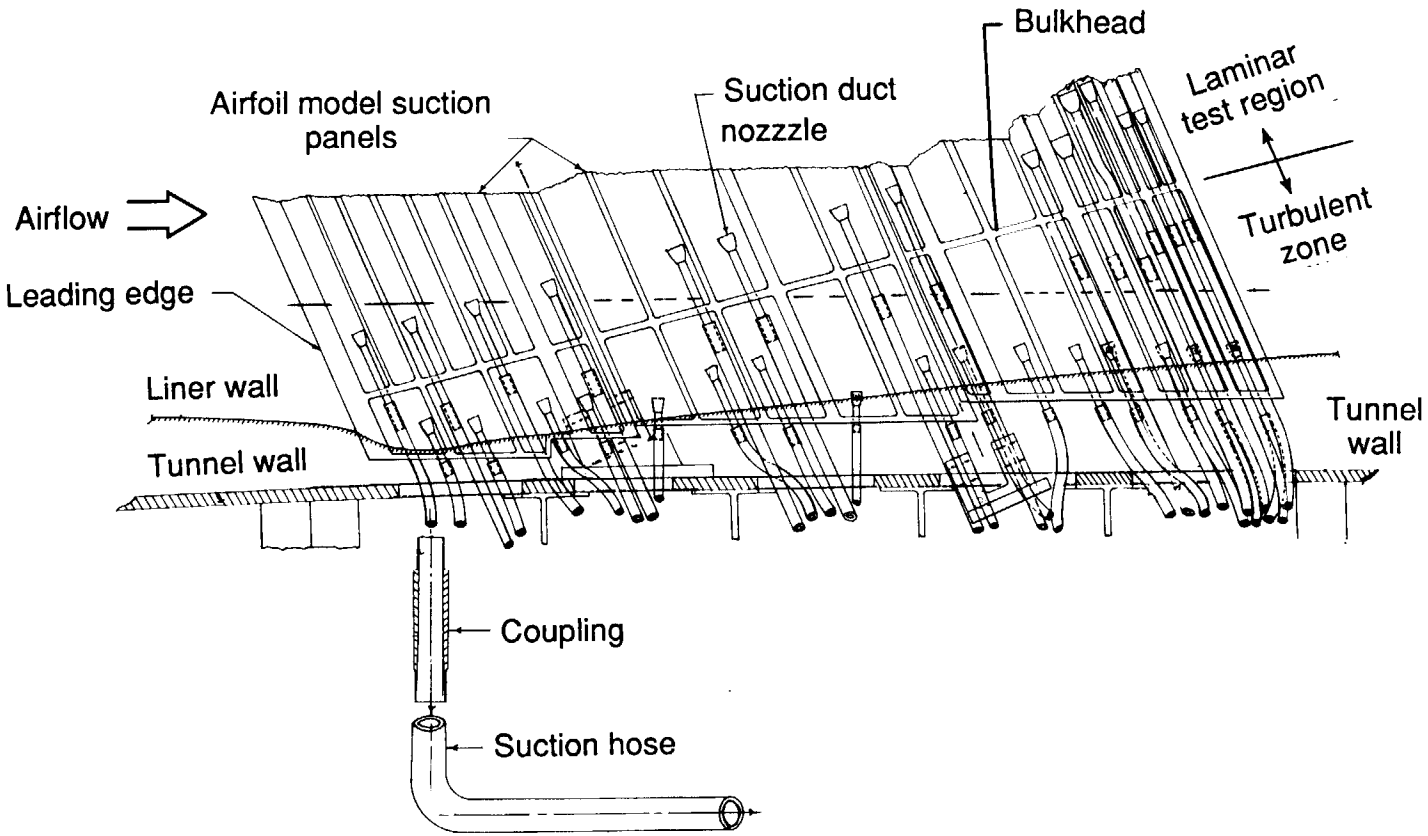

(d) Sketch of end of model nearest test section floor.

Figure 13. Continued.

L-82-7940

(e) Photograph of external connector hoses between end of model nearest test section floor and airflow control boxes.

Figure 13. Continued.

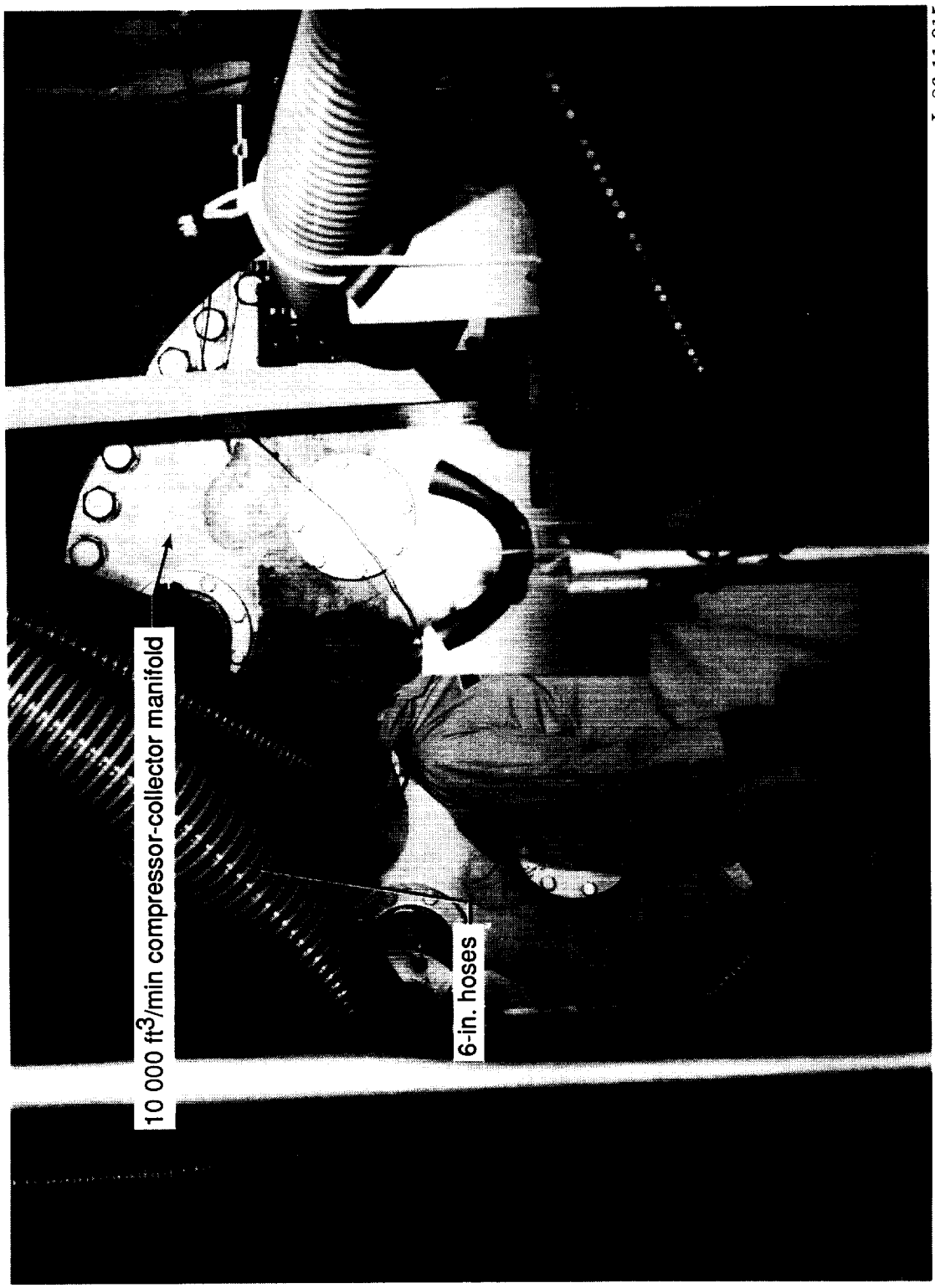

L-86-11,915

(f) The 10 000 ft^3/min compressor collector manifold.

Figure 13. Concluded.

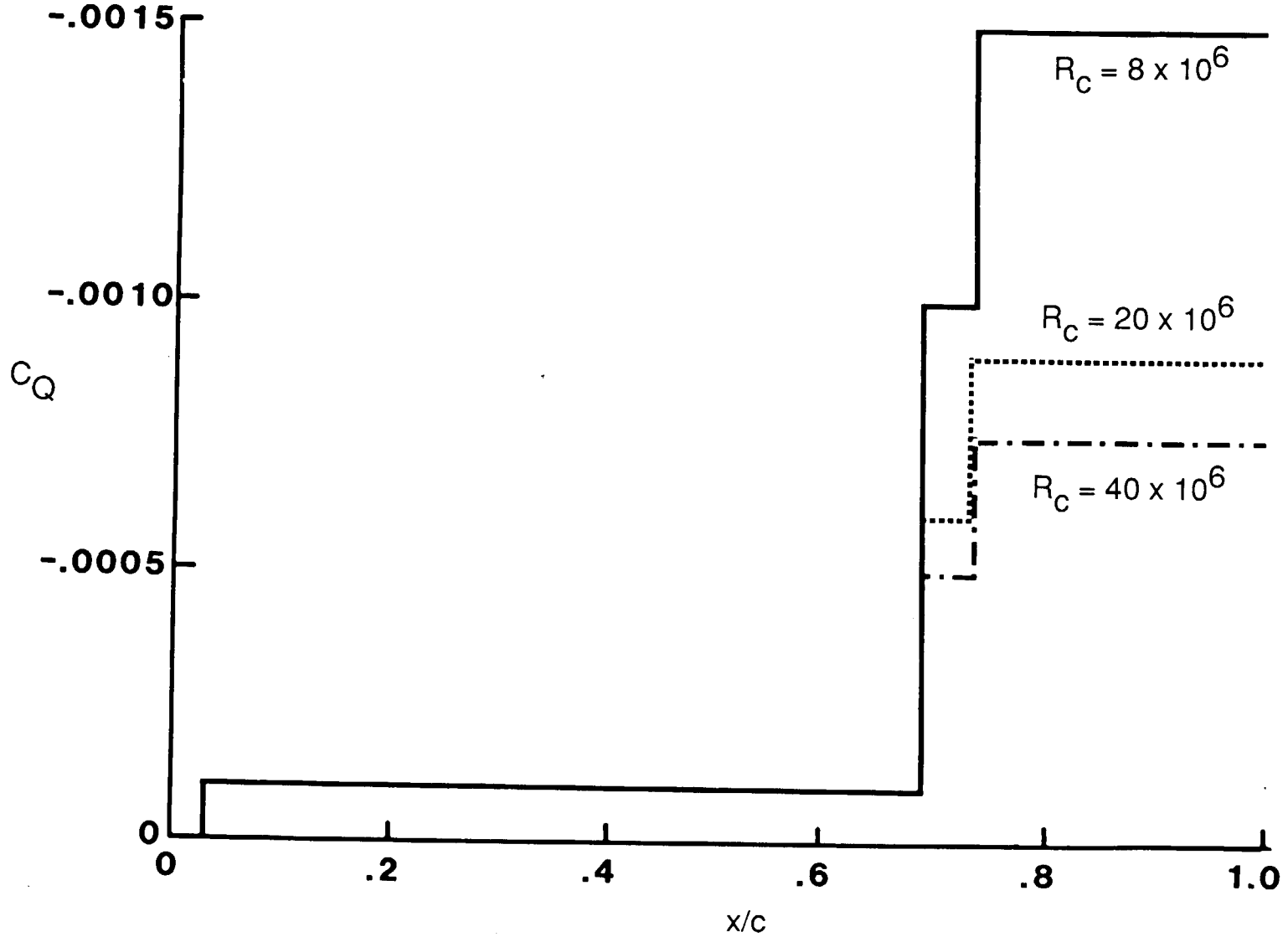

Figure 14. Theoretical upper-surface suction distributions for the perforated model at various chord Reynolds numbers.

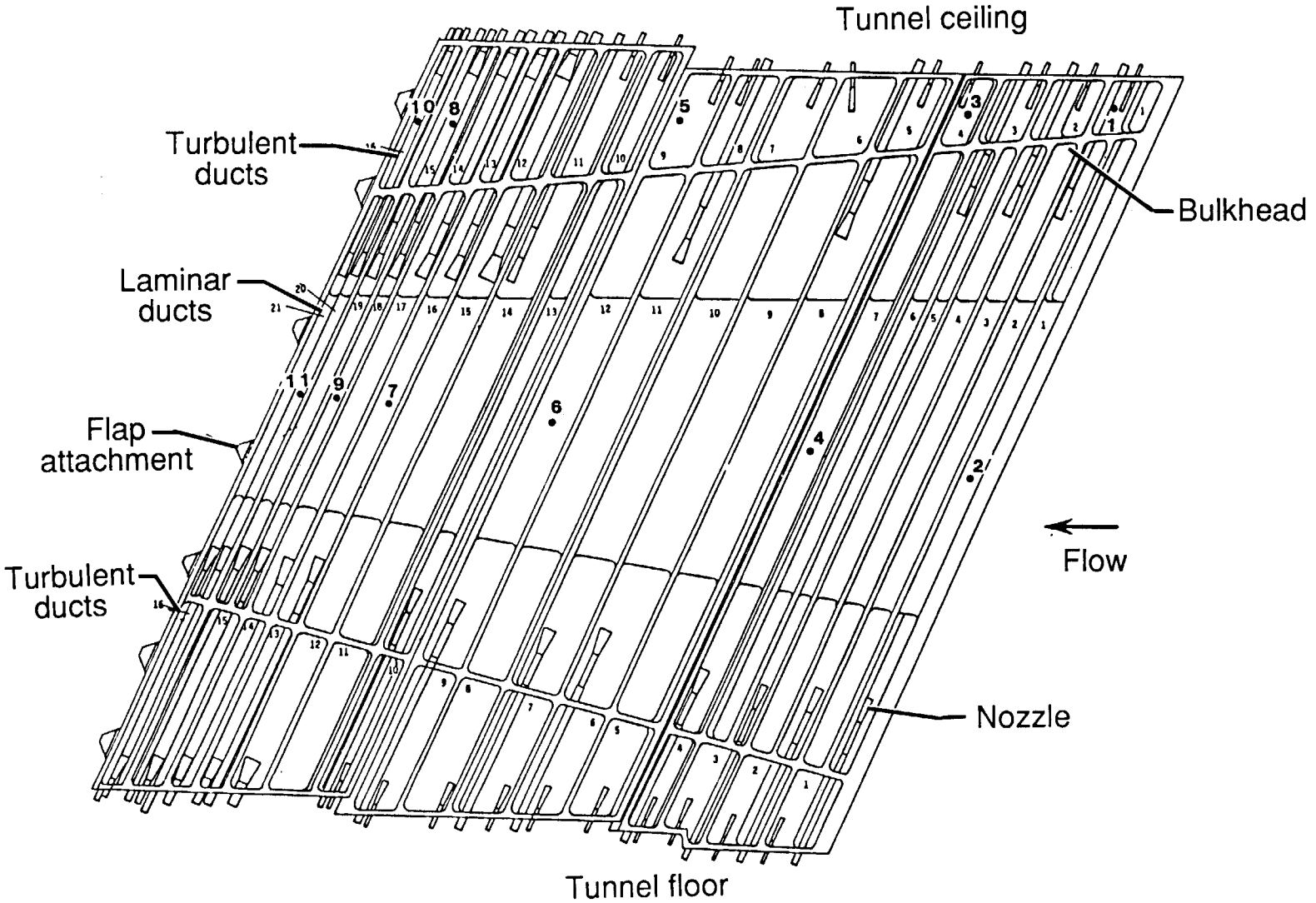

(a) Sketch of nozzle locations.

Figure 15. Suction duct nozzles.

(b) Photograph of nozzles in ducts.

Figure 15. Concluded.

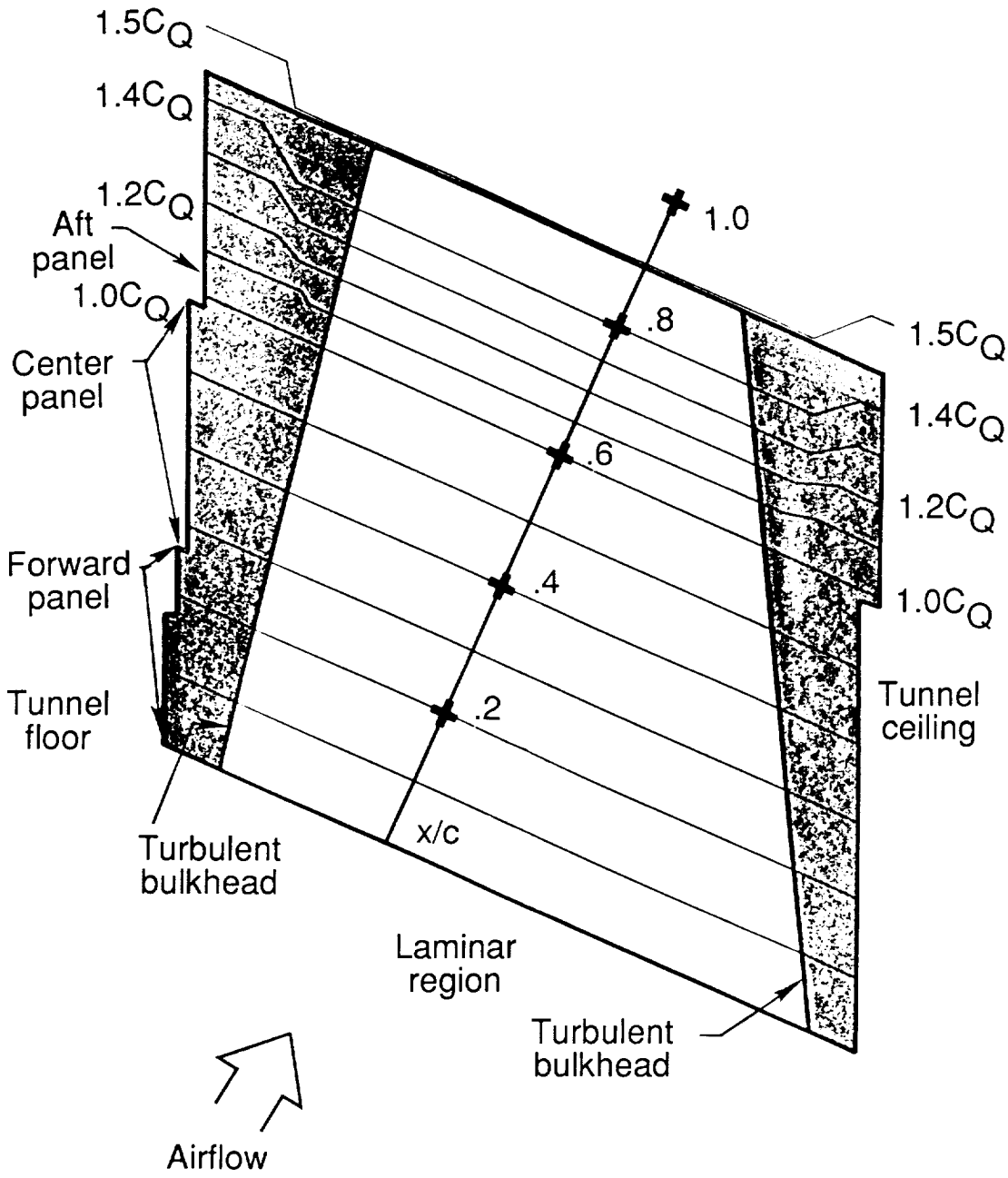

Figure 16. Upper-surface spanwise suction distribution.

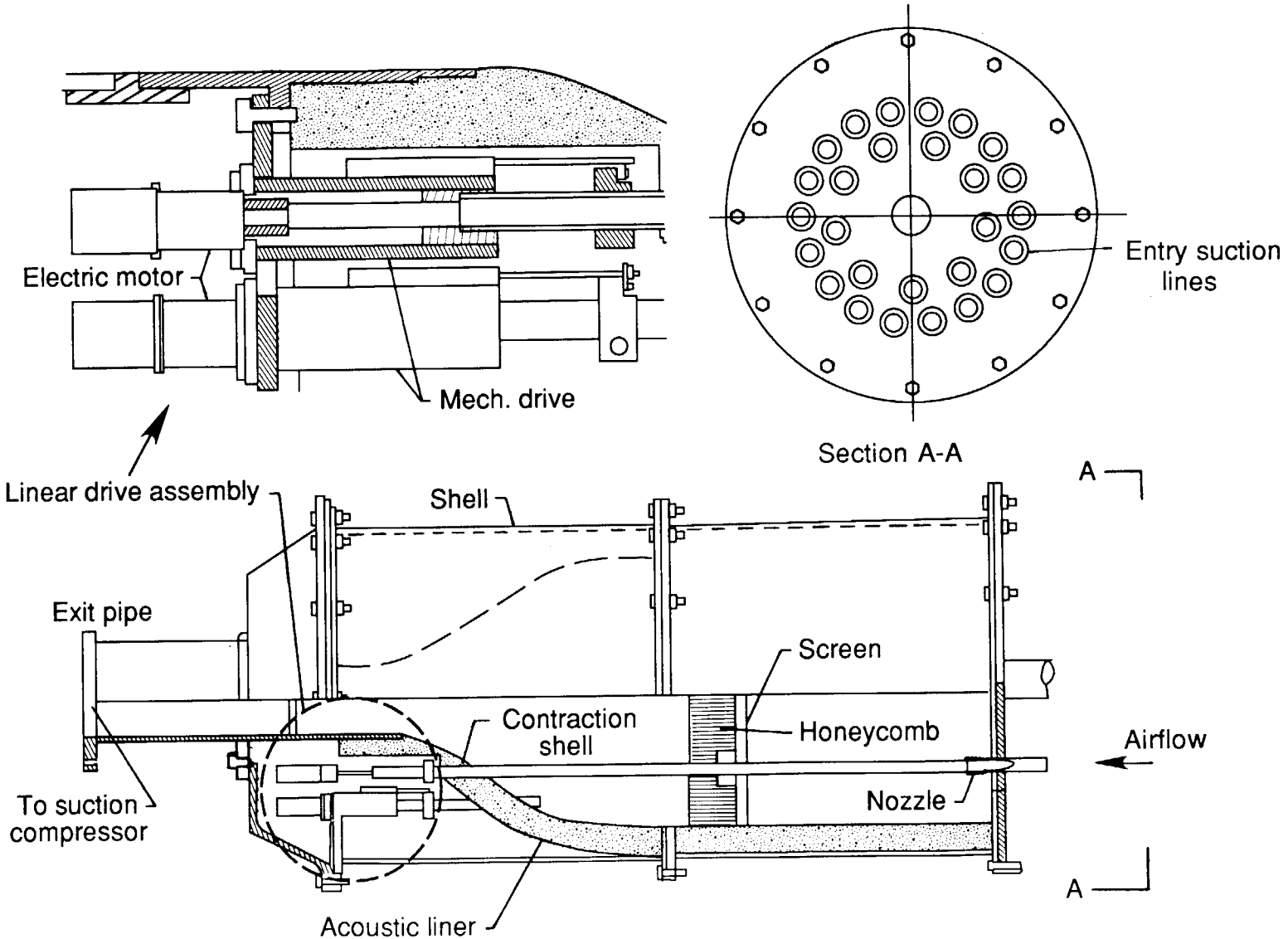

Figure 17. Airflow control boxes.

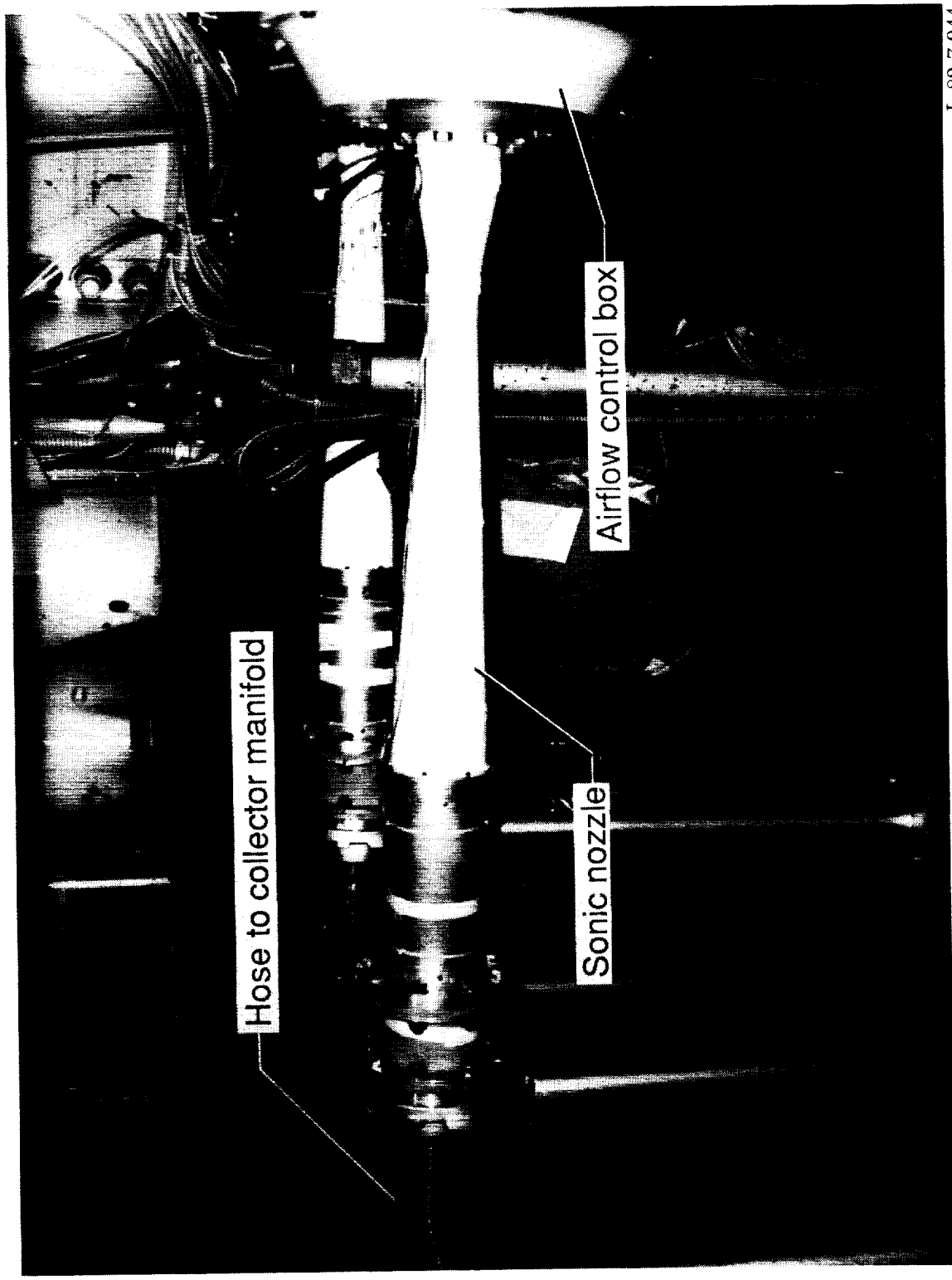

L-82-7,944

Figure 18. Photograph of installed variable sonic nozzles.

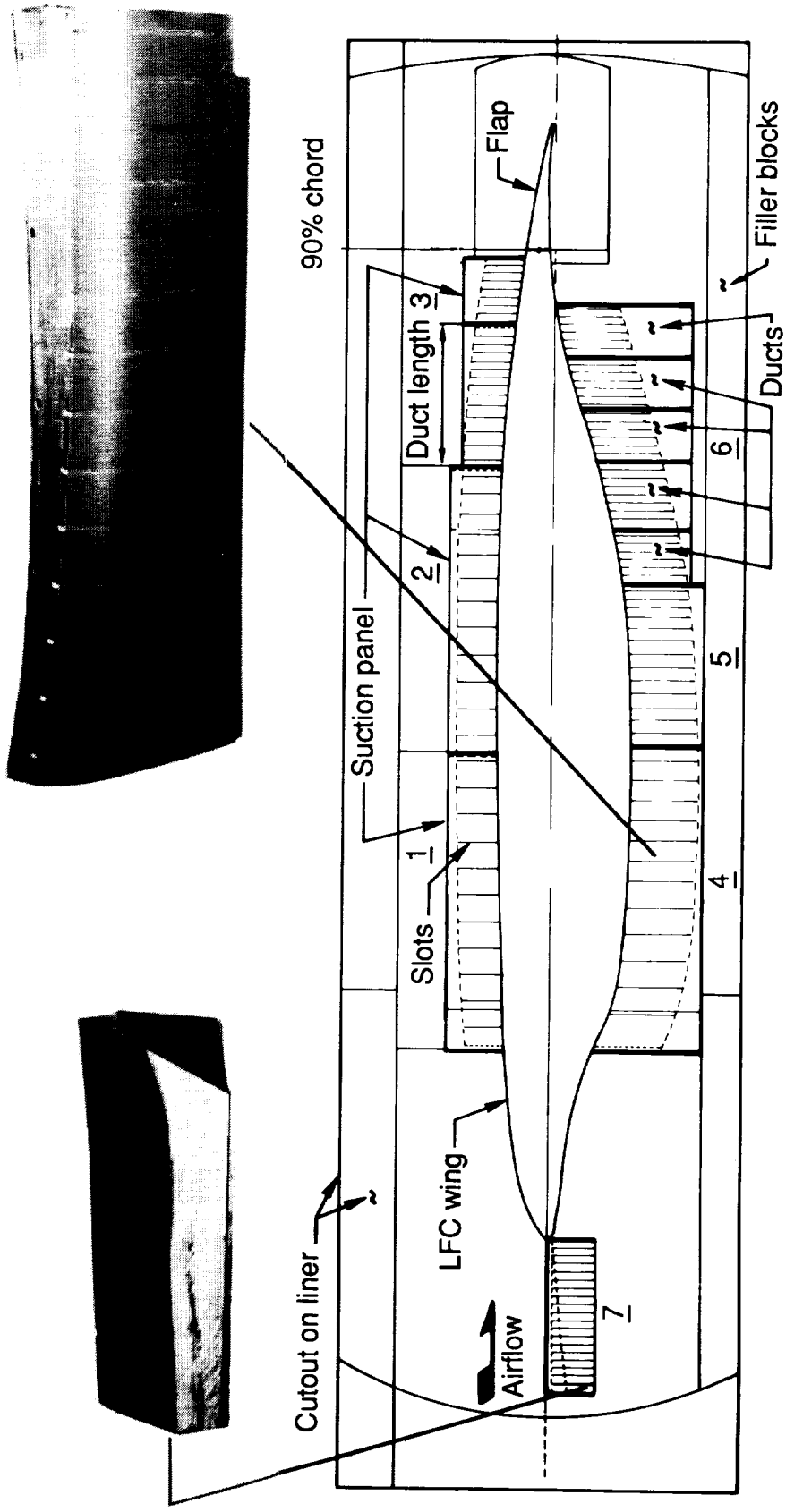

Figure 19. Liner suction collar.

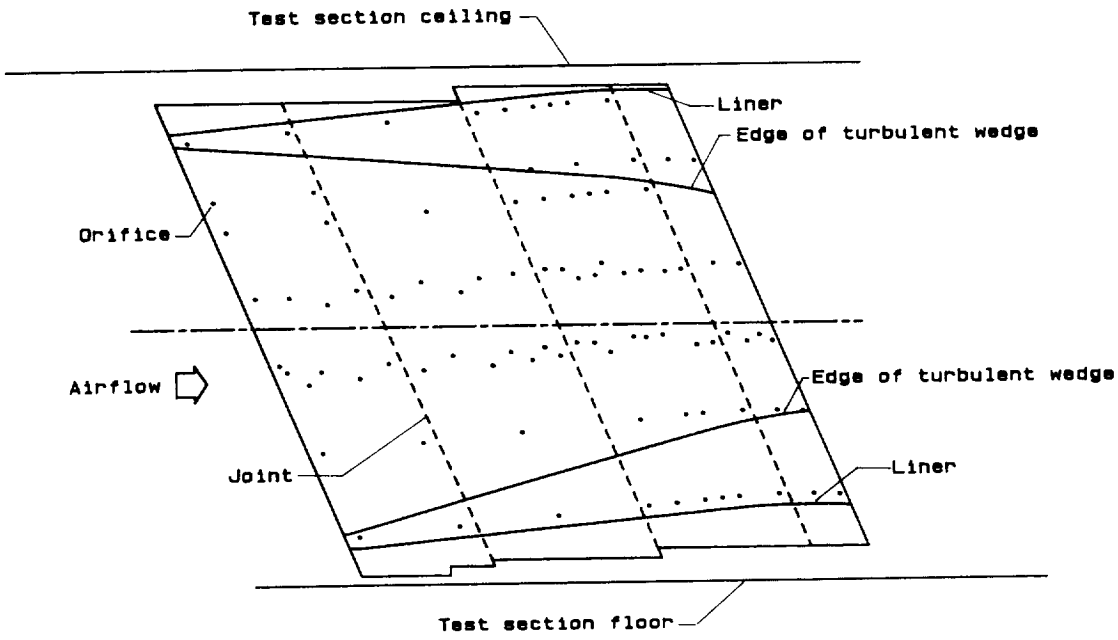

(a) Upper surface.

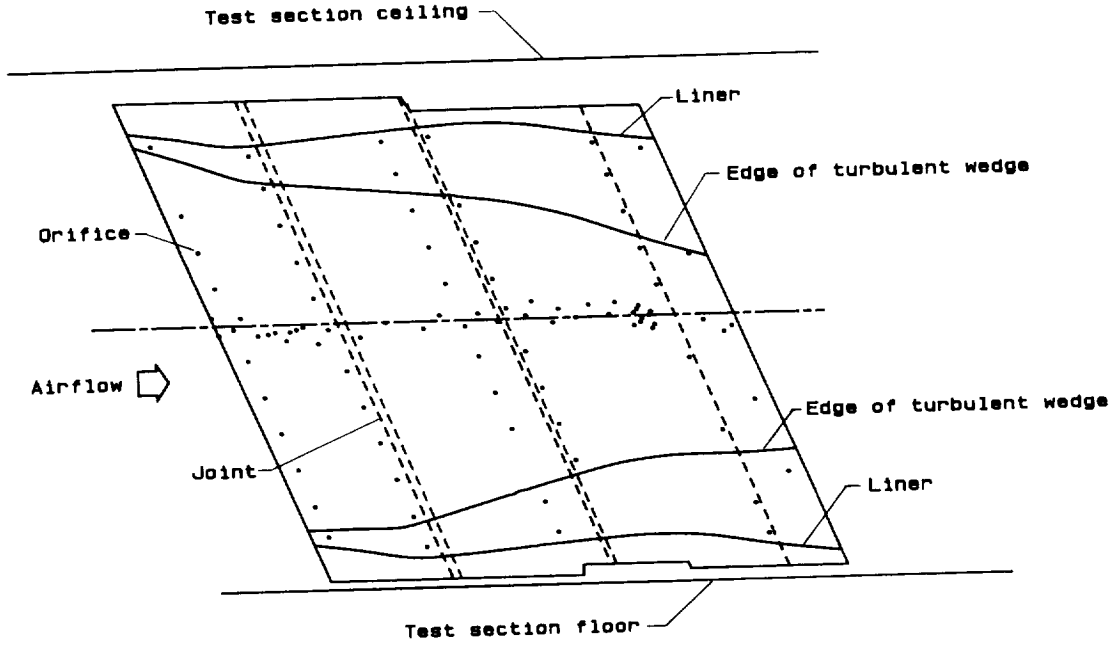

(b) Lower surface.

Figure 20. Sketches of planform of perforated LFC model showing actual locations of pressure orifices.

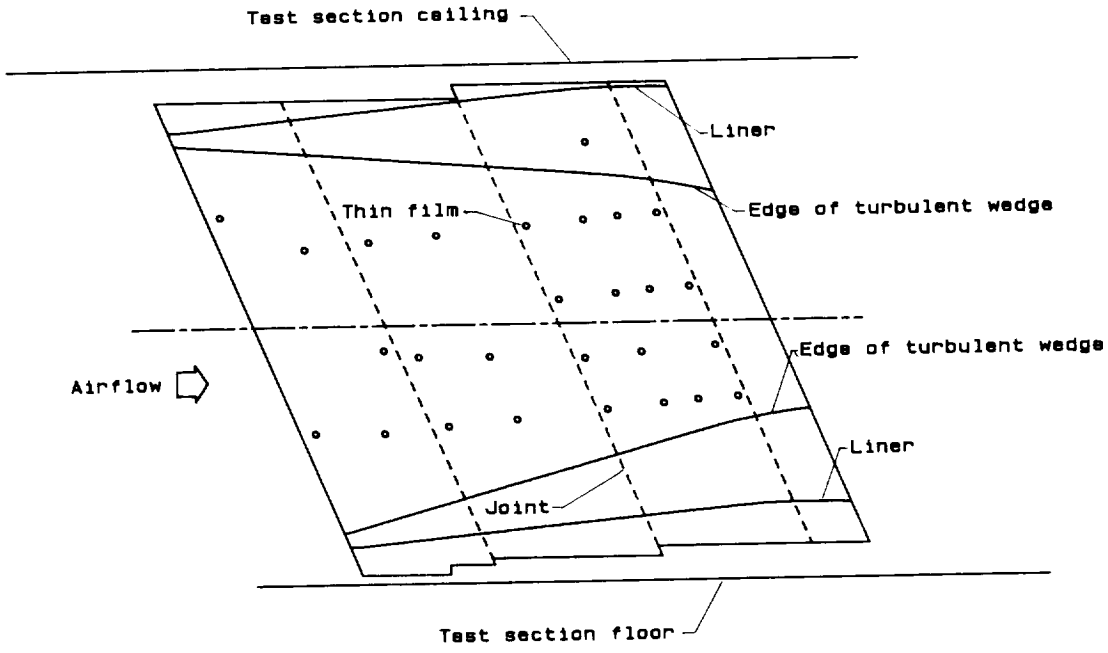

(a) Upper surface.

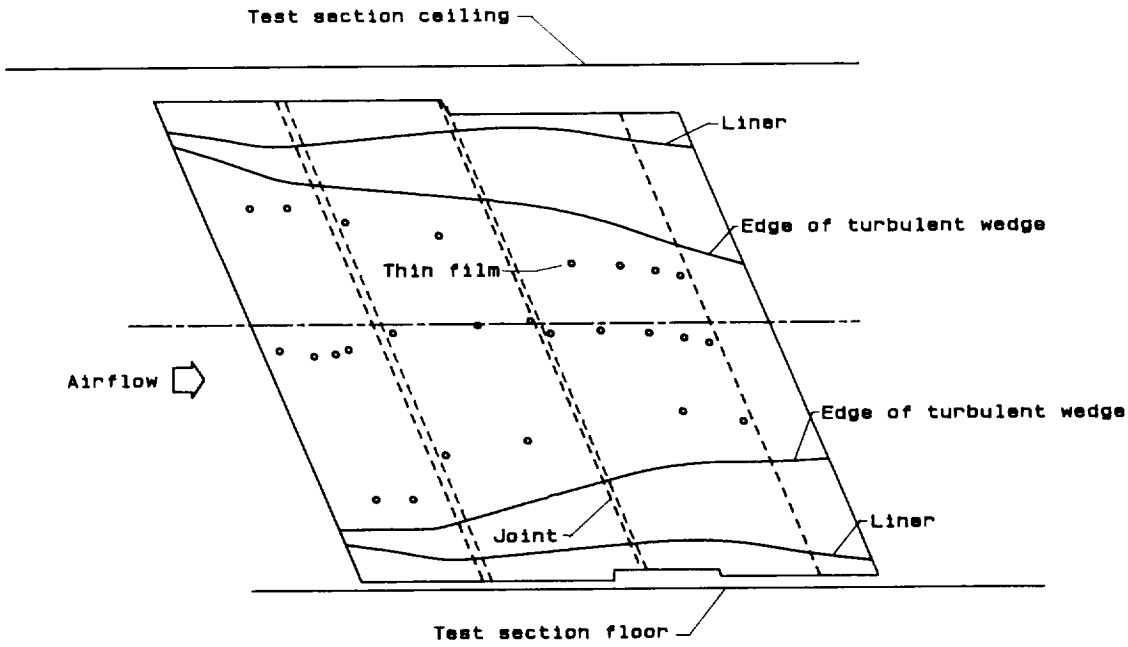

(b) Lower surface.

Figure 21. Sketches of planform of perforated LFC model showing actual locations of thin films.

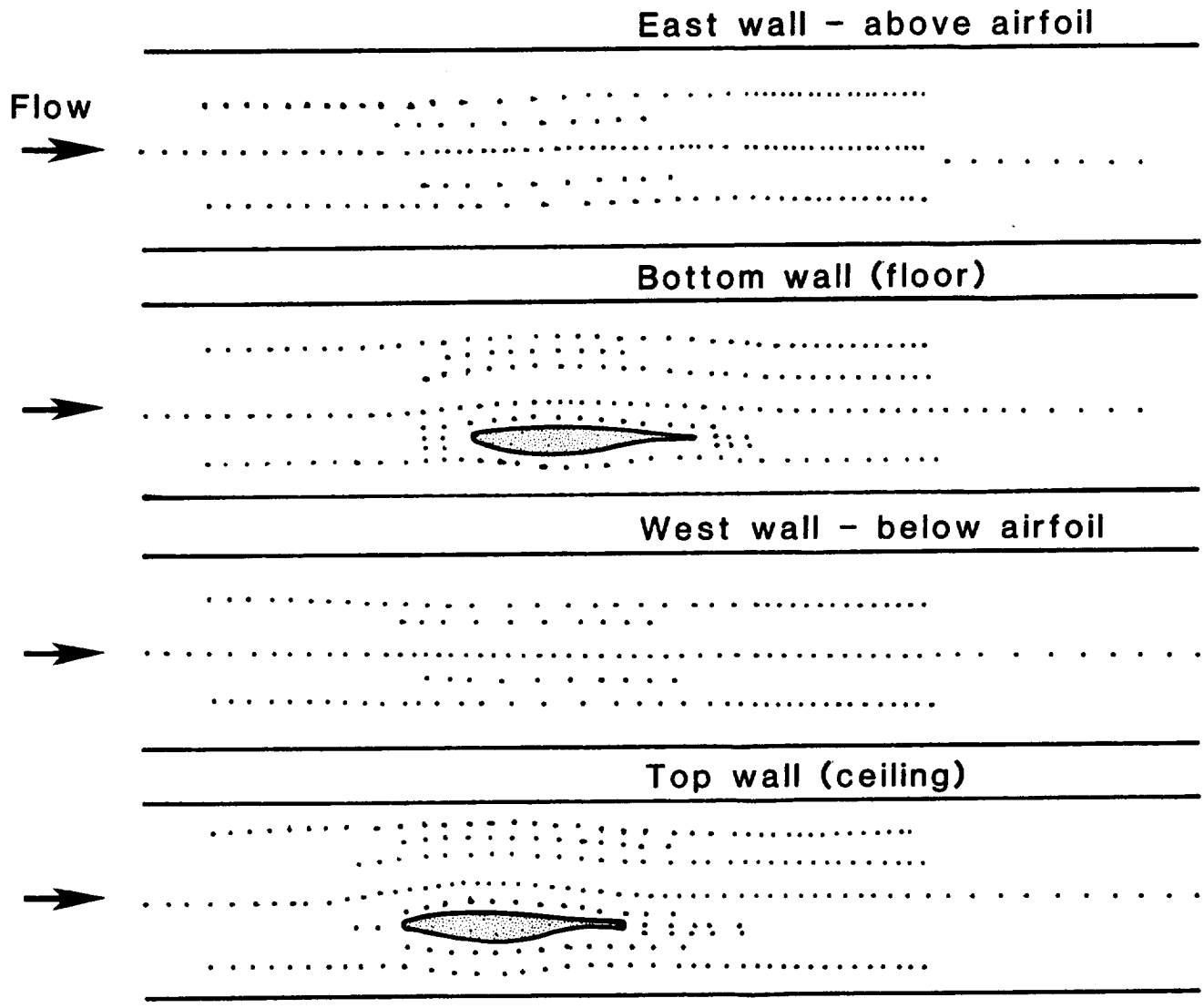

(a) Overall locations.

Figure 22. Static-pressure orifice locations over four walls of liner.

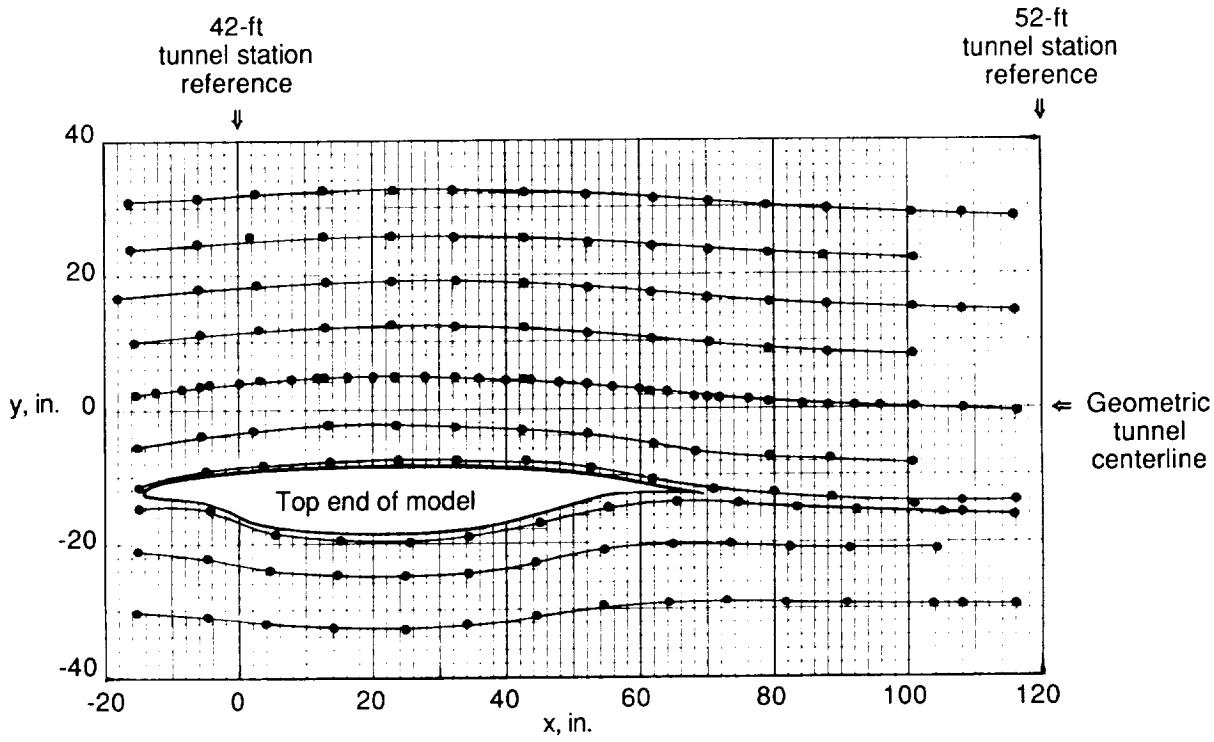

(b) Orifices around model on ceiling of test section.

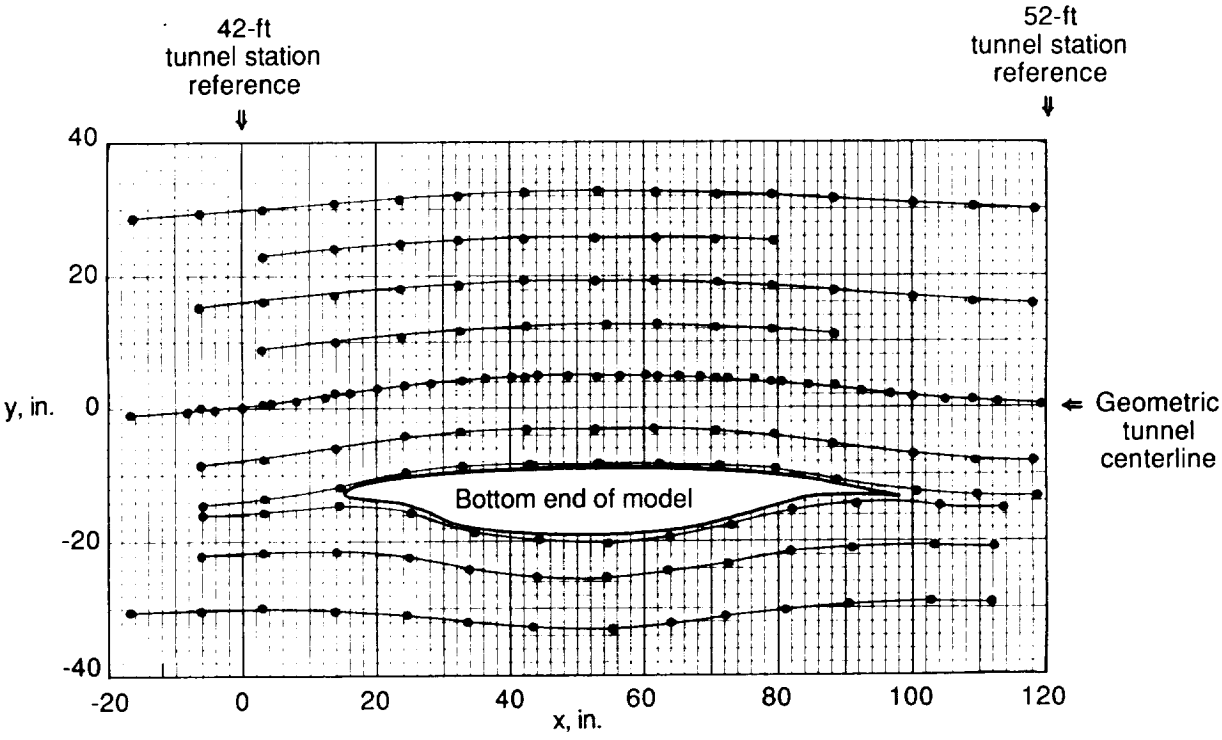

(c) Orifices around model on floor of test section.

Figure 22. Concluded.

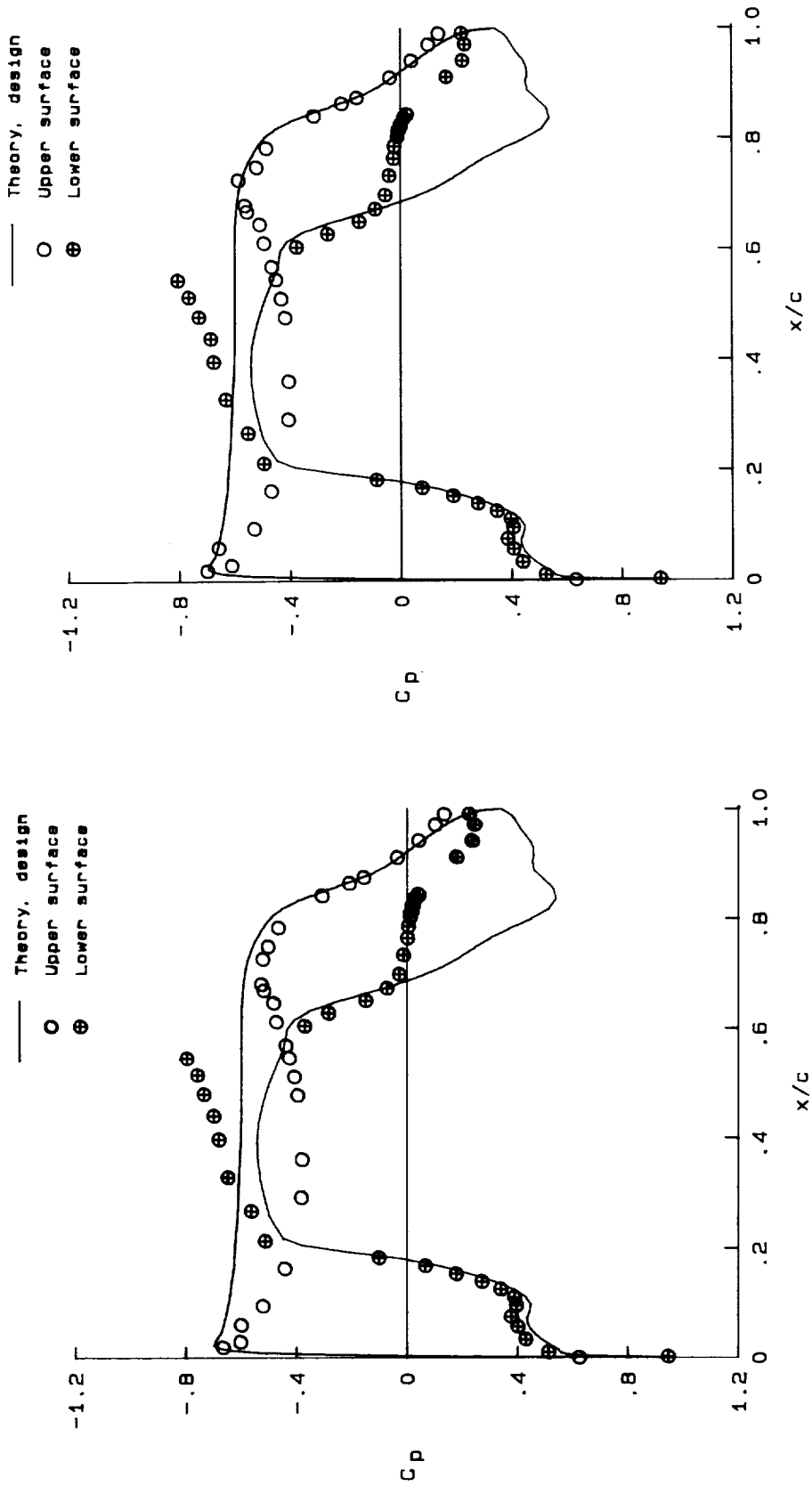

(a) $R_c = 10 \times 10^6$; $M_\infty = 0.814$.

(b) $R_c = 15 \times 10^6$; $M_\infty = 0.817$.

Figure 23. Experimental pressure distributions for initial model and test section configurations. Floor and ceiling fixed choke; floor area strip no. 6; $\alpha = 0.42°$; $\delta_t = 2.1°$; δ_c adjustable; $\delta_b = 2.6°$.

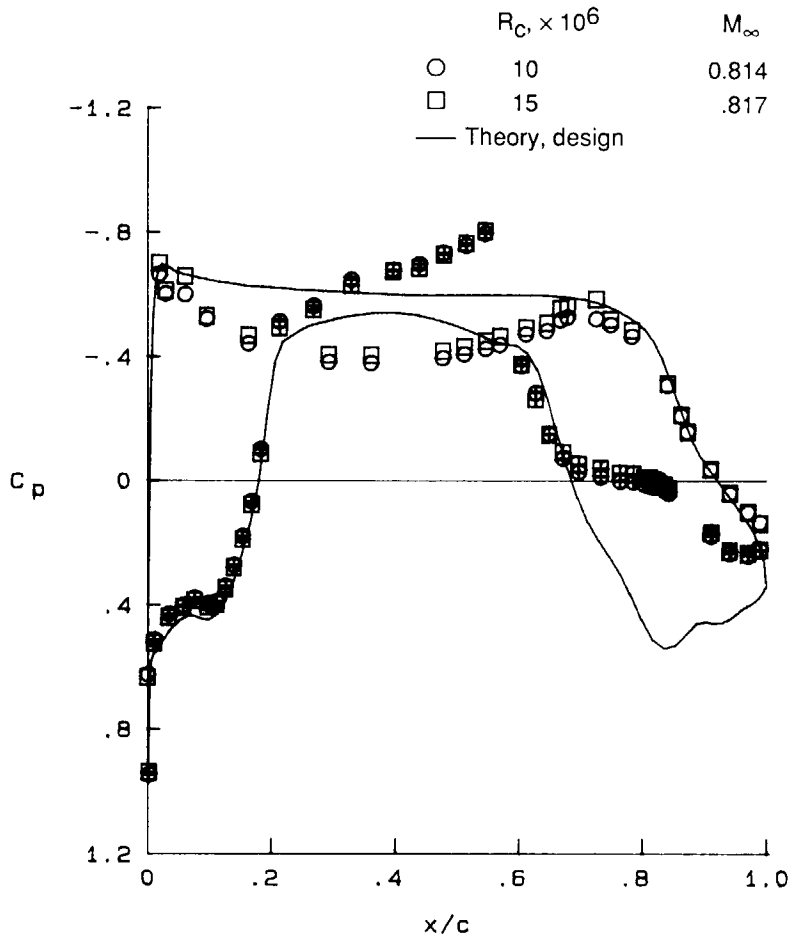

Figure 24. Effect of Reynolds number on experimental pressure distribution. Floor and ceiling fixed choke; floor area strip no. 6; $\alpha = 0.42°$; $\delta_t = 2.1°$; δ_c adjustable; $\delta_b = 2.6°$. Open symbols denote upper surface. Crosshatched symbols denote lower surface.

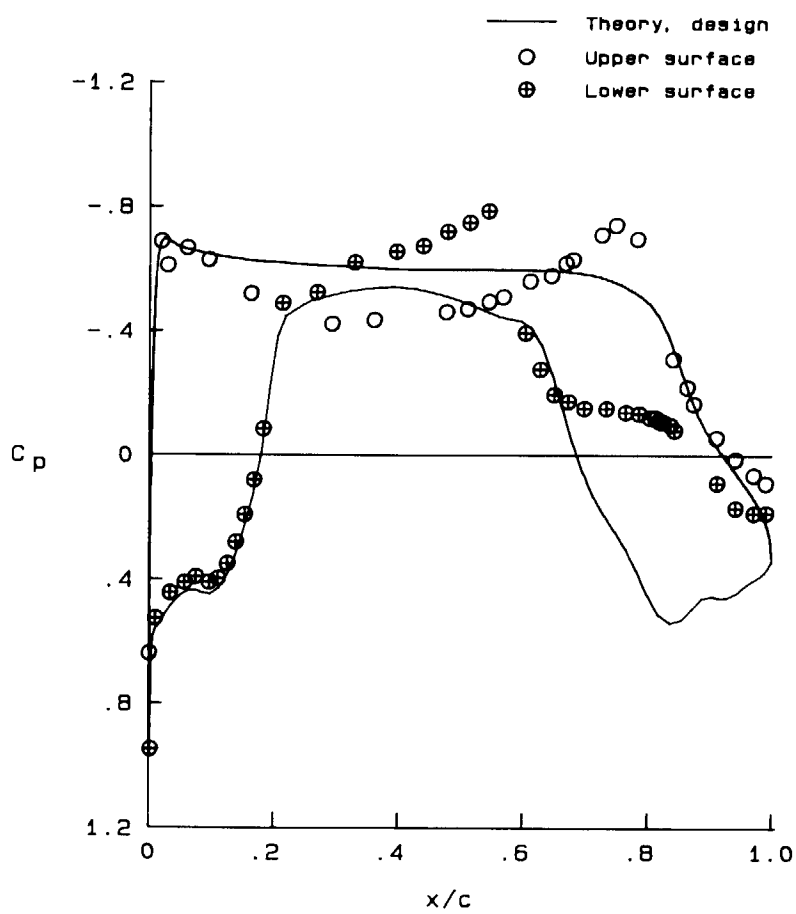

Figure 25. Experimental pressure distribution for δ_c adjustable. Ceiling fixed choke; floor area strip no. 6; $\alpha = 0.42°$; $M_\infty = 0.822$; $R_c = 10 \times 10^6$; $\delta_t = 2.1°$; $\delta_b = 2.6°$. Open symbols denote upper surface.

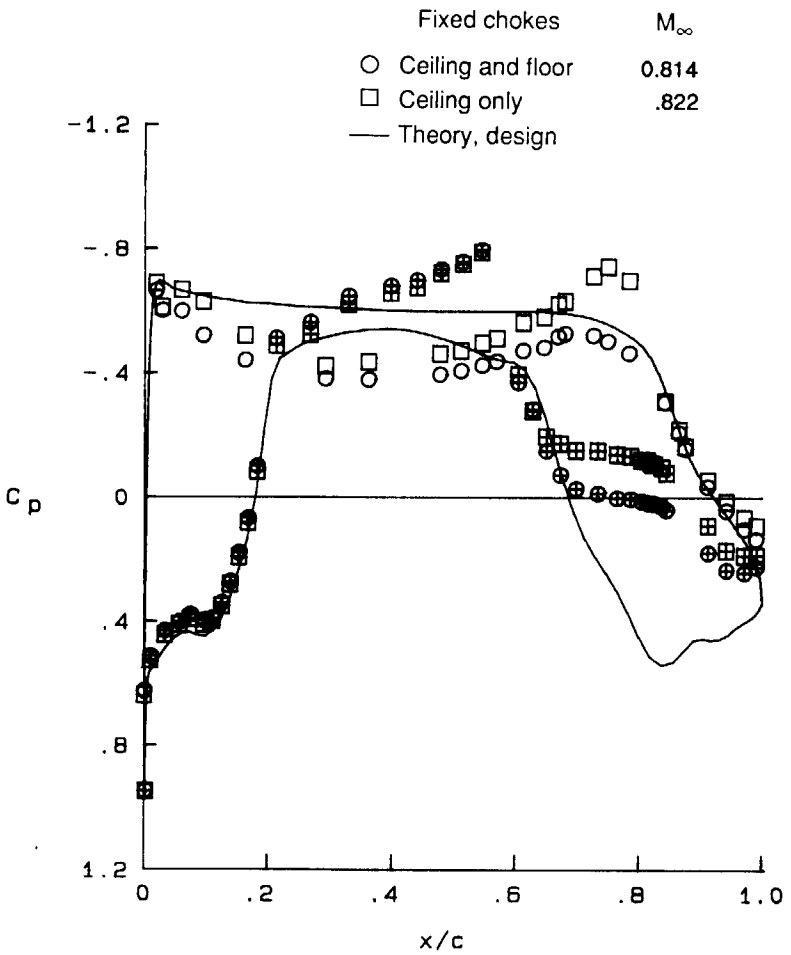

Figure 26. Effect of removing floor fixed choke on experimental pressure distribution. Floor area strip no. 6; $\alpha = 0.42°$; $\delta_t = 2.1°$; δ_c adjustable; $\delta_b = 2.6°$. Open symbols denote upper surface. Crosshatched symbols denote lower surface.

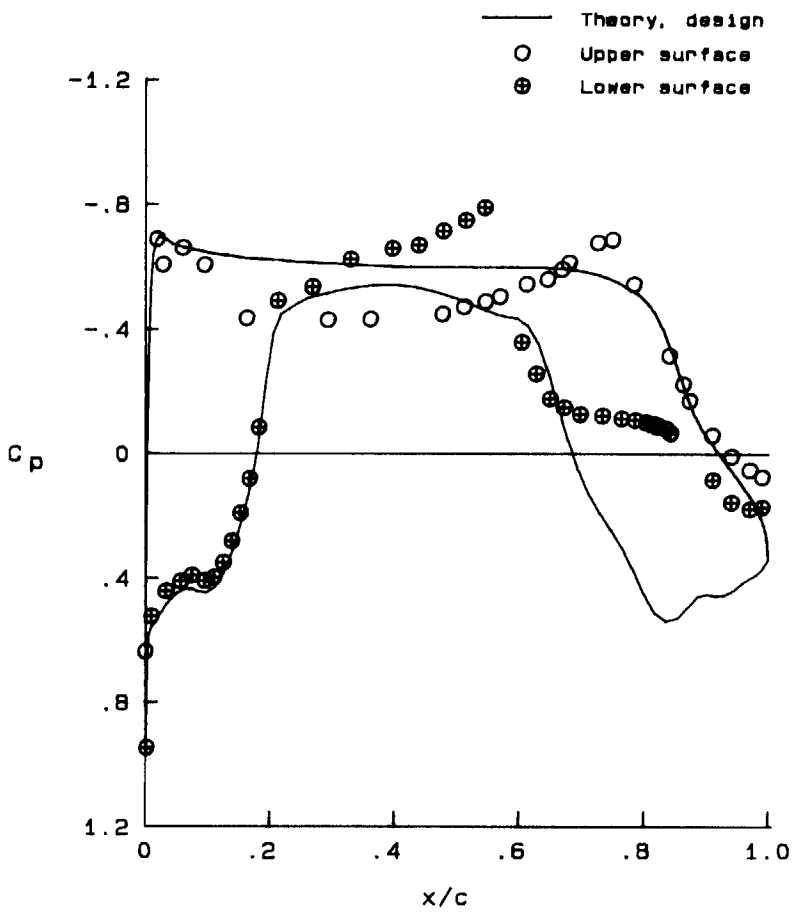

Figure 27. Effect of the movable flap on experimental pressure distribution. Ceiling fixed choke; floor area strip no. 6; $M_\infty = 0.821$; $R_c = 10 \times 10^6$; $\alpha = 0.42°$; $\delta_t = 2.1°$; $\delta_c = 1.0°$; $\delta_b = 2.6°$. Open symbols denote upper surface.

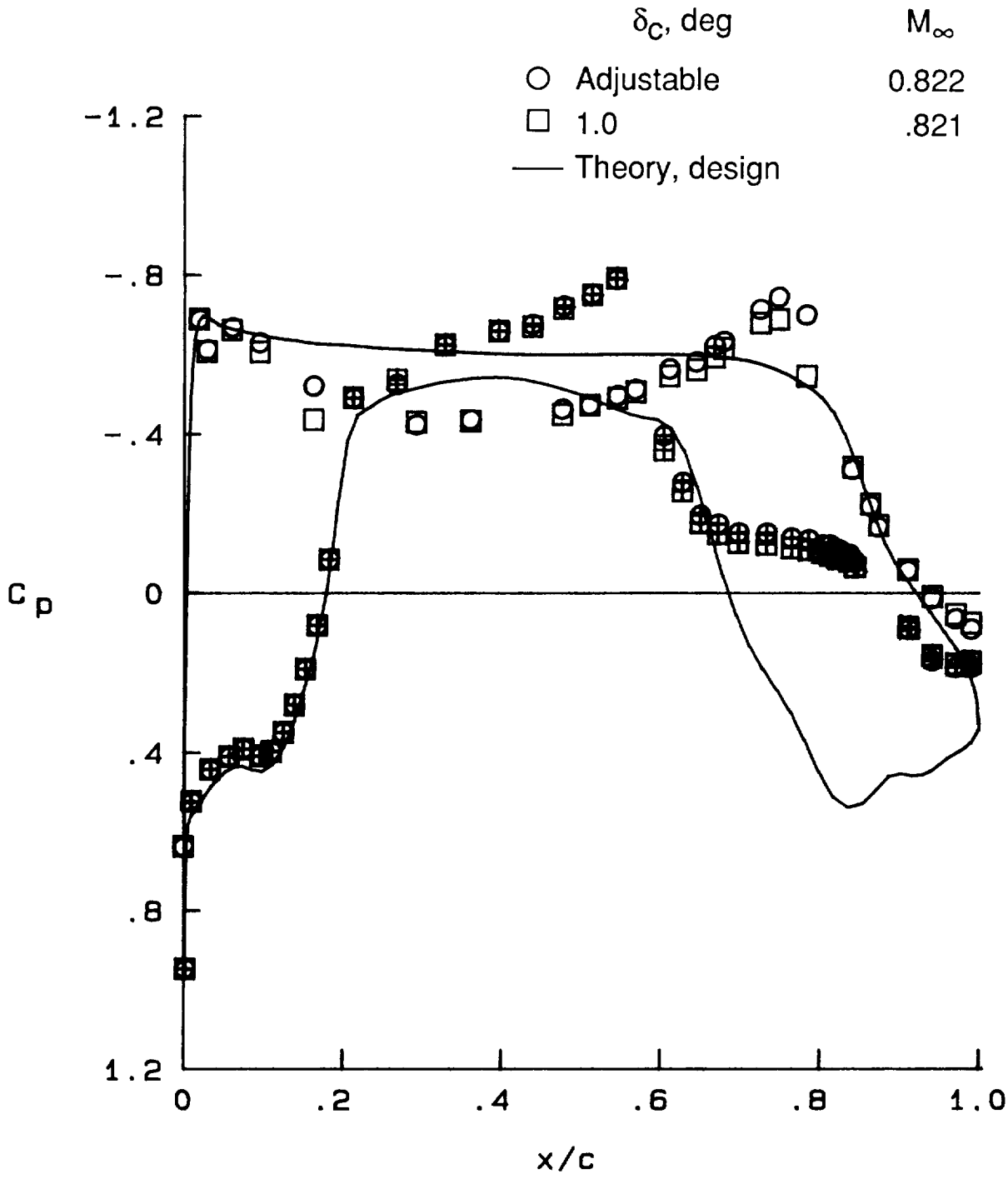

Figure 28. Effect of fixing central-flap deflection on experimental pressure distribution. Ceiling fixed choke; floor area strip no. 6; $\alpha = 0.42°$; $R_c = 10 \times 10^6$; $\delta_t = 2.1°$; $\delta_b = 2.6°$. Open symbols denote upper surface. Crosshatched symbols denote lower surface.

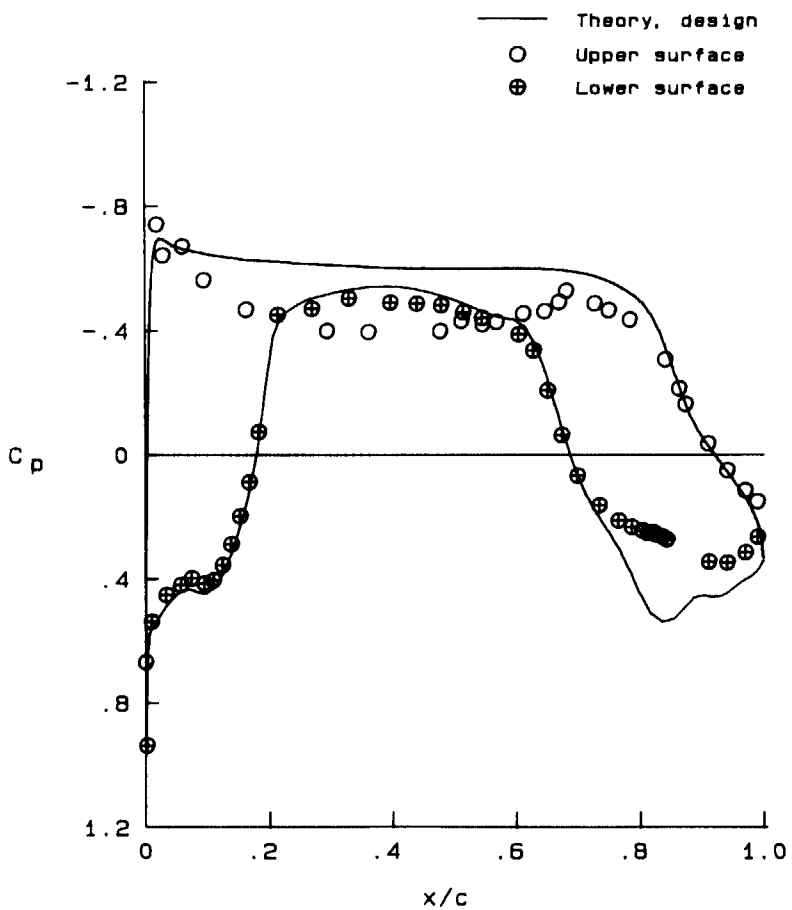

(a) $M_\infty = 0.809$.

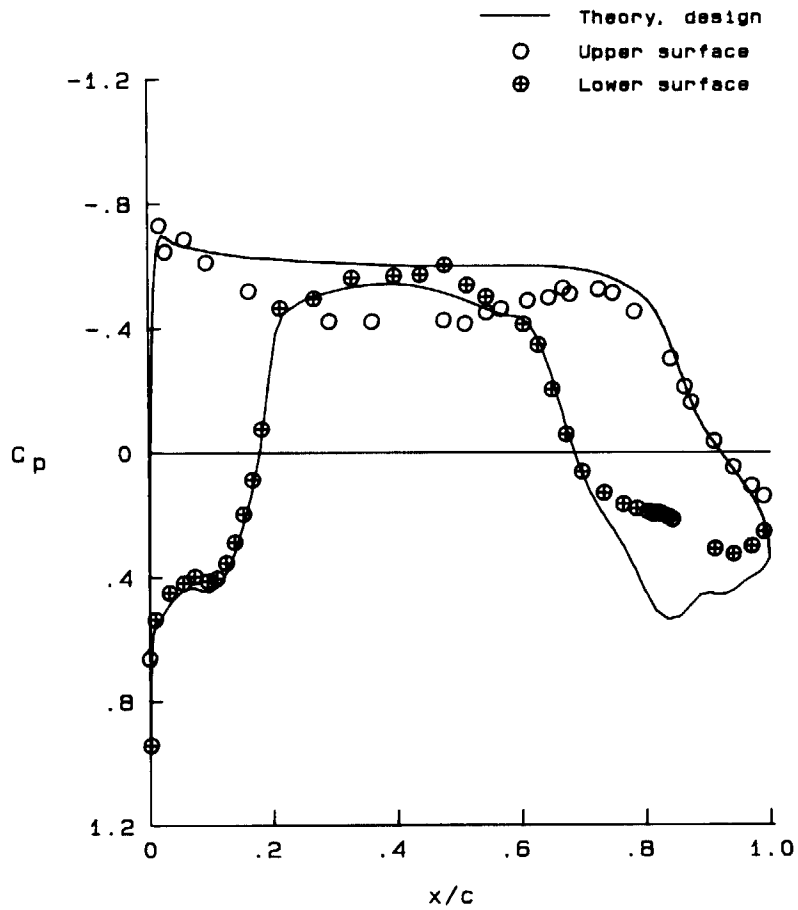

(b) $M_\infty = 0.818$.

Figure 29. Effect of Mach number on experimental pressure distribution. Ceiling fixed choke; $\alpha = 0.60°$; $R_c = 11 \times 10^6$; $\delta_t = 2.1°$; $\delta_c = 1.0°$; $\delta_b = 2.6°$.

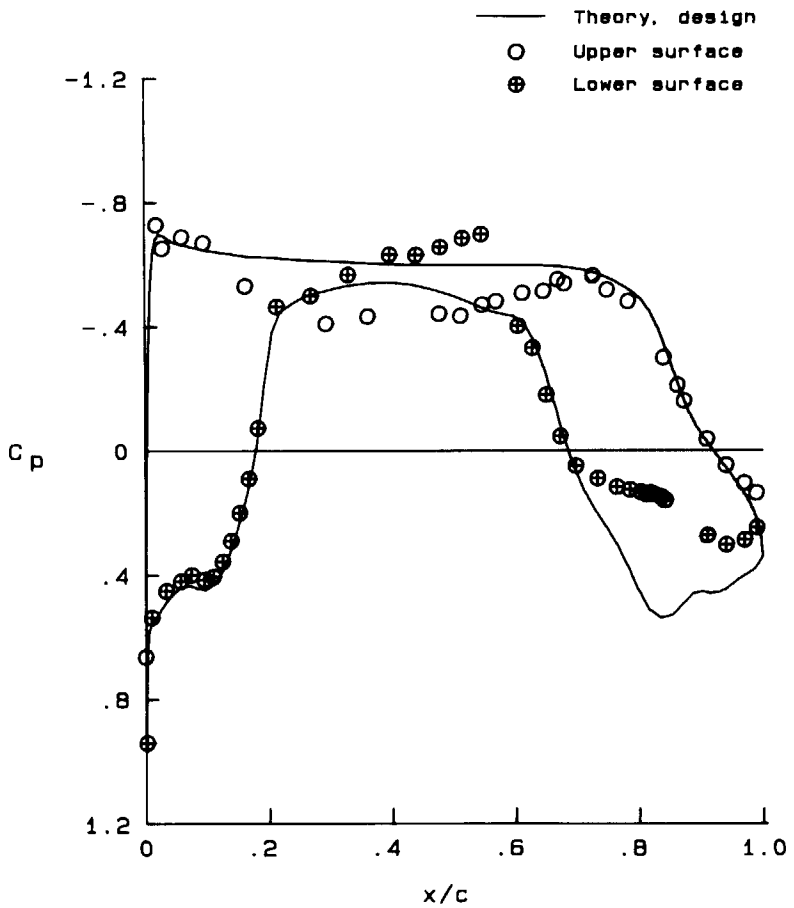

(c) $M_\infty = 0.821$.

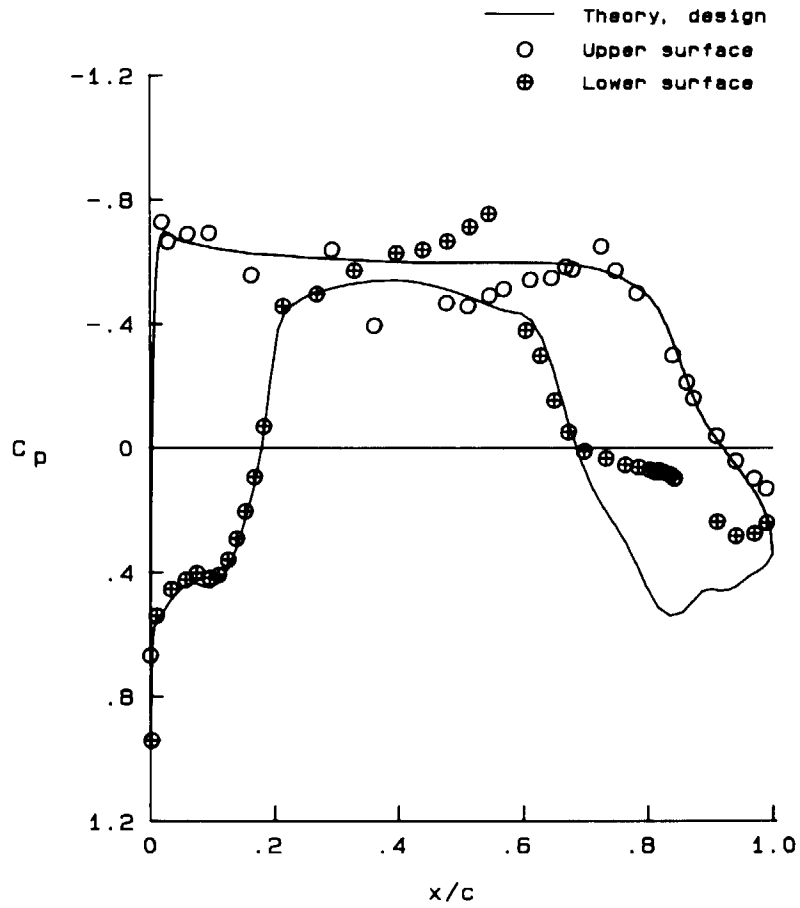

(d) $M_\infty = 0.823$.

Figure 29. Continued.

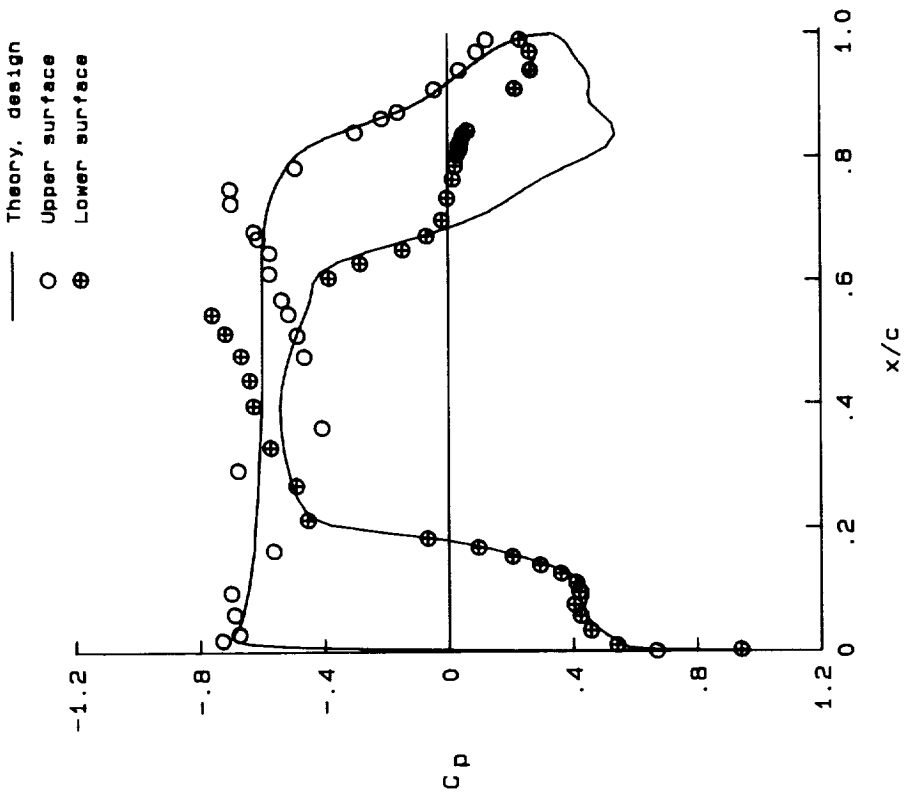

(e) $M_\infty = 0.824$.

Figure 29. Concluded.

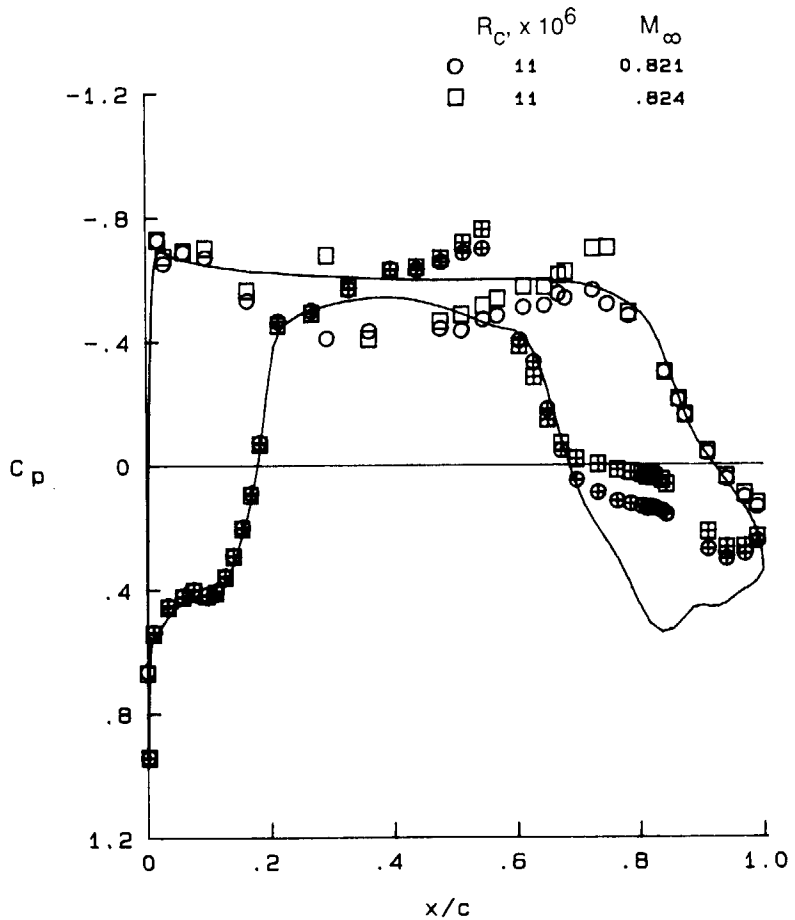

Figure 30. Summary of effect of Mach number on experimental pressure distribution. Ceiling fixed choke; $\alpha = 0.60°$; $\delta_t = 2.1°$; $\delta_c = 1.0°$; $\delta_b = 2.6°$. Open symbols denote upper surface. Crosshatched symbols denote lower surface.

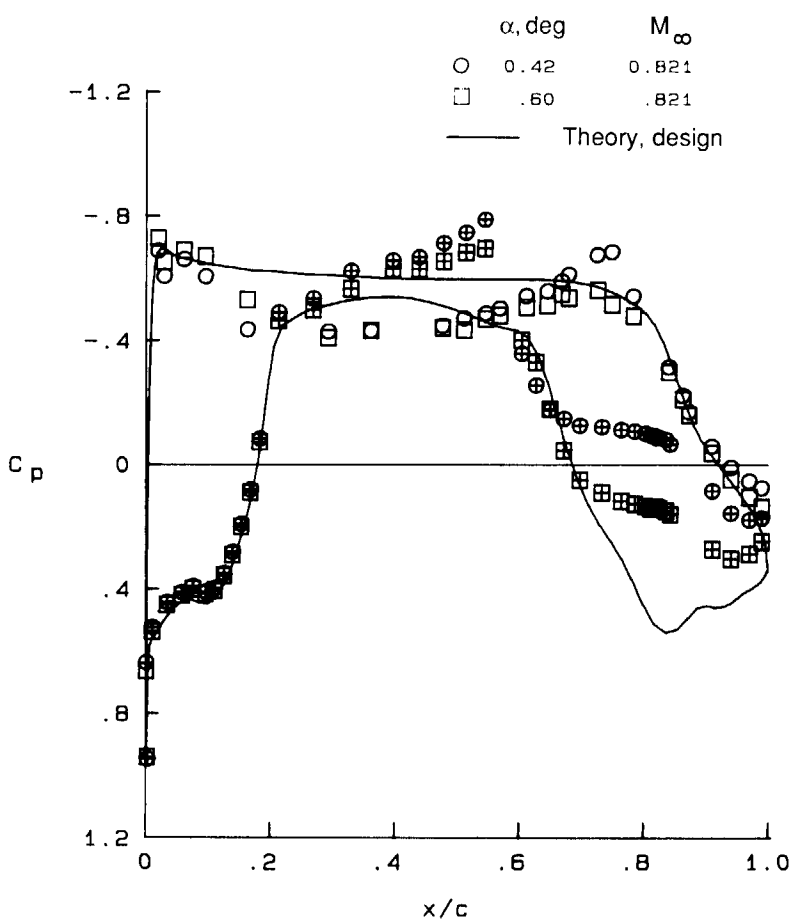

Figure 31. Effect on experimental pressure distribution of increasing the angle of attack. Ceiling fixed choke; $R_c = 11 \times 10^6$; $\delta_t = 2.1°$; $\delta_c = 1.0°$; $\delta_b = 2.6°$. Open symbols denote upper surface. Crosshatched symbols denote lower surface.

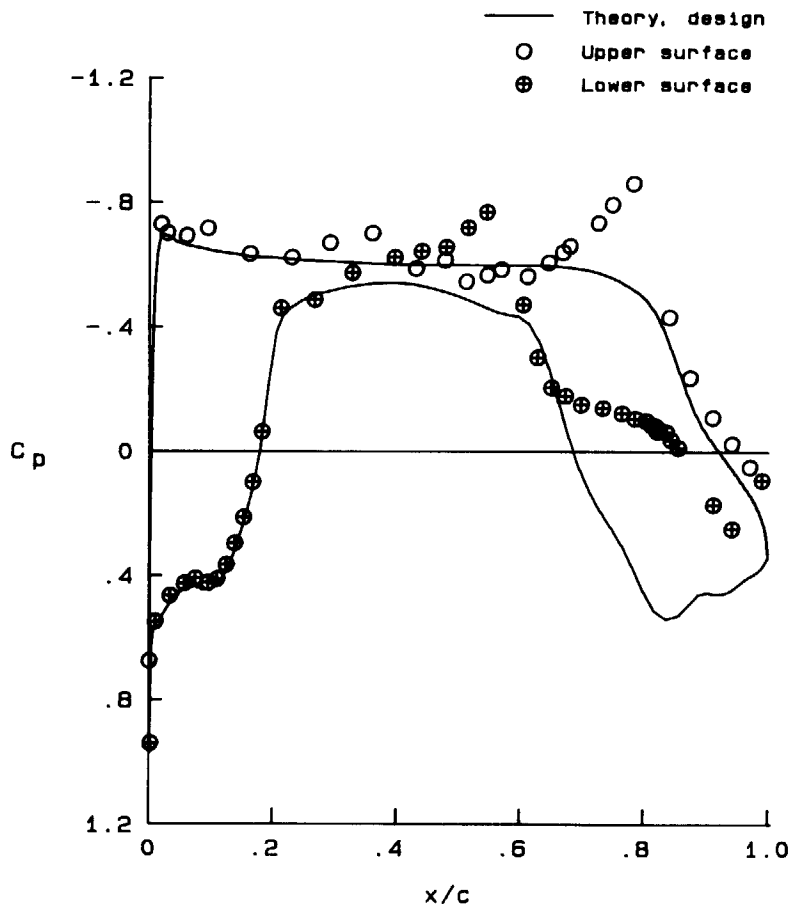

Figure 32. Experimental pressure distribution. Ceiling fixed choke; floor area strip no. 6; $M_\infty = 0.826$; $R_c = 10 \times 10^6$; $\alpha = 0.60°$; $\delta_t = 2.1°$; $\delta_c = 1.0°$; $\delta_b = 2.6°$.

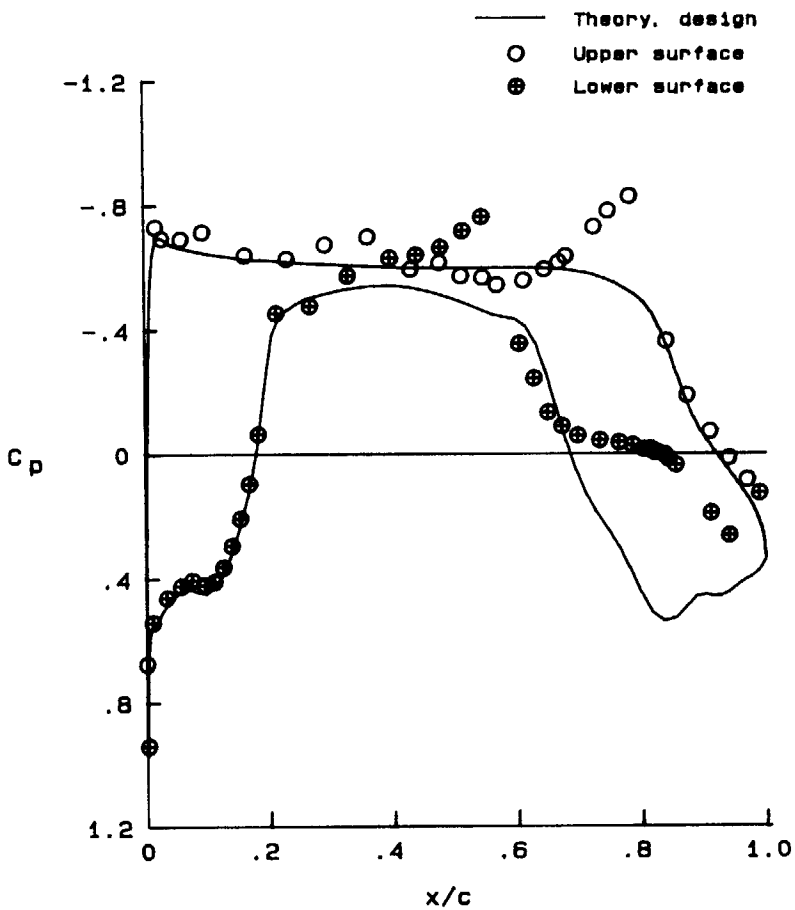

Figure 33. Experimental pressure distribution after removal of fixed choke. Floor area strip no. 6; $M_\infty = 0.826$; $R_c = 9 \times 10^6$; $\alpha = 0.60°$; $\delta_t = 3.2°$; $\delta_c = 1.0°$; $\delta_b = 2.6°$.

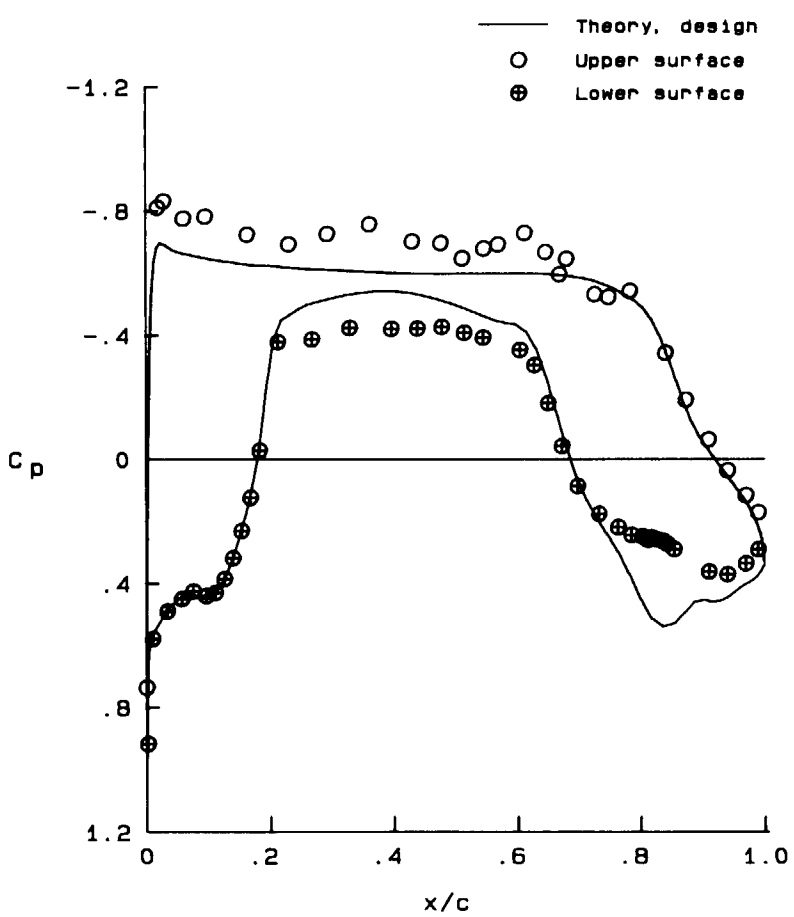

Figure 34. The effect of increasing angle of attack on experimental pressure distribution. Floor area strip no. 6; $M_\infty = 0.815; R_c = 9 \times 10^6; \alpha = 0.81°; \delta_t = 3.2°; \delta_c = 1.0°; \delta_b = 2.6°$.

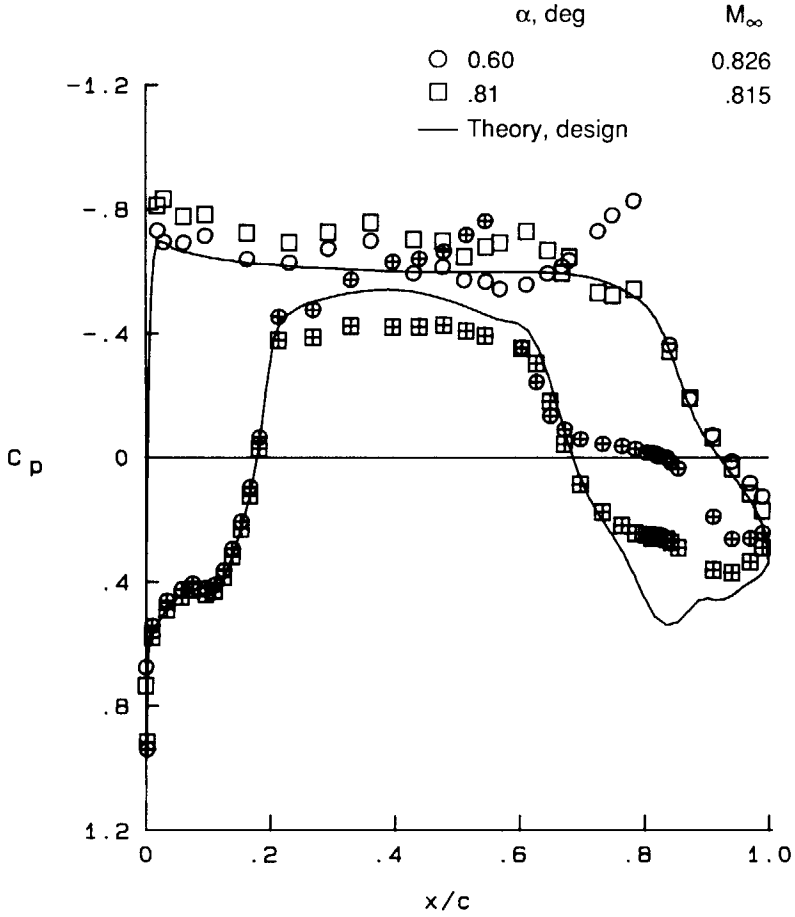

Figure 35. Effect of angle of attack on experimental pressure distribution. Floor area strip no. 6; $R_c = 9 \times 10^6$; $\delta_t = 3.2°$; $\delta_c = 1.0°$; $\delta_b = 2.6°$. Open symbols denote upper surface. Crosshatched symbols denote lower surface.

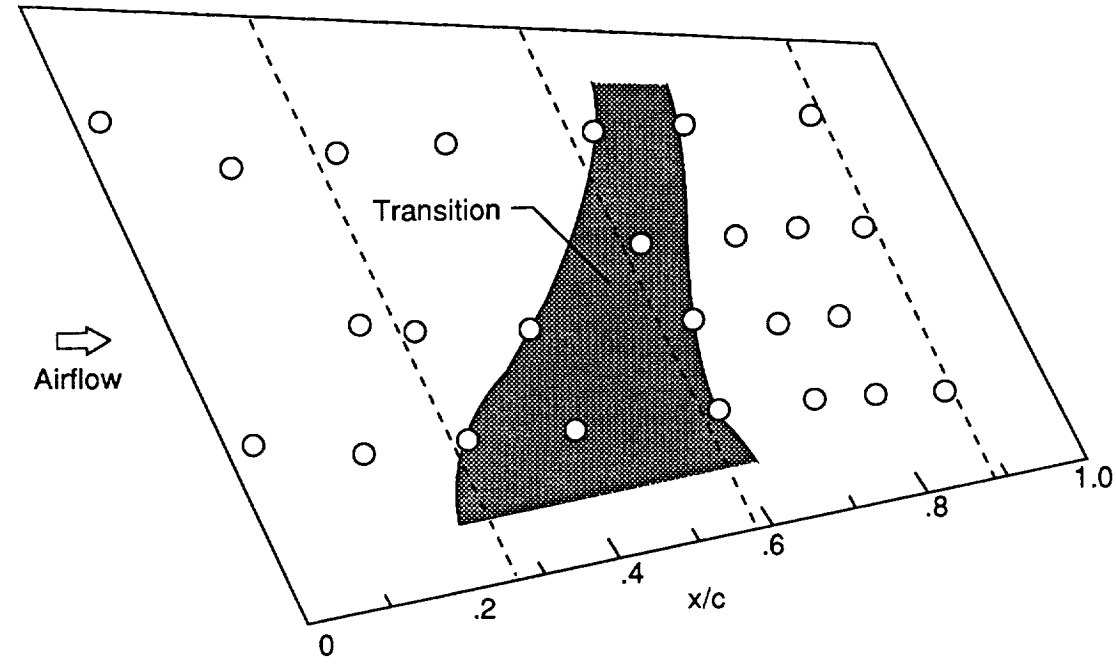

(a) Upper surface.

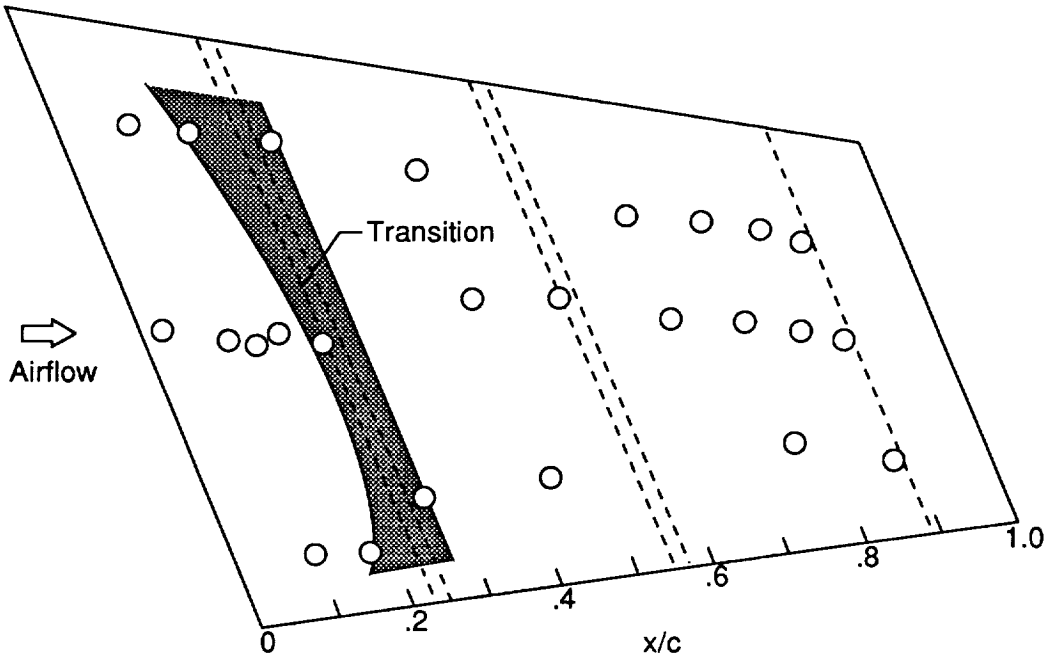

(b) Lower surface.

Figure 36. Laminar-flow pattern. Floor area strip no. 6; $M_\infty = 0.815$; $R_c = 9 \times 10^6$; $\alpha = 0.81°$; $\delta_t = 3.2°$; $\delta_\ell = 1.0°$; $\delta_b = 2.6°$.

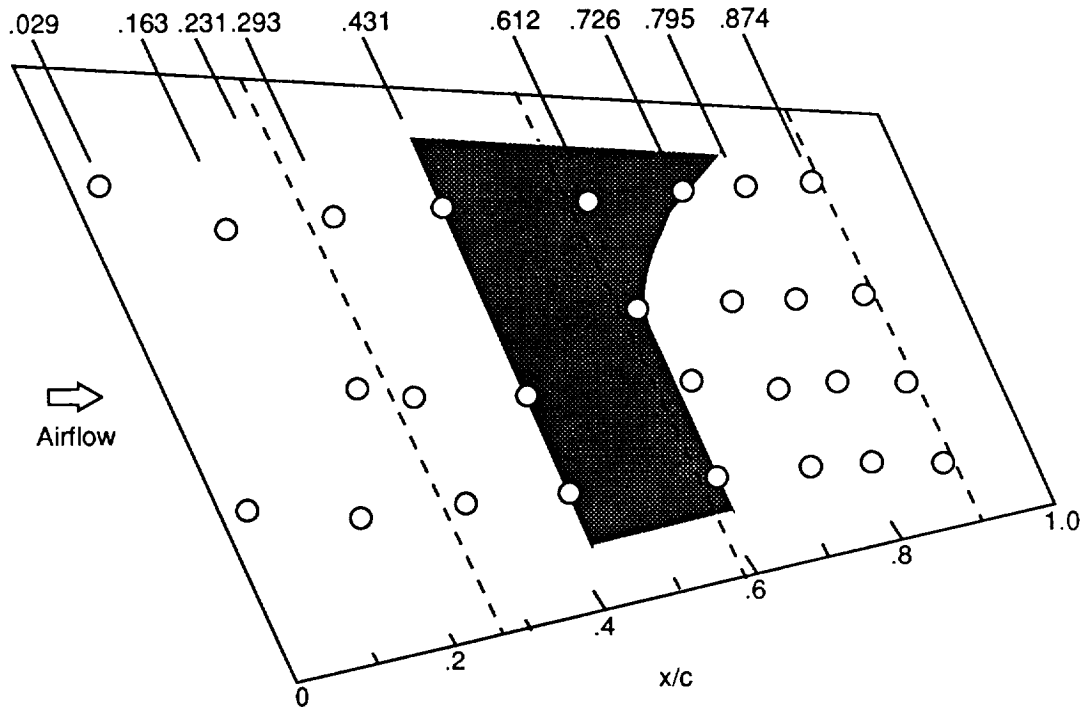

(a) Temperature = 80°F; time = 0.

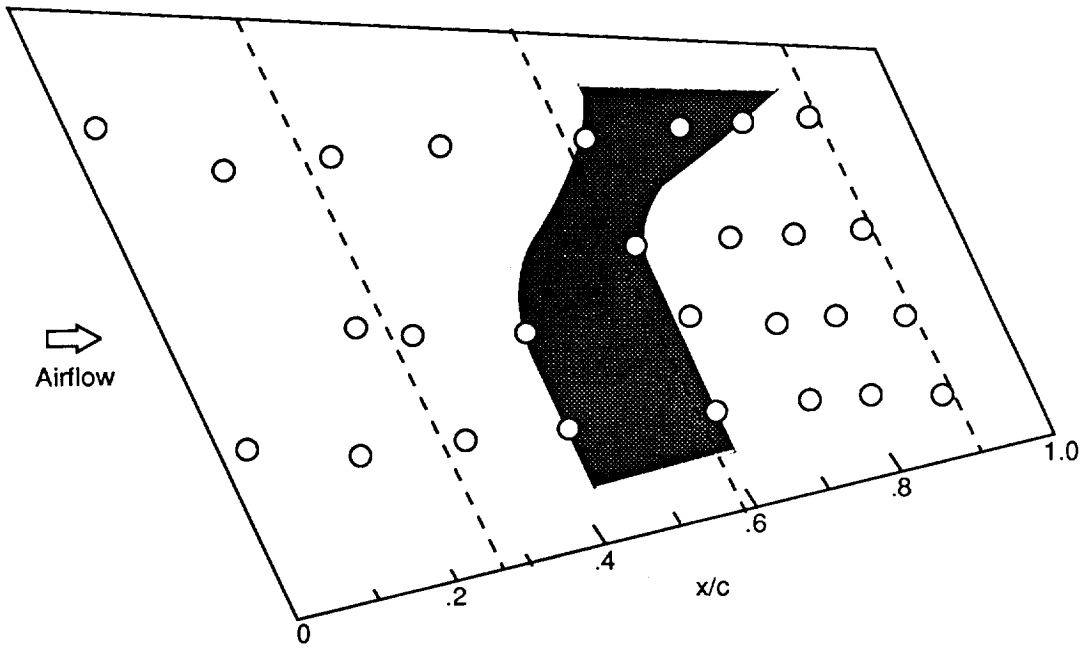

(b) Temperature = 80°F; time = 0 + 67 minutes.

Figure 37. Effect of stagnation temperature and temperature equilibrium on upper-surface laminar-flow pattern at operational design Mach number. $R_c = 10 \times 10^6$.

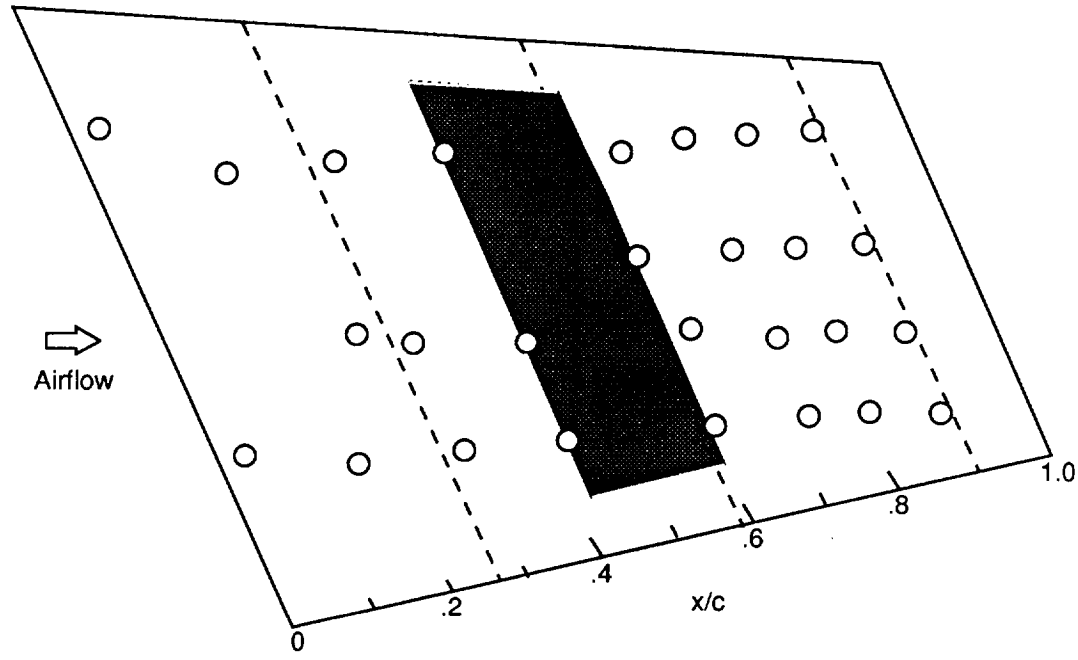

(c) Temperature = 100°F; time = 0.

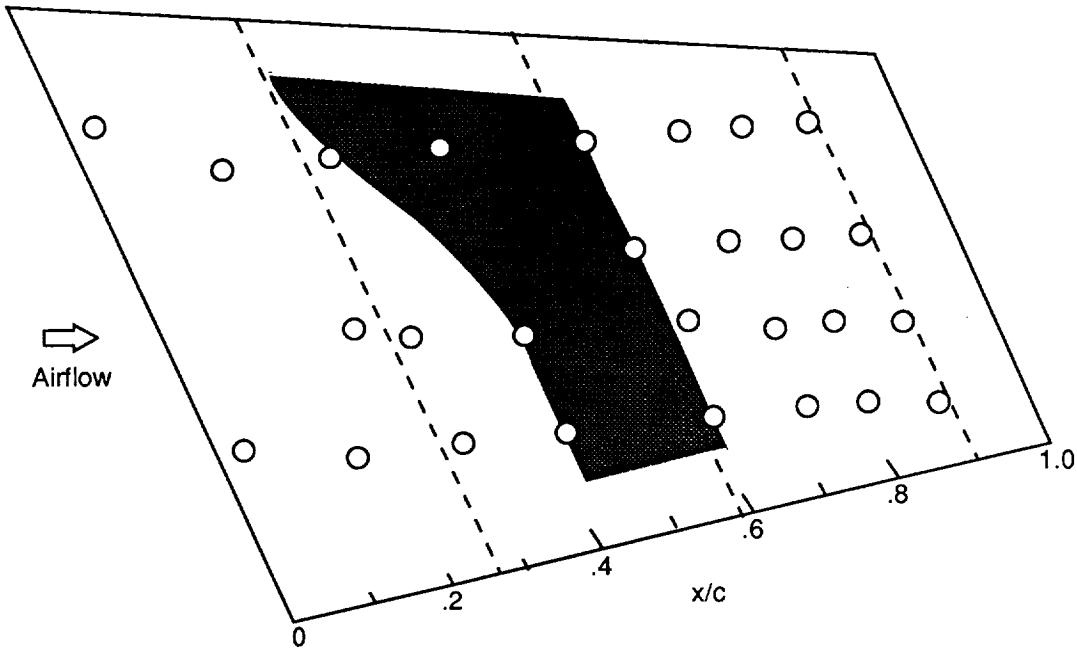

(d) Temperature = 100°F; time = 0 + 13 minutes.

Figure 37. Continued.

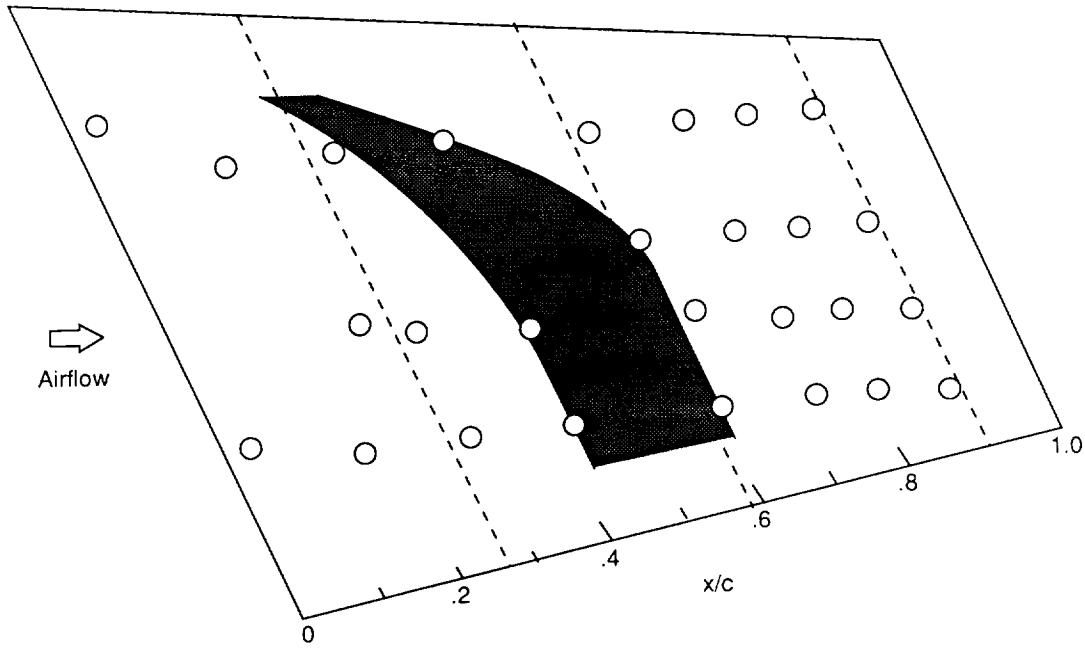

(e) Temperature = 100°F; time = 0 + 19 minutes.

Figure 37. Concluded.

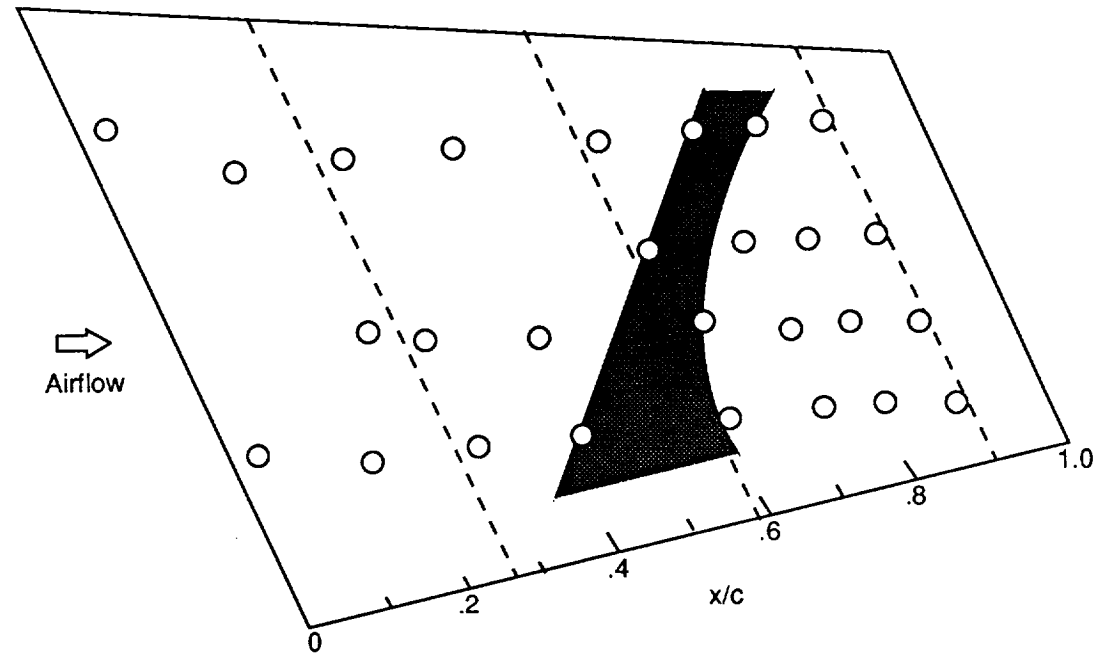

(a) $R_c = 8 \times 10^6$.

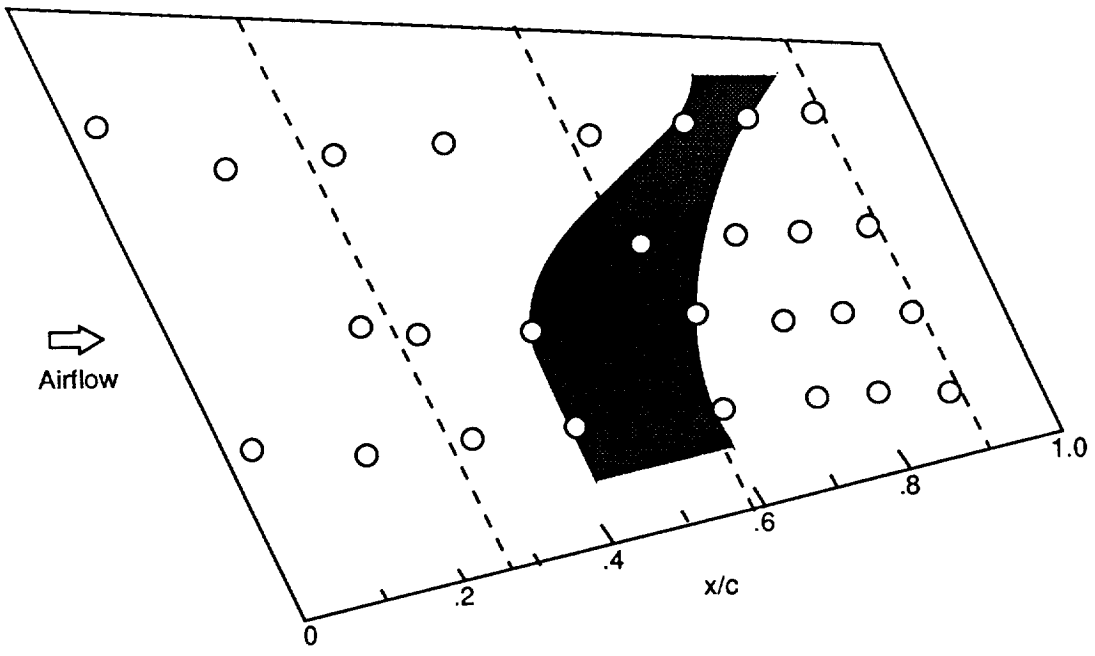

(b) $R_c = 9 \times 10^6$.

Figure 38. Most extensive areas of laminar-flow patterns obtained on upper surface at operational design Mach number.

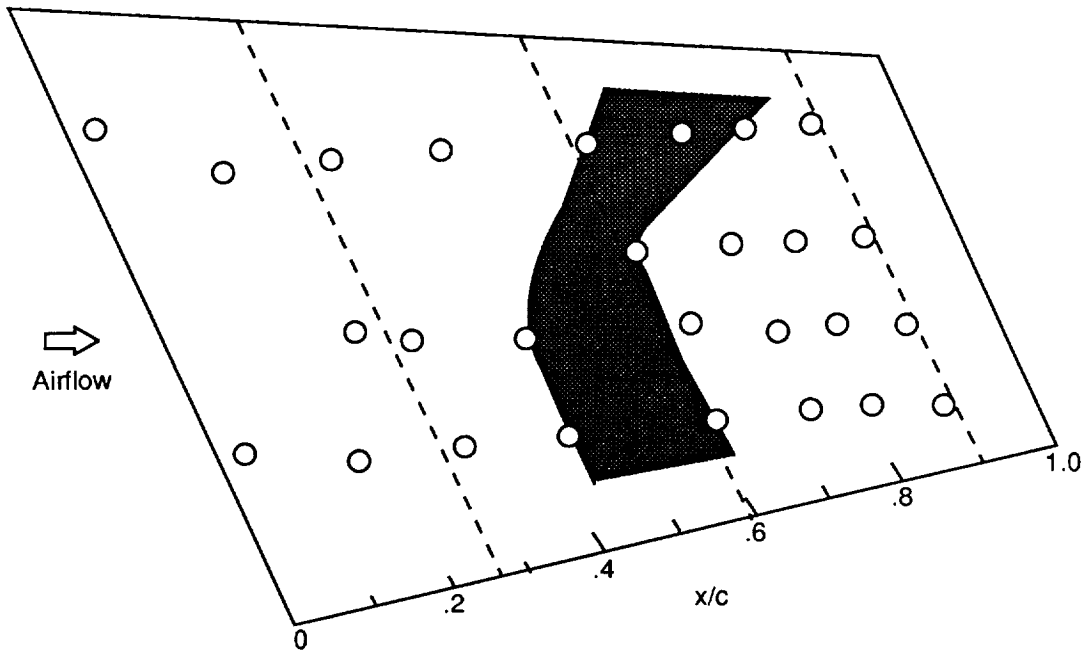

(c) $R_c = 10 \times 10^6$.

Figure 38. Concluded.

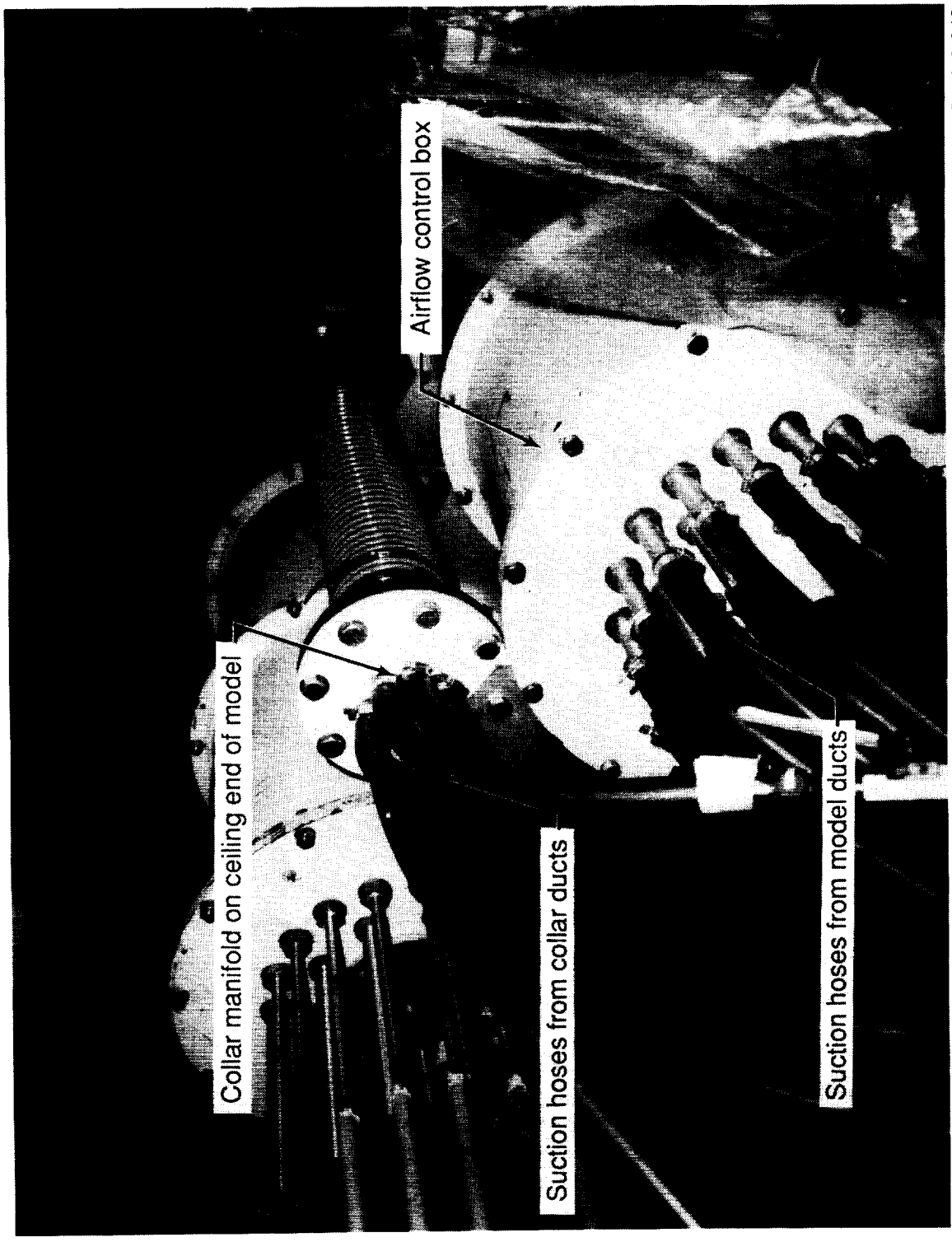

L-82-9,343

(a) Collar manifold.

Figure 39. Suction-collar manifolds and manually operated valves.

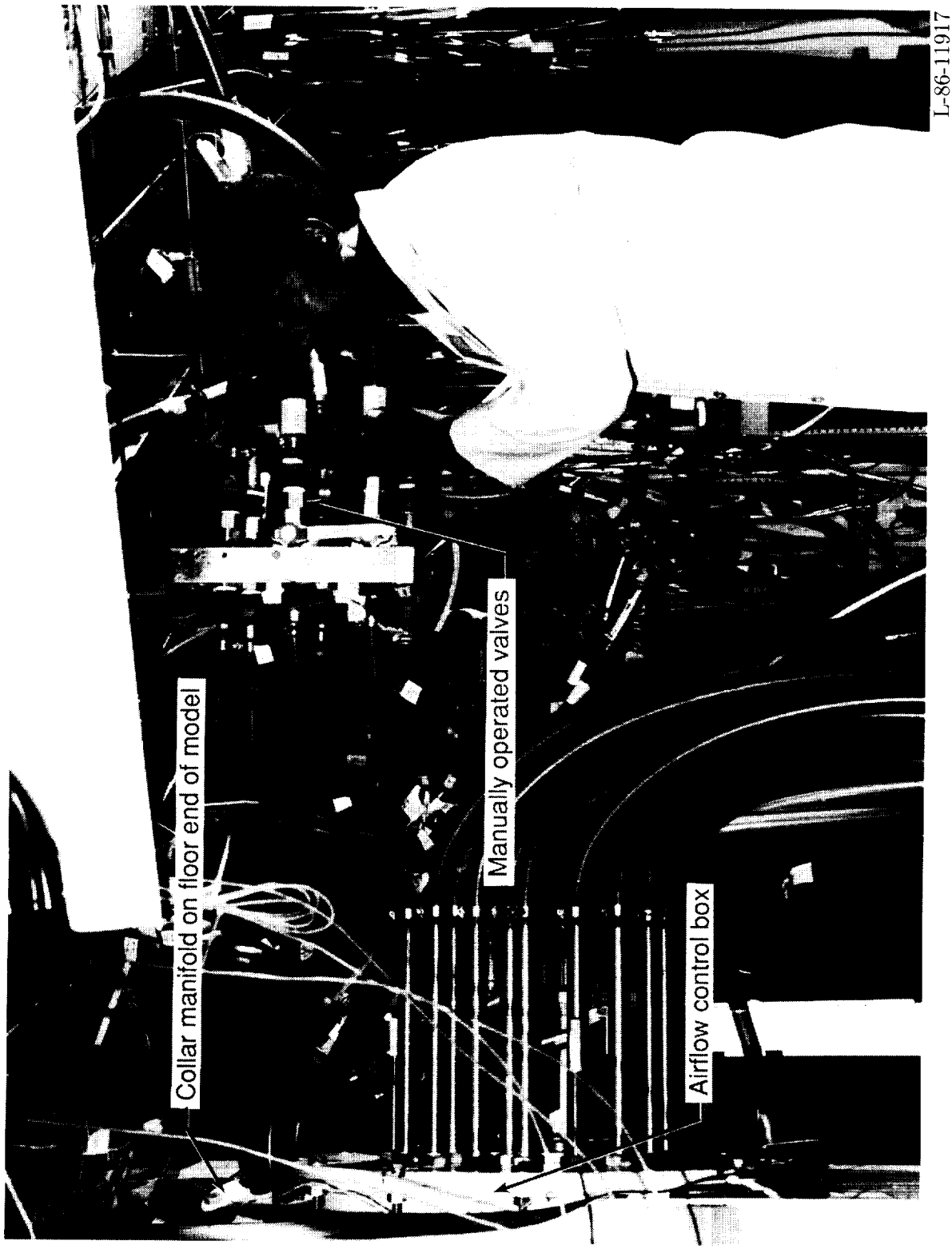

(b) Manually operated valve.

Figure 39. Continued.

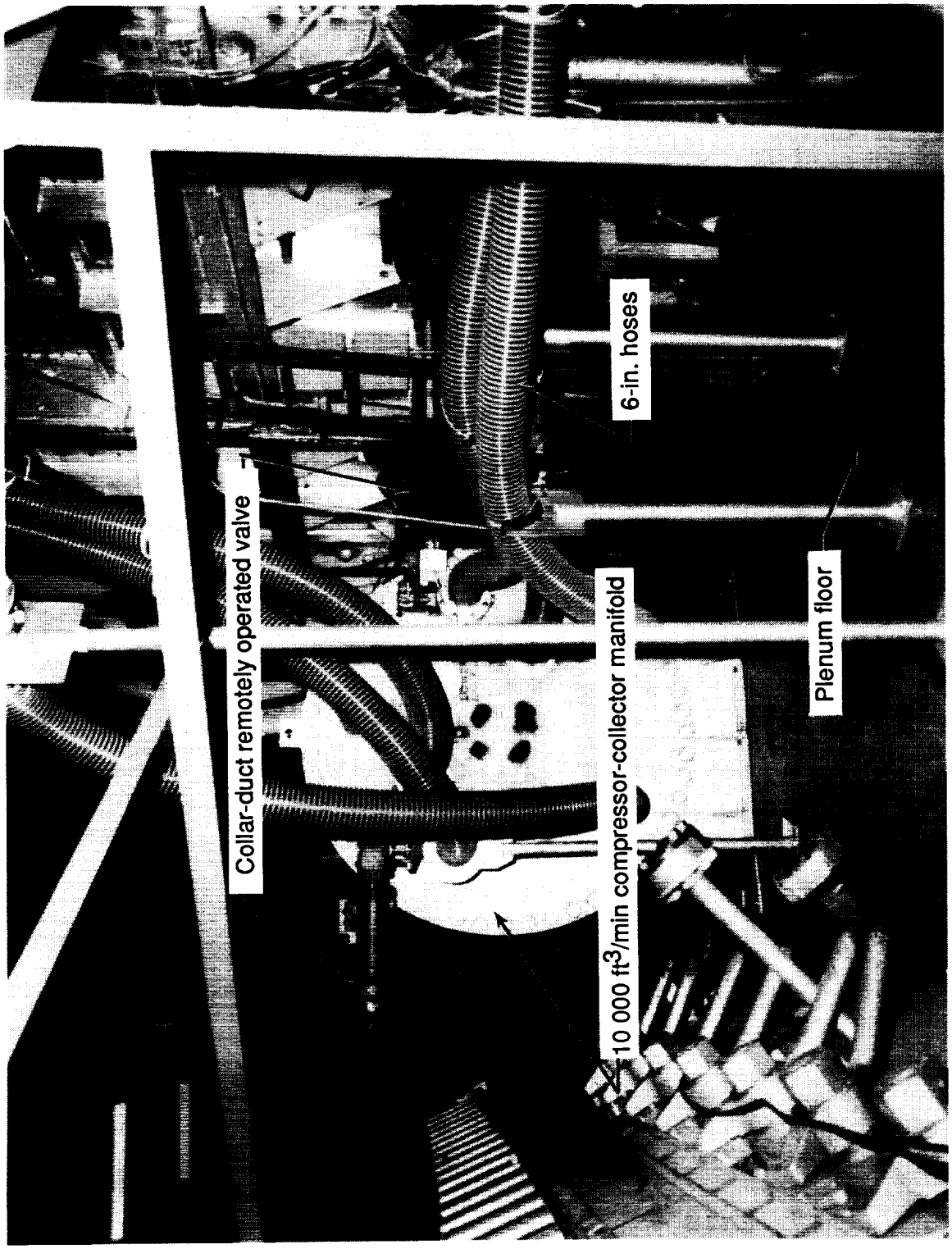

L-82-11,851

(c) Remotely operated valve.

Figure 39. Concluded.

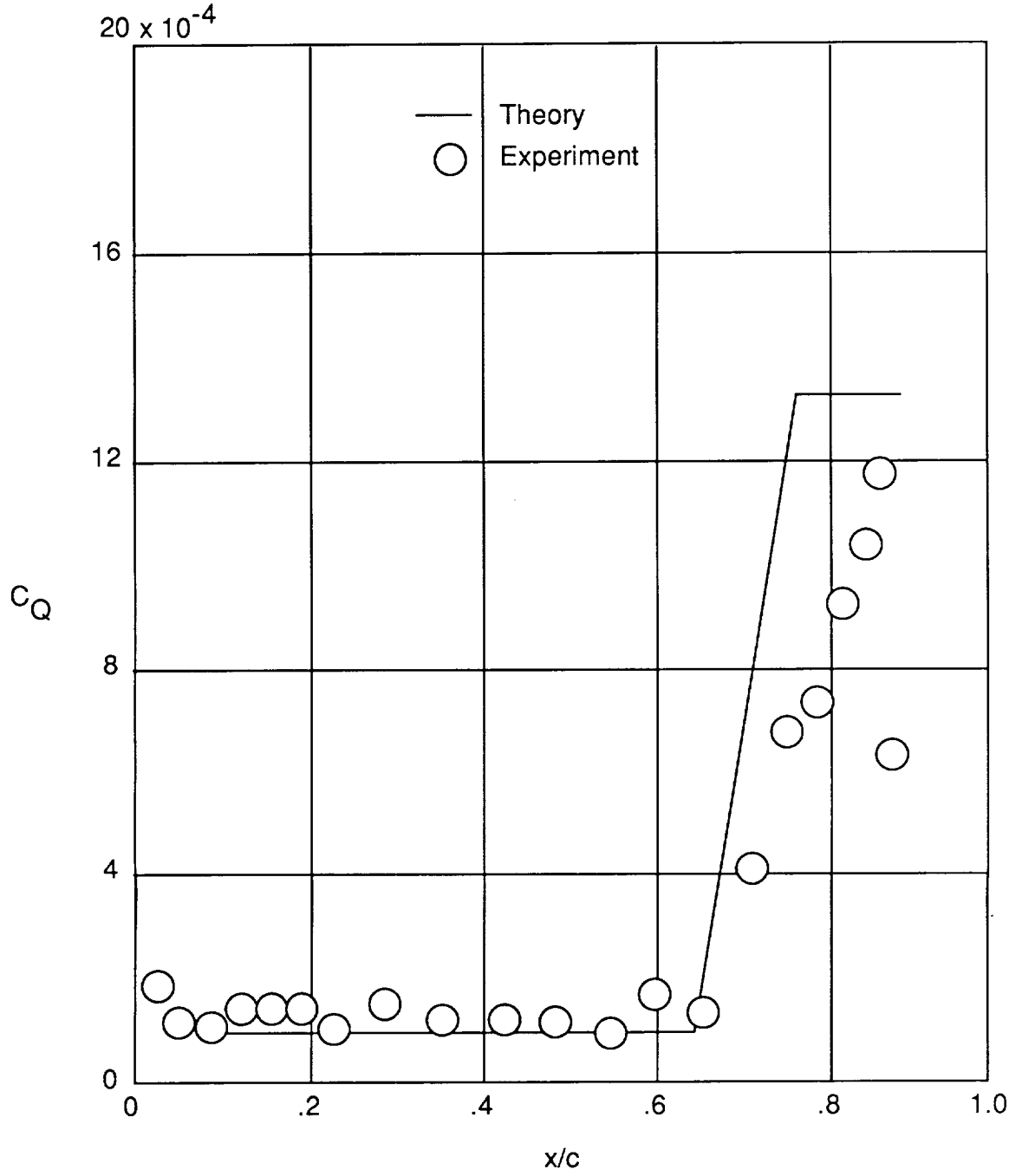

(a) $R_c = 10 \times 10^6$.

Figure 40. Measured and theoretical suction distribution on upper surface of perforated model. $M_\infty = 0.8155$.

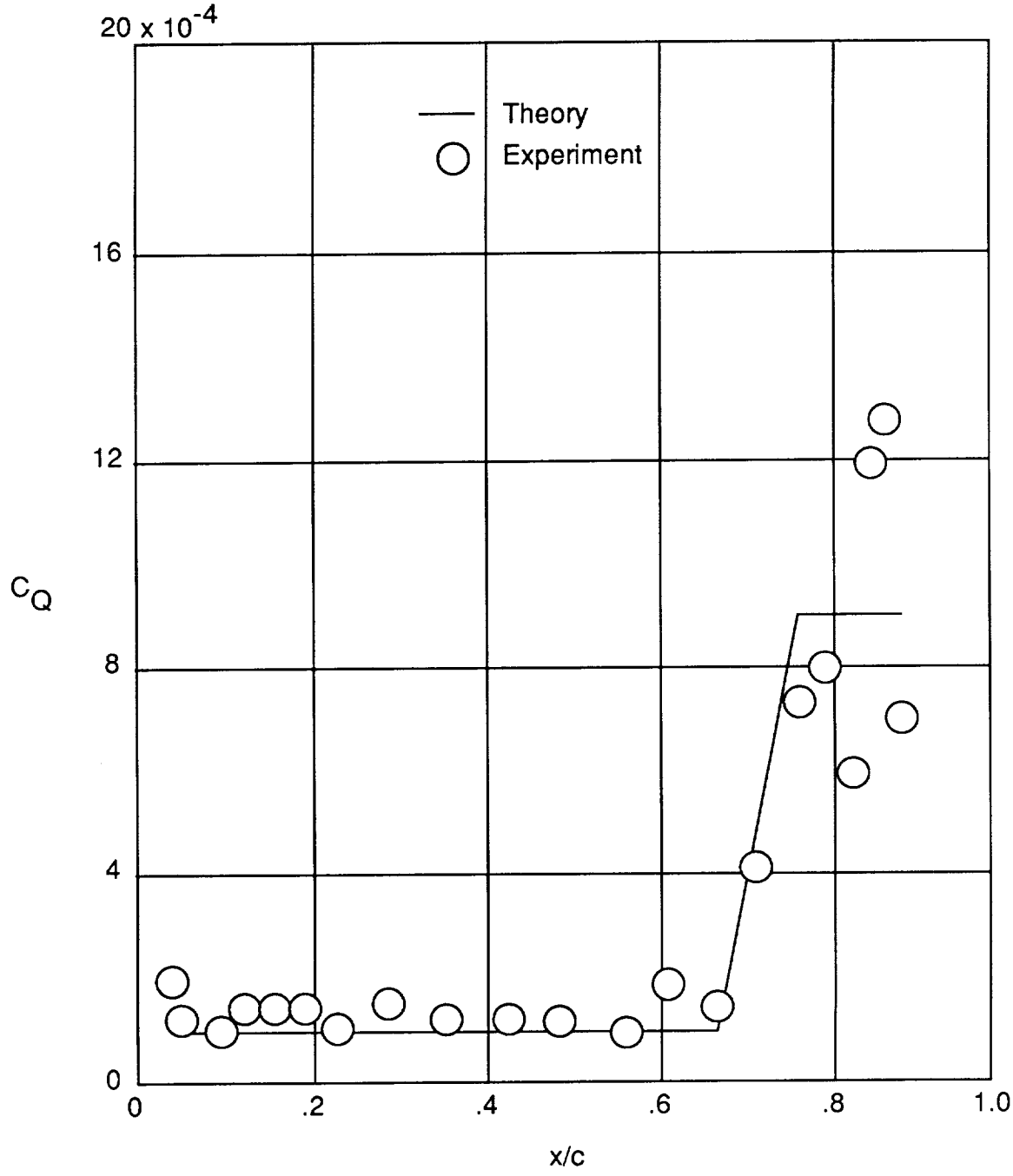

(b) $R_c = 20 \times 10^6$.

Figure 40. Concluded.

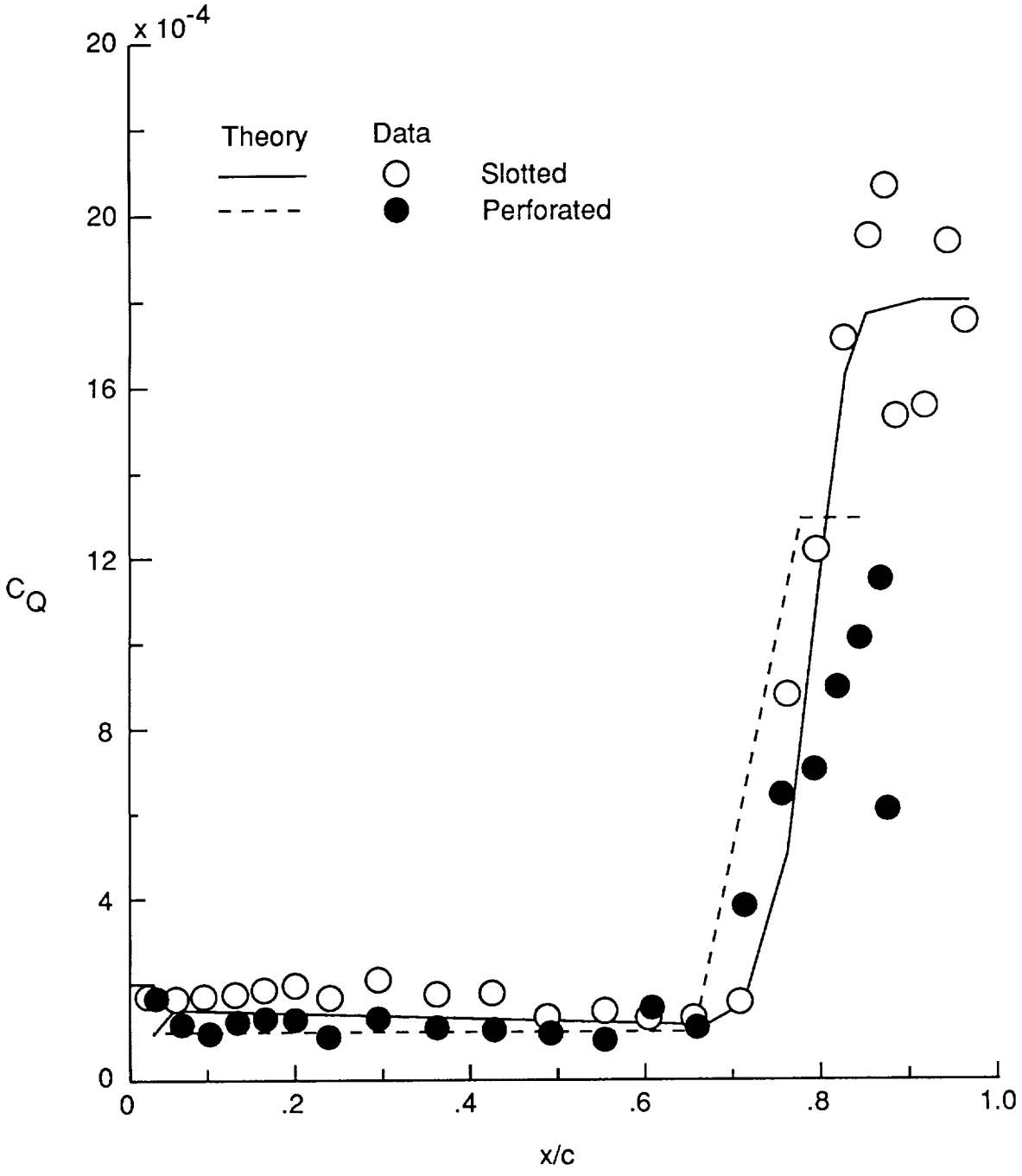

Figure 41. Comparison of maximum suction distributions on upper surface of perforated and slotted models. $R_c = 10 \times 10^6$.

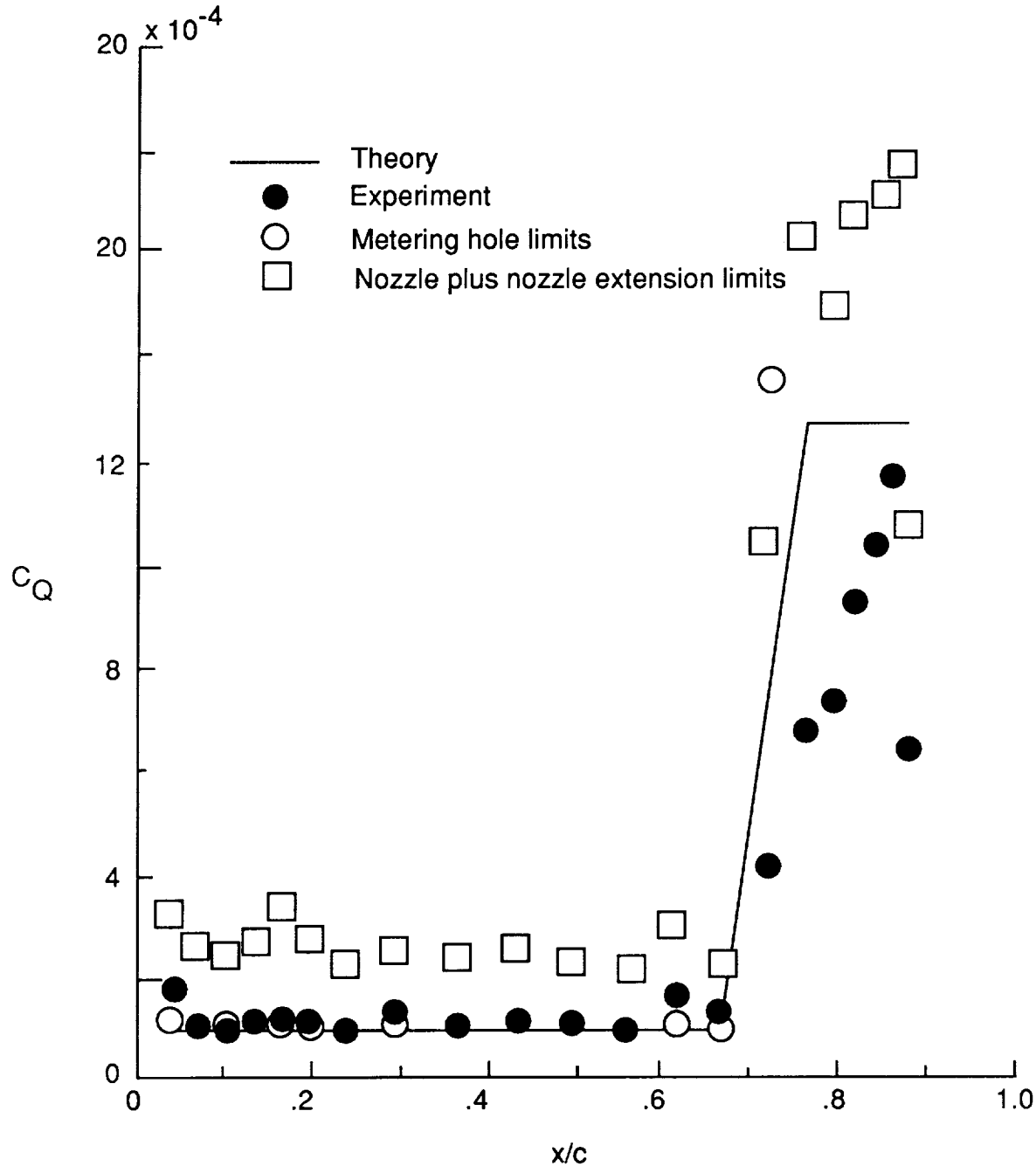

(a) Metering holes and nozzle plus nozzle extensions.

Figure 42. Comparison of theoretical and measured suction distributions with limiting suction capacities of various elements of model suction system. $R_c = 10 \times 10^6$.

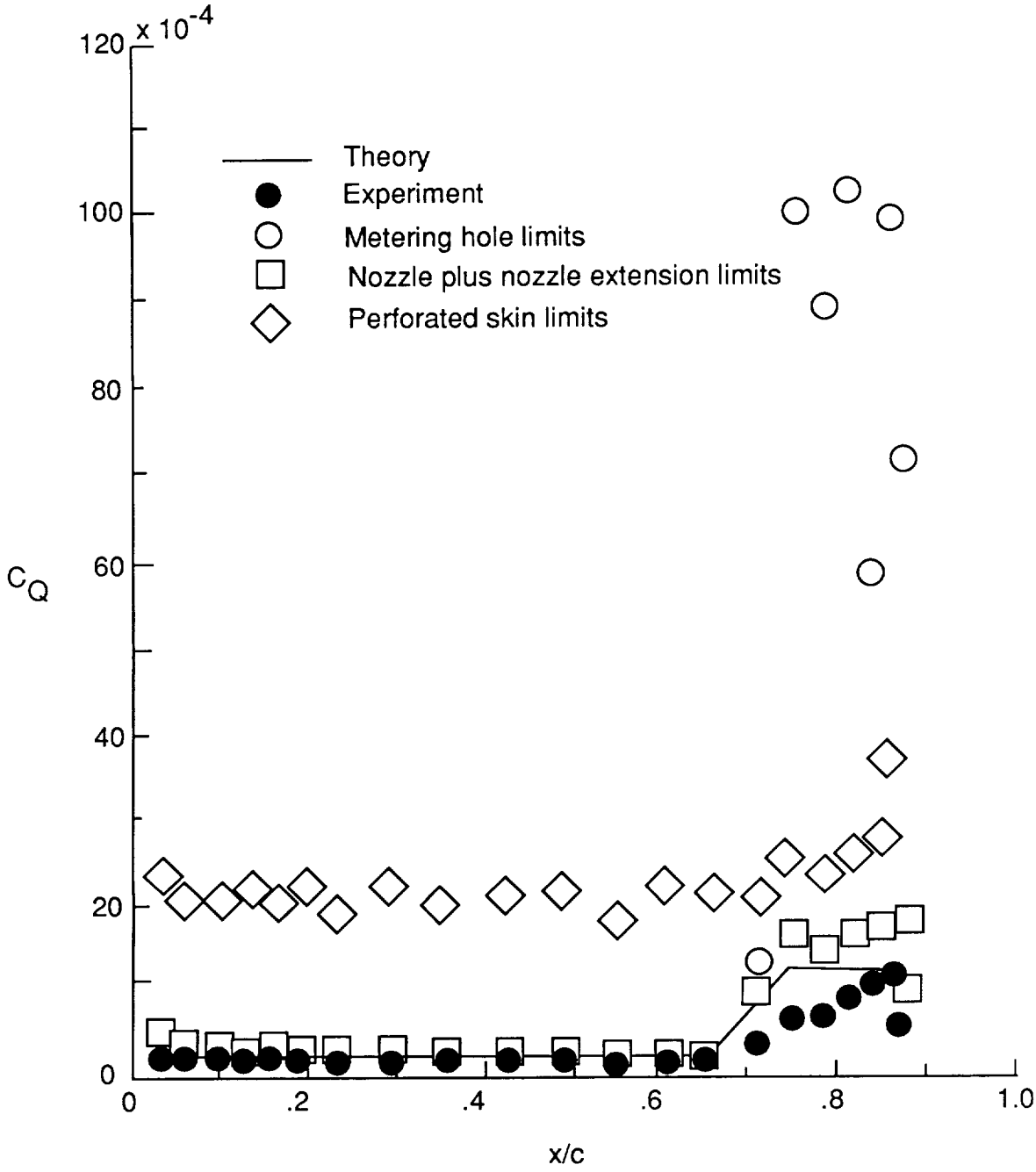

(b) Perforated skin.

Figure 42. Concluded.

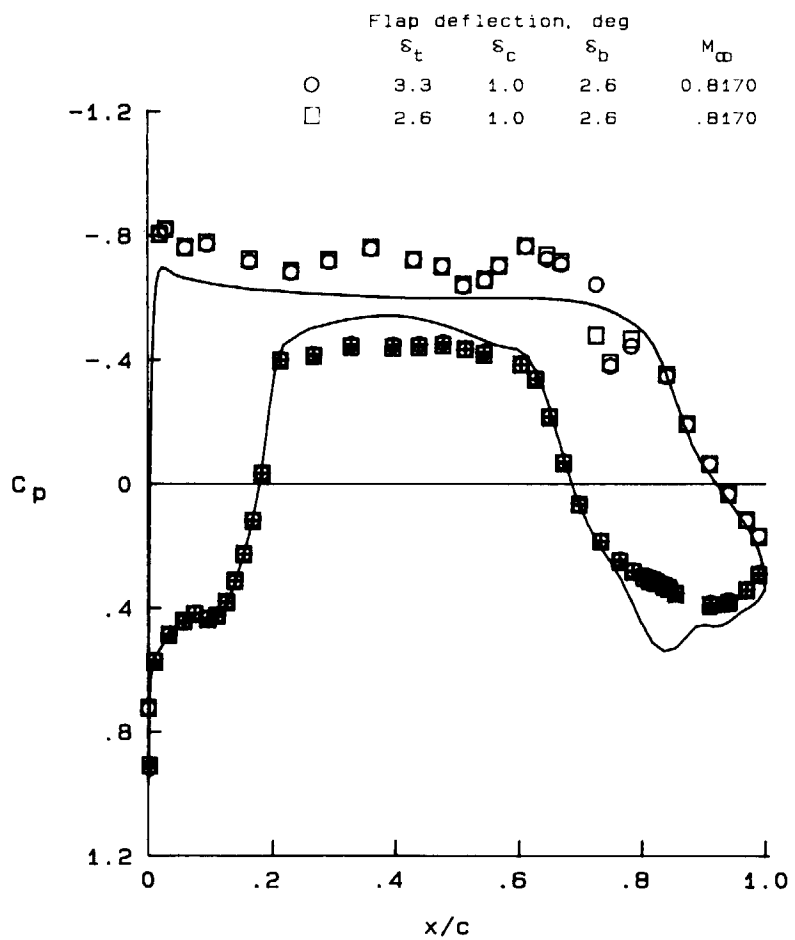

(a) Matching Mach numbers.

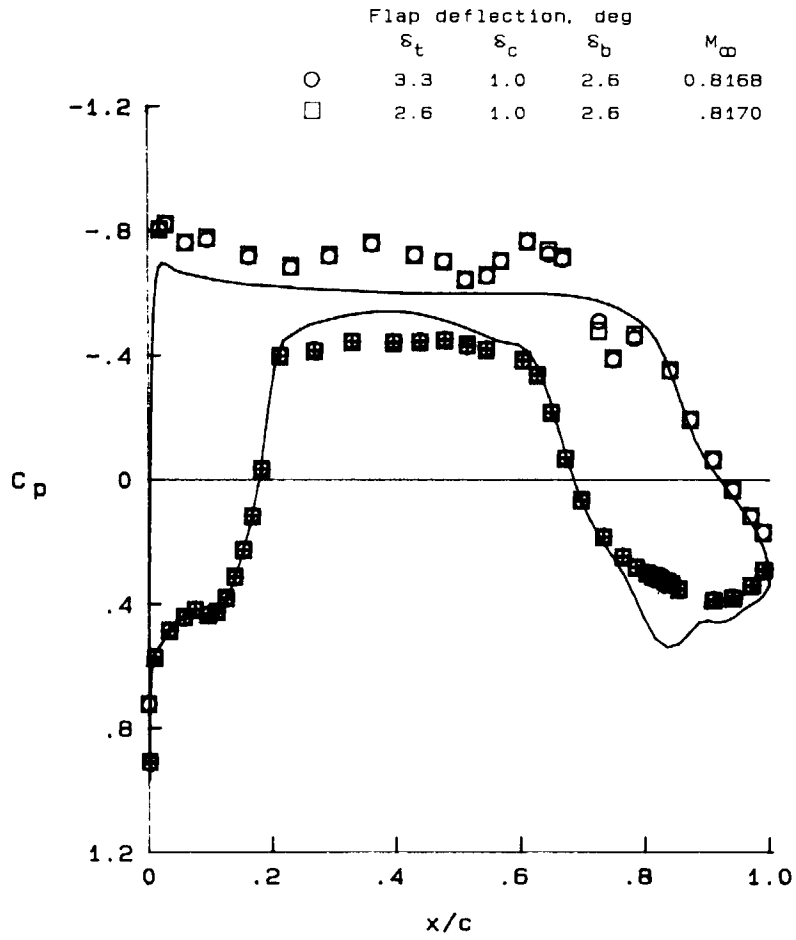

(b) Matching pressure distributions.

Figure 43. Effect of top-flap deflection on experimental pressure distributions. Floor area strip no. 1; $R_c = 10 \times 10^6$; $\alpha = 0.81°$. Open symbols denote upper surface.

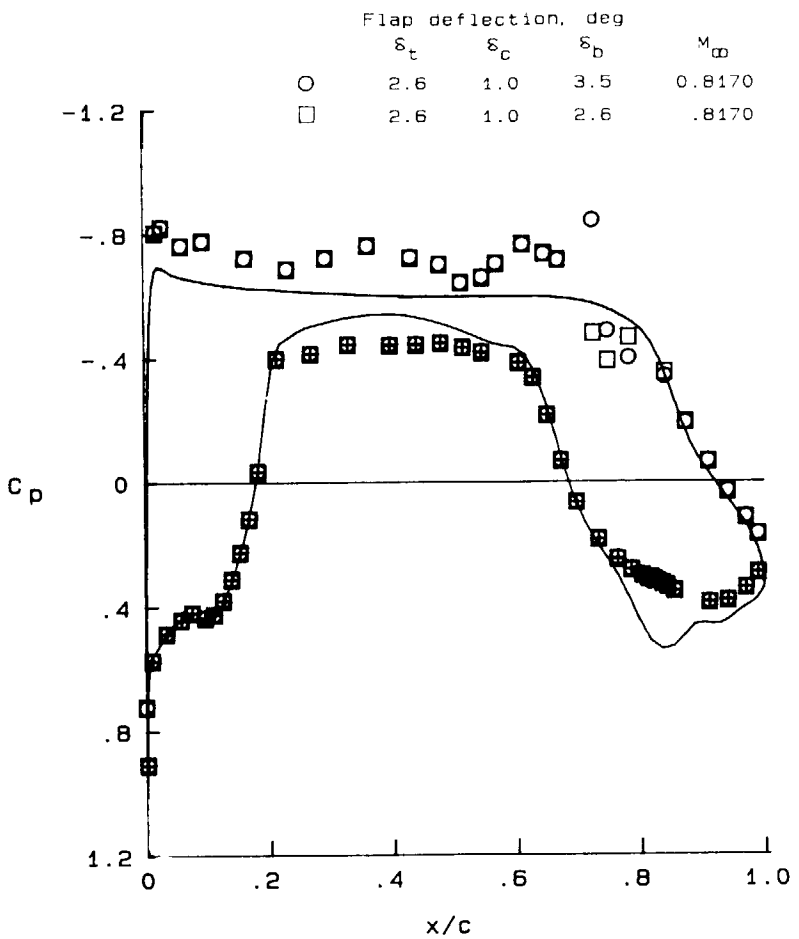

(a) Matching Mach numbers.

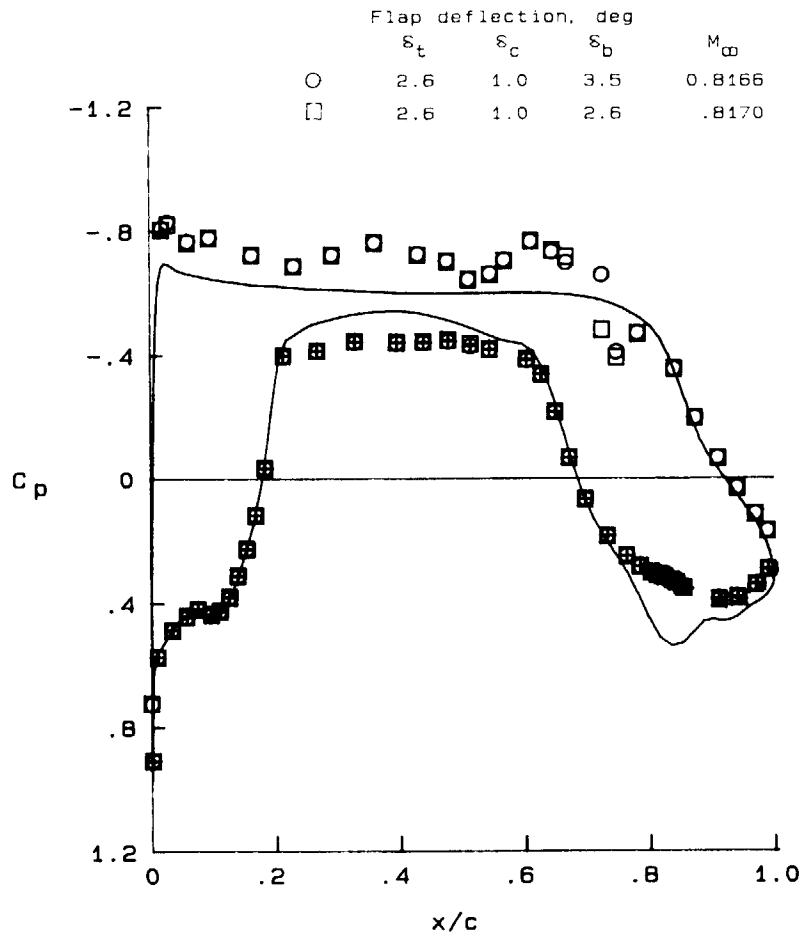

(b) Matching pressure distributions.

Figure 44. Effect of bottom-flap deflection on experimental pressure distributions. Floor area strip no. 1; $R_c = 10 \times 10^6$; $\alpha = 0.81°$. Open symbols denote upper surface.

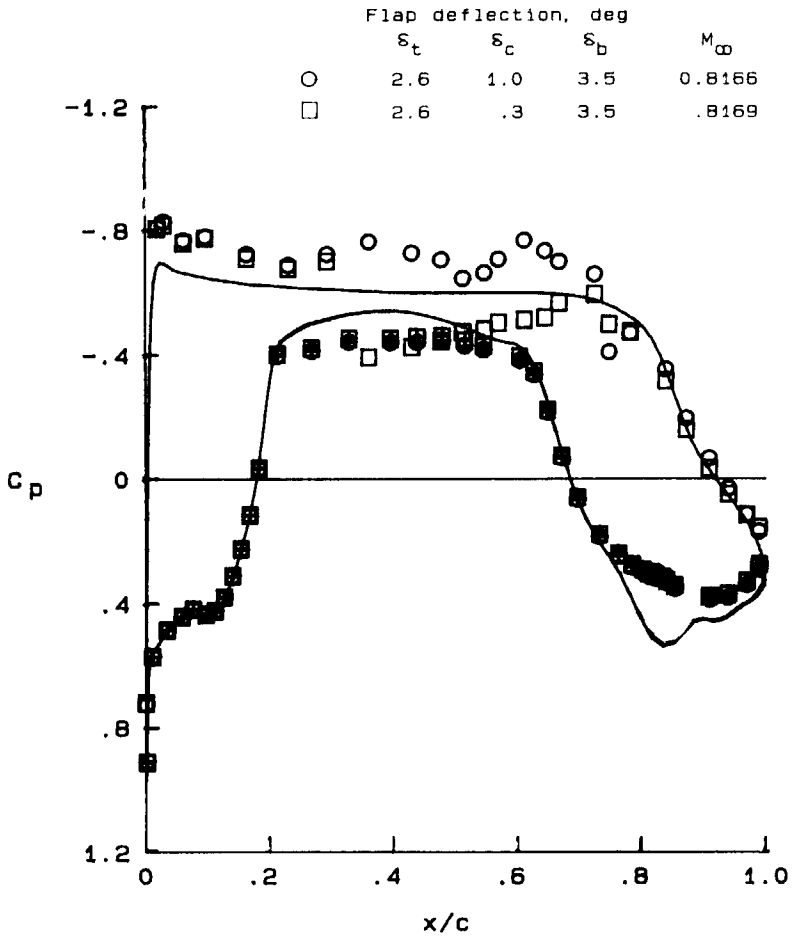

(a) Matching Mach numbers.

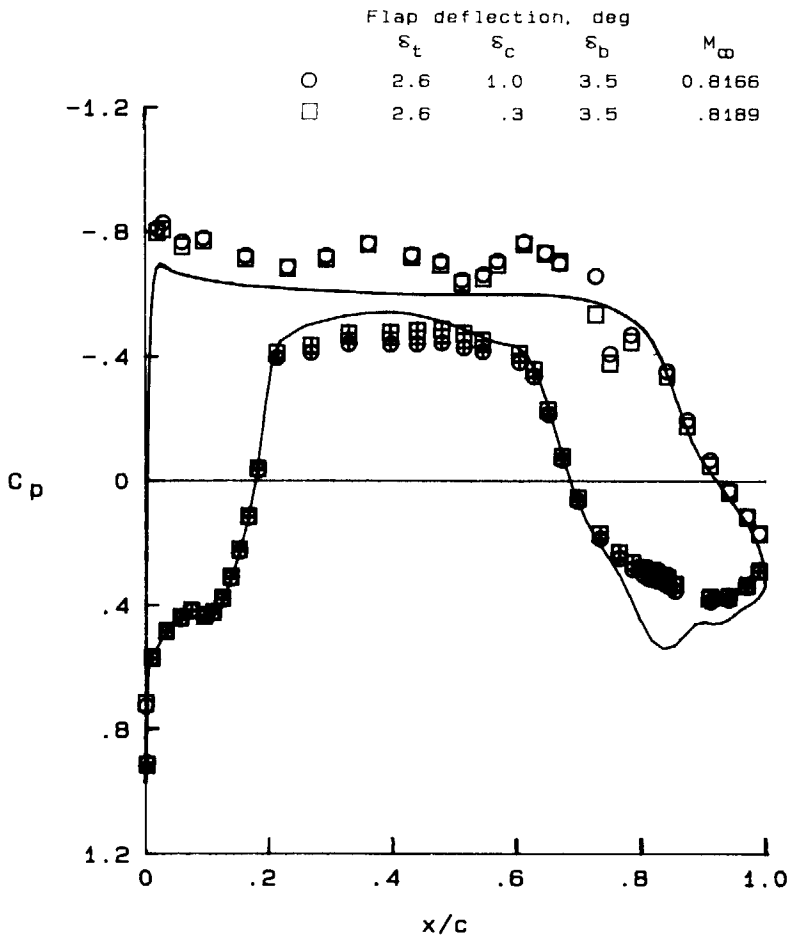

(b) Matching pressure distributions.

Figure 45. Effect of central-flap deflection on experimental pressure distributions. Floor area strip no. 1; $R_c = 10 \times 10^6$; $\alpha = 0.81°$. Open symbols denote upper surface.

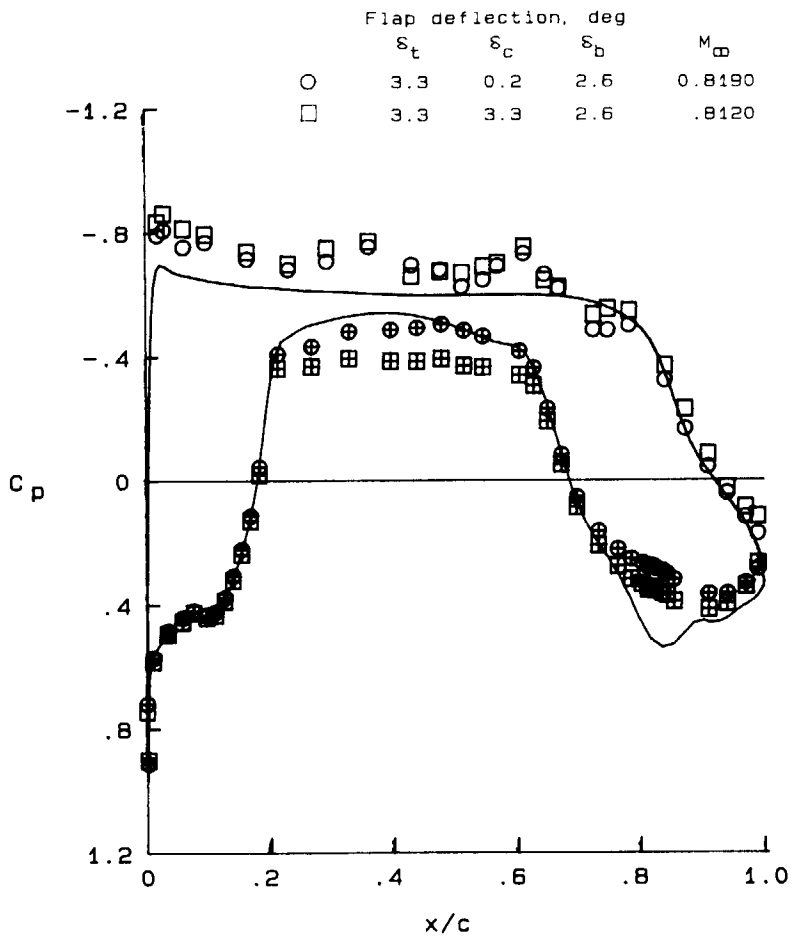

Figure 46. Effect of large central-flap deflection on experimental pressure distributions. Floor area strip no. 1; $R_c = 10 \times 10^6$; $\alpha = 0.81°$. Open symbols denote upper surface.

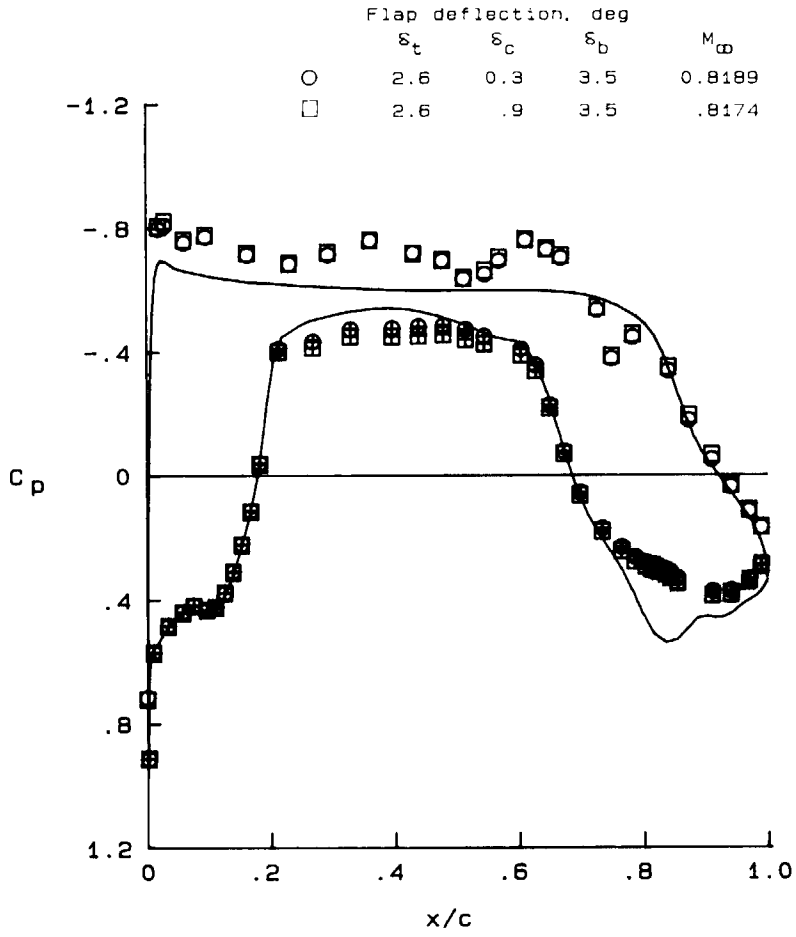

Figure 47. Experimental pressure distribution with flaps deflected for "final" configuration compared with earlier configuration with slightly smaller central-flap deflection. Floor area strip no. 1; $R_c = 10 \times 10^6$; $\alpha = 0.81°$. Open symbols denote upper surface.

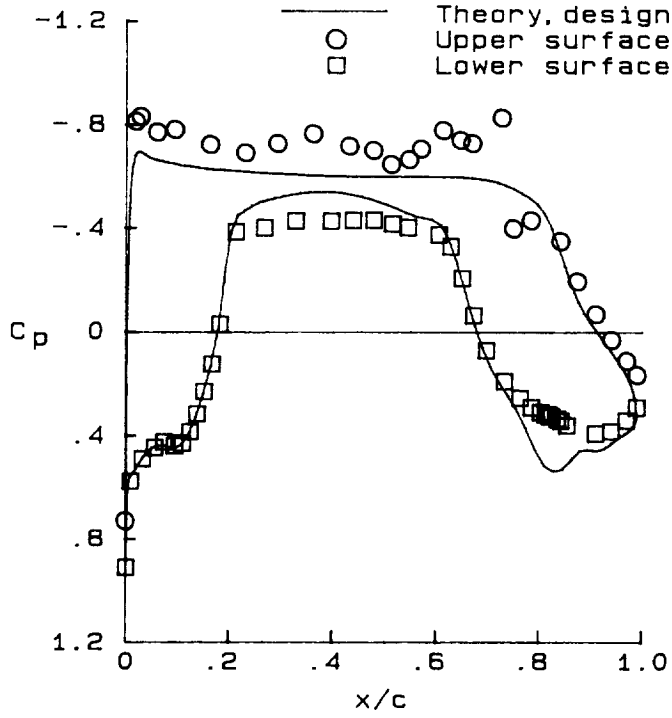

(a) $M_\infty = 0.8155; c_l = 0.573.$

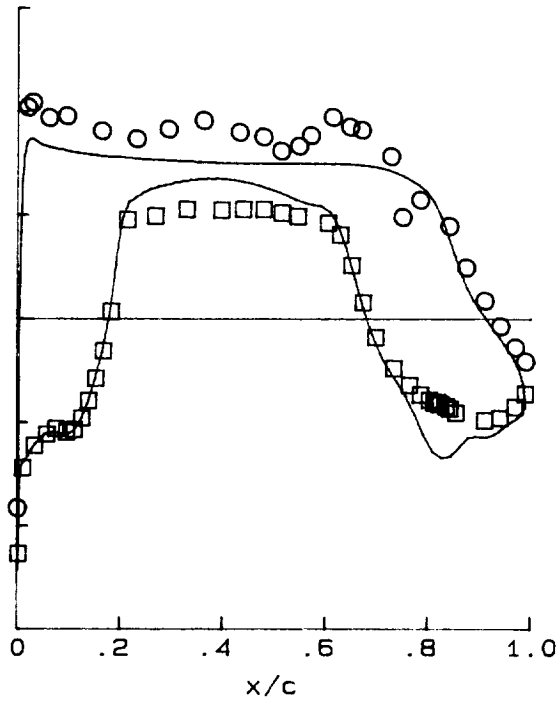

(b) $M_\infty = 0.8151; c_l = 0.573.$

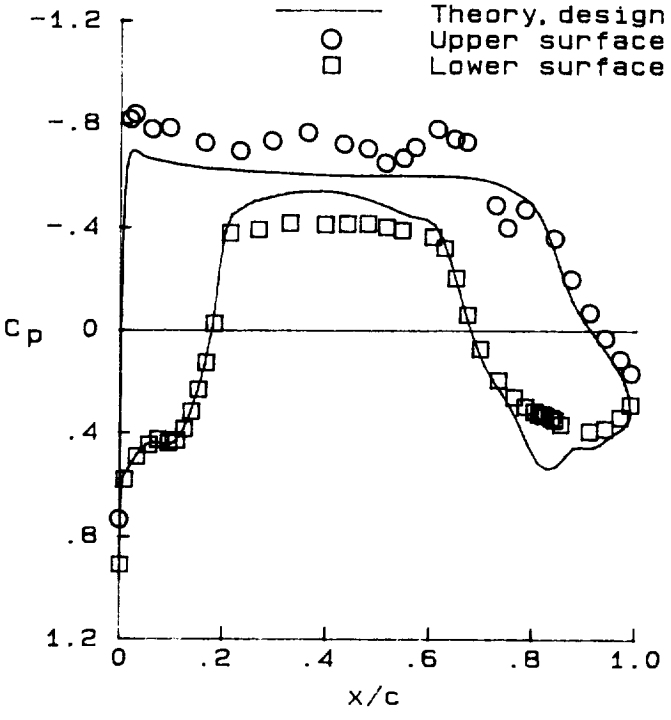

(c) $M_\infty = 0.8147; c_l = 0.572.$

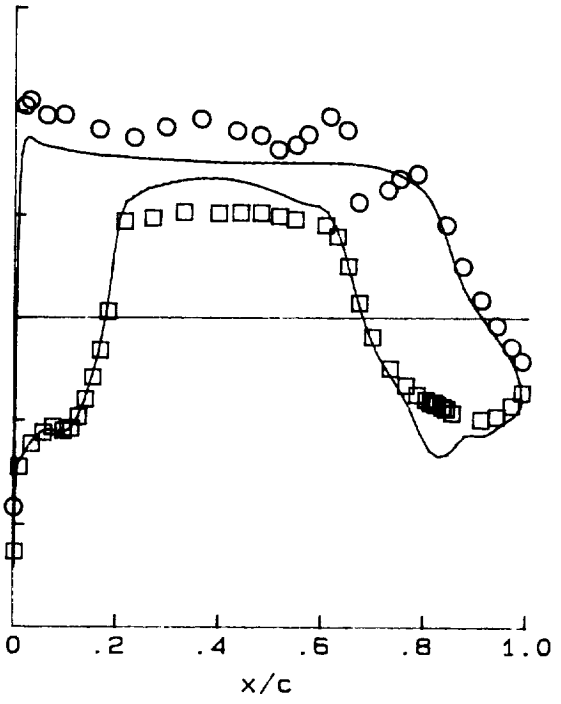

(d) $M_\infty = 0.8144; c_l = 0.572.$

Figure 48. Effect on experimental chordwise pressure distribution of varying Mach number near design Mach number. Floor area strip no. 1; $\alpha = 0.81°$; $R_c = 10 \times 10^6$; $\delta_t = 2.6°$; $\delta_c = 0.9°$; $\delta_b = 3.5°$.

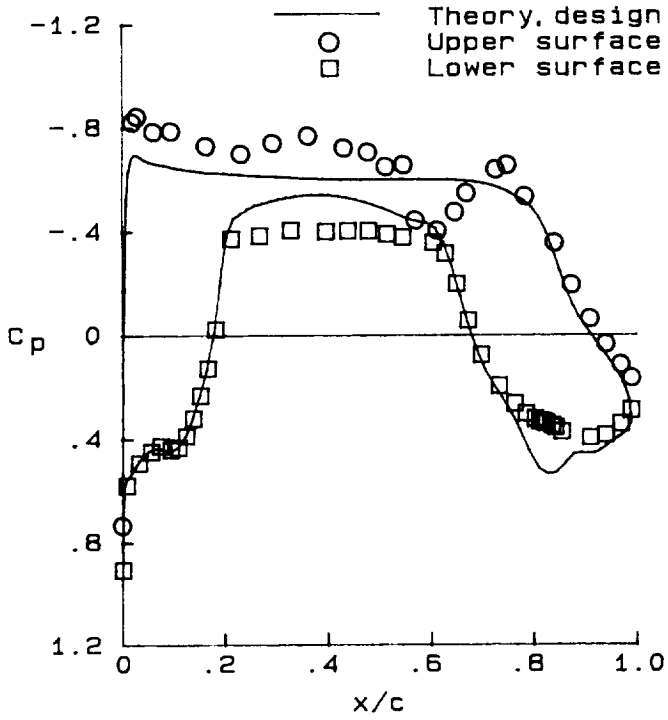

(e) $M_\infty = 0.8140; c_l = 0.555$.

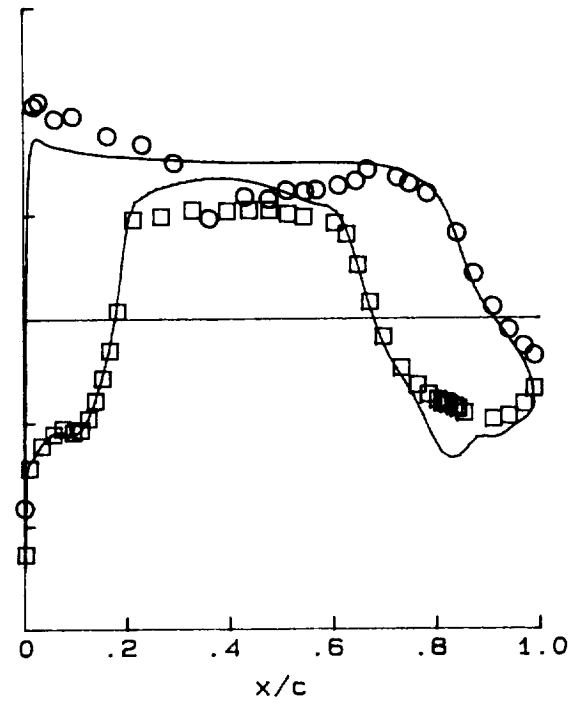

(f) $M_\infty = 0.8134; c_l = 0.467$.

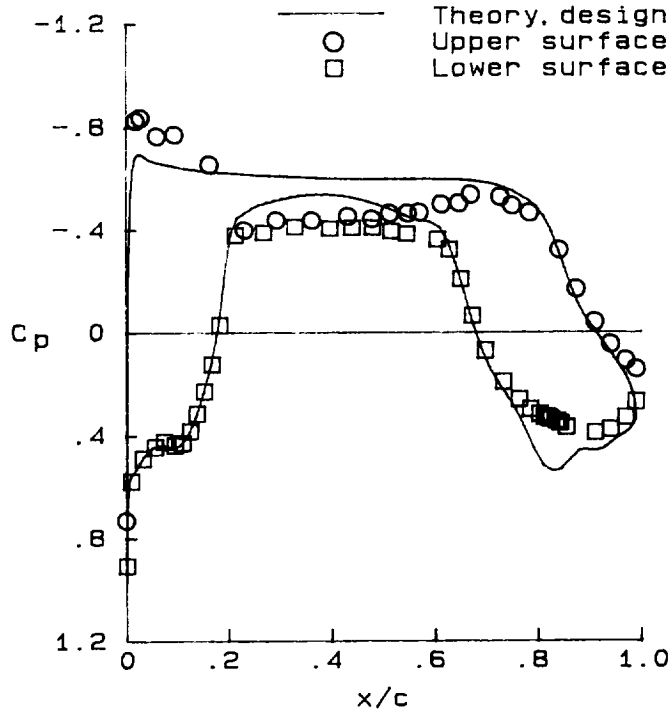

(g) $M_\infty = 0.8102; c_l = 0.434$.

Figure 48. Concluded.

C-2

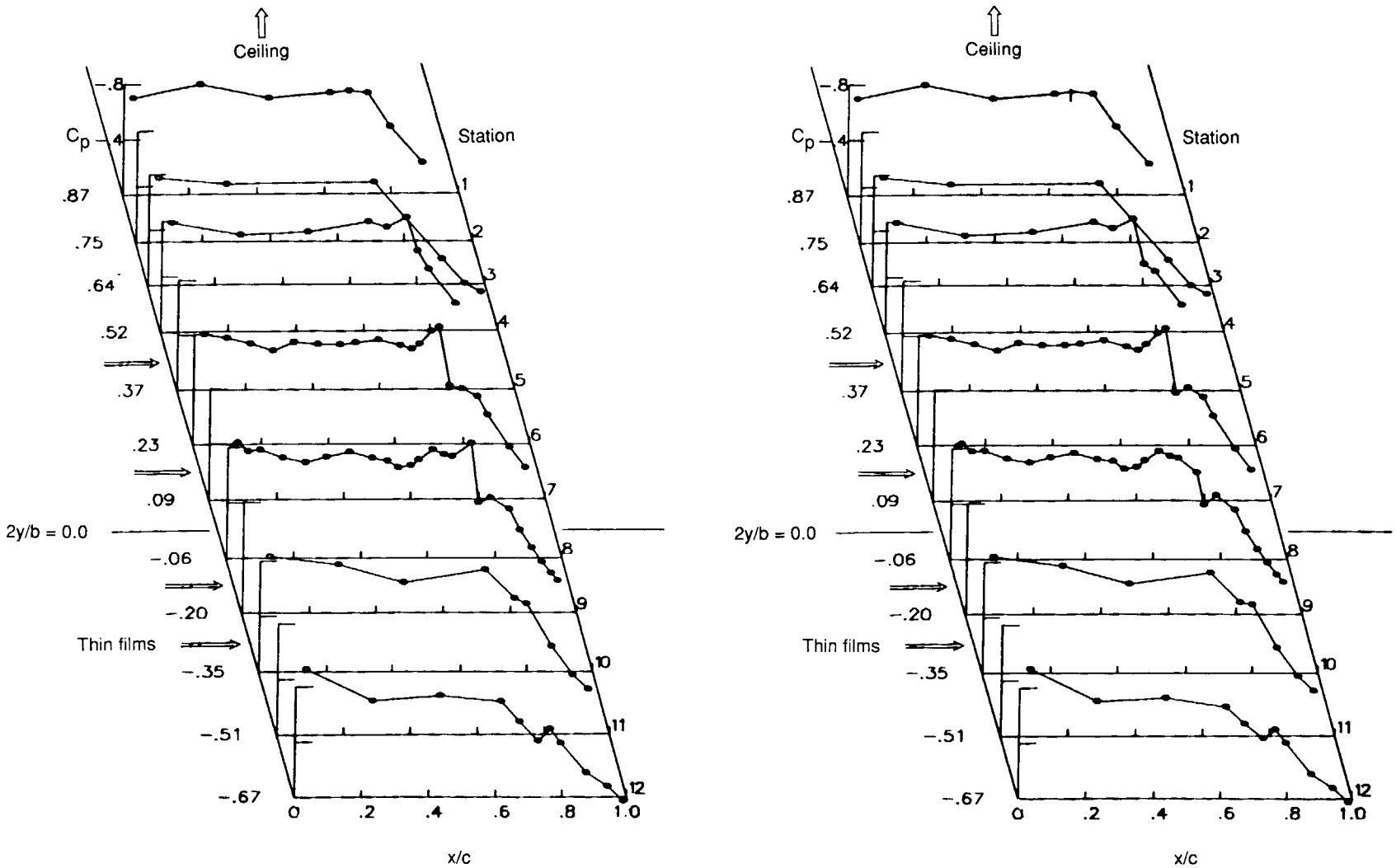

(a) $M_\infty = 0.8155; c_l = 0.573.$

(b) $M_\infty = 0.8151; c_l = 0.573.$

Figure 49. Effect on experimental spanwise pressure distribution of varying Mach number near design Mach number. Floor area strip no. 1; $\alpha = 0.81^\circ; R_c = 10 \times 10^6; \delta_t = 2.6^\circ; \delta_c = 0.9^\circ; \delta_b = 3.5^\circ.$

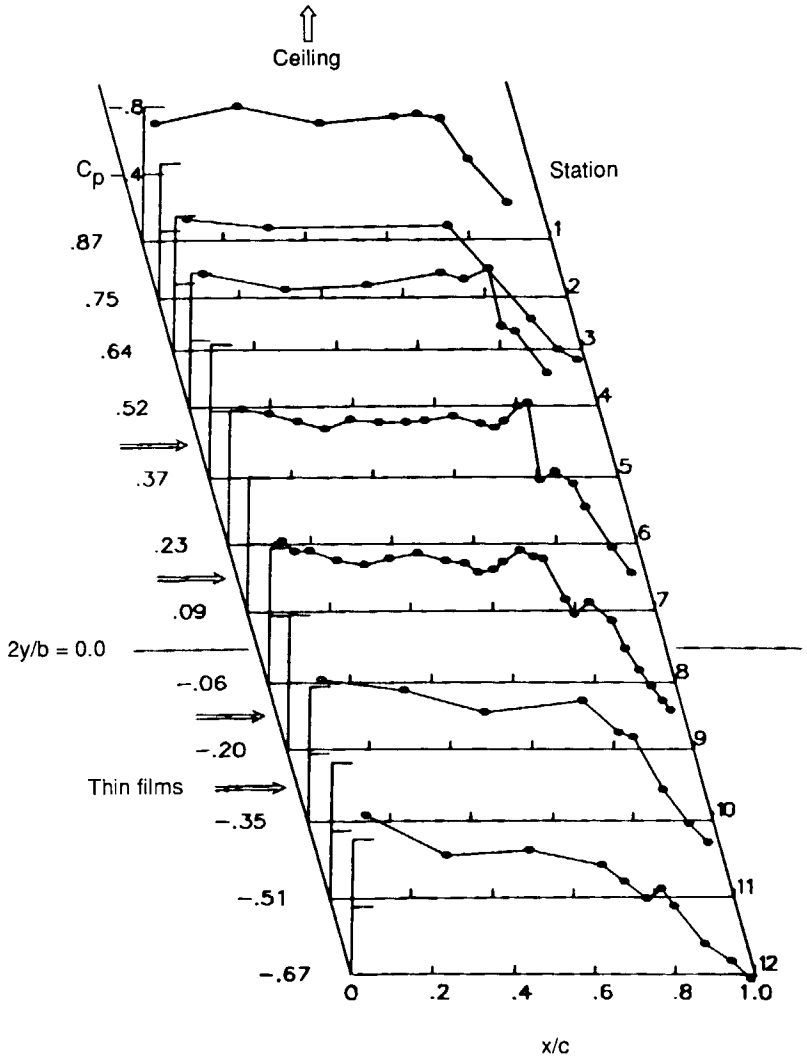

(c) $M_\infty = 0.8147; c_l = 0.572.$

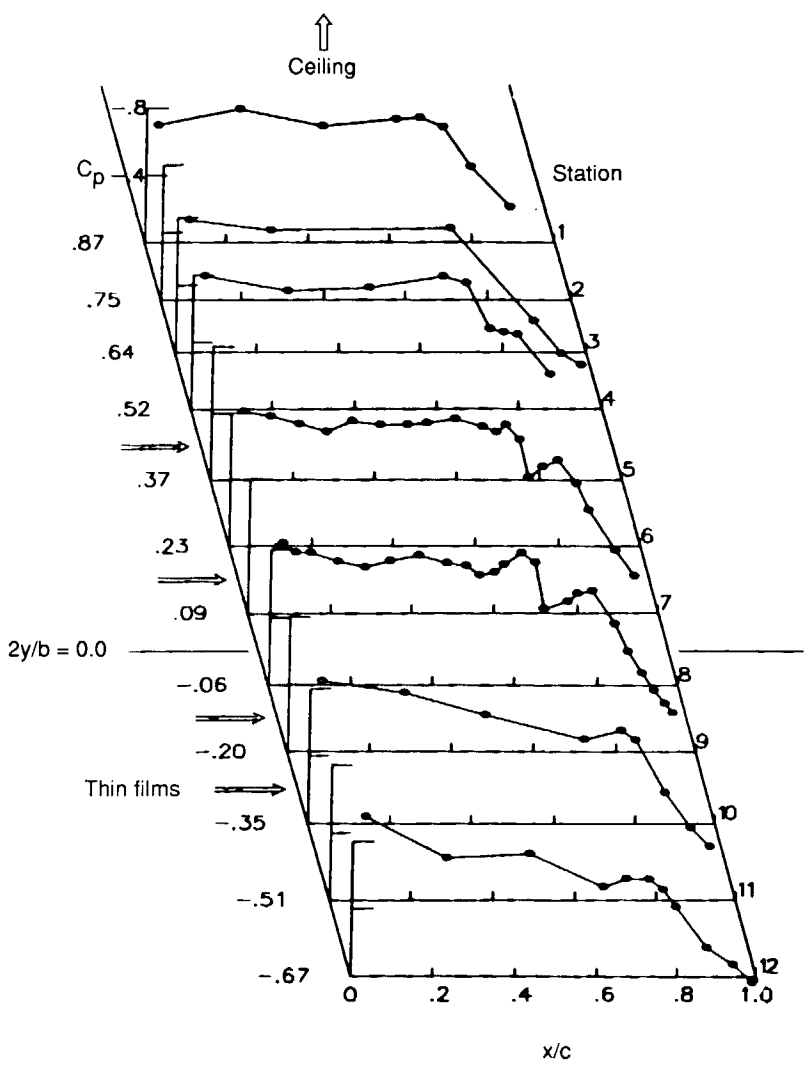

(d) $M_\infty = 0.8144; c_l = 0.572.$

Figure 49. Continued.

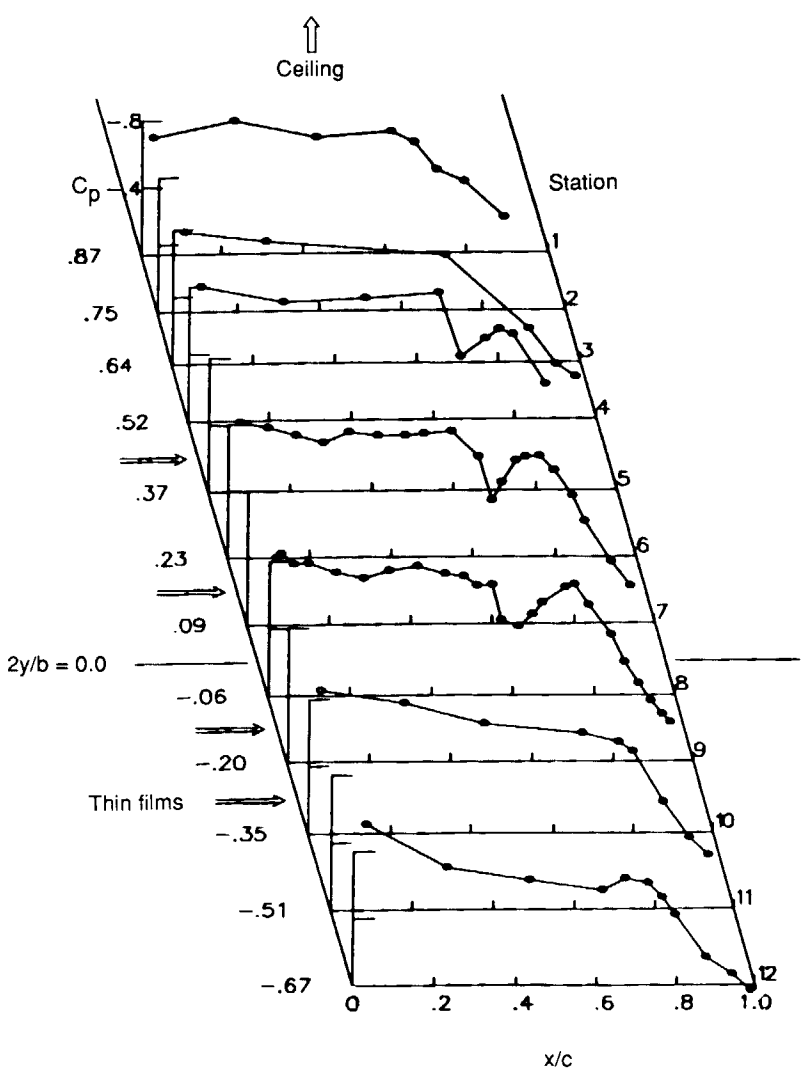

(e) $M_\infty = 0.8140; c_l = 0.555.$

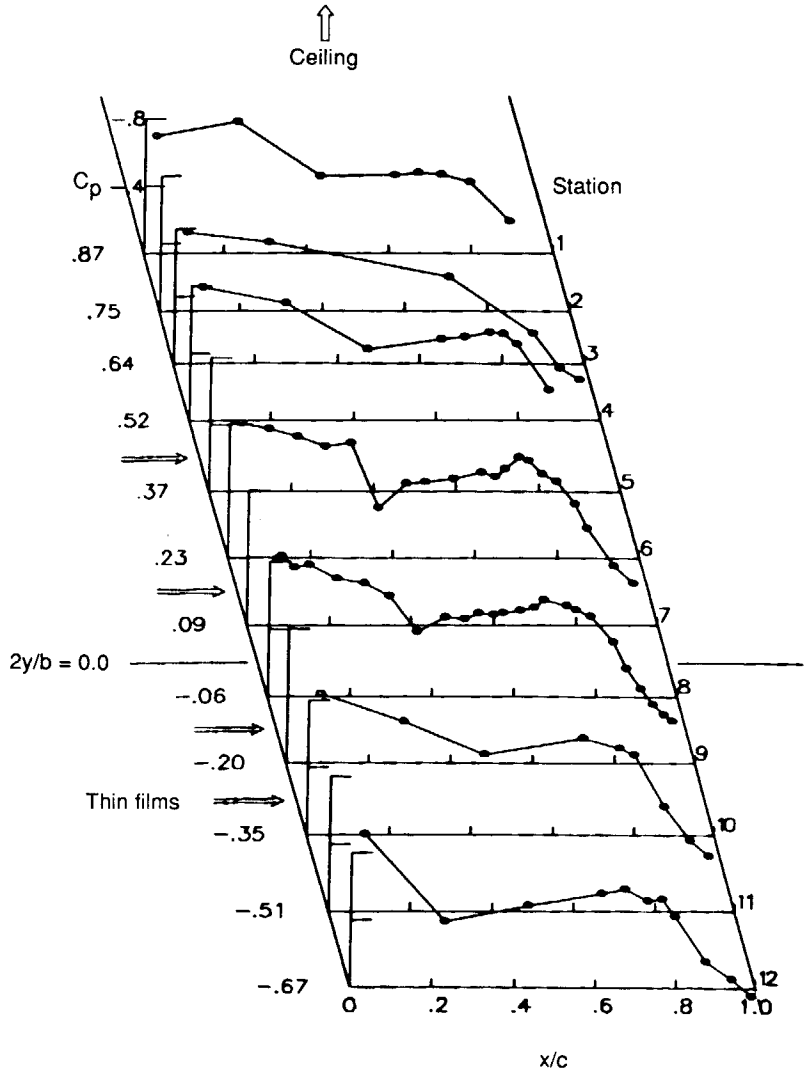

(f) $M_\infty = 0.8134; c_l = 0.467.$

Figure 49. Continued.

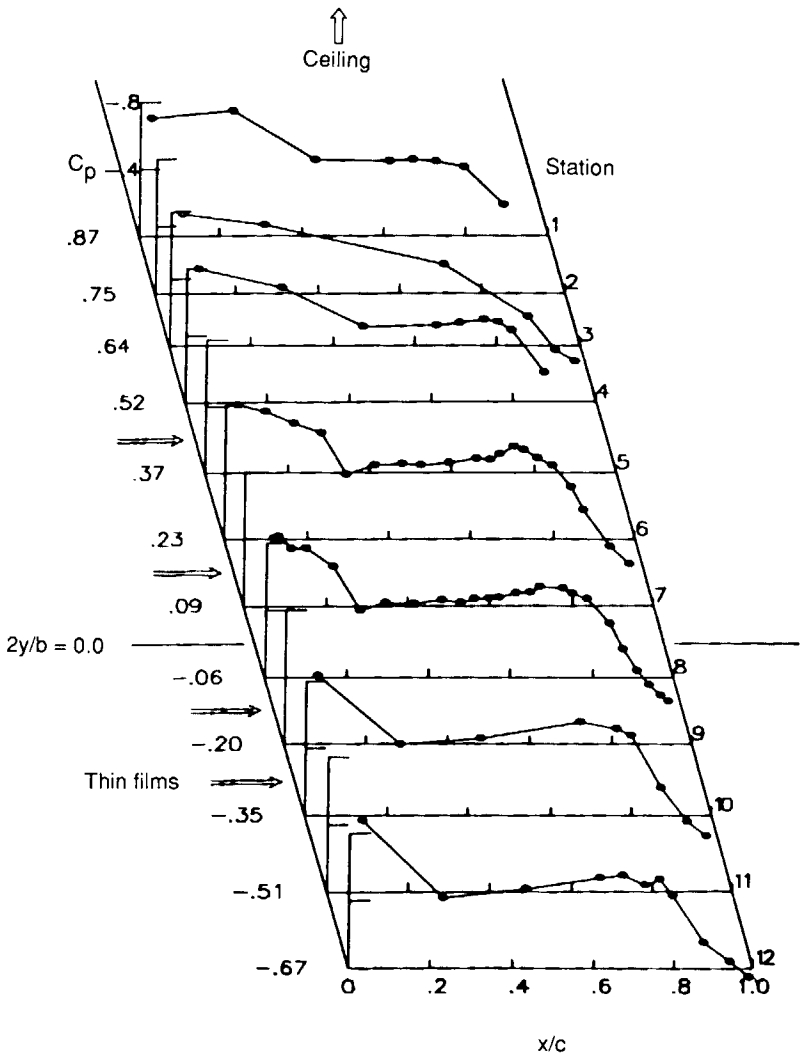

(g) $M_\infty = 0.8102; c_l = 0.434.$

Figure 49. Concluded.

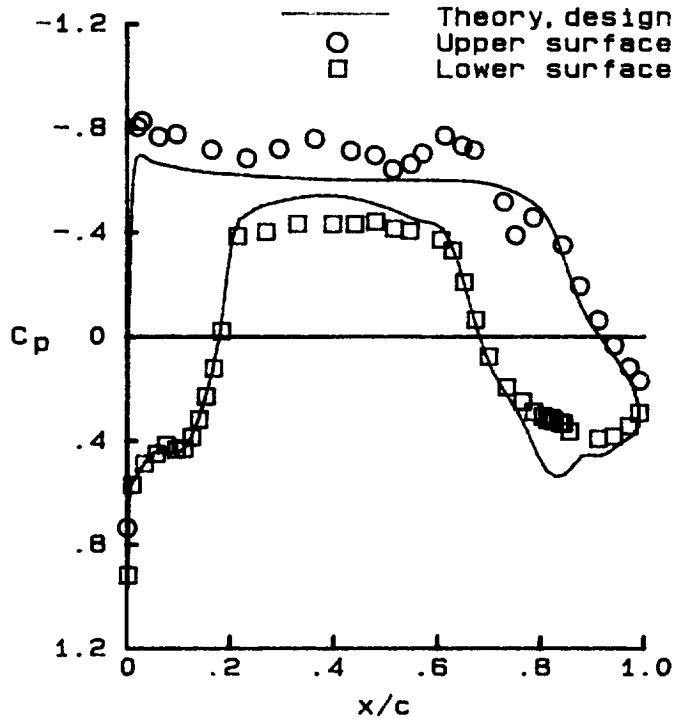

(a) $M_\infty = 0.816; c_l = 0.557.$

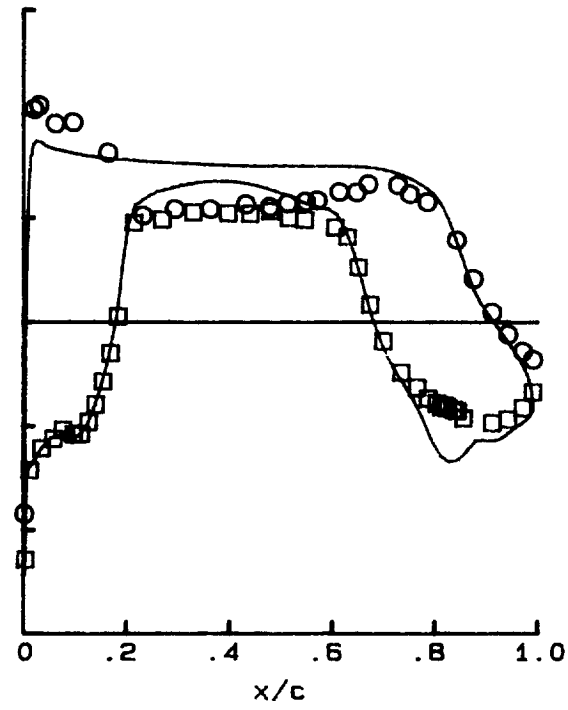

(b) $M_\infty = 0.810; c_l = 0.427.$

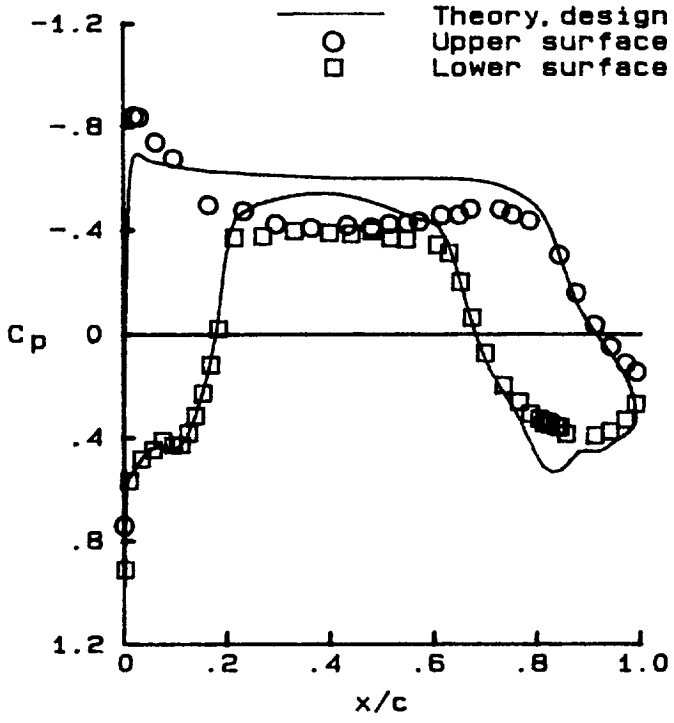

(c) $M_\infty = 0.800; c_l = 0.410.$

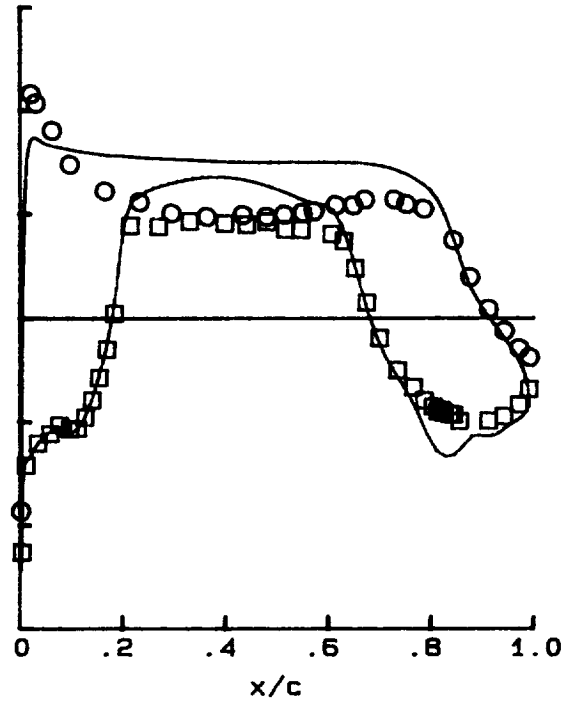

(d) $M_\infty = 0.790; c_l = 0.402.$

Figure 50. Effect on experimental chordwise pressure distribution of varying Mach number over a wide range. Floor area strip no. 1; $\alpha = 0.81°$; $R_c = 10 \times 10^6$; $\delta_t = 2.6°$; $\delta_c = 0.9°$; $\delta_b = 3.5°$.

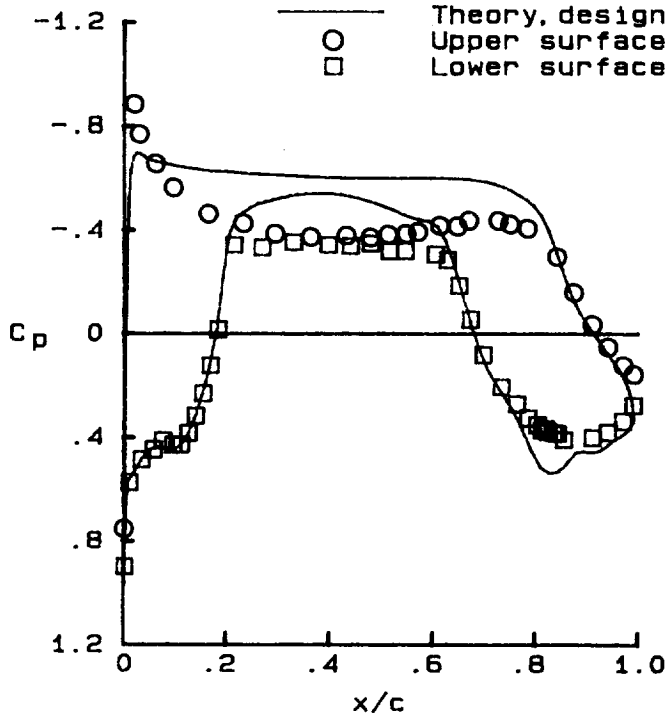

(e) $M_\infty = 0.780; c_l = 0.396.$

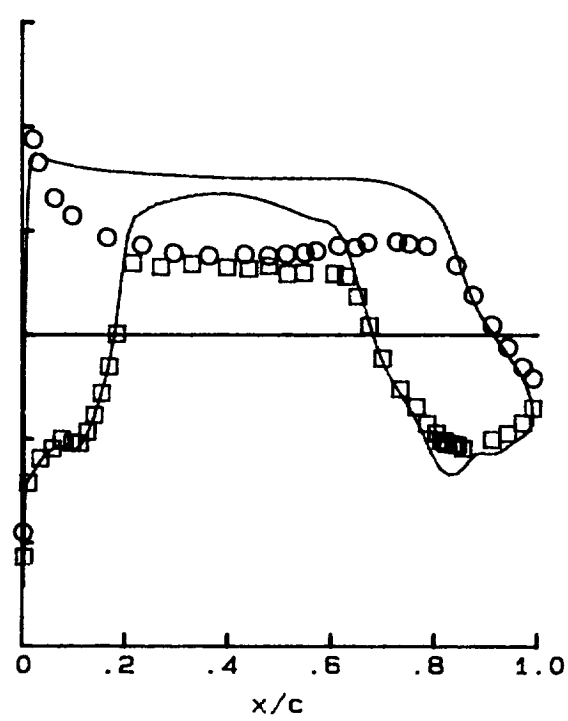

(f) $M_\infty = 0.700; c_l = 0.366.$

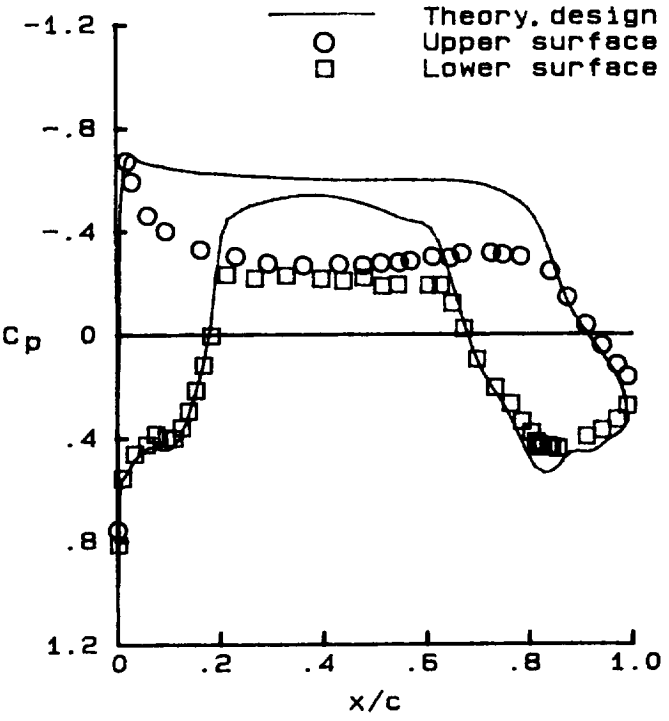

(g) $M_\infty = 0.600; c_l = 0.346.$

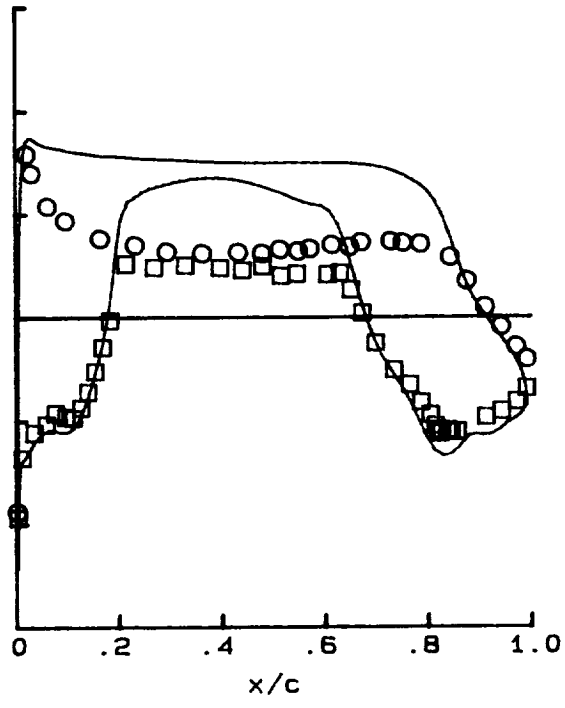

(h) $M_\infty = 0.500; c_l = 0.337.$

Figure 50. Continued.

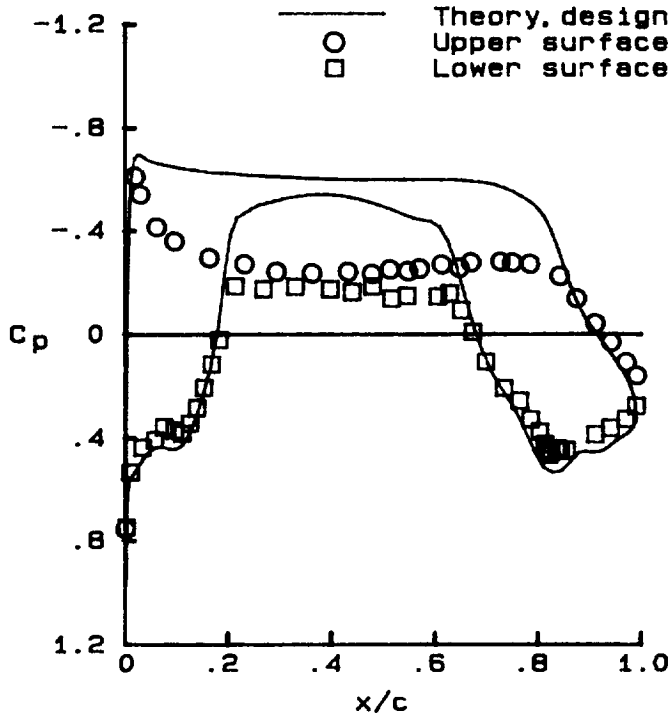

(i) $M_\infty = 0.400; c_l = 0.335$.

Figure 50. Concluded.

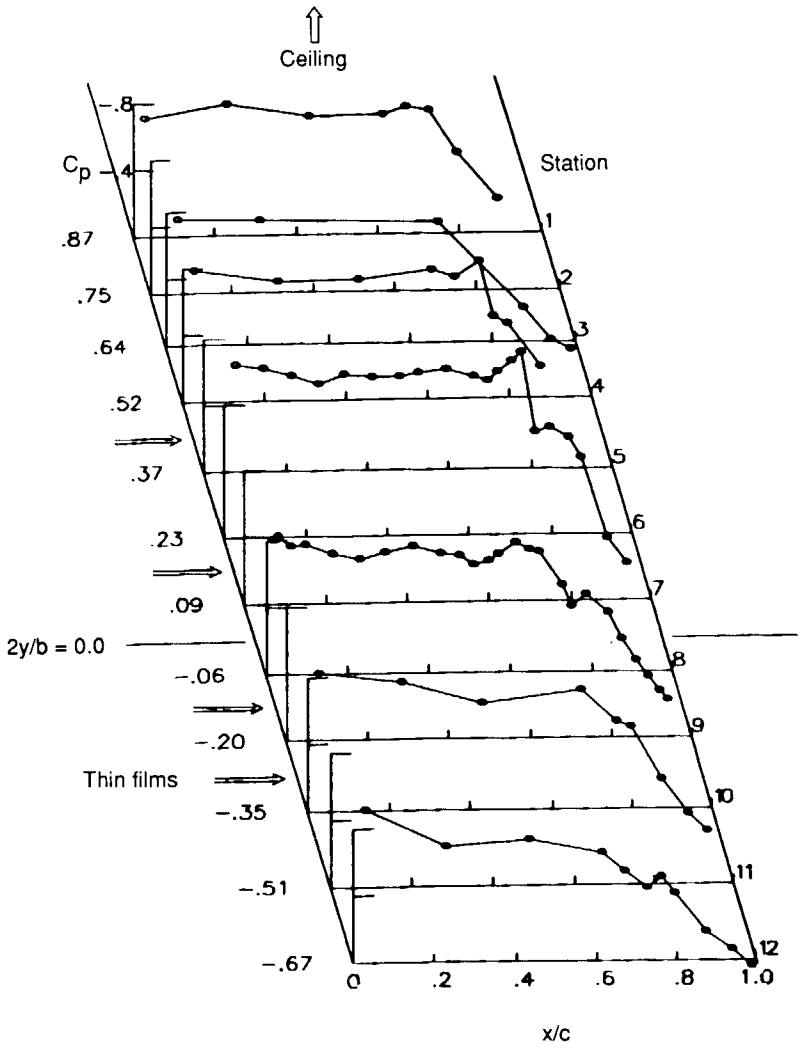

(a) $M_\infty = 0.816; c_l = 0.557$.

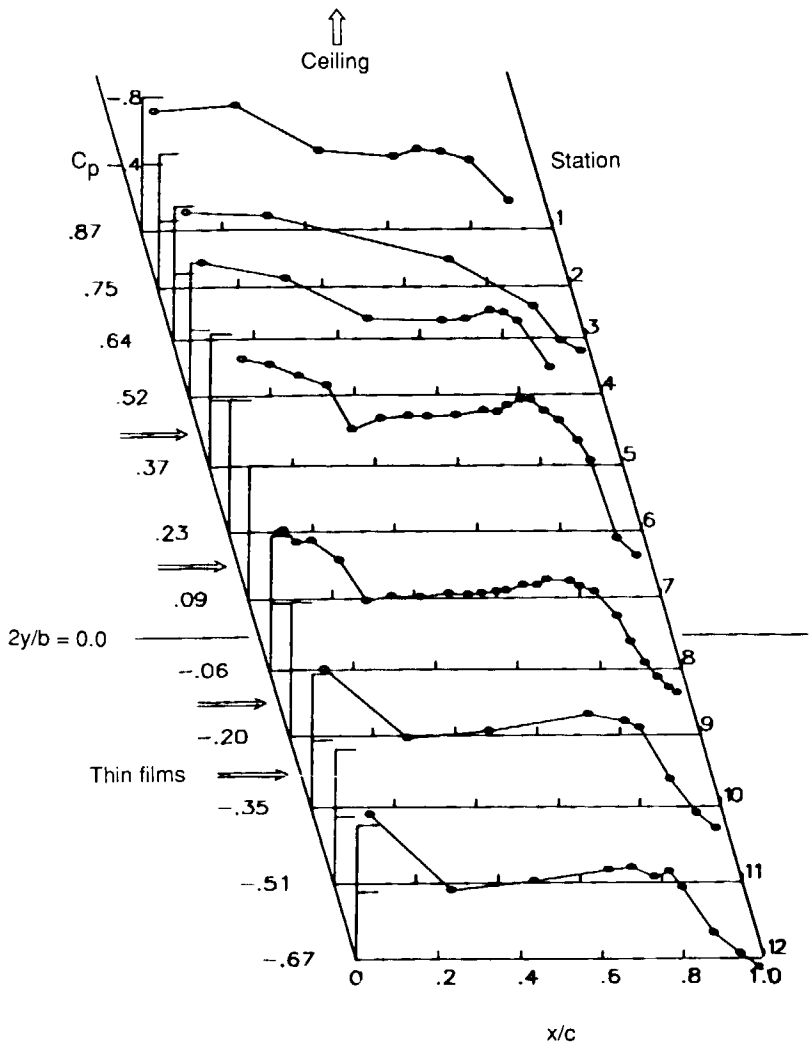

(b) $M_\infty = 0.810; c_l = 0.427$.

Figure 51. Effect on experimental spanwise pressure distribution of varying Mach number over a wide range. Floor area strip no. 1; $\alpha = 0.81°$; $R_c = 10 \times 10^6$; $\delta_t = 2.6°$; $\delta_c = 0.9°$; $\delta_b = 3.5°$.

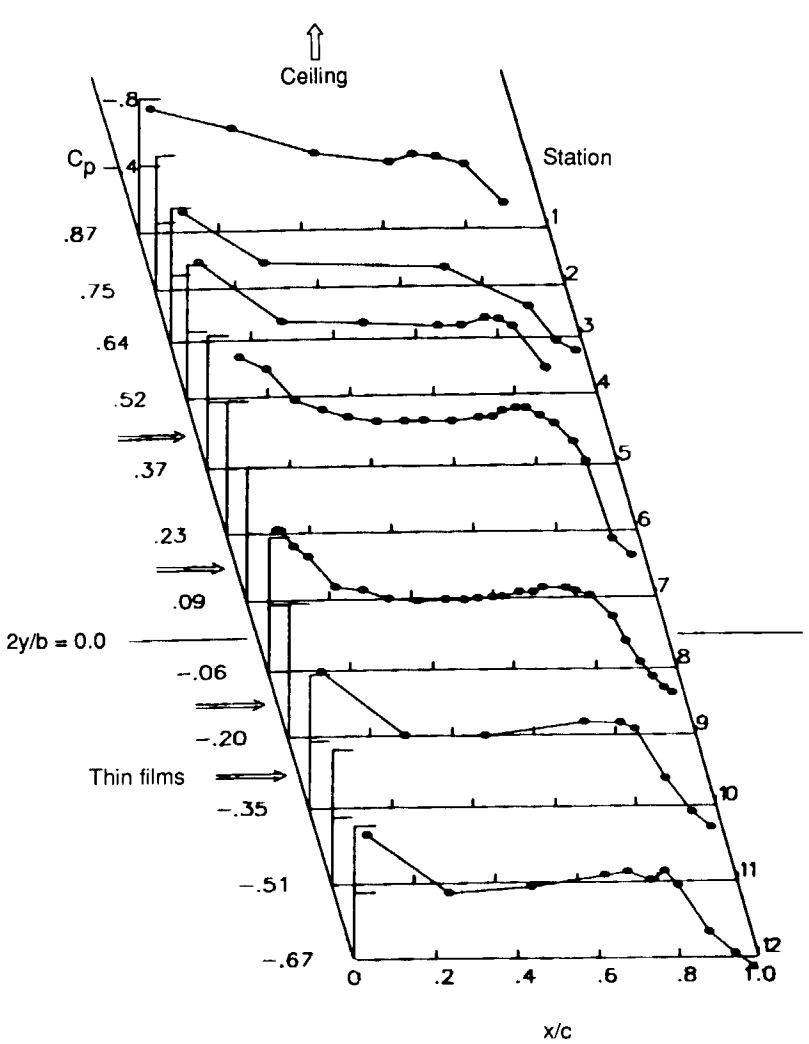

(c) $M_\infty = 0.800; c_l = 0.410.$

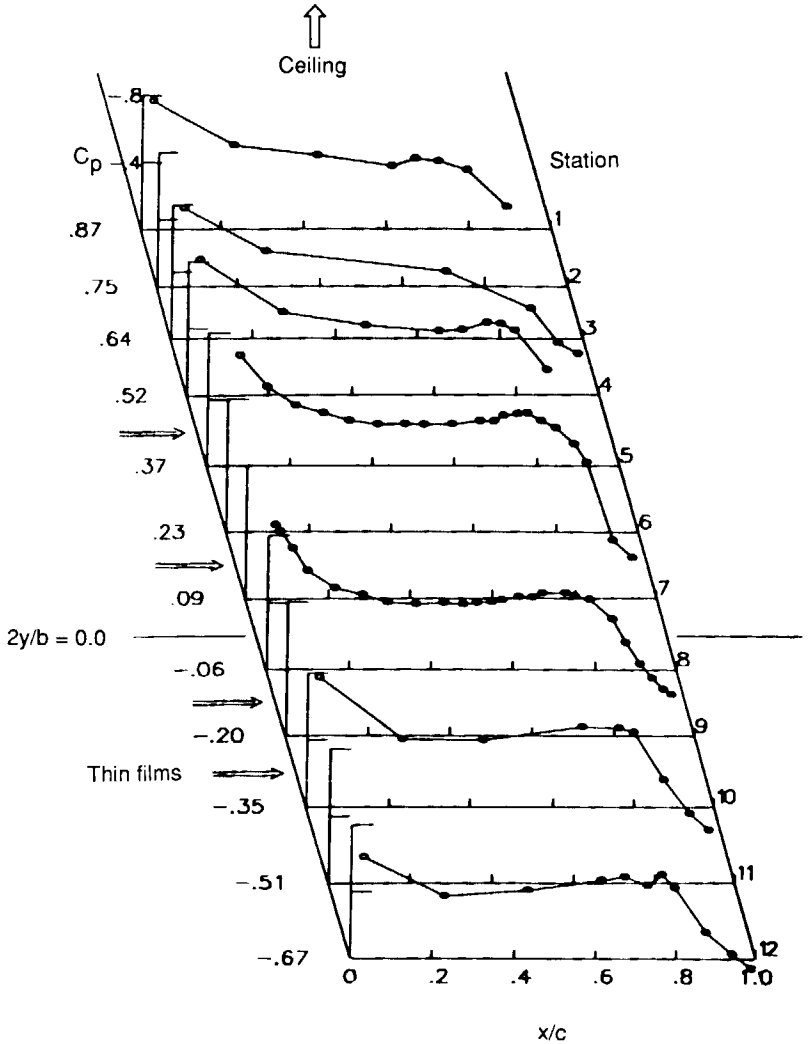

(d) $M_\infty = 0.790; c_l = 0.402.$

Figure 51. Continued.

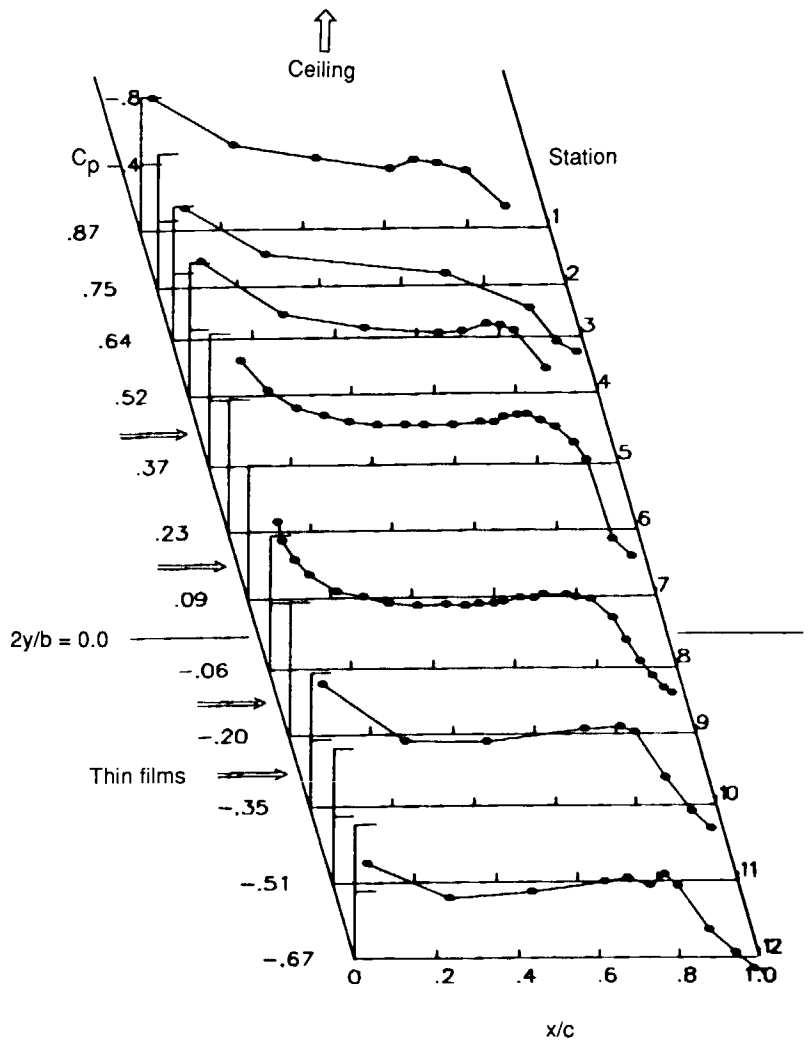

(e) $M_\infty = 0.780; c_l = 0.396.$

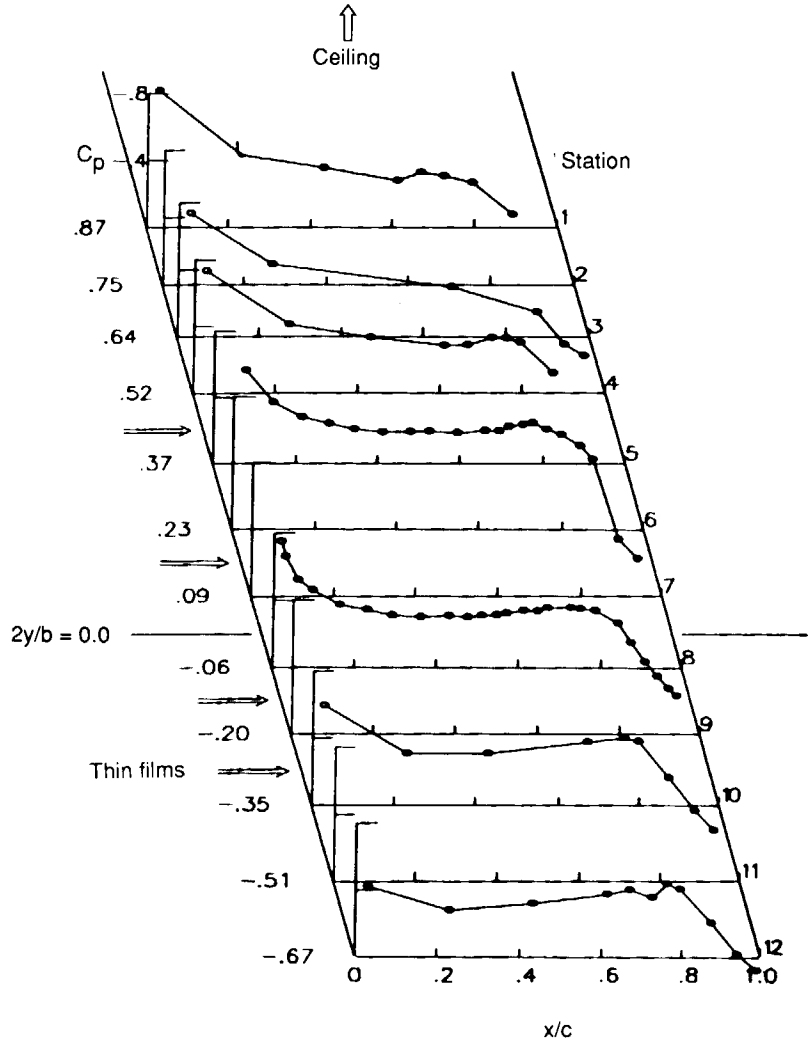

(f) $M_\infty = 0.700; c_l = 0.366.$

Figure 51. Continued.

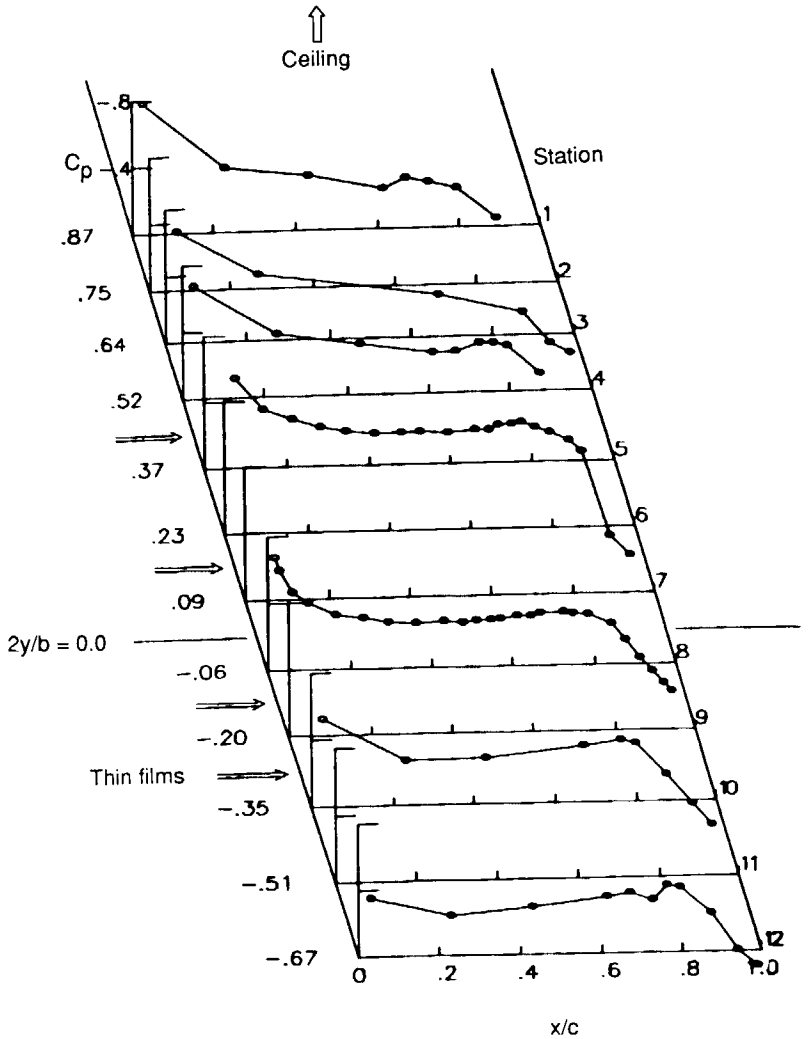

(g) $M_\infty = 0.600; c_l = 0.346$.

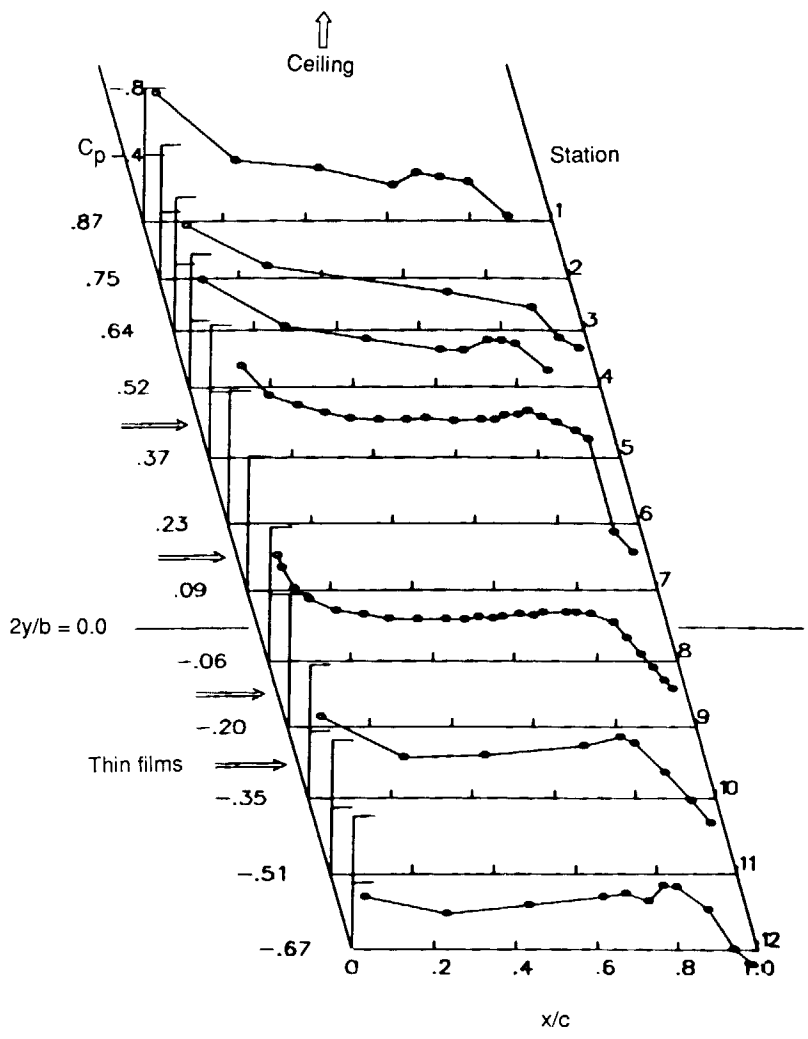

(h) $M_\infty = 0.500; c_l = 0.337$.

Figure 51. Continued.

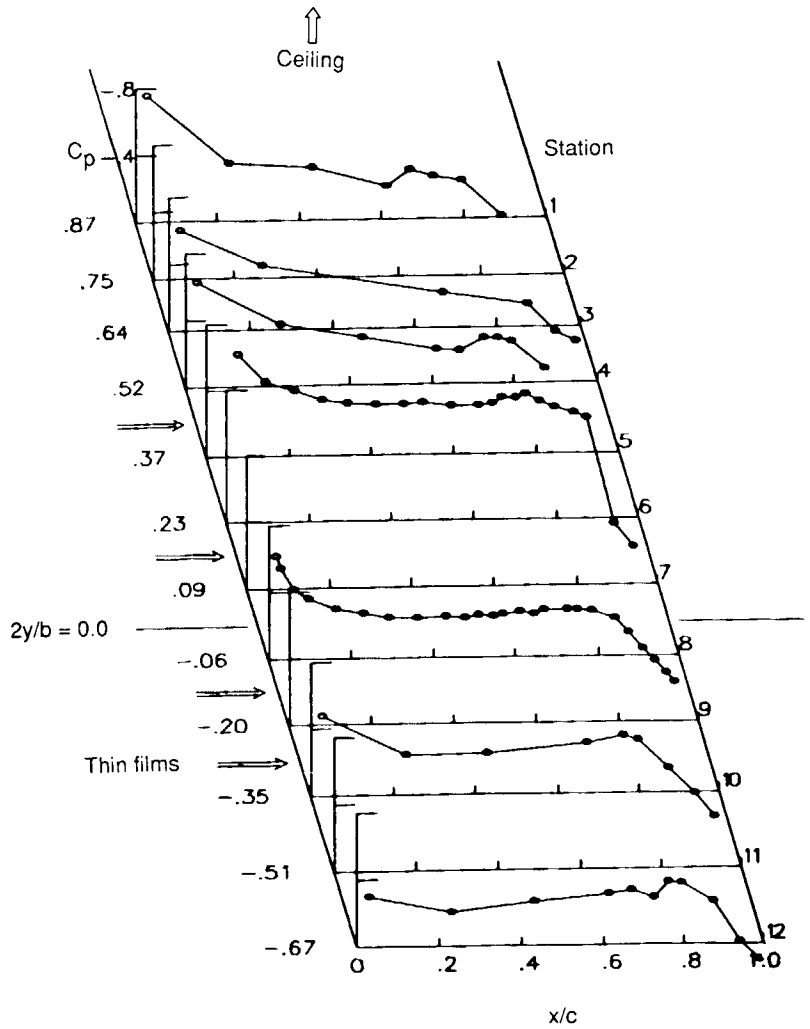

(i) $M_\infty = 0.400; c_l = 0.335$.

Figure 51. Concluded.

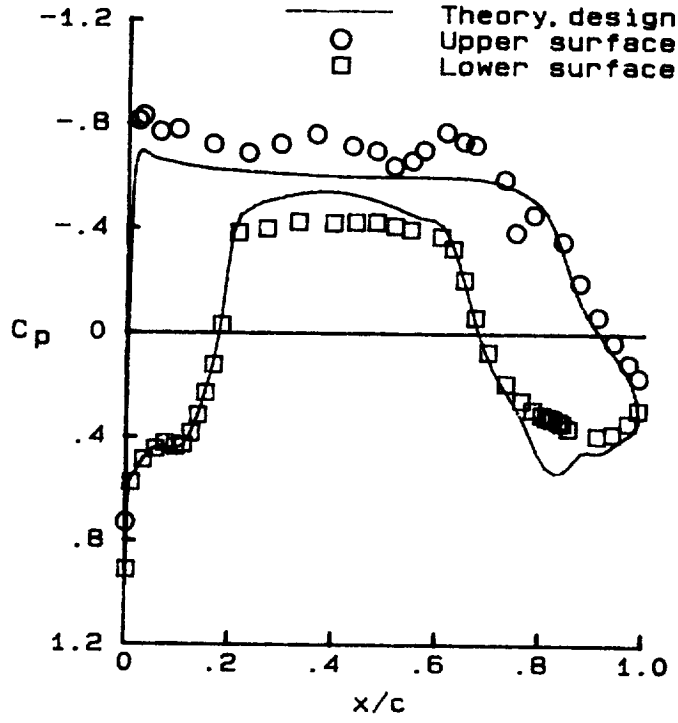

(a) $R_c = 10 \times 10^6$; $M_\infty = 0.8155$; $c_l = 0.568$.

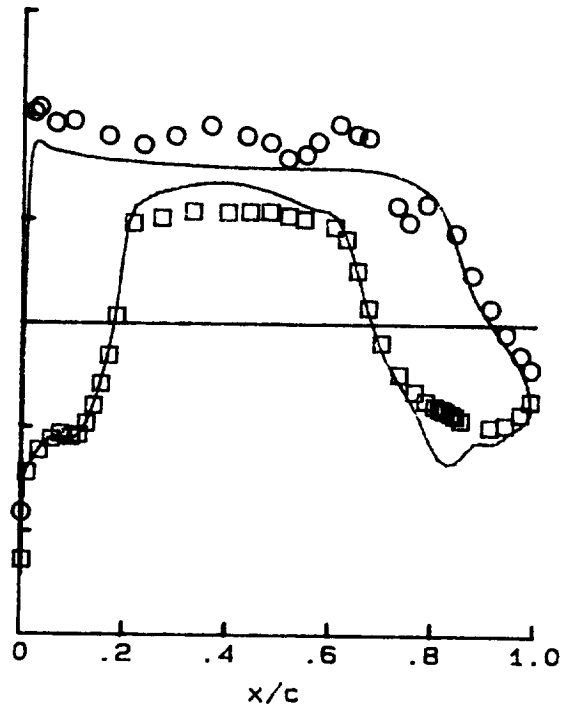

(b) $R_c = 11 \times 10^6$; $M_\infty = 0.8161$; $c_l = 0.559$.

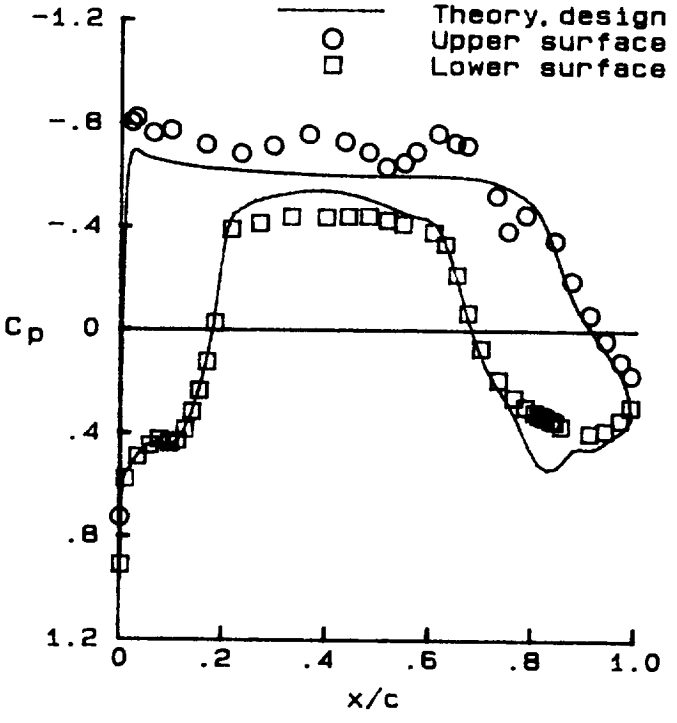

(c) $R_c = 12 \times 10^6$; $M_\infty = 0.8170$; $c_l = 0.554$.

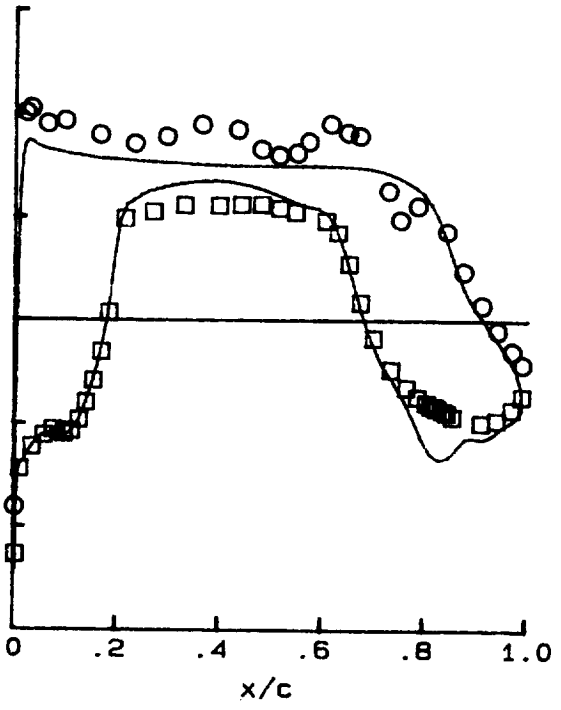

(d) $R_c = 13 \times 10^6$; $M_\infty = 0.8176$; $c_l = 0.548$.

Figure 52. Effect of experimental chordwise pressure distribution of varying Reynolds number near design Mach number. Floor area strip no. 1; $\alpha = 0.81°$; $\delta_t = 2.6°$; $\delta_c = 0.9°$; $\delta_b = 3.5°$.

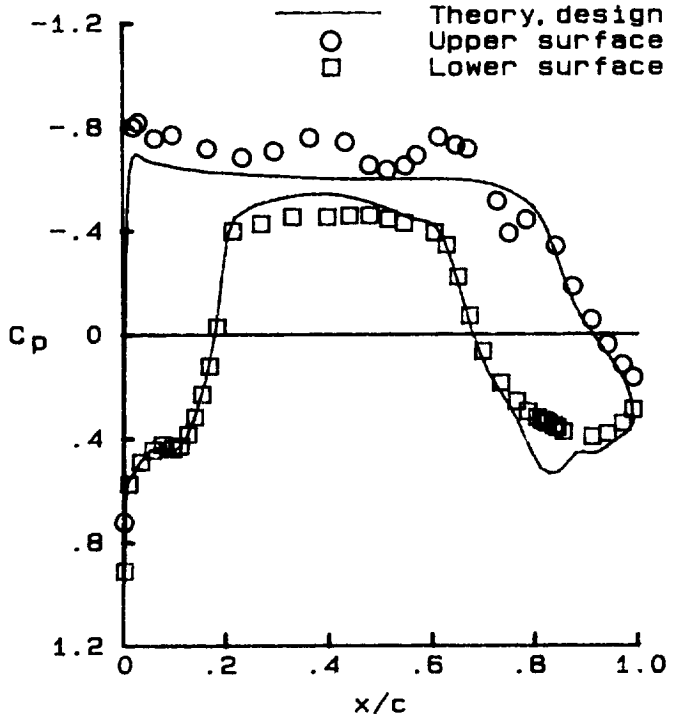

(e) $R_c = 14 \times 10^6$; $M_\infty = 0.8179$; $c_l = 0.543$.

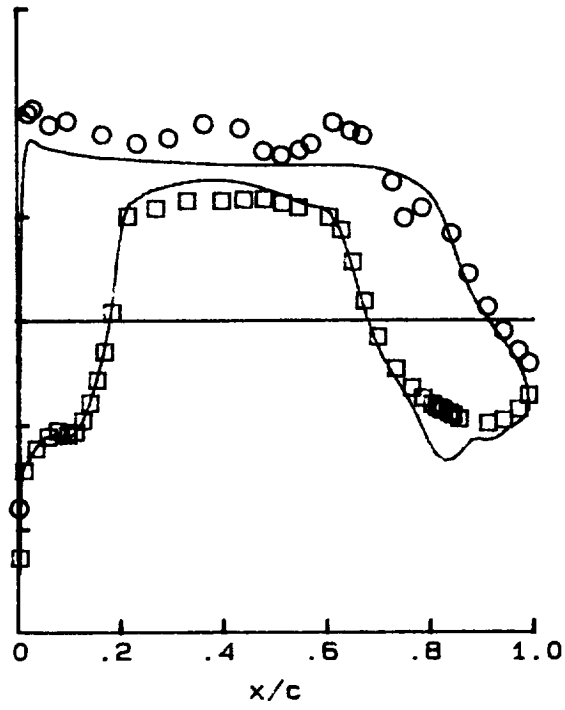

(f) $R_c = 15 \times 10^6$; $M_\infty = 0.8185$; $c_l = 0.538$.

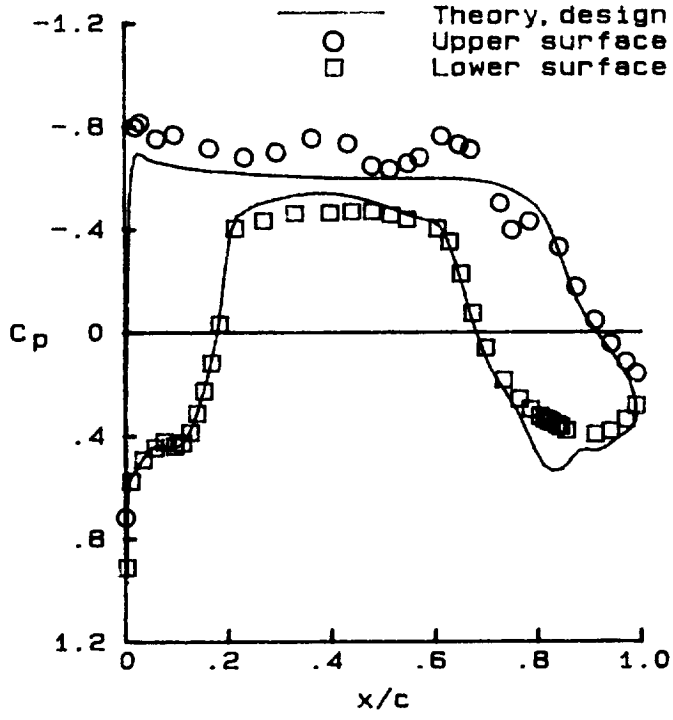

(g) $R_c = 16 \times 10^6$; $M_\infty = 0.8188$; $c_l = 0.535$.

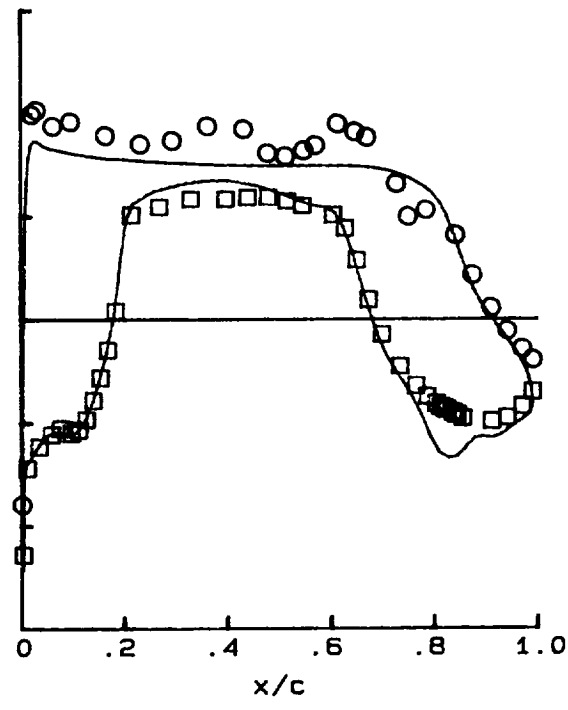

(h) $R_c = 17 \times 10^6$; $M_\infty = 0.8189$; $c_l = 0.533$.

Figure 52. Continued.

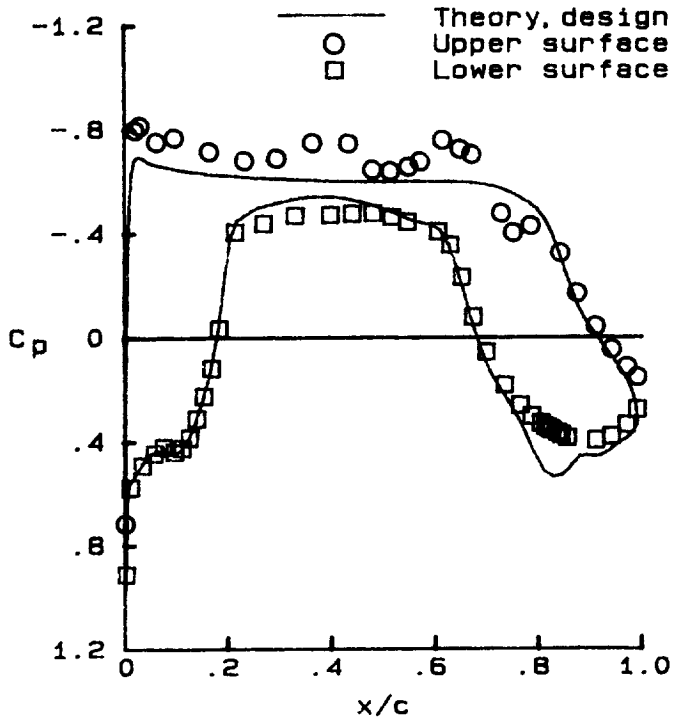

(i) $R_c = 18 \times 10^6$; $M_\infty = 0.8192$; $c_l = 0.529$.

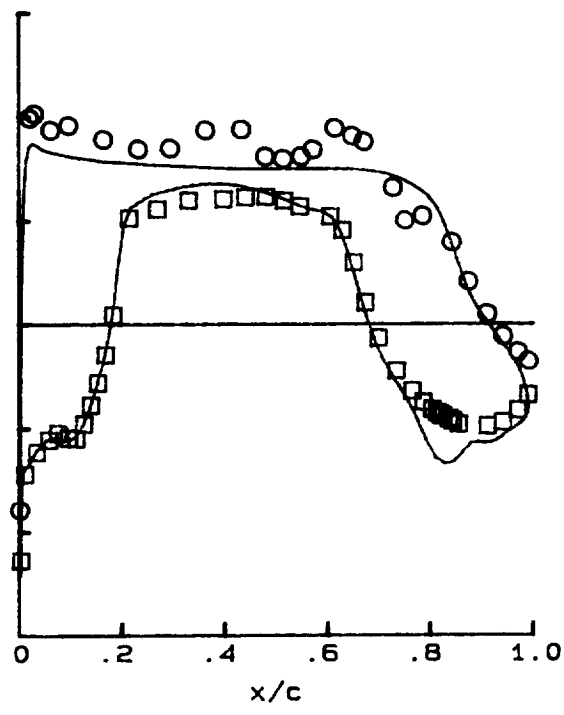

(j) $R_c = 19 \times 10^6$; $M_\infty = 0.8196$; $c_l = 0.523$.

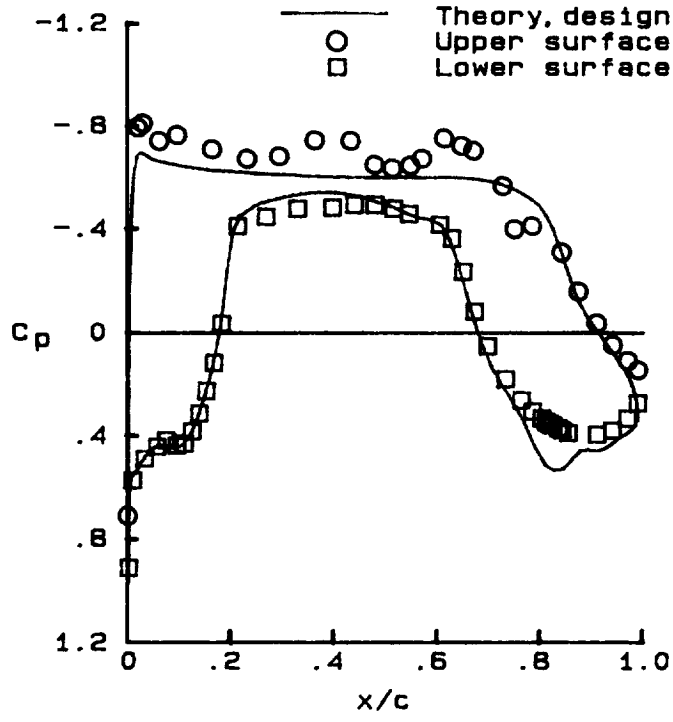

(k) $R_c = 20 \times 10^6$; $M_\infty = 0.8198$; $c_l = 0.523$.

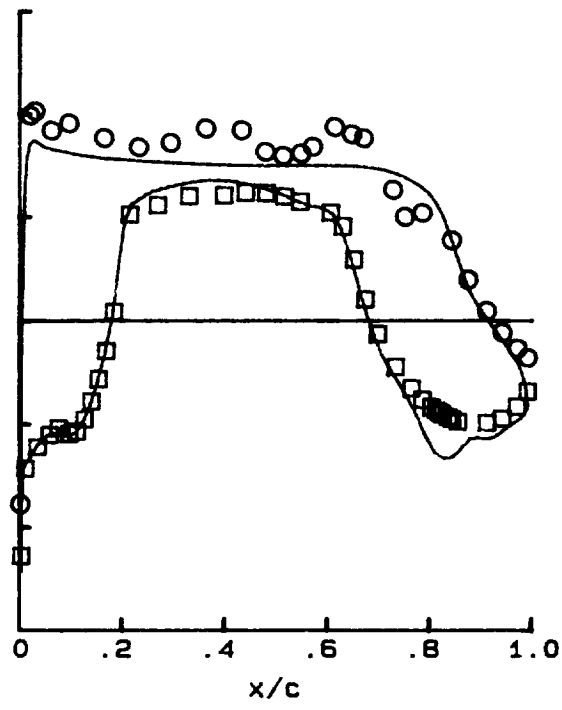

(l) $R_c = 21 \times 10^6$; $M_\infty = 0.8197$; $c_l = 0.520$.

Figure 52. Continued.

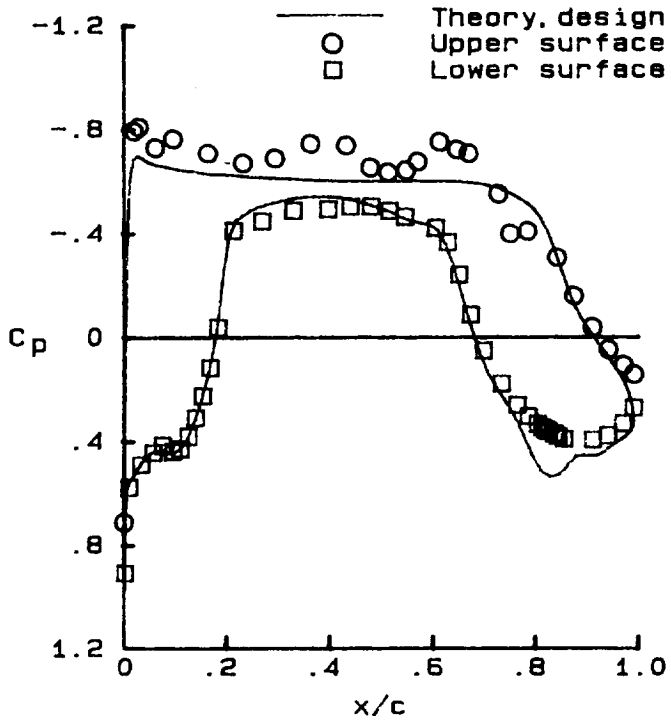

(m) $R_c = 22 \times 10^6$; $M_\infty = 0.8201$; $c_l = 0.517$.

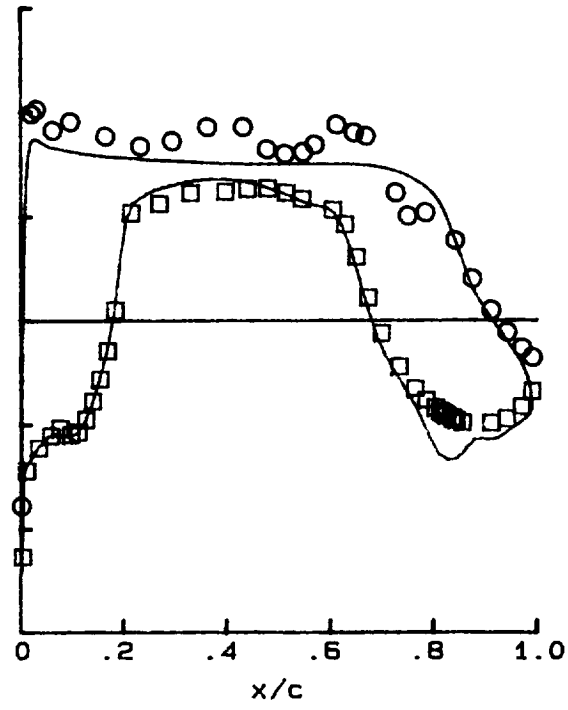

(n) $R_c = 23 \times 10^6$; $M_\infty = 0.8200$; $c_l = 0.514$.

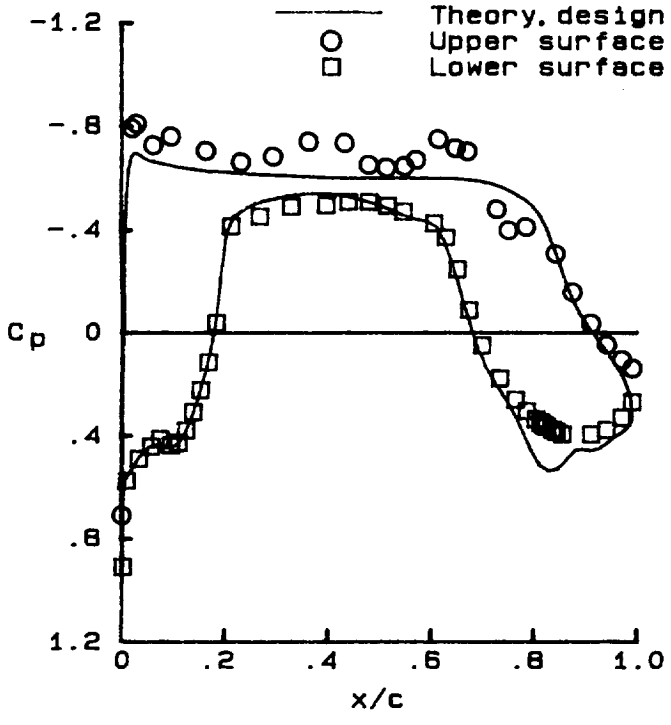

(o) $R_c = 24 \times 10^6$; $M_\infty = 0.8203$; $c_l = 0.510$.

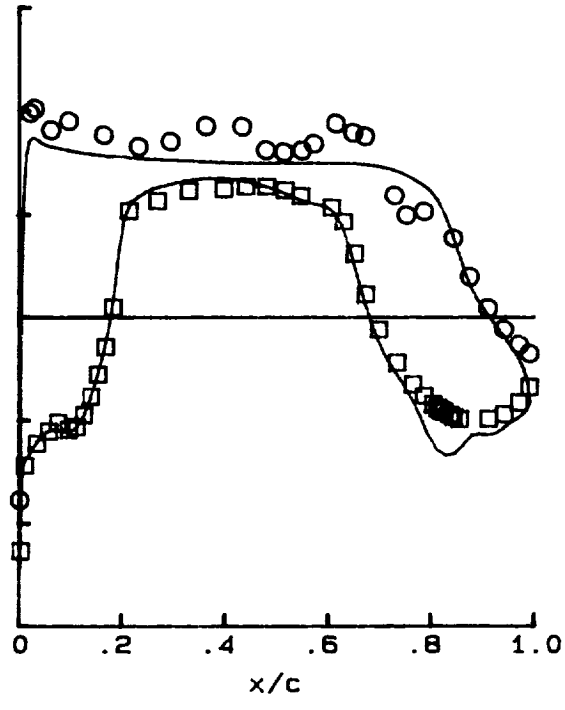

(p) $R_c = 25 \times 10^6$; $M_\infty = 0.8202$; $c_l = 0.511$.

Figure 52. Concluded.

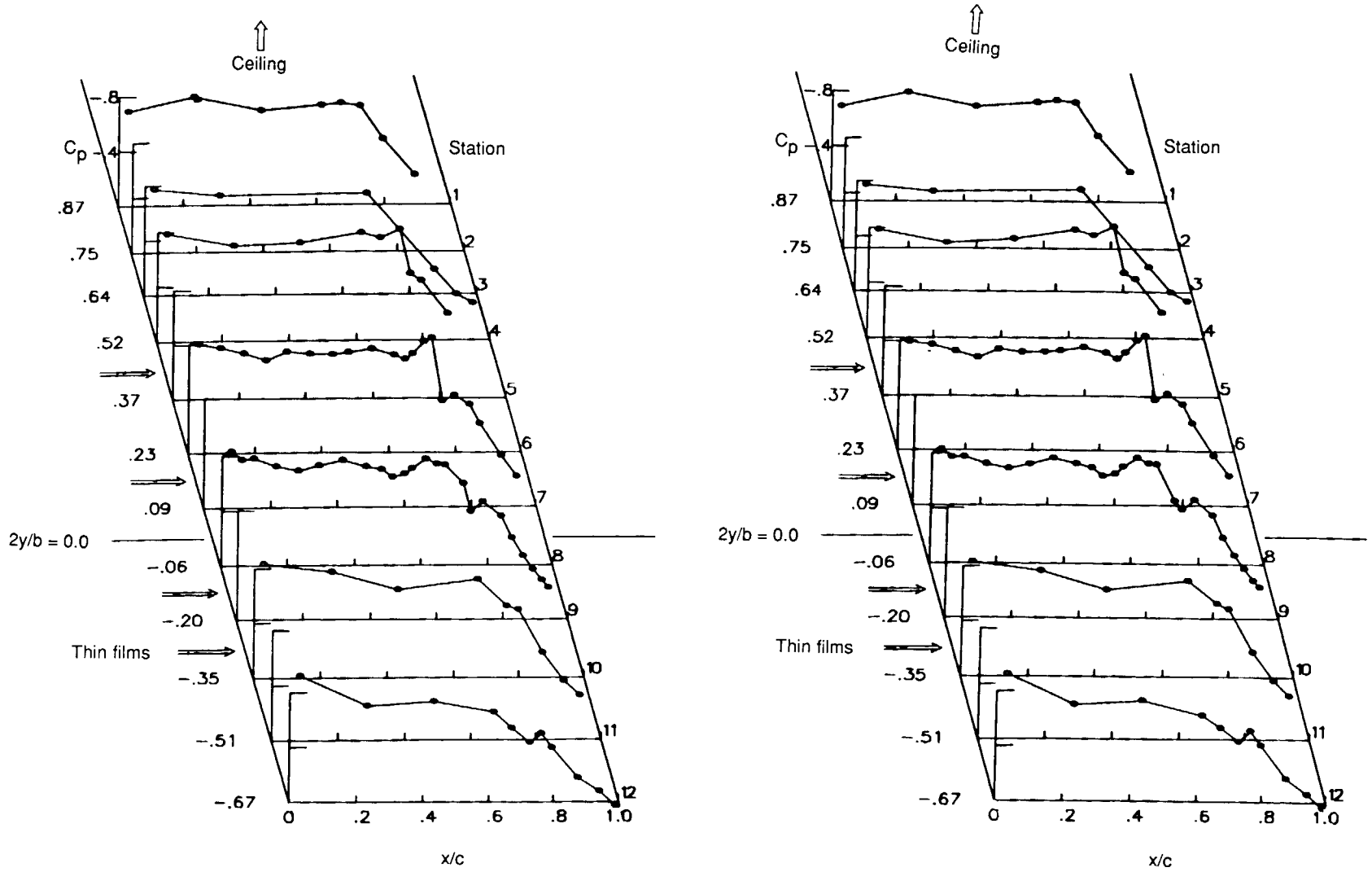

(a) $R_c = 10 \times 10^6; M_\infty = 0.8155; c_l = 0.586.$

(b) $R_c = 11 \times 10^6; M_\infty = 0.8161; c_l = 0.559.$

Figure 53. Effect of experimental spanwise pressure distribution of varying Reynolds number near design Mach number. Floor area strip no. 1; $\alpha - 0.81°; \delta_t - 2.6°; \delta_c = 0.9°; \delta_b = 3.5°$.

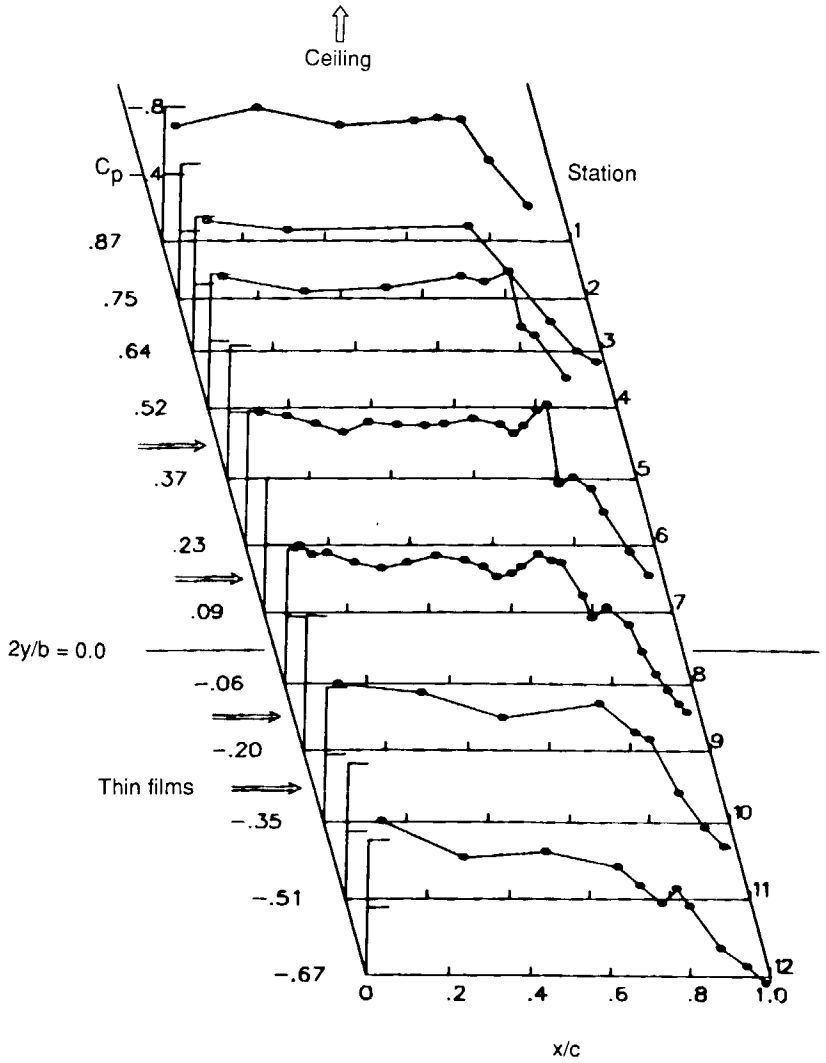

(c) $R_c = 12 \times 10^6; M_\infty = 0.8170; c_l = 0.554.$

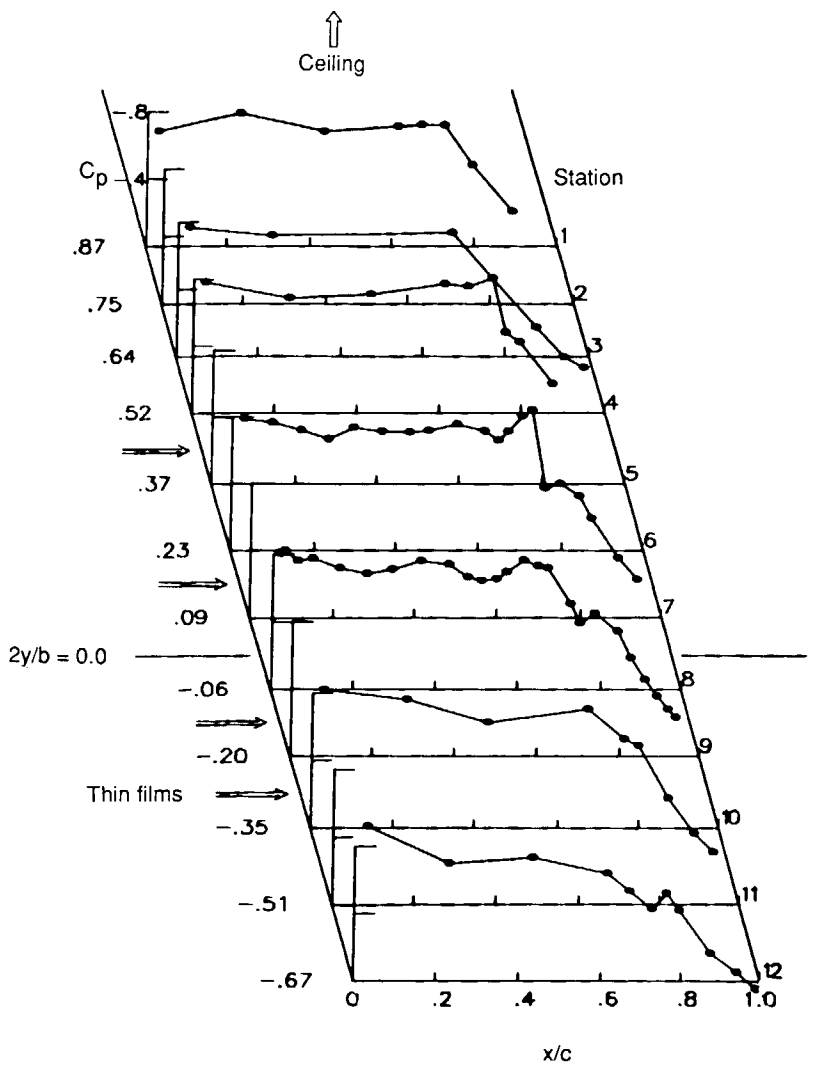

(d) $R_c = 13 \times 10^6; M_\infty = 0.8176; c_l = 0.548.$

Figure 53. Continued.

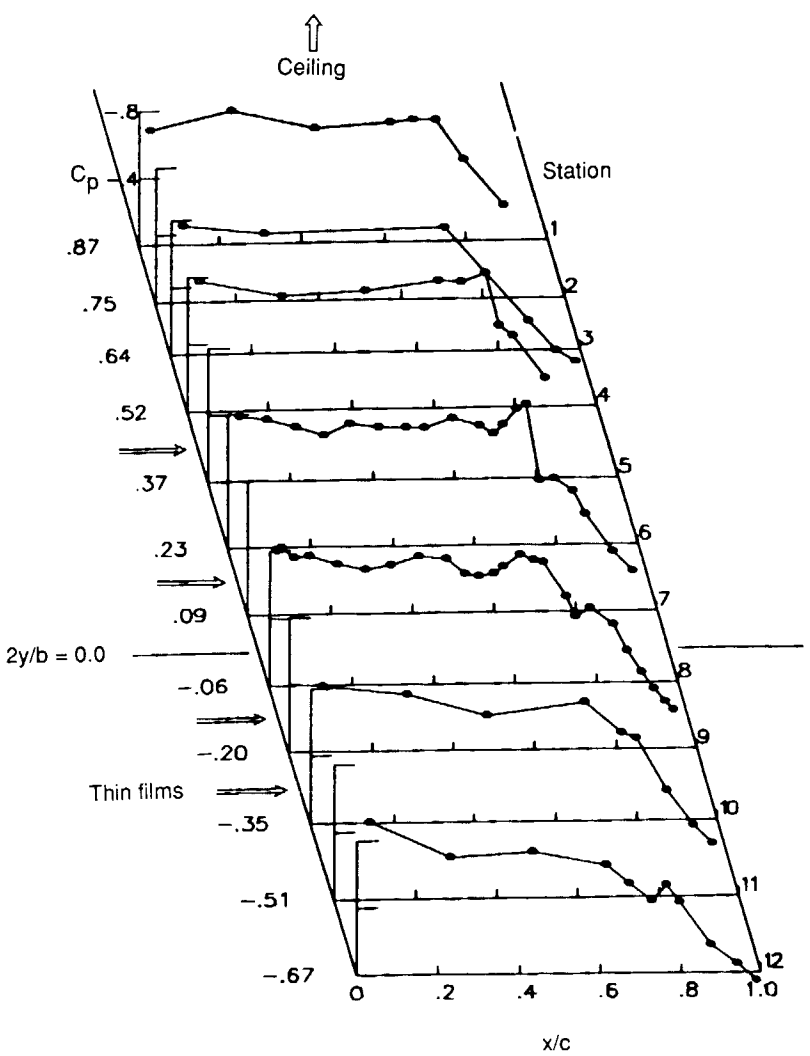

(e) $R_c = 14 \times 10^6; M_\infty = 0.8179; c_l = 0.543.$

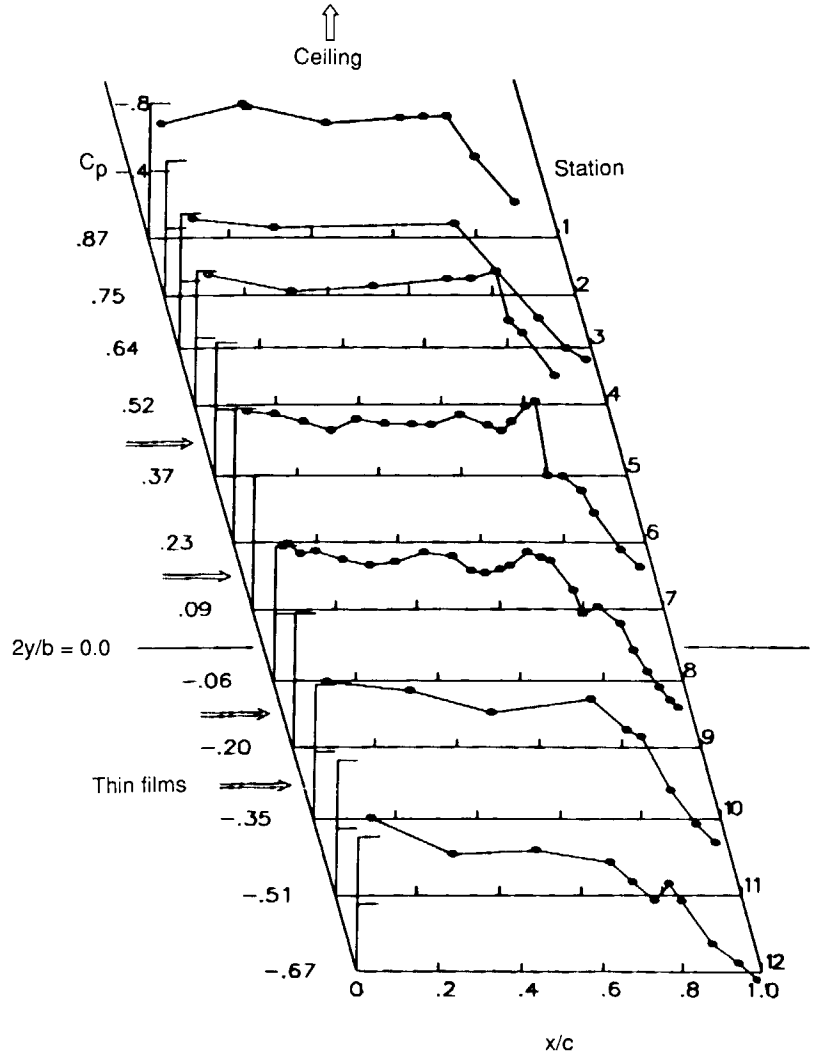

(f) $R_c = 15 \times 10^6; M_\infty = 0.8185; c_l = 0.538.$

Figure 53. Continued.

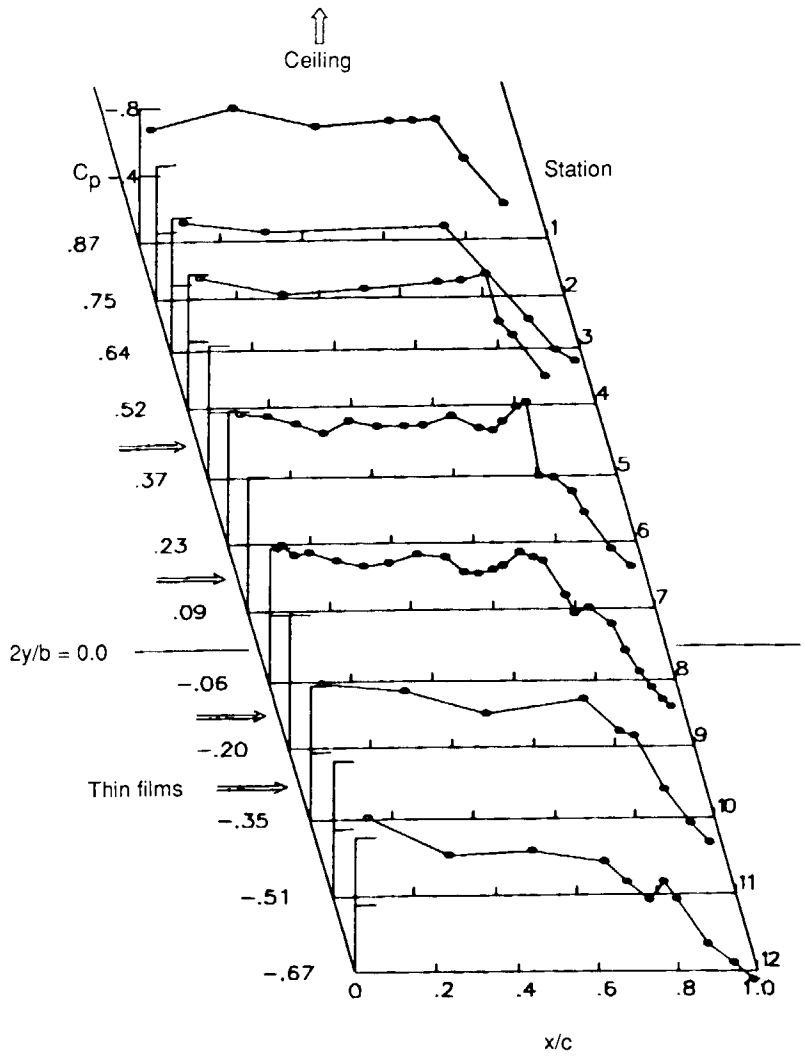

(g) $R_c = 16 \times 10^6$; $M_\infty = 0.8188$; $c_l = 0.535$.

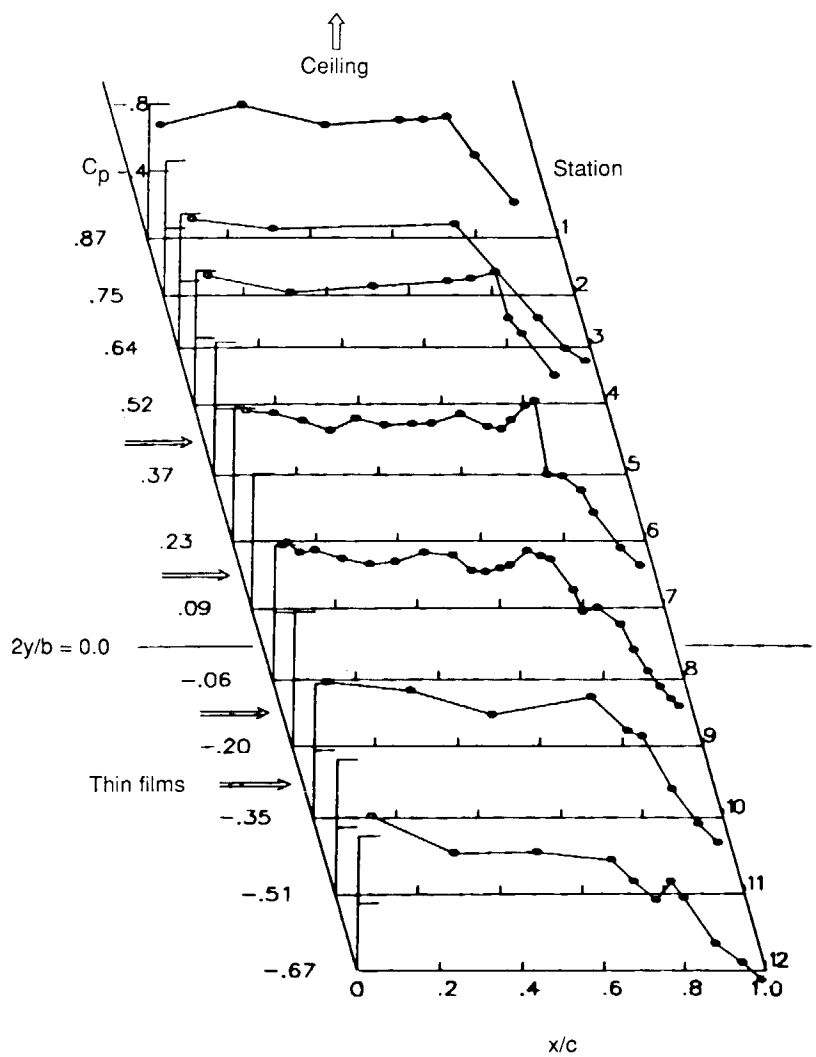

(h) $R_c = 17 \times 10^6$; $M_\infty = 0.8189$; $c_l = 0.533$.

Figure 53. Continued.

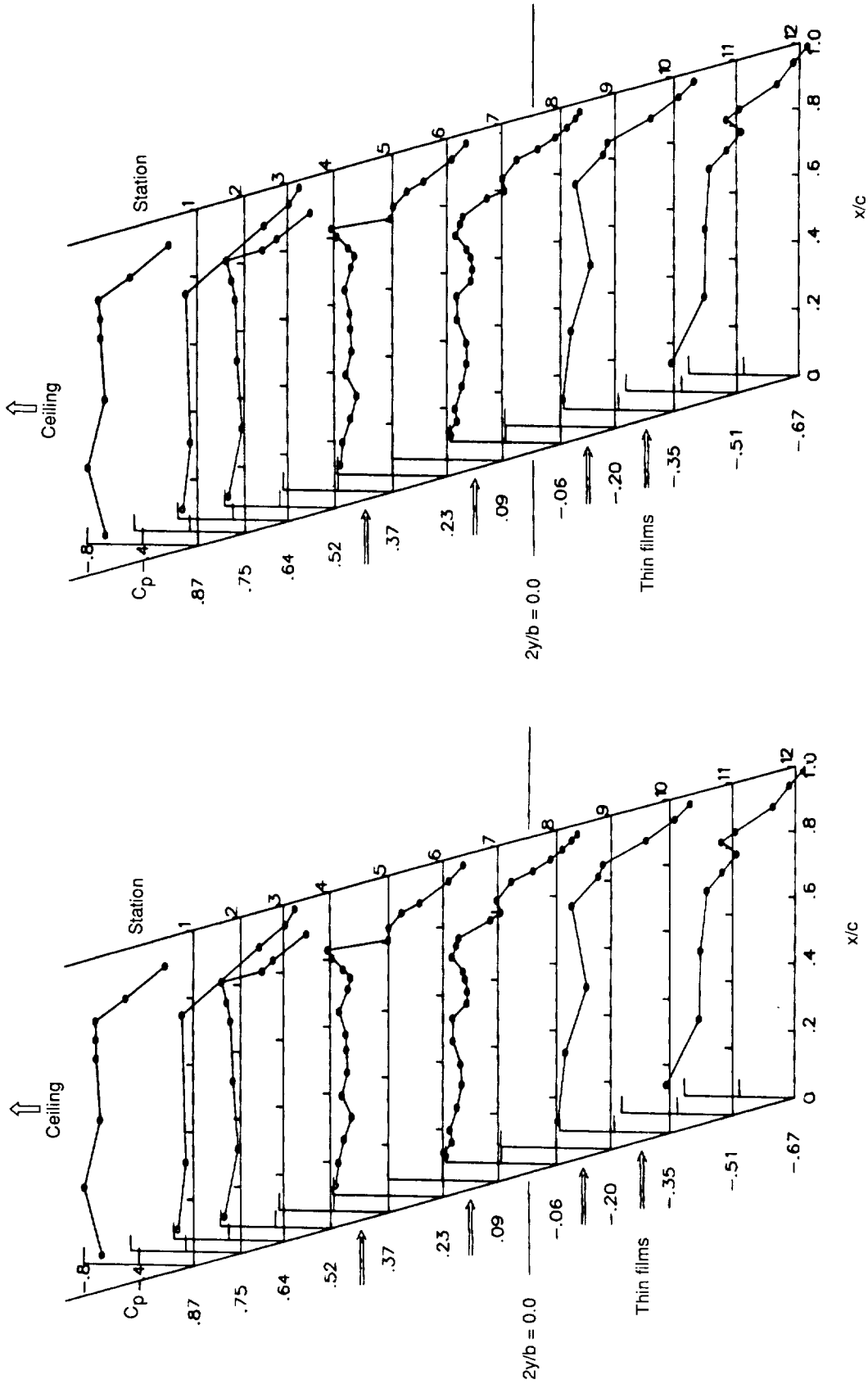

(i) $R_c = 18 \times 10^6$; $M_\infty = 0.8192$; $c_l = 0.529$.

(j) $R_c = 19 \times 10^6$; $M_\infty = 0.8196$; $c_l = 0.523$.

Figure 53. Continued.

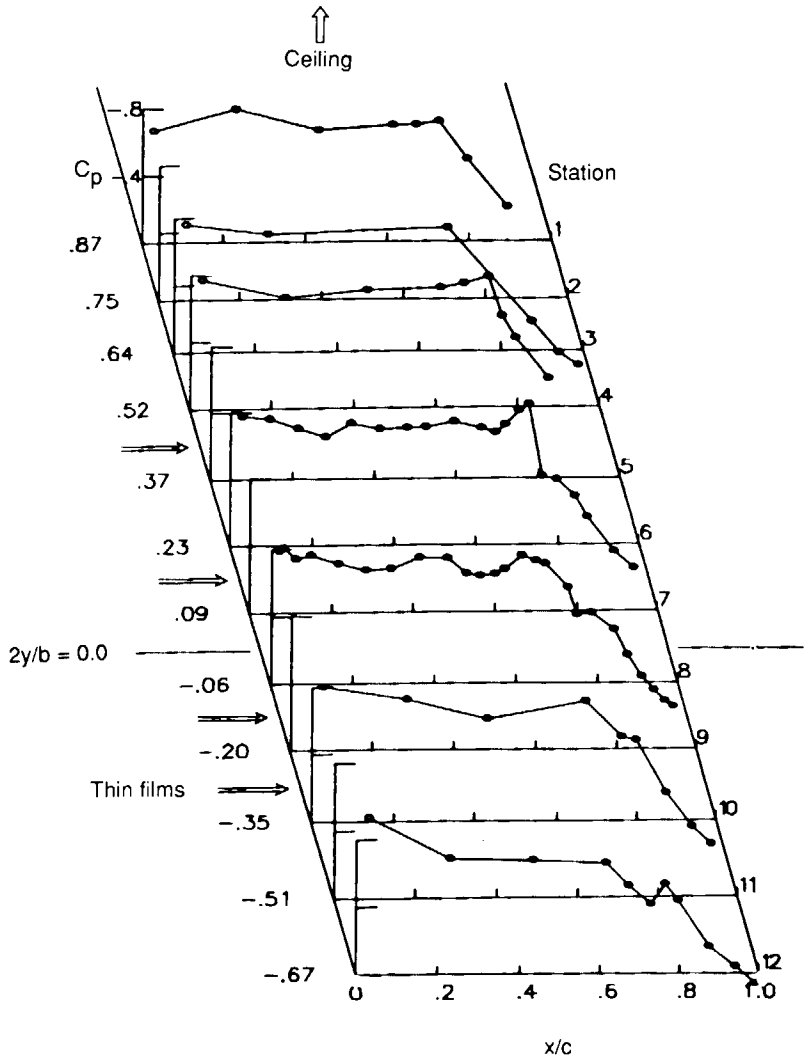

(k) $R_c = 20 \times 10^6$; $M_\infty = 0.8198$; $c_l = 0.523$.

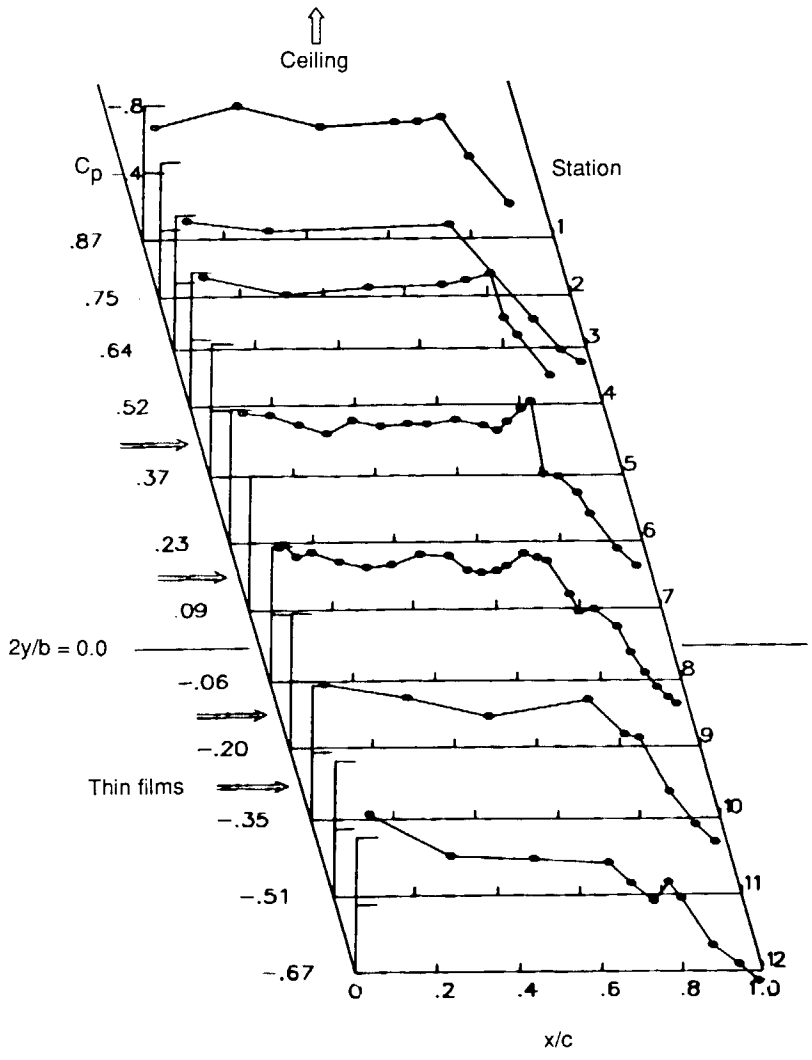

(l) $R_c = 21 \times 10^6$; $M_\infty = 0.8197$; $c_l = 0.520$.

Figure 53. Continued.

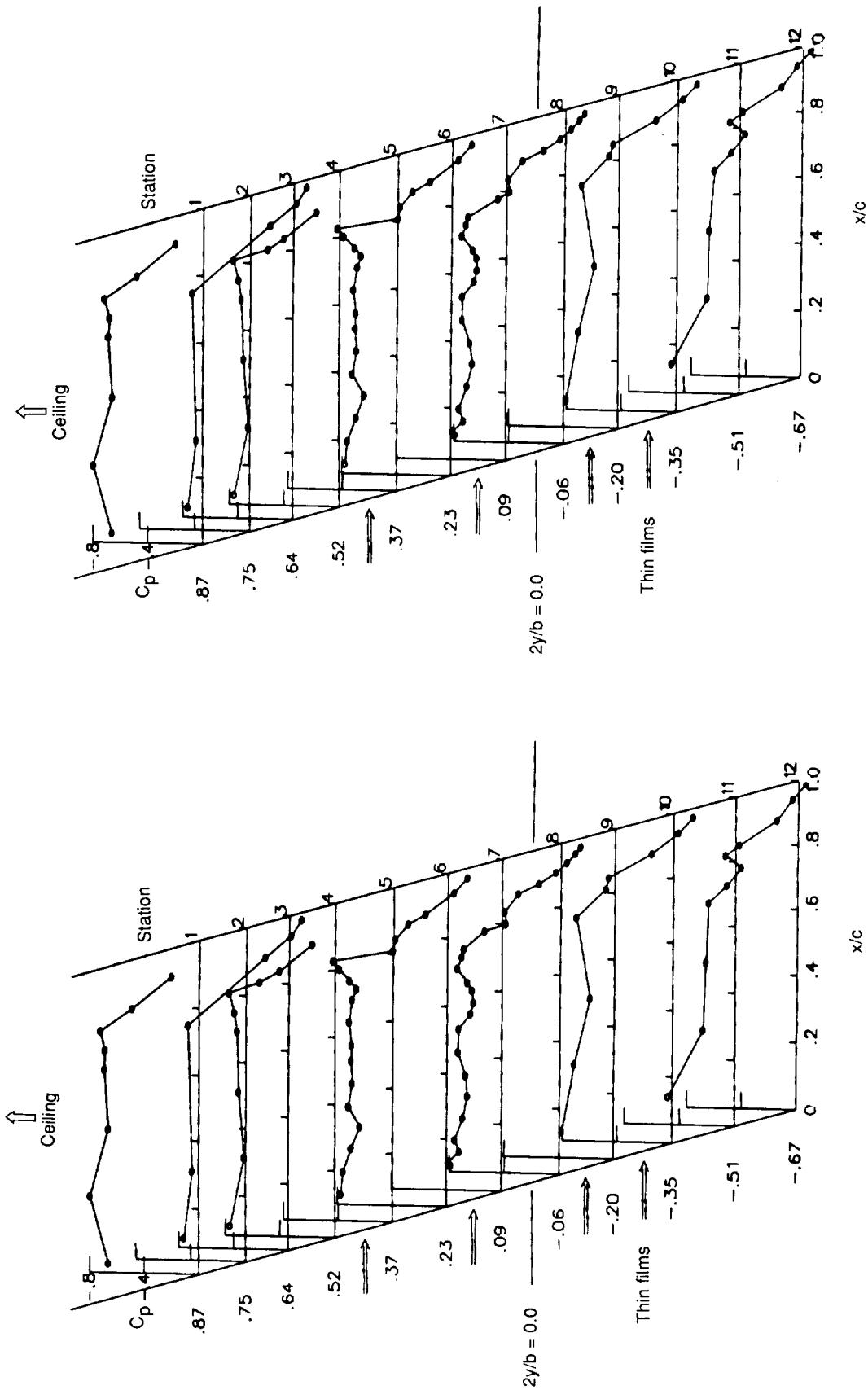

(m) $R_c = 22 \times 10^6$; $M_\infty = 0.8201$; $c_l = 0.517$.

(n) $R_c = 23 \times 10^6$; $M_\infty = 0.8200$; $c_l = 0.514$.

Figure 53. Continued.

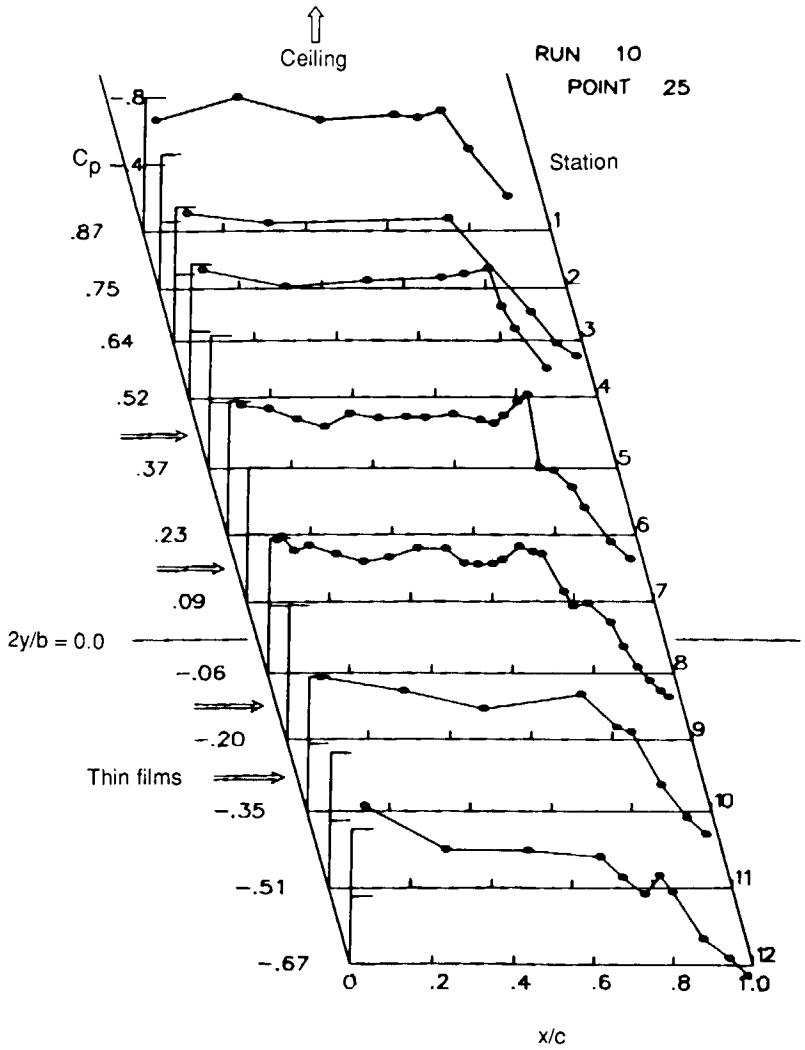

(o) $R_c = 24 \times 10^6; M_\infty = 0.8203; c_l = 0.510.$

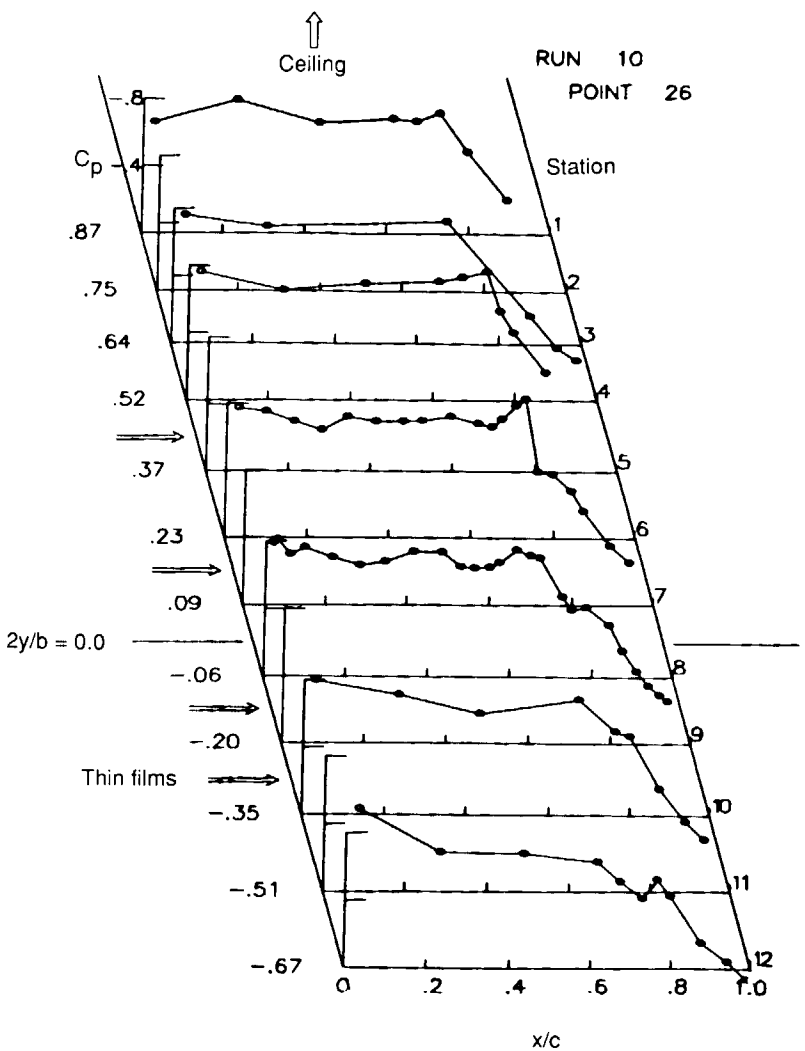

(p) $R_c = 25 \times 10^6; M_\infty = 0.8202; c_l = 0.511.$

Figure 53. Concluded.

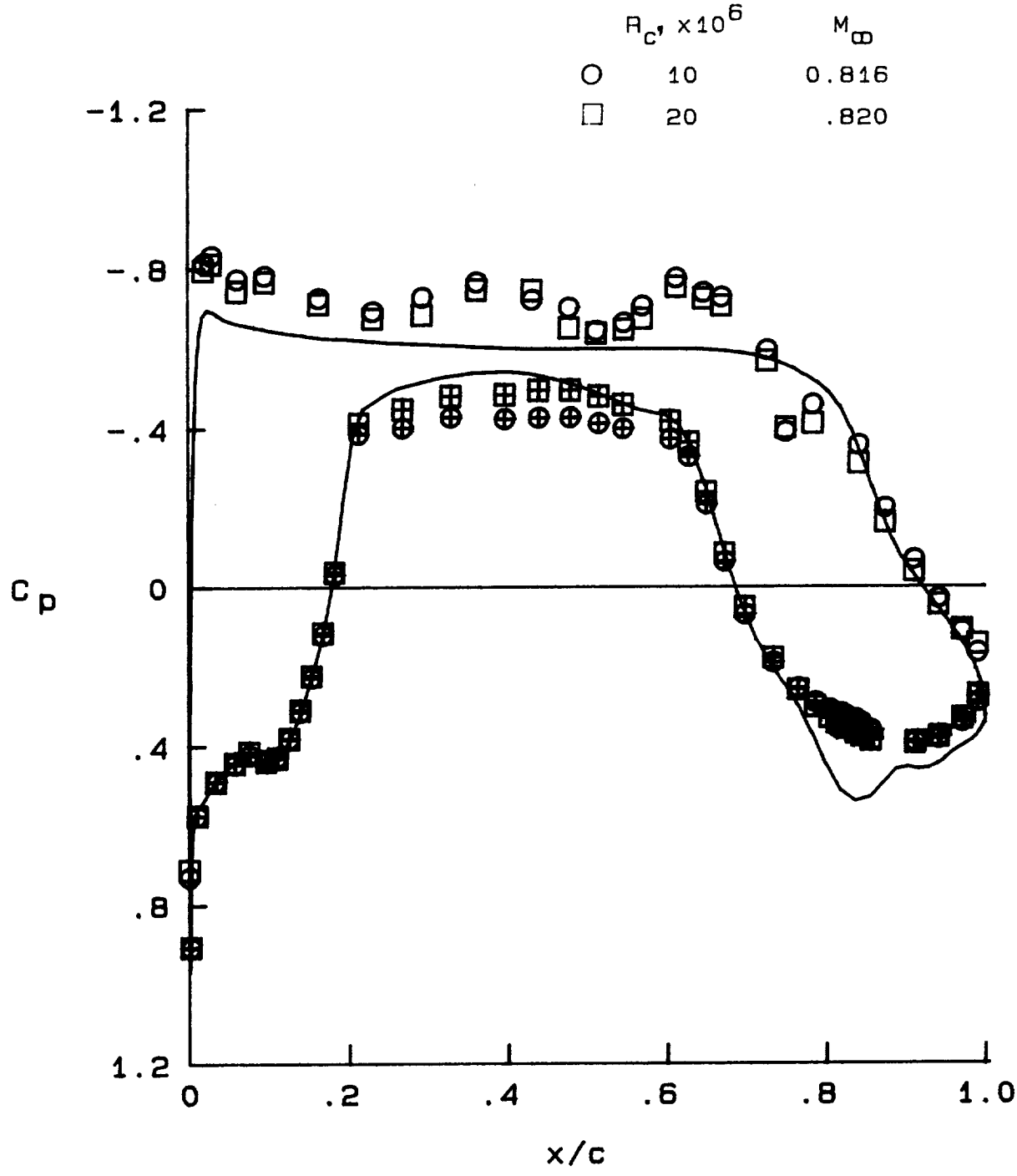

Figure 54. Summary of effect of Reynolds number on experimental chordwise pressure distribution. Floor area strip no. 1; $\alpha = 0.81°$; $\delta_t = 2.6°$; $\delta_c = 0.9°$; $\delta_b = 3.5°$. Open symbols denote upper surface.

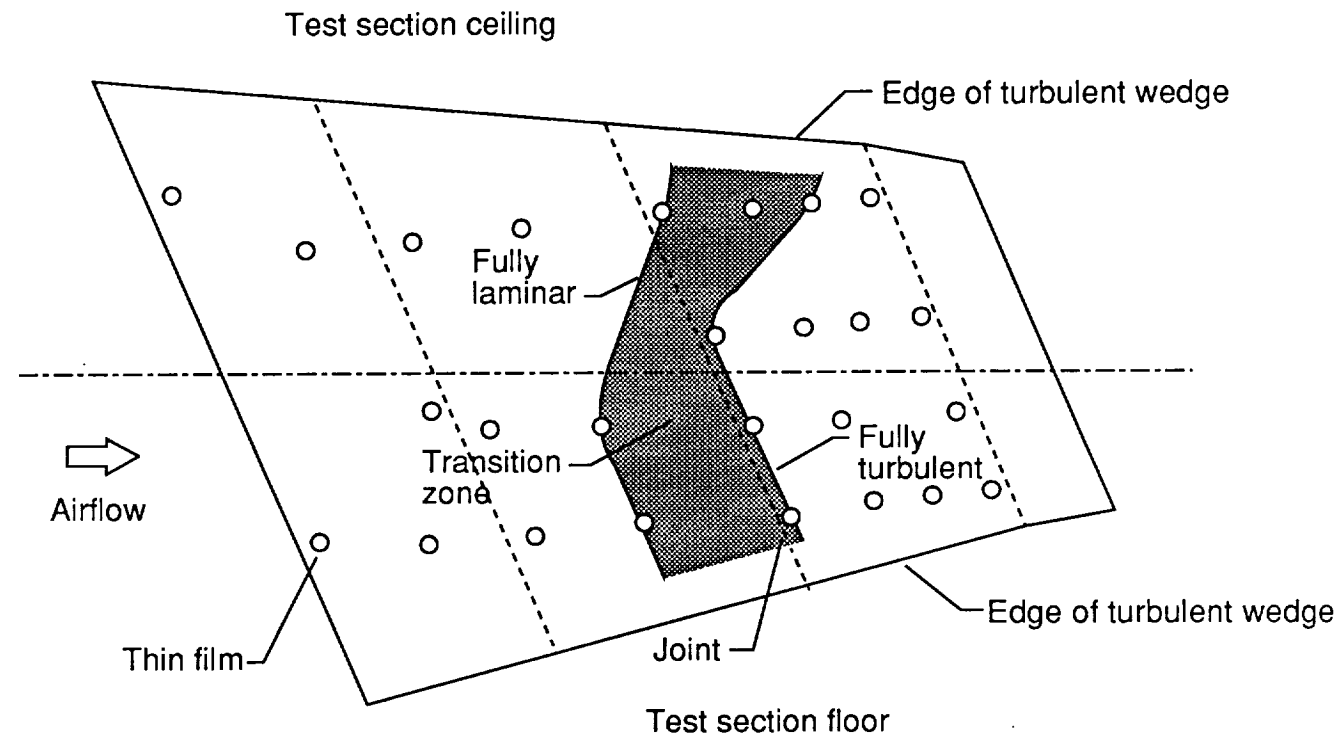

(a) $R_c = 10 \times 10^6$; upper surface.

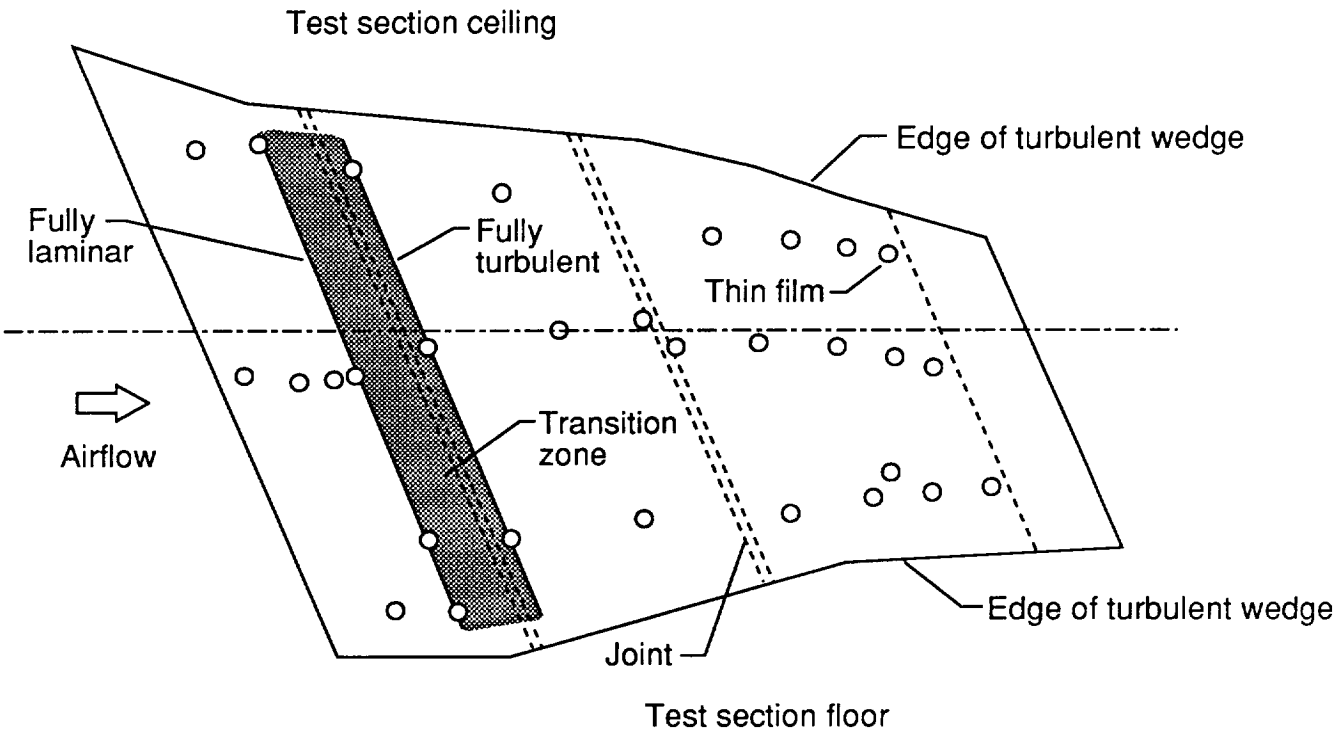

(b) $R_c = 10 \times 10^6$; lower surface.

Figure 55. Transition patterns on initial perforated LFC model with nonsuction forward lower-surface panel.

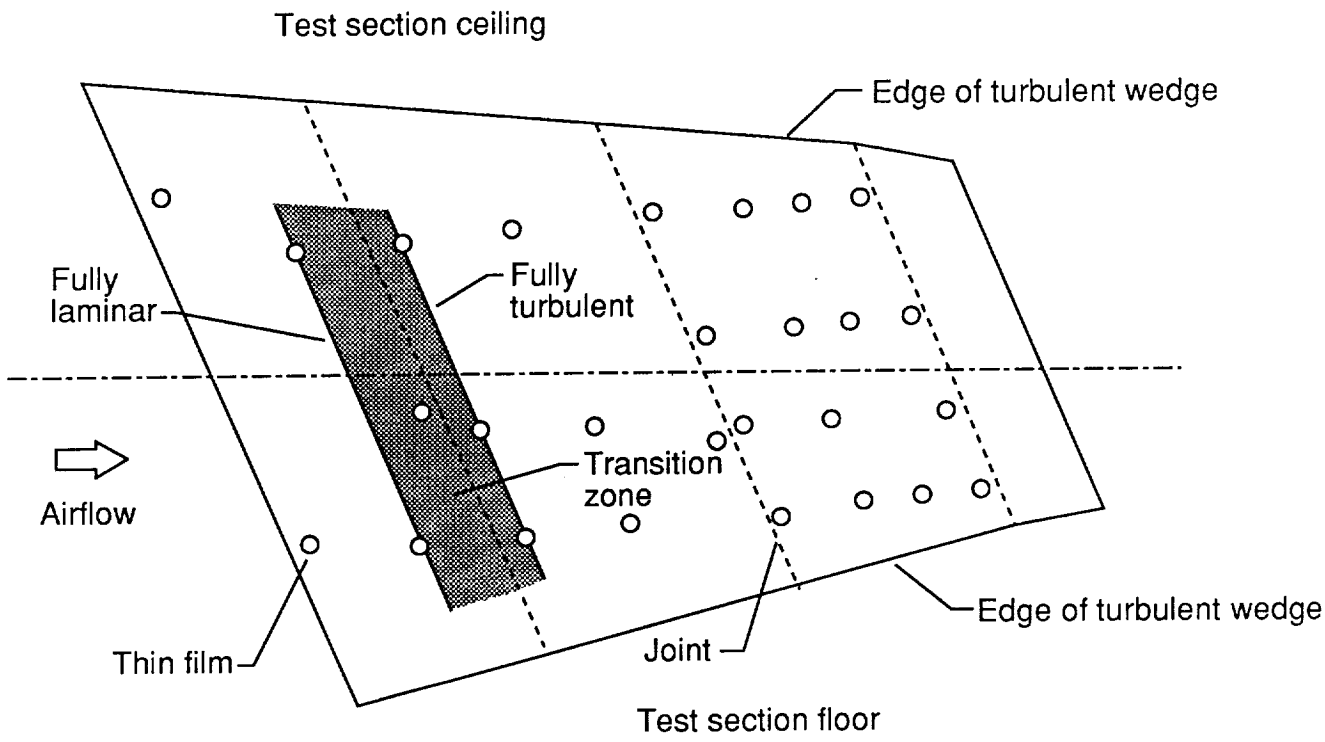

(c) $R_c = 20 \times 10^6$; upper surface.

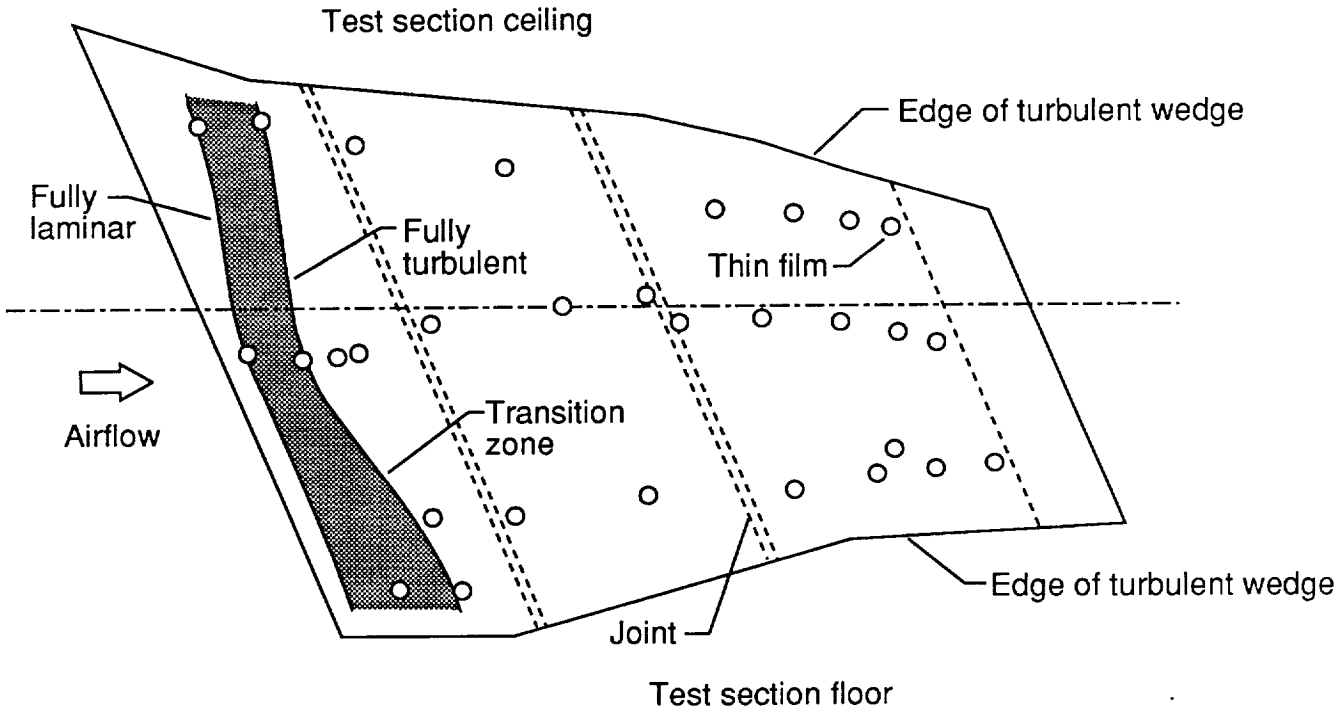

(d) $R_c = 20 \times 10^6$; lower surface.

Figure 55. Concluded.